



Naseer, Shahid Mohammad (2016) *Shaping surface acoustic waves for cardiac tissue engineering*. PhD thesis.

<http://theses.gla.ac.uk/7740/>

Copyright and moral rights for this thesis are retained by the author

A copy can be downloaded for personal non-commercial research or study, without prior permission or charge

This thesis cannot be reproduced or quoted extensively from without first obtaining permission in writing from the Author

The content must not be changed in any way or sold commercially in any format or medium without the formal permission of the Author

When referring to this work, full bibliographic details including the author, title, awarding institution and date of the thesis must be given

Glasgow Theses Service  
<http://theses.gla.ac.uk/>  
theses@gla.ac.uk

# **Shaping Surface Acoustic Waves for Cardiac Tissue Engineering**

A thesis for the degree of

*Doctor of Philosophy*

submitted to the Faculty of Engineering

University of Glasgow

By

**Shahid Mohammad Naseer**

September 2016

## Abstract

The heart is a non-regenerating organ that gradually suffers a loss of cardiac cells and functionality. Given the scarcity of organ donors and complications in existing medical implantation solutions, it is desired to engineer a three-dimensional architecture to successfully control the cardiac cells *in vitro* and yield true myocardial structures similar to native heart. This thesis investigates the synthesis of a biocompatible gelatin methacrylate hydrogel to promote growth of cardiac cells using biotechnology methodology: surface acoustic waves, to create cell sheets.

Firstly, the synthesis of a photo-crosslinkable gelatin methacrylate (GelMA) hydrogel was investigated with different degree of methacrylation concentration. The porous matrix of the hydrogel should be biocompatible, allow cell-cell interaction and promote cell adhesion for growth through the porous network of matrix. The rheological properties, such as polymer concentration, ultraviolet exposure time, viscosity, elasticity and swelling characteristics of the hydrogel were investigated. In tissue engineering hydrogels have been used for embedding cells to mimic native microenvironments while controlling the mechanical properties. Gelatin methacrylate hydrogels have the advantage of allowing such control of mechanical properties in addition to easy compatibility with Lab-on-a-chip methodologies.

Secondly in this thesis, standing surface acoustic waves were used to control the degree of movement of cells in the hydrogel and produce three-dimensional engineered scaffolds to investigate in-vitro studies of cardiac muscle electrophysiology and cardiac tissue engineering therapies for myocardial infarction. The acoustic waves were characterized on a piezoelectric substrate, lithium niobate that was micro-fabricated with slanted-finger interdigitated transducers for to generate waves at multiple wavelengths. This characterization successfully created three-dimensional micro-patterning of cells in the constructs through means of one- and two-dimensional non-invasive forces. The micro-patterning was controlled by tuning different input frequencies that allowed manipulation of the cells spatially without any pre-treatment of cells, hydrogel or substrate. This resulted in a synchronous heartbeat being produced in the hydrogel construct.

To complement these mechanical forces, work in dielectrophoresis was conducted centred on a method to pattern micro-particles. Although manipulation of particles were shown, difficulties were encountered concerning the close proximity of particles and hydrogel to the microfabricated electrode arrays, dependence on conductivity of hydrogel and difficult manoeuvrability of scaffold from the surface of electrodes precluded measurements on cardiac cells. In addition, COMSOL Multiphysics software was used to investigate the mechanical and electrical forces theoretically acting on the cells.

Thirdly, in this thesis the cardiac electrophysiology was investigated using immunostaining techniques to visualize the growth of sarcomeres and gap junctions that promote cell-cell interaction and excitation-contraction of heart muscles. The physiological response of beating of co-cultured cardiomyocytes and cardiac fibroblasts was observed in a synchronous and simultaneous manner closely mimicking the native cardiac impulses. Further investigations were carried out by mechanically stimulating the cells in the three-dimensional hydrogel using standing surface acoustic waves and comparing with traditional two-dimensional flat surface coated with fibronectin. The electrophysiological responses of the cells under the effect of the mechanical stimulations yielded a higher magnitude of contractility, action potential and calcium transient.

## **Acknowledgement**

I would like to sincerely express gratitude to my research supervisor, Prof. Jon Cooper for giving me an opportunity to work in his lab under his guidance. I really appreciate his patience, efforts, support, enthusiasm and constructive suggestions from start of the research till the very end. His profound knowledge of the topic gave me confidence to achieve success in completing this work. Without his support, I would not have been able to network and extend my research at Harvard Medical School and MIT with Prof. Ali Khademhosseini and receive travel grant from Royal Society of Edinburgh. I would like to extend my gratitude to Prof. Ali Khademhosseini for giving me an opportunity to collaborate with this lab and work with his postdoc Su Ryon who is an amazing hard working person and guided me through-out my stay at Harvard.

I would also like to thank Julien Reboud and Rab Wilson for their support and constructive dialogues at times when solutions were hard to come by. Julien has been my mentor and an amazing person from the start of my studies who understood my weakness and strengths despite my shy personality. Furthermore, I would like to sincerely and humbly also thank Andrew Glidle for supporting and guiding me with constructive feedbacks.

All praises be to Allah for giving me strength, blessings, sound health and miracles. I would like to wholeheartedly thank my mum and dad for making it possible for me to get to where I am with their love, guidance, faith and belief in me and financially supporting me. I can't forget my younger brother, Zaahid for constantly cheering me up and being there for me at all times.

I would humbly like to thank my love Sisi Wu kitty baobe for constantly cheering and motivating me during the times when I faced challenges, especially during the dark gloomy rainy days in Glasgow. She has been my emotional support who with her bright smiles and amazing personality had the magic to bring positivity in my life. You are indeed a pious and modest lady. I truly admire and adore you and am honoured to have you in my life. University of Glasgow brought us closer and united us for our future.

Finally I would like to thank my colleagues Emrah, Arslan, Srinivas, Nuno, Alberta, Valeria, Pip, Moritz, Sol, Julio, Parissa and Serena and rest of the lab group for having interesting conversations and helping me during the course of my research.

## Conferences/Publications

1. Shahid M. Naseer., J. Reboud, R. Wilson, J. M. Cooper, “Surface acoustic wave based cell measurements in a disposable chamber”, International congress on Ultrasonics, Metz, France, 2015
2. Shahid M. Naseer, Amir Manbachi, Su Ryon Shin, Mohamadmahdi Samandari, Philipp Walch, Farideh Davoudi, Yuan Gao, Yu Shrike Zhang, Jonathan M. Cooper, Ali Khademhosseini, “3D Micro-organization of Cells in Hydrogel Using Surface Acoustic Waves”, *Advanced Healthcare Materials*, *In submission*
3. Shahid M. Naseer, J. Reboud, V. Zamora, G. Smith, J. M. Cooper, “Effect on cardiac physiology in 3D GelMA hydrogel scaffold under mechanical stimulations using surface acoustic waves”, *manuscript in preparation*

## **Table of contents**

Abstract .....	2
Acknowledgement .....	4
Conferences/Publications .....	6
Table of Contents .....	7
List of Figures .....	14
List of Tables .....	27
List of Abbreviations .....	29
Chapter 1 – Introduction .....	32
1.1 Scope of Tissue engineering .....	32
1.2 Cardiac Tissue engineering .....	35
1.3 Biomaterials : Hydrogel .....	37
1.4 Microscale technologies for tissue engineering .....	38
1.4.1 Photolithography .....	39
1.4.2 Micromolding .....	39
1.4.3 Dielectrophoresis in Cell Engineering .....	40
1.4.4 Acoustics in tissue engineering .....	41
1.4.4.1 SAW microfluidics advantages .....	44
1.5 Aim and Objectives .....	45
1.6 Thesis outline .....	46
Chapter 2 - Literature Review .....	48
2.1 Introduction .....	48
2.2 Tissue engineering: an Engineering Feat .....	48
2.3 Biomaterials and Scaffolds for Tissue Engineering .....	51
2.4 Extracellular matrix .....	52

2.5 Hydrogels in tissue engineering .....	53
2.5.1 Swelling .....	54
2.5.2 Scaffold requirements .....	55
2.6 Cardiac tissue engineering .....	58
2.6.1 Regulating cardiac regeneration and assembly .....	61
2.7 Principles of Surface acoustic waves .....	62
2.7.1 Piezoelectricity and crystal symmetry .....	63
2.7.2 SAW transducers .....	65
2.7.3 Advantages of SAW-based biosensing devices .....	65
2.8 Travelling surface acoustic waves .....	67
2.8.1 Acoustic streaming .....	69
2.9 Standing surface acoustic waves .....	71
2.9.1 Formation of SSAW fields .....	71
2.9.2 Primary acoustic radiation force .....	74
2.10 Patterning in stagnant fluid using SSAW .....	78
2.11 Dielectrophoresis .....	78
2.11.1 Dielectrophoretic force .....	81
2.12 Similarities between SAW and DEP .....	84
2.13 COMSOL Multiphysics modelling .....	84
2.13.1 Finite element modelling of surface acoustic waves .....	84
2.13.2 Electrostatics module modelling for dielectrophoresis .....	86
 Chapter 3 - Materials and Methods .....	 89
3.1 Introduction .....	89
3.2 Microfabrication techniques .....	89
3.2.1 Photolithography .....	89

3.2.2	Preparation of lithium niobate wafers .....	89
3.2.3	Photoresist application and soft baking .....	90
3.2.4	Exposure and post-exposure treatment .....	92
3.2.5	Pattern transfer .....	94
3.2.6	Metal evaporation and lift-off .....	94
3.3	SAW device fabrication .....	95
3.4	DEP device fabrication .....	97
3.5	Cardiac cell isolation protocol .....	98
3.5.1	Neutralize trypsin .....	99
3.5.2	Collagenase treatment .....	99
3.5.3	Preplating .....	100
3.6	Freezing .....	101
3.7	Cell thawing .....	101
3.8	Cardiac fibroblast cell culture .....	102
3.9	Cardiomyocytes seeding and encapsulation .....	102
3.10	Beating analysis .....	103
3.11	TMSPMA coating .....	103
3.12	Agarose preparation .....	104
3.13	Gelatin methacrylate preparation .....	105
3.14	Prepolymer preparation .....	106
3.15	Photoinitiator and UV device .....	106
3.16	Viscosity measurements .....	106
3.17	Swelling characteristics .....	107
3.18	Cell imaging techniques .....	107
3.18.1	Bright field microscopy .....	107

3.18.2	Phase contrast microscopy .....	<b>108</b>
3.18.3	Fluorescence microscopy .....	<b>110</b>
3.18.4	Confocal image analysis .....	<b>112</b>
3.18.5	Scanning electron microscopy .....	<b>113</b>
3.19	Cell alignment evaluation .....	<b>114</b>
3.19.1	Cell counting .....	<b>114</b>
3.19.2	Cell viability-Live/dead assay .....	<b>114</b>
3.19.3	Immunostaining cardiac cells .....	<b>115</b>
3.19.4	F-actin and DAPI staining .....	<b>115</b>
3.20	Stimulation construct preparation .....	<b>116</b>
3.21	Beating analysis .....	<b>116</b>
3.22	Mechanical stimulation using surface acoustic waves .....	<b>117</b>
3.23	Action potential and Calcium imaging .....	<b>117</b>
3.23.1	Image processing algorithm .....	<b>118</b>
3.24	Buffer solution – osmolarity, conductivity and pH measurements .....	<b>119</b>
3.25	Thermal camera imaging .....	<b>119</b>
3.26	Hydrogel and scaffold mechanical properties .....	<b>120</b>
3.27	Numerical modelling of SAW in COMSOL Multiphysics .....	<b>121</b>
3.27.1	Finite element modelling .....	<b>123</b>
3.28	Laser Doppler vibrometer .....	<b>123</b>
Chapter 4 – Gelatin Methacrylate synthesis .....		<b>125</b>
4.1	Introduction .....	<b>125</b>
4.2	Material and methods .....	<b>125</b>
4.2.1	GelMA scaffold preparation .....	<b>125</b>
4.2.2	GelMA swelling analysis .....	<b>125</b>
4.2.3	GelMA porosity analysis .....	<b>125</b>

4.3 Gelatin methacrylate (GelMA) hydrogel synthesis .....	126
4.4 Rheological measurements of GelMA .....	128
4.4.1 Pore size .....	128
4.4.2 GelMA swelling characteristics .....	129
4.4.3 Compressive modulus of GelMA .....	130
4.4.4 Shear elastic (storage) vs shear viscous (loss) modulus .....	131
4.4.5 Viscosity of GelMA hydrogel .....	133
4.5 Conclusion .....	134
 Chapter 5 - SAW device characterization .....	 135
5.1 Introduction .....	135
5.2 Material and methods .....	135
5.2.1 Device and experimental setup .....	135
5.2.2 Data Analysis .....	136
5.3 SAW device – Slanted finger IDTs (SFIDTs) .....	136
5.4 Temperature effect on lithium niobate wafer .....	139
5.5 Quantifying Laser Doppler vibrometry .....	140
5.6 Chamber design and characterization .....	143
5.7 SAW device setup and quantifying acoustic forces .....	147
5.8 SAW compared with DEP technique .....	154
5.9 COMSOL Multiphysics simulations for SAW and DEP forces .....	157
5.9.1 Modelling SAW forces .....	157
5.9.2 Modelling DEP forces .....	162
5.10 Conclusion .....	165

Chapter 6 – Cardiac tissue engineering using SAWs .....	<b>167</b>
6.1 Introduction .....	<b>167</b>
6.2 Micropatterned 3D heart constructs in GelMA using standing surface acoustic waves .....	<b>167</b>
6.3 Live/dead analysis .....	<b>174</b>
6.4 Actin cytoskeleton organization .....	<b>176</b>
6.5 Conclusion .....	<b>182</b>
 Chapter 7 – Electrophysiology of cardiac cells .....	<b>184</b>
7.1 Introduction .....	<b>184</b>
7.2 Theory .....	<b>184</b>
7.2.1 Mechanical stretching of cells using SAW .....	<b>184</b>
7.2.2 Electrophysiological responses of cardiac cells .....	<b>186</b>
7.2.2.1 Beating and contraction characteristics .....	<b>186</b>
7.2.2.2 Action potential and calcium transients .....	<b>187</b>
7.3 Beating characteristics of co-cultured cardiac fibroblasts and myocytes in GelMA .....	<b>189</b>
7.4 Effects of mechanical stimulation on cell orientation and contraction .....	<b>190</b>
7.5 Effects of mechanical stimulation on action potentials and calcium transients .....	<b>197</b>
7.6 Conclusion .....	<b>201</b>
 Chapter 8 - Conclusion and Future Work .....	<b>203</b>
8.1 Conclusion .....	<b>203</b>
8.2 Future Work Introduction .....	<b>206</b>
8.3 Nano-patterning in tissue engineering .....	<b>206</b>

8.4 Creating responsive hydrogels using SAWs .....	208
8.5 In Summary .....	210
References .....	211

## List of Figures

Figure 1.1, schematic representation of tissue engineering principle, a) cells are isolated from patient and cultivated, b) allow in-vitro 2D surface expansion, c) cells are seeded in porous scaffold along with growth factors, d) cells constructs are further cultivated in bioreactors to provide optimal conditions for organization into a functioning tissue, e) once the successfully engineered tissue is formed the construct is transplanted on the injured site to restore function [2]

Figure 1.2, schematic representation of approaches in TE, bottom-up approach (left) and traditional top-down approach (right) [5]

Figure 1.3, schematic representation of in-vitro (a) and in-vivo (b) approached of CTE performed to create engineered scaffolds for implantation [8].

Figure 1.4, schematic representation of micro-scale technologies for tissue engineering, A) scaffolds and bioreactors have been fabricated using micro-technologies to directly or indirectly study cellular behaviour in controlled conditions, B) a microfabricated PDMS scaffold with vasculature embedded into the scaffold, C) different micro-scale techniques to control different aspects on cell-microenvironment interactions [25].

Figure 1.5, schematic diagram of photolithography technique to micro-engineer size and shape of hydrogels.

Figure 1.6, schematic representation of micromolding technique to micro-engineer shape and size of hydrogels.

Figure 1.7, schematic representation of Dielectrophoretic patterning of cells in 3D matrix gel sandwiched between two conductive plates [30].

Figure 1.8, illustration of cell assembly on acoustic nodes, a) random distribution of cells on a low adhesion surface, b) spheroid formation after 2 days of incubation, c) demonstration of standing waves applied to create patterns of spheroids on nodes, d) schematic of node and antinode zones on standing waves in fluidic environment, e) patterned spheroids are immobilized in fibrin hydrogel in culture medium to form larger organoid, f) fluorescence image of fused tissue construct of GFP-HUVEC cell spheroids.

Figure 1.9, schematic of microgel assembly process, a) show the fabrication of microgels using photolithography, b) shows the assembly of microgels during acoustic excitation using acoustic assembler [216].

Figure 1.10, illustration of SAWs propagating and the particle motion on the surface is elliptical in a direction opposite to the wave propagation due to the transverse and longitudinal modes of rayleigh waves [41].

Figure 2.1, is a schematic representation of existing cell-based therapeutical approaches for tissue engineering and regeneration purpose to restore the function of the damaged tissue or organ.

Figure 2.2, a) shows the widening gap between the number of people on the waiting list for kidney organ vs number of donors and b) shows steep increase in percentage of gap since 1991 [86].

Figure 2.3, schematic representation of TE approaches in three stages, i) individual cells, ii) cells with scaffolds, iii) scaffolds alone, which enhance in-vitro microenvironmental factors before forming a tissue substitute [64]

Figure 2.4, schematic representation of roles such as delivering signal factors, recruiting targeted cells and implanting the transplanted cells, and formats, such as gel, porous scaffolds and fibers, of biomimetic scaffolds in tissue engineering [65]

Figure 2.5, representation of main components of ECM and cells at cellular microenvironment illustrating different component involved cell-cell and cell-ECM interaction to provide cell adhesion, proliferation and differentiation in the ECM to mimic natively [68].

Figure 2.6 schematic representation of hydrogel structure, a) an organized tetre-branched network of covalent or non-covalent junctions (visualized as dots), B) random multi-branched network (clear and filled dots), C) a network of entangled chains (shaded), D) a network with defect R, E) two networks with loops in shaded region considered to be defects that do not provide mechanical strength to the hydrogel [69].

Figure 2.7, schematic illustration of triad of TE showing cells, signals, and scaffold that act as template from tissue formation by allowing cells to migrate, adhere and form tissue [4].

Figure 2.8, a, and b) shows confocal image of osteoblasts (green) attached to highly porous collagen-GAG scaffold (red) [71].

Figure 2.9 show statistics published by British Heart Foundation 2014 for Cardiovascular Disease in United Kingdom draw a comparison of deaths between men and women who suffered from majority of cardiovascular diseases as opposed to other diseases such as cancer, diabetes, Alzheimer's [61].

Figure 2.10, schematic representation of employing stem cells with scaffolds and growth factor to produce patches of heart tissue and inject into an infarcted myocardium heart to restore the functionality of a functioning heart [5].

Figure 2.12, schematic representation of longitudinal, (a) direct, (b) converse, (c) shear piezoelectric effects on a piezoelectric substrate [75].

Figure 2.13, schematic representation of SAW travelling motion just like waves roll on the surface of lake or an ocean. Due to the rolling motion, the wave produces stress up and down the substrate and side to side in the same direction of propagation [97].

Figure 2.14, schematic representation of SAWs generated on piezoelectric substrate a) generation of waves propagating in both directions, b) represents the integration of acoustic wave into a droplet, c) shows wave integration onto a superstrate through a coupling layer of water or gel d) shows slanted-finger IDTs producing a narrow band of waves along with length of the IDTs [98].

Figure 2.15, SAW induced acoustic streaming of Rayleigh SAW excited by IDTs. Upon contact with the liquid SAWs refract and convert to leaky SAW at an angle  $\theta_R$  into the fluid.

Figure 2.16, schematic representation of SSAW modelled in COMSOL Multiphysics software 5.0a, a) computational modelling of SSAW on lithium niobate substrate propagating towards each other, b) model of SSAWs from two opposing IDTs to create 1D patterning (top-view), c) model of SSAWs from subsequent four IDTs designed on the substrate to create 2D patterning (top-view), d) shows the movement of cells (red) moving towards the node on experiencing acoustic waves and bubble (blue) moving towards anti-nodes.

Figure 2.17, schematics illustrating a uniform IDT design with pitch (or period)  $p$  with equally spaced electrodes and a constant electrode overlap  $A$ .

Figure 2.18, schematic representation of SSAW based patterning of group of particles in a stagnant fluid, a) using 1D patterning through two parallel IDTs, b) 2D patterning using two orthogonal IDTs, c) distribution of fluorescent microbeads before and after 1D SSAW is applied, d) demonstrates distribution of fluorescent microbeads before and after 2D SSAW is applied. The aforementioned devices have a narrow frequency patterning range due to design of regular IDTs. By designing slanted-finger IDTs a broader range of frequencies is available allowing dynamic control of particle patterning [95].

Figure 2.19: An electric dipole consisting of two charges  $+q$  and  $-q$ , separated by vector distance  $2a$  which is called length of the dipole.

Figure 2.20: (a) The net force acting on the dipole of strength, (b) Coulombic forces creating net torque [142].

Figure 2.21: (a) Potential distribution of Point-Dipole, (b) Similar potential distribution as a Point-Dipole due to an assumption of formation of effective dipole moment

Figure 2.22: The particle will experience a greater force of repulsion because of high Electric field near the positive electrode (due to nDEP) and if the particle had reversed polarity it would experience a strong force of attraction (due to pDEP).

Figure 2.22: The particle will experience a greater force of repulsion because of high Electric field near the positive electrode (due to nDEP) and if the particle had reversed polarity it would experience a strong force of attraction (due to pDEP).

Figure 3.1: Emission spectrum for Hg-Xe source

Figure 3.2: Different types of lithographic exposures. Contact printing-masks make direct contact with the substrate. Proximity printing- masks are slightly raised above the substrate. Projection printing- the photomask is projected image through a high-resolution lens system onto the substrate [152].

Figure 3.3, shows the fabrication protocol followed for fabricating the IDTs on lithium niobate substrate.

Figure 3.4, a) a cleaned glass substrate, b) spin coat S1818 photo resist, c) exposure under UV light and developed, d) deposition of Ti/Au layer on the substrate, e) lift-off process

Figure 3.5, schematic representing isolation of cardiomyocytes and cardiac fibroblasts from hearts of neonatal rat pups, a) neonatal rat pups were ordered for surgery procedures to isolate hearts, b) hearts from the neonatal rat pups were surgically removed and placed in trypsin, c) the hearts were sliced into thinner pieces using surgical knife under the cell culture hood, d) the heart pieces were exposed to enzymatic digestion using Collagenase type II, e) centrifuged cells (cardiomyocytes and cardiac fibroblasts) settled at the bottom of the Eppendorf tubes, f) plating of cardiac fibroblasts in the experimental samples in 12-well cell culture plate.

Figure 3.6, Schematics of encapsulating cells in a hydrogel matrix and crosslinking the fibres to promote cell proliferation to generate an engineered tissue

Figure 3.7: Chemical structure of agarose [210]

Figure 3.8: Schematic illustration of the phase shifts in a cell. There are very small differences between in phase shift between surrounding medium and cell cytoplasm (b) and the cell nucleus (c) while there is no phase shift in the surrounding medium (a) [158].

Figure 3.9: Schematic illustration of the phase contrast microscope [158]

Figure 3.10, Jablonski diagram illustrates absorption and emission mechanisms of fluorescence, phosphorescence, or delayed fluorescence. A) When a fluorophore absorbs light energy, it is usually excited to a higher vibrational energy level in the first excited state (S1) before rapidly relaxing to the lowest energy level. B) Phosphorescence decay is similar to fluorescence, except the electron undergoes a spin conversion into a forbidden triplet state (T1) instead of the lowest singlet excited state. Emission from the triplet state occurs with lower energy relative to fluorescence, hence emitted photons have longer wavelengths. C)

With delayed fluorescence, the electron first decays into the triplet state, and then crosses back over into the lowest singlet excited state before returning to the ground state ( $S_0$ ) [158].

Figure 3.11: Schematic diagram of a microscope for fluorescence microscopy [157]

Figure 3.12 shows basic construction of SEM [207].

Figure 3.13, the path of laser beam travelling on the specimen in a confocal laser microscope [210].

Figure 3.14, a) setup of Instron (Instron 5943) instrumentation for measuring mechanical properties of hydrogel scaffolds, b) Mold with 1 mm depth and cylindrical samples obtained using a 5mm diameter puncher, c) shows the cylindrical plates attached to the Instron, where samples are placed at bottom plate and the top plate is vertical positioned at the surface of the scaffold without collapsing it.

Figure 3.15, illustration of a LDV setup used for determining vibration velocity and displacement at a fixed point over a defined region using Doppler effect by sensing the frequency shift of back scattered light from the vibrating piezoelectric surface [159].

Figure 4.1, schematic representation of preparation of photo-crosslinked GelMA hydrogel, a) shows the reaction of gelatin with methacrylic anhydride at 50C for grafting methacryloyl substitution groups. This modification occurs at the site of primary amine and hydroxyl groups. The RGD domain is highlighted in red along with their chemical structure in the GelMA chains [185-187]. B) Shows the reaction during the photo-crosslinking of GelMA to form hydrogel network. The free radicals generated from photo-initiator that initiate the chain polymerization of methacryloyl substitution cause for the propagation to occur on same chain and on different chains. The termination step occurs between two of these propagating chains or between one propagating chain and a second radical [188-190]

Figure 4.2, a) SEM images of 10% and b) 5% concentration of GelMA photo-crosslinked with 0.25%(w/v) I2959 photoinitiator. Sample mounted on studs and sputter coated with 8nm Iridium layer using Emitech K575X and examined in SEM (FEI XL30 ESEM FEG) operated at 5kV in vacuum mode. Porosity was determined using the projected area of the pores for multiple pores using NIH ImageJ software. c) The largest pores were achieved with lower concentration of GelMA for the same amount of photo-initiator at same UV exposure rate of 12 secs (n=3) (p<0.05).

Figure 4.3, swelling properties of methacrylated gelatin hydrogel. The mass swelling ratio of GelMA at different % (w/v) and degree of methacrylation have shown significant differences, as the swelling ratio increases the degree of methacrylation decreases (n=3) (p<0.05).

Figure 4.4, a,b) shows cylindrical 3D scaffold of 5% GelMA (w/v) prepared for quadruplicate compressive mechanical testing (Instron 5542) using 0.25% photo-initiator exposed to UV

light (360-480nm) for 12 secs at 800mW, c) characterization of GelMA hydrogels with different concentrations to measure compressive modulus. It was noted that the compressive modulus of 5% GelMA scaffold seeded with cells was higher than 5% GelMA without cells indicating the cells being adhered into the matrix due to the porous network (n=3).

Figure 4.5, shows the dynamical rheological observations of crosslinked and non-crosslinked GelMA of different concentrations stored at 4°C, a,b,c) shows the effect of different degree of concentration of GelMA (5%, 7%, 10% respectively) with increase in temperature in presence of 0.25% (w/v) photo-initiator. The samples were brought to room temperature and then immediately exposed to UV light. d,e) show the effect on storage and loss modulus in absence of photo-initiator (n=3).

Figure 4.6, a,b) shows the increase of viscosity as the temperature decreases for different concentration of GelMA with 0.25% (w/v) photo-initiator (I2959) (n=3)

Figure 5.1, schematic of SAW Device microfabricated IDTs patterned on LiNbO<sub>3</sub> 128° Y-X cut double polished substrate, a) parallel identical SFIDTs designed at opposite ends of the wafer to create 1D patterning at centre region of interest b) four identical SFIDTs orthogonal IDTs designed to create 2D patterning of bioparticles, c) shows varying thickness width of the SFIDTs with magnified image of either ends of the IDTs (124.69µm and 332.5µm, respectively).

Figure 5.2, shows the resonance frequencies observed from the excitation of SFIDTs at frequency range of 3MHz-8MHz, a) for one end of SFIDTs, b) for opposite designed SFIDTs at the other end showing a resemblance of resonance frequencies measured that is important for creating phase match at creating acoustic waves. The measurements show the resonance performance of the SAW transducer at four frequencies 3.4MHz, 4.6MHz, 5.34MHz and 6.4MHz respectively using network analyser (n=2).

Figure 5.3, a) shows infrared image (IR) of an orthogonally active SFIDTs SAW device using an IR camera (Fluke Ti-25), b) temperature changes on the surface of the wafer during the application of 3.4MHz frequency and c) temperature changes on the surface of piezoelectric wafer on applying 6.4MHz. At least three measurements were taken (n=3).

Figure 5.4, a) shows the setup of the Laser Doppler Vibrometry (Polytec UHF-120) to investigate the surface displacement on two opposite SFIDTs for SSAWs, b) transducer being used to investigate the displacement at the centre of the SFIDTs over an area of 1cm<sup>2</sup>, c) schematic representation of a Polytec vibrometer system used for determining the displacement at fixed region. Using Doppler-effect principle the system senses the frequency shift of reflected scattered signal from the source.

Figure 5.5, schematic of working principle of SAW beam generated by SFIDTs, a) shows the excitation of SAW waves at 3.4MHz and 6.4MHz through surface displacement on the LiNbO<sub>3</sub> 0.5mm thick wafer obtained by LDV, b) shows the graph of working frequency

(3.4MHz and 6.4MHz) over a aperture of 1.33mm ( $\pm 0.5$ mm) using the results from LDV and IR camera (n=3).

Figure 5.6, shows the surface displacement magnitude measured by LDV (Polytec UHF-120) using water as coupling layer and gel as a coupling layer at a) 3.4MHz and b) 6.4MHz at 180mW (n=3).

Figure 5.7, a) shows the rectangular gasket chamber of 0.8 x 0.6 cm dimension and depth of 0.8 mm. The internal hollow dimensions were 0.6 x 0.4 cm, b) schematic representation of the sandwiched superstrate chamber, c) experimental setup of the superstrate used with sterilized water as a coupling agent with LiNbO<sub>3</sub> wafer.

Figure 5.8, schematic representation of characterizing the SAWs to generate patterns in the chamber by adjusting the power level at input frequencies of 6.4MHz, -5dBm. a) shows the random distribution of fluorescent beads (6 $\mu$ m) in 5% GelMA (w/v), b) The acoustic streaming patterns were observed when on excitation of SSAWs at high power (220mW) and large inner perimeter of chamber, c) fluorescent beads were forming aggregates due to formation of streaming vortex.

Figure 5.9, schematic representation of characterizing the SAWs to generate patterns in the chamber by adjusting the power level at input frequencies of 6.4MHz, -14dBm. a) shows the randomly distributed fluorescent beads in 5% GelMA (w/v), b) The acoustic wavy distorted patterns were observed when on excitation of SSAWs, c) the wavy and distorted patterning of beads was observed and the yet parallel arrangement of beads were not observed.

Figure 5.10, Figure 5.10, schematic representation of cell alignment due to SSAWs to generate patterns in the chamber by adjusting input frequency at 6.4MHz, -10dBm. The acoustic 1D patterns were observed when on excitation of SSAWs without creating fluid turbulence or vortex formations in the medium using a phase contrast microscope at magnification (5x).

Figure 5.11, show 1D patterning of cardiac fibroblasts in 5% GelMA (w/v) before photo-crosslinking and polymerization of the hydrogel with UV at 12sec. 1D patterning at a) frequency 3.4MHz, b) frequency 6.4MHz sat 180mW by oppositely paired IDTs on the LiNbO<sub>3</sub>. c and d) show formation of cell aggregates due to 2D patterning of cells at 4.6MHz using the orthogonally excited SFIDTs at 220mW.

Figure 5.12, a) schematic representation of SSAWs exhibited on the particles that push them towards the pressure nodes and pattern cells in lines corresponding to the wavelength, b) schematics of the setup employed to generate SSAWs on LiNbO<sub>3</sub> wafer using one dimensional waves created by SFIDTs, c) top-view of the microfabricated SAW device, D) image of the experimental setup including the transducers on piezoelectric wafer placed on heat sink.

Figure 5.13, a) schematic representation of forces acting on a particle before experiencing acoustic force causing it to move towards the pressure node, b) experimental image of cells dispersed randomly in 5% GelMA medium in the chamber, c) shows the 1D alignment of cardiac fibroblast cells when exposed to SSAWs at 6.4MHz at 180mW.

Figure 5.14, a) shows the distribution of ARF acting on cardiac fibroblasts pushing them towards the pressure node trap at 3.4MHz and b) 6.4MHz respectively. It can be seen that at higher frequency higher ARF was experienced by the cells, c) shows the motion of particles in SSAW field at 3.4MHz in different mediums, d) represents the alignment time of the cells at 3.4MHz SSAW in different mediums. The alignment time was faster for beads in buffer medium as opposed to beads suspended in GelMA or agar (n=3).

Figure, 5.15, shows the dependence of ARF with respect to particle size, fluorescent beads (6 $\mu$ m), cardiac fibroblasts (10 $\mu$ m), MCF-7 (17 $\mu$ m) cells, as the dimension of the particle increases the larger the force it will experience. As the diameter of the particle increased the acoustic forces increased in 5% GelMA (w/v) at different frequencies (3.4MHz and 6.4MHz)

Figure 5.16, shows spatial patterning of cells in SSAW region at 3.4MHz and 6.4MHz in the chamber on LiNbO<sub>3</sub> substrate (n=5) (\*\*p<0.05)

Figure 5.17, shows the phase contrast images of the patterned co-cultured cardiac fibroblasts and cardiomyocytes in 5% GelMA concentration at frequency 3.4MHz 180mW in the photo-crosslinked hydrogel. a) patterning on day 0 of experiments, b) patterning on day 1 on post culture, c, d) show the dislodgement of cells from the alignment positions on day 2 of the culture. (Scale bar 200 $\mu$ m)

Figure 5.18, shows the maintained alignment of cardiomyocytes and cardiac fibroblasts cells in 3D scaffold of 5% GelMA at 6.4MHz even on, a) day 0, b) day 2 of the cell culture. (Scale bar 200 $\mu$ m)

Figure 5.19 a) shows microfabricated gold SFIDTs on LiNbO<sub>3</sub> substrate and titanium deposited DEP IDTs on a glass slide (1mm) which acts as a superstrate on the piezoelectric substrate when coupled using an ultrasonic gel. The SAWs excited at complementary to the DEP in the region of interest. Both the DEP and ARF depend on the radius of the particle, b) shows random dispersion of polystyrene beads in the buffer medium of 8mS/m conductivity at pH 7.2. When the SAWs are generated at 3.4MHz beads align at the closest pressure nodes. Upon turning ON the DEP device at 10Vp-p, 3.8MHz the beads exhibited n-DEP .c) When the SAWs are generated at 3.4MHz the beads align at the pressure nodes as shown and when an AC voltage of 10Vp-p at 60KHz is applied the beads were aligned orthogonal to the IDTs exhibiting p-DEP.

Figure 5.20, schematic representation of numerical modelling of ARF at 6.4MHz on LiNbO<sub>3</sub> showing the dark and bright field regions of pressure and anti-pressure nodes, a) cross-sectional view of acoustic wave device setup used for patterning cells encapsulated in GelMA in the chamber, b) shows the random distribution of particles at t=0sec in x- and y-axis, c)

shows the particle movement towards pressure nodes upon experiencing acoustic forces in x- and y-axis ( $t = 0.05\text{ms}$ )

Figure 5.21, a) shows the z-axis of the acoustic pressure field creating pressure and anti-pressure nodes as demonstrated by elliptical and circular lines respectively which causes cells to move from one region to another as shown by midline A-B, b) shows the random dispersion of cells at time  $t=0\text{secs}$ , c, d) show the movement of particles toward the pressure nodes in 0.02 and 0.05 msec.

Figure 5.22, a) graph represent the acoustic force decreases as the cells approach the pressure node which is in similar terms with experimental data, b) represents velocity of the cells travelling towards the pressure and decreases in magnitude as it gets closer to it.

Figure 5.23, a) shows the pressure (red) and anti-pressure (blue) fields corresponding to SSAWs to create patterning of cells in the x-y axis and the movement of particles away from the anti-pressure nodes towards the pressure nodes at frequency 6.4MHz, b) shows the movement of particles moving to adjacent pressure fields, c) show the particles symmetrically aligning at the pressure fields as observed in a x-y axis plane.

Figure 5.24, schematic representation of the simulation of 2D orthogonal acoustic waves generated at 4.6MHz and creating a 2D patterning due to standing waves which is corresponded with the complex patterns achieved during experimental visualizations using cardiac fibroblasts in 5% GelMA pre-polymer solution.

Figure 5.25, a) shows the 3D geometry of the model created in electrostatics module of COMSOL Multiphysics software 5.0a and the slice analysis of the DEP force in log scale at  $10\text{Vp-p}$ , b,c,d) are plots of electric field,  $\nabla E^2$  ( $\text{V}^2/\text{m}^3$ ) gradient around the edges of the electrodes at varying heights of  $40\mu\text{m}$ ,  $20\mu\text{m}$  and  $10\mu\text{m}$  respectively. It was noted that as the height decreased the force increased.

Figure 6.1, schematic representation of the experimental setup, a) shows the generation of SSAWs on  $\text{LiNbO}_3$  substrate by SFIDTs. The input frequencies applied in this work are 3.4MHz and 6.4MHz at 180mW. The SSAWs integrate in to the PMMA chamber of 0.8mm thick on top of 1mm thick TMSPMA glass slide (superstrate) filled with cell encapsulated

Figure 6.2, a) shows 3D scaffold of 5% (w/v) GelMA hydrogel, 0.25% (w/v) photo-initiator (I2959) photo-crosslinked at 15sec on a TMSPMA cut glass piece. b,c) The image also shows the thickness retained in the scaffold after removal of cover glass and PMMA chamber therefore creating a 3D architecture of patterned cells in this scaffold.

Figure 6.3, phase contrast images of cardiac fibroblasts. Column A shows the patterning of cardiac fibroblasts cells at 3.4MHz (180mW) in 5% GelMA (w/v) 3D hydrogel scaffold. The spatial distance corresponded with the theoretical wavelength of  $320\mu\text{m} \pm 10\mu\text{m}$  with assembling time of 1.5 secs (I) Alignment of cells before UV irradiance, (II) and (III) show alignment of cells after UV treatment, (IV) shows magnified image of single cell alignment. Column B shows patterning of cells at 6.4MHz at the input power show closer alignment of

cells due to the shorter wavelength of the generated waves. (I) alignment of cells before UV treatment, (II) show cardiac fibroblasts aligned at the pressure nodes of the waves before UV, (III) shows the single cell alignment between three pressure nodes, (IV) show magnified image of single cell alignment. Post exposure has shown increased fidelity of cells in the hydrogel.

Figure 6.4 shows the cardiac cell density dependence on two different frequencies, 3.4MHz and 6.4MHz in 5% and 10% GelMA concentration hydrogel. a) The alignment time shows the dispersion of aligned cells after switching off the SAW device but without UV crosslinking in pre-polymer solution of 5% GelMA

Figure 6.5 a) shows the intactness of the patterned cells after switching off the SAW device (3.4MHz and 6.4MHz) and crosslinked under a UV chamber for 12s, b) Shows the spatial distance of alignment of co-cultured cells in the hydrogel scaffold at different wavelengths of the acoustic waves generated using SFIDTs on the piezoelectric substrate in the pre-polymer solution of 5% GelMA (w/v) containing cardiac fibroblasts and myocytes.

Figure 6.6, Show the viability of cardiac fibroblasts in the 3D construct of 5% (w/v) GelMA with 0.25% (w/v) photo-initiator (I2959) on consecutive days of cell culture in cardiac media. Live cells were stained with Calcein AM (green) and dead cells stained with ethium homodimer (red). The hydrogel scaffold photo-crosslinked at 12sec under UV light.

Figure 6.7 , shows quantification of percentage of viability of co-cultured cardiac fibroblasts and cardiomyocytes in 5% GelMA at different UV exposure rates for a period of 7 culturing days (n=5) (\*\*p<0.05)

Figure 6.8, co-culture of cardiac fibroblasts and cardiomyocytes marked with F-actin and DAPI stains in 5% GelMA 3D scaffold micro-patterned at 6.4MHz, a) image of patterned stretching myofibers on day 5 (Scale bar 100µm), b) cell alignment and proliferation can be visually seen on day 7 of culture along the patterns created, c) on day 9 cell expansion and adherence was observed with alignments intact (x10), d) magnified image showing cell nucleus and f-actin fibre stretching and elongating along the patterns and spreading in the scaffold

Figure 6.9 shows immunohistochemical staining to analyse protein expression of differentiating cardiac cells fixed with paraformaldehyde and permeabilised with 0.5% Triton X-100 in 3% paraformaldehyde and stained with Connexin43 (CX43), Sarcomeric  $\alpha$ -actinin and nucleus stained with DAPI. These images show the expansion of cardiac myofibers necessary for cell-cell communication between each aligned pattern. A1 and B1 images show the staining of connexin43.

Figure 6.10 shows immunohistochemical staining to analyse protein expression of differentiating cardiac cells fixed with paraformaldehyde and permeabilised with 0.5% Triton X-100 in 3% paraformaldehyde and stained with cardiac troponin I (labelled secondary

antibody, green), Sarcomeric  $\alpha$ -actinin and nucleus stained with DAPI. These images show the formation of cell and clonal expansion of cardiac cells.

Figure 6.11, A and A1 shows staining of cells to show gap junction formation in the hydrogel and striations of sarcomeric organization observed in the scaffold

Figure 6.12, a) shows 20X image showing cardiac fibroblasts and cardiac myocytes stained with F-actin and DAPI at the pressure of standing wave at 6.4MHz elongating in the direction of alignment on day 5, b,c) show confocal images of cardiac fibroblasts and cardiac myocytes cells in the 3D scaffold. The image analysed consisted of 20 Z-stacks in order to show the alignment and development of cell growth 3-dimensionally. In this image the alignments are different heights and growing x-, y-, and z- axis, d) characterizing the layer of patterns by measuring the pixel density of the alignment using the MATLAB code to indicate the presence of alignments at different heights of the 3D scaffold.

Figure 7.1, schematic representation of in-vitro assembly of cardiomyocytes in hydrogel being exposed to physical stimuli using SAW based platform to create a functional syncytium.

Figure 7.2, schematic representation of uniform longitudinal stretching of the scaffold in perpendicular direction of patterned cells.

Figure 7.3, schematic representation of different layers in myocardium, showing cardiomyocytes and sarcomeres [203].

Figure 7.4, representation of 1 cycle of mechanical stimulation applied every 30 sec activation and 30 sec relaxation period using SFIDTs at 3.4MHz and 180mW.

Figure 7.5, Co-cultured cardiac fibroblasts and cardiomyocytes beating characteristics in 5% GelMA which was photo-polymerized for 12sec using UV light. The quantitative analysis of synchronous beats per minute (BPM) of different samples (n=3) from day 6 to day 12 demonstrating an increase in beating, with peak reaching at day 9, when cells have matured and decreased as the culturing days increased. The beating frequency was higher for cells that were patterned by standing surface acoustic waves than the cells were randomly distributed in the GelMA hydrogel scaffold.

Figure 7.6, A) shows hiPSC-cardiomyocytes (GE Cytiva Cardiomyocytes) seeded on well plated coated with Fibronectin providing a 2D platform, B) shows cardiomyocytes encapsulated on a TMSPPMA glass slide coated with fibronectin but not exposed to SAWs, C) show clear elongation growth of cardiomyocytes in 3D scaffolds when stimulated mechanically with SAWs at 3.4MHz, 180mW for 3mins during consecutive cell culture days. SAWs control and align the cell nucleus and actin in the direction of propagation that affects the cell migration as shown.

Figure 7.7, hiPSC-cardiomyocytes alignment, stretching and elongation of cardiomyofibers on day 7 inside the GelMA hydrogel. Representative images of F-actin and DAPI stained cells in 5% GelMA (Scale bar: A-20 $\mu$ m, B, C, D - 10 $\mu$ m)

Figure 7.8, shows the contraction of hiPSC-cardiomyocytes (GE cytiva) seeded GelMA 5% constructs represented by motion maps obtained from image analysis of video data processed in Clyde Biosciences ImageJ plugin. The contour image (A) shows the no displacement of cell contractility at  $t = 0$ ms and the contraction of cardiomyocytes starting from bottom of the frame at  $t=10$ ms on a flat 2D well surface bottom coated with fibronectin, (B) shows the no displacement of cell contractility at  $t = 0$ ms and the contraction of hiPSc-cardiomyocytes at  $t=10$ ms in a 3D 5% GelMA hydrogel scaffold exposed to mechanical stimulations at 3.4MHz on a periodic cycle. The single cell contraction was observed at  $\geq 40$ x magnification (Scale bar: 10 $\mu$ m)

Figure 7.9, contraction rates of hiPSC-cardiomyocytes in three different samples. The video was visually observed and the data quantified using ImageJ plugin that was developed by Clyde Biosciences. The plugin will record 100 frames of images taken in 10 secs and create a series of contour images as shown earlier. A video processing algorithm based on “block-matching” methodology was written in Matlab and linked into ImageJ. The different dark and bright spots are then quantified through the plugin automatically with respect to time, pixel density and cell displacement. Image a) shows control sample 1 consisting of cell seeded on a 2D surface of well-plate coated with fibronectin to allow cell adhesion has shown 1/5<sup>th</sup> of lower amplitude when compared to sample 2 consisting of cells seeded into 3D hydrogel scaffold for duration of 1msec, b) shows the contraction amplitude of both the control samples in 1ms, c) shows the contraction amplitude of cardiomyocytes 8-fold times higher than the control samples due to cell alignment and mechanical stimulation over 10sec, d) shows the higher amplitude of contraction of cells in 3D micro-patterned and mechanical stimulated sample in 1ms.

Figure 7.10, quantifying contraction of cardiomyocytes seeded in different mediums, a) the contraction amplitude on 2D coated cell culture well plate with fibronectin yielded the peak contraction on day of  $100 \pm 10$  contractions, but b) when cells were seeded with 5% GelMA hydrogel the contraction amplitude increased on the day of maturation (day9), c) and when the scaffolds were mechanical stimulated periodically during the in-vitro culture days the contractions were significantly higher on day 9 with peak reaching  $1000 \pm 100$  contractions. The experiments were repeated at least three times ( $n \geq 3$ ) compared to the three different samples.

Figure 7.11, Spontaneous action potential and ion channel recording, a) the generated action potentials stained with voltage-sensitive dye di-4 ANEPPS in a control sample of 2D flat surface coated with fibronectin and, b) 3D scaffold 5% GelMA hydrogel sample which was stimulated periodically with SAWs at 3.4MHz, c) show an increase in magnitude of action potential when comparing both the samples for at least three samples ( $n \geq 3$ ).

Figure 7.12, Recording of calcium transients were measured as peak fluorescence in Fura-2 AM (340/380nm) cultured a) on flat surface coated with fibronectin, b) cultured in a 3D scaffold of 5% GelMA and micropatterned, c) comparing magnitude of fluorescence intensity between the two different samples. At least three samples ( $n \geq 3$ ) were experimentally tested for measuring calcium transients.

Figure 8.1, a) schematic representation of electrospinning nanofibers for tissue engineering, b) anisotropic nanofibers aligned to organize cells to enhance cell-cell interactions and create tissue-like structure [191]

Figure 8.2, schematic representation of 1D nanowire patterning using SSAWs, b) shows patterning of Silver (Ag) nanowires and microspheres in 1D SSAW field showing their relative position with respect to alignment [194].

Figure 8.3, shows the effect of low frequency ultrasound pulse intensity (A) and duration (B) on release of trypan blue (dye) in hydrogel (dextran-CHO/CMC-ADH) at 37°C [198]

Figure 8.4, shows the ultrasound standing wave field exposure altering collagen fibre microstructure collected antinode(A) and node (B) using second harmonic generation microscopy (SHGM) [199]

## **List of Tables**

Table 2.1 Acoustic wave generation on different piezoelectric substrates

Table 2.2: Boundary Conditions for Electrostatics implemented in COMSOL Multiphysics software [14]

Table 3.1 – UV Light illumination regions

Table 3.2, degree of methacrylation of GelMA

Table 3.3. Simulation Model Parameters at 37°C

Table 5.1: Constants and Equations used in Electrostatics Module in COMSOL Multiphysics

## Author's Declaration

The work presented in this thesis was conducted by the author and has not previously been submitted for a degree or diploma from this university or any other institution.

Shahid Mohammad Naseer

## List of Abbreviations

2D	Two-dimensional
3D	Three-dimensional
AC	Alternating current
ACF	acoustic contrast factor
ANEP	aminonaphthylethylenylpyridinium
AP	Action potentials
ARF	Acoustic radiation forces
BAW	Bulk acoustic waves
CTE	Cardiac tissue engineering
CHF	Congestive heart failure
CAD	Coronary artery diseases
CNT	Carbon nanotubes
DC	Direct current
DEP	Dielectrophoresis
ECM	Extracellular matrix

FEM	Finite element method
GelMA	Gelatin methacrylate
GMP	Good manufacturing practices
h-iPSc	human-induced pluripotent stem cells
IDT	Interdigitated transducers
iPSc	induced pluripotent stem cells
LDV	Laser Doppler vibrometry
LOC	Lab-on-a-chip
n-DEP	negative-dielectrophoresis
PCM	Phase contrast microscopy
PMMA	polymethyl methacrylate
PDMS	Polydimethylsiloxane
PAC	Photoactive compound
PI	Photo-initiator
PBS	Phosphate buffered saline
pDEP	positive-dielectrophoresis

RGD	Arginine, glycine, aspartic acid
RF	Radio frequency
SEM	Scanning electron microscope
SAW	surface acoustic waves
SSAW	standing surface acoustic waves
SFIDT	Slanted-finger interdigitated transducers
TMAH	tetramethylammonium hydroxide
TMSPMA	3-(Trimethoxysilyl)propyl methacrylate
UV	Ultraviolet

# Chapter 1

## Introduction

### 1.1 Scope of Tissue engineering

Tissue damage or losses due to congenital diseases, trauma or accidents as well as end-stage organ failures are the two major causes of illness and death. The modalities conventionally employed for treating these are either the transplantation of tissues and organs (autograft, allograft/xenograft) or by implanting mechanical assist devices [1]. Although medical research has provided such treatments to improve the patient survival rate, there are limitations that seriously affect the patient. For example, autografts, which are tissues isolated from the same patient, have limitation such as donor-site morbidity, infection risks and lack of availability. Allografts (tissues or organ isolated from another individual but of the same species) whilst xenografts (tissues or organs isolated from another species) both of which pose serious risks of immunocompatibility [1]. All these could cause the patient to face lifelong immunosuppression treatment. Increased risk of infection, viral disease transmission, tumor developments are some of the serious issues that therefore need to be addressed by biomedical research [3].

Organ or tissue transplantation is an expensive and complex surgical task which is limited by donor shortages and the limited time-frame for the organ to be preserved outside the body. Mechanical replacement devices such as artificial hearts and stents are affected by thrombo-embolization, infections and durability [6]. Engineering and developing tissues in-vitro to specifically meet the needs of individual patients can overcome the shortcomings of organ or tissue transplantation. Thus tissue engineering has emerged as a novel therapeutic methodology to reconstruct and repair the damaged organ or tissue. The definition of tissue engineering has been widely defined as the application of biological, chemical and engineering principles to restore, repair and regenerate living tissues using biomaterials, cells and growth factors either alone or in combination (Figure 1.1) [7].

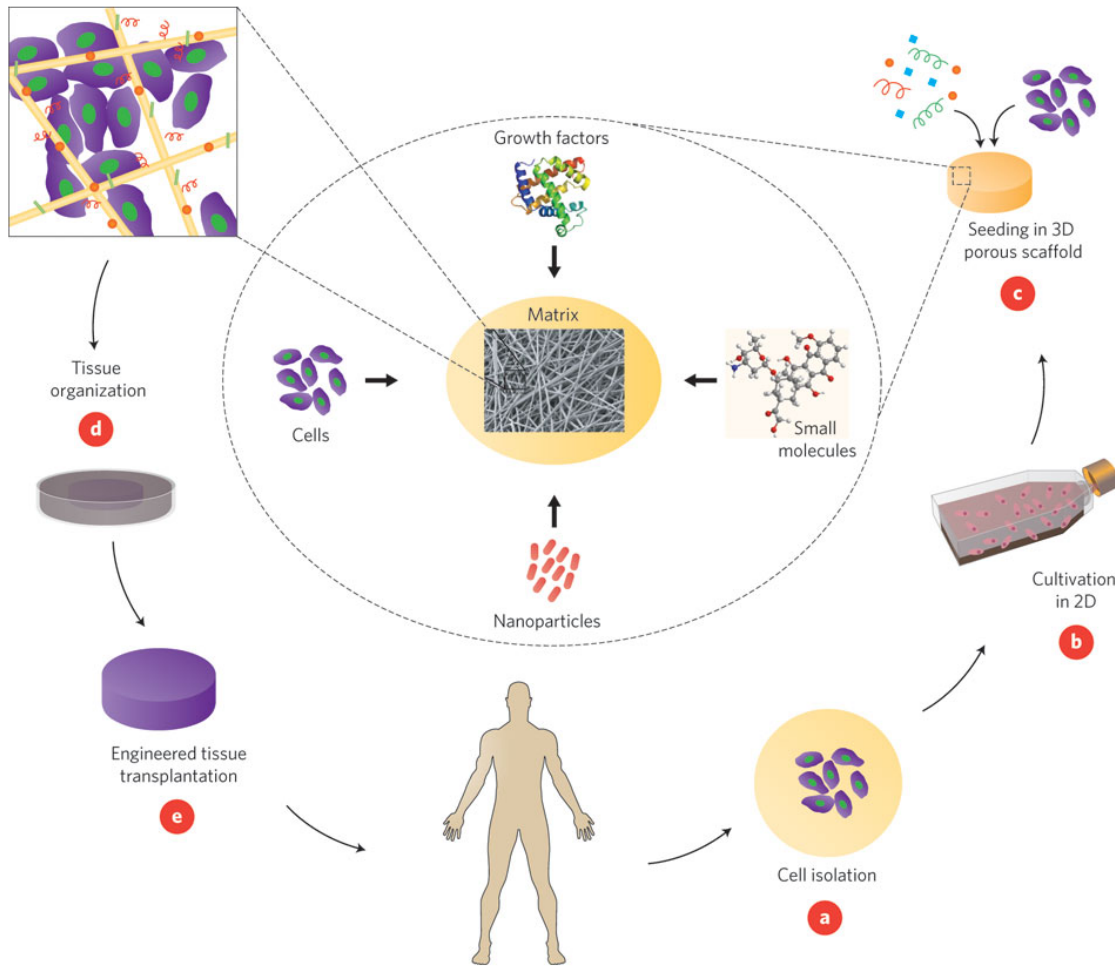


Figure 1.1, schematic representation of tissue engineering principle, a) cells are isolated from patient and cultivated, b) allow in-vitro 2D surface expansion, c) cells are seeded in porous scaffold along with growth factors, d) cells constructs are further cultivated in bioreactors to provide optimal conditions for organization into a functioning tissue, e) once the successfully engineered tissue is formed the construct is transplanted on the injured site to restore function [2]

Natural tissues are three-dimensional (3D) structures composed of cells encapsulated in extracellular matrix (ECM) [4]. ECM forms the supporting material for the cells to adhere, reside and create cell-cell and cell-ECM network for maintaining cell differentiation and function. Tissue engineering utilizes this approach of nature to develop a cell-matrix construct as shown in Figure 1.1 by seeding cells from the same patient into biomaterial scaffolds to in-vitro develop functioning tissues. There are two different approaches followed in tissue engineering for seeding cells to develop a functionalized tissue, namely the top-down approach and the bottom-up approach [4].

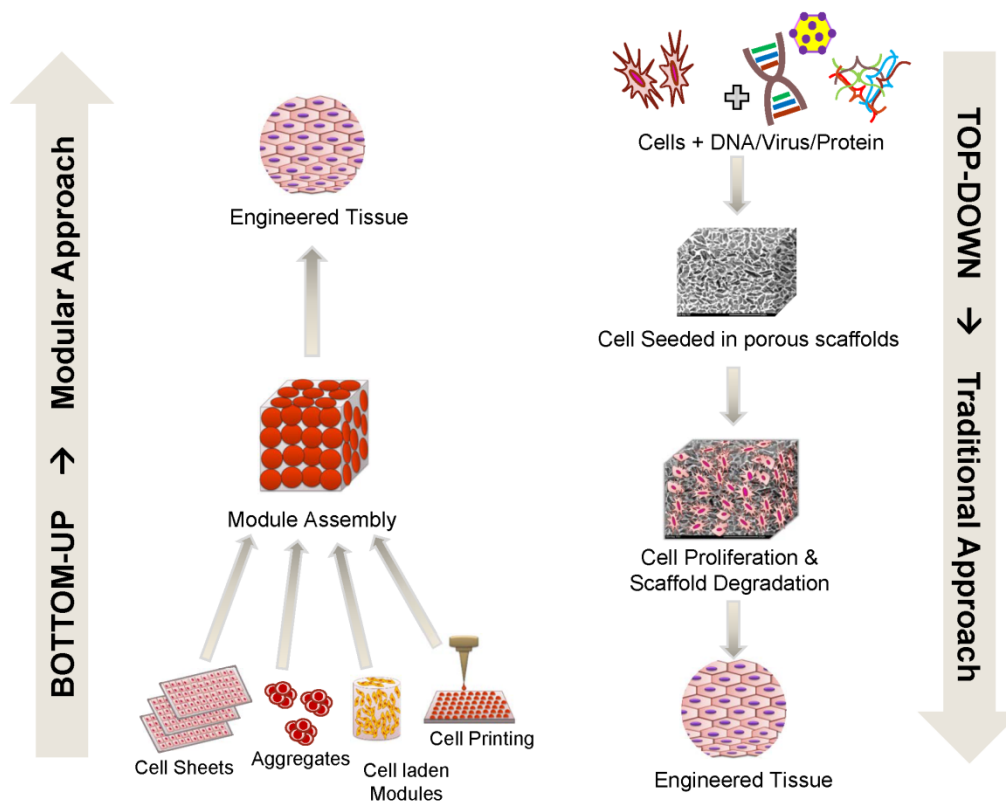


Figure 1.2, schematic representation of approaches in TE, bottom-up approach (left) and traditional top-down approach (right) [5]

The bottom-up approach shown in left in Figure 1.2, involves small cell laden modules, cell sheets to form larger engineered structures as opposed to traditional top-down approach where cells are seeded into porous scaffolds to form tissue constructs. The bottom-up approach overcomes the shortcomings of the top-down approach which is characterized by non-uniform distribution of cells and slow vascularization.

In the past two decades extensive research has been conducted to develop materials viable for use as scaffolds in tissue engineering [1]. Parameters that need to be taken into account when choosing the materials for scaffold depend on the application and tissue or organ. The primary function of biomaterial-engineered scaffold is to provide natural microenvironment to the cell to promote cell adhesion, growth and structural support as a guide for new tissue formation. This structural support requires the scaffold to have appropriate mechanical properties depending on the tissue and organ transplantation application. This is to be able to withstand wear and tear over a prolonged period of time [3]. It should only undergo degradation after in-

vivo transplantation for the seeded cells to organize themselves into the tissue. The volume of the tissue scaffold depends on the pore size of the 3D matrices to allow cell infiltration and nutritional/gas exchange, which are crucial for tissue development in-vitro and for angiogenesis in-vivo [5].

Apart from mechanical and 3D architecture of the scaffold, cell adhesiveness plays an important role in determining the fate of cell organization and growth. These adhesive properties depend on the physical and chemical properties of scaffold surface and the type of cell seeded into the scaffold [6]. In addition the properties of a scaffold should allow modulation of cells in the matrix to differentiate and maintain their phenotype expression.

## **1.2 Cardiac Tissue Engineering**

Cardiac tissue engineering is a field of tissue engineering that allows direct cell transplantation with the aim of regenerating an injured myocardial ventricular wall or to repair congenital defects [1]. Congestive heart failure (CHF) and coronary artery diseases (CAD) are two of the leading causes of morbidity and mortality in the developed countries. The rates of patients being diagnosed with CHF are doubling each year [8]. Over the past decade, medical and surgical therapies have been made available to treat cardiovascular diseases and have improved quality of life of patients and with limited strategies to prevent development of heart failure. Heart failure is observed due to the loss of cardiomyocytes thereby comprising the complete myocardial contraction function [10,11]. At the end-stage of a heart failure patient, heart transplantation is seen as the last option but the severe shortage of donor hearts and the increased risks of rejection hamper this approach.

Tissue engineered constructs can address the need for restoring cardiac function. Insertion of patches or conduits is often required for correct congenital heart defects in infants or heart diseases in adults in the form of synthetic graft materials [9]. However, these materials could become stiff, calcify and may require another surgical invasive operation due to thrombosis [12]. Cardiac tissue engineering is an approach to combine scaffold materials and cells to develop a regenerative approach to restore myocardial tissue. In order to limit ventricular wall dilation, the matrix should provide adequate mechanical support and provide a favourable environment to the transplanted cells and enhance their survival rate, proliferation and differentiation [10]. The matrix should therefore be biodegradable in-vivo, not induce immune

response to the host, support electro-mechanical properties of the heart and be replaced with the newly formed ECM.

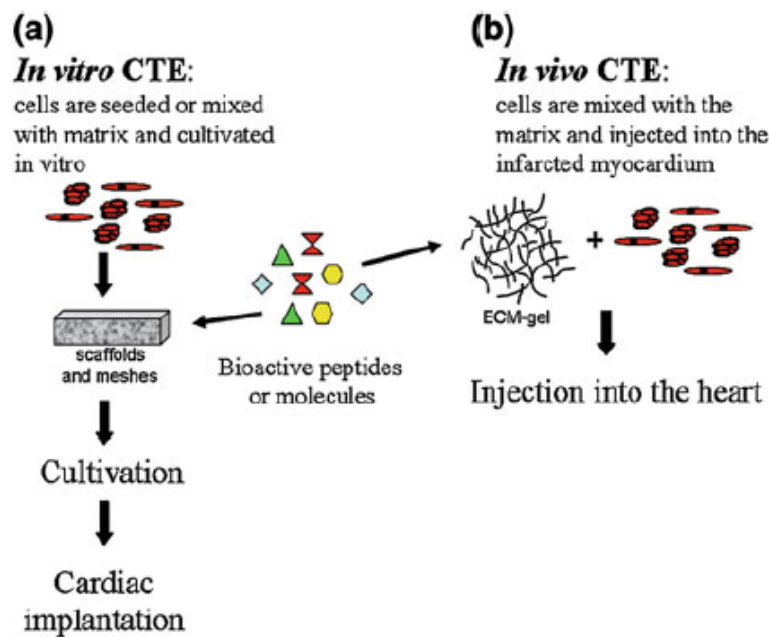


Figure 1.3, schematic representation of in-vitro (a) and in-vivo (b) approaches of CTE performed to create engineered scaffolds for implantation [8].

Cells can be seeded into pre-formed porous scaffolds in in-vitro cardiac tissue engineering under precise culture conditions to enhance survival and differentiation (Figure 1.3(a)). The patch formed is then applied on to the epicardial surface of the heart to provide mechanical support to the damaged heart. The matrix and cultivation parameters guide and organize the seeded cells to control and obtain a myocardial patch similar to native heart tissues. This approach allows control over the shape and size of the construct as well as cell differentiation rate and organization of cells in the scaffold [8].

Over the recent years, injections of mixture of biomaterials and cells have been applied in-vivo in cardiac tissue engineering (Figure 1.3(b)). This approach allows retention of transplanted cells improves survival and damaged tissue at the same time. This is a feasible approach and easy to perform, but the cell growth and differentiation cannot be controlled as in in-vitro models [14]. Extensive research has been conducted on developing various scaffold fabrication techniques and no single biomaterial can provide the multitude of properties required for producing engineered matrices. Therefore, the material selection and synthesis technique should be based on the requirements of the application [14].

### 1.3 Biomaterials: Hydrogel

Biomaterials are materials that interface with biological systems to evaluate, augment or replace any tissue, organ or function of the body [15]. The most important prerequisite for a biomaterial is that it should be biocompatible and perform with an appropriate host response in a specific application [16]. The biophysical nature and biochemical properties of the microenvironment critically modulates the 3D multicellular morphogenesis. The biomaterial biophysical properties, surface chemistry and topography are critical in determining the outcome of cell morphogenesis and resultant cell function [17-20]. Classical materials such as metals, ceramics, glasses and polymers have been investigated as biomaterials. Recent studies have shown cellular functions such as adhesion, spreading, migration and differentiation can be altered just by substrate manipulation [12]. Integrin receptors mediate the cell adhesion to adsorbed proteins. Integrins are a family of heterodimeric transmembrane receptors that bind to adhesive motifs present in various ECM proteins including fibronectin, vitronectin, laminin and collagen. They cluster and associate with cytoskeletal elements to form focal adhesions [15].

Focal adhesions are supramolecular assemblies that provide structure and signalling proteins to anchor forces and activate signals to regulate cell cycle progression and differentiation [16]. Biomaterials can be designed to prevent non-specific protein adsorption and favour specific interaction by presenting biomimetic motifs such as tripeptide sequence of amino acids RGD (arginine, glycine, aspartic acid) to promote adhesion of cells in the matrix [14,17]. ECM is an instructive scaffold that allows cells to attach to, sense and interact at the microenvironment in native tissues. Cells perform best in their native environment and therefore having the right scaffold properties is important [11].

In the heart, ECM is produced and regulated by cardiac fibroblasts that create and maintain a functional syncytium [1-4]. The ratio of the cardiomyocytes to fibroblasts greatly influences the macroscopic tissue properties in cardiac organoids. Encapsulating these cells in a hydrogel that consists of ECM components is one way of controlling their spatial orientation. Hydrogels consist of high percentage of water and, during remodelling, cells exert tractional forces on the matrix molecules that cause the water to be released as the gel compacts [26-27]. Among different biomaterials, hydrogels have stood out as potential candidates for mimicking physical, chemical, electrical and biological properties of biological tissues [19-22]. They allow the creation of a 3D microenvironment of hydrated polymeric network that can hold up

to 20- to 40- fold more water compared with dry weight counterpart biomaterials [23]. The shape and size of these scaffolds can be controlled and organized [23].

Recent studies have shown hydrogels being used in applications such as sensors, actuators, drug delivery, stem cell engineering, regenerative medicine and other biomedical devices [24]. The synthesis and fabrication of hydrogel to create a 3D scaffold provides a more native tissue environment for cells as opposed to 2D platform traditional techniques.

#### 1.4 Microscale technologies for tissue engineering

In the past years microfabrication has been increasingly been used for biomedical and biological applications due to the emergence of soft lithography techniques to fabricate microscale devices (Figure 1.4).

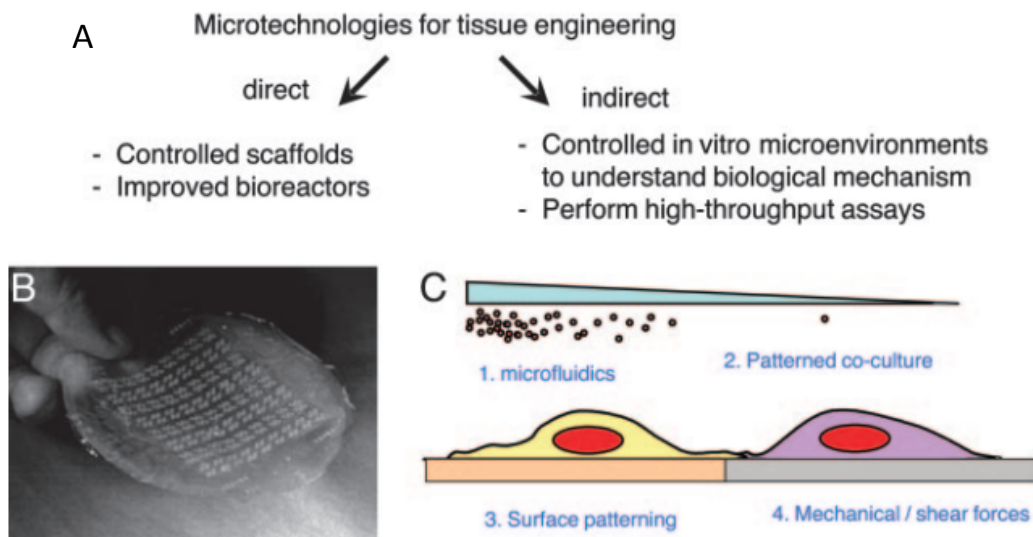


Figure 1.4, schematic representation of micro-scale technologies for tissue engineering, A) scaffolds and bioreactors have been fabricated using micro-technologies to directly or indirectly study cellular behaviour in controlled conditions, B) a microfabricated PDMS scaffold with vasculature embedded into the scaffold, C) different micro-scale techniques to control different aspects on cell-microenvironment interactions [25].

### 1.4.1 Photolithography

Photolithography as a technique is widely used in microelectronic applications. Recently this technique has been used for creating micro-engineered hydrogels by developing synthetic and natural photo-crosslinkable pre-polymers to form hydrogel after crosslinking (Figure 1.5) [28].

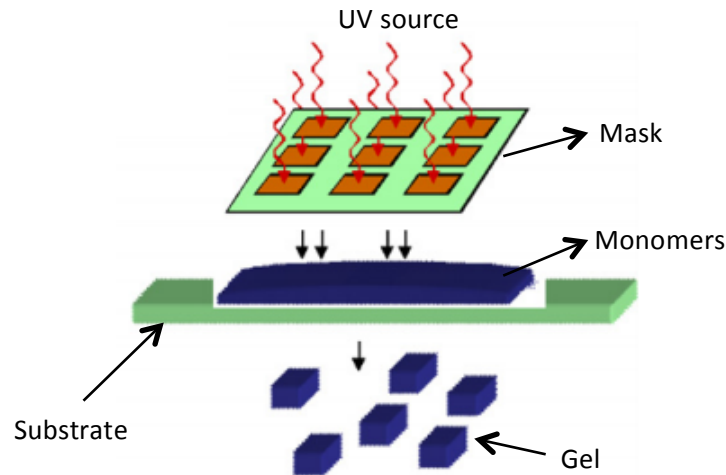


Figure 1.5, schematic diagram of photolithography technique to micro-engineer size and shape of hydrogels.

In this process, ultraviolet (UV) light is passed through a mask on a thin film of polymer. When this light reaches the photosensitive polymer through transparent regions of mask it causes photoreaction that crosslinks the polymer. This technique has been used to create micro-structured hydrogel scaffolds to immobilize cells within the hydrogels [28].

### 1.4.2 Micromolding

Micromolding is another technique used for generating hydrogels with controlled features [28]. It is a soft lithography process which makes it easier for fabrication of poly (dimethyl siloxane) (PDMS) molds from prefabricated silicon wafers (Figure 1.6).

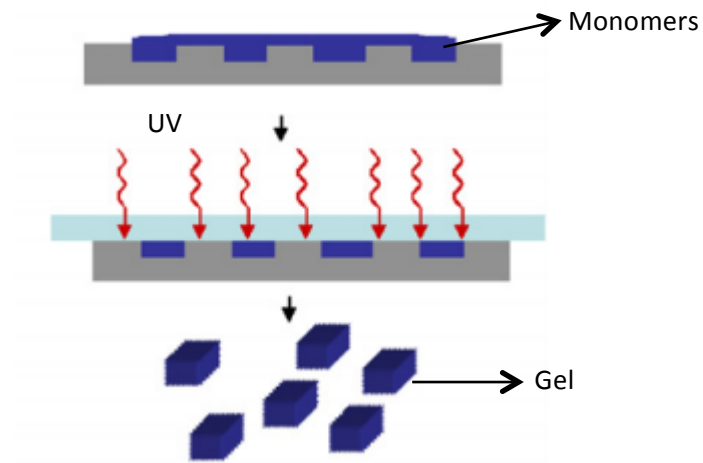


Figure 1.6, schematic representation of micromolding technique to micro-engineer shape and size of hydrogels.

In order to generate a hydrogel mold using this technique precursor polymers are initially molded and gelled to generate structure of different shapes and sizes in 3D geometry.

### 1.4.3 Dielectrophoresis in Cell Engineering

Dielectrophoresis is a microtechnology that combines 3D Dielectrophoretic (DEP) forces in photo-polymerizable gels to manipulate and control arrangements of cells in complex patterns [29-30]. Cells are manipulated when subjected to non-uniform electric field produced by interdigitated transducers for cell trapping and separation.

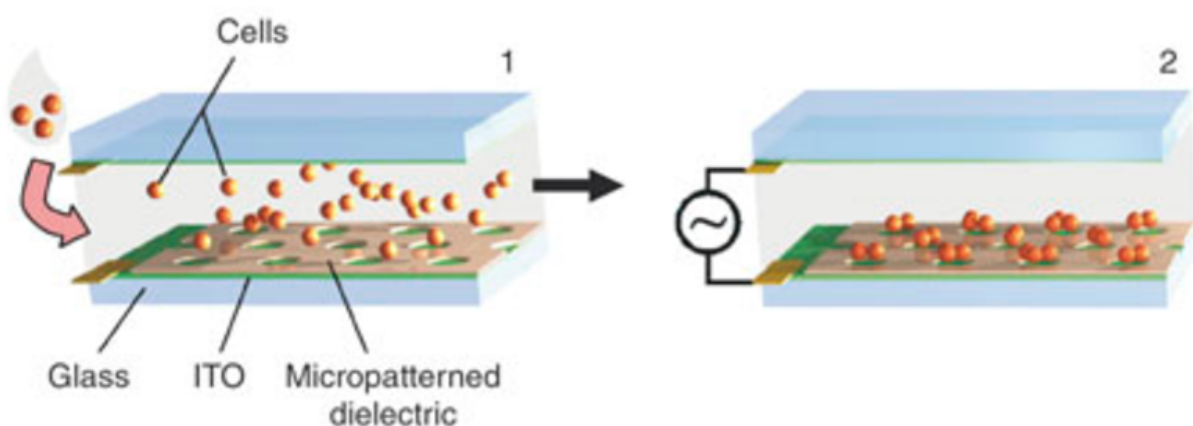


Figure 1.7, schematic representation of Dielectrophoretic patterning of cells in 3D matrix gel sandwiched between two conductive plates [215].

Figure 1.7 shows how a conductive plate was formed when coated with SU-8 photoresist on a patterned metallic substrate. A mix of cells in an unpolymerized gel were sandwiched between the two conductive plates, one with the patterns which act as conducting region and second to provide an alternating current, to generate a high electric field strength [215]. Consequently, due to polarity of cells, they move towards regions of high DEP force within minutes and remain trapped in those regions after polymerizing the gel with UV.

#### 1.4.4 Acoustics in tissue engineering

Recent advances in microfluidics and lab-on-a-chip technologies have enabled many portable biosensors and diagnostic instruments for biomedical research and healthcare. Key advantages of the technologies include reducing the sample size, increasing sensitivity and reducing processing times [31]. Chen et. al [214] employed biotunable acoustic assembly technique to create cell spheroids in a scaffold free fashion. Different cell patterns on a low-adhesion surface were created by altering frequency using a vibration exciter (Figure 1.8).

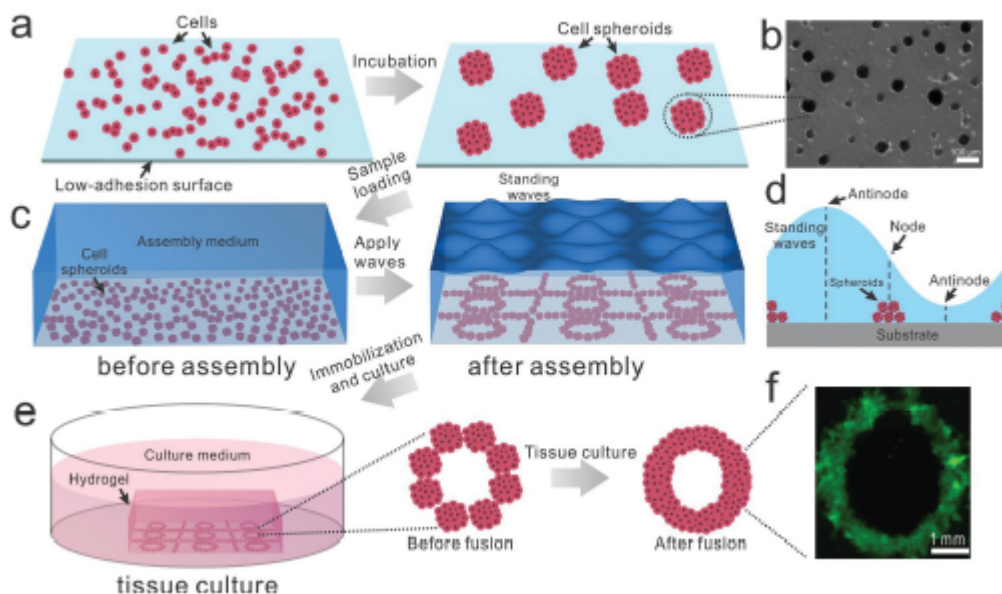


Figure 1.8, illustration of cell assembly on acoustic nodes, a) random distribution of cells on a low adhesion surface, b) spheroid formation after 2 days of incubation, c) demonstration of standing waves applied to create patterns of spheroids on nodes, d) schematic of node and antinode zones on standing waves in fluidic environment, e) patterned spheroids are immobilized in fibrin hydrogel in culture medium to form larger organoid, f) fluorescence image of fused tissue construct of GFP-HUVEC cell spheroids.

Different cellular patterns were created in the fluid medium using the acoustic exciter. After obtaining the patterns the hydrogel mold was placed over the patterns to initiate cell growth in the hydrogel. However, this study does not allow 3D cell growth in the hydrogel as the cells are attached towards the bottom of the mold acting as a conventional platform. Feng et. al [216] have demonstrated encapsulated cells in hydrogel using acoustic waves. The hydrogel molds were created using photolithography techniques and pre-treated with plasma to prevent microgels from sticking to the surface of petri dish (Figure 1.9).

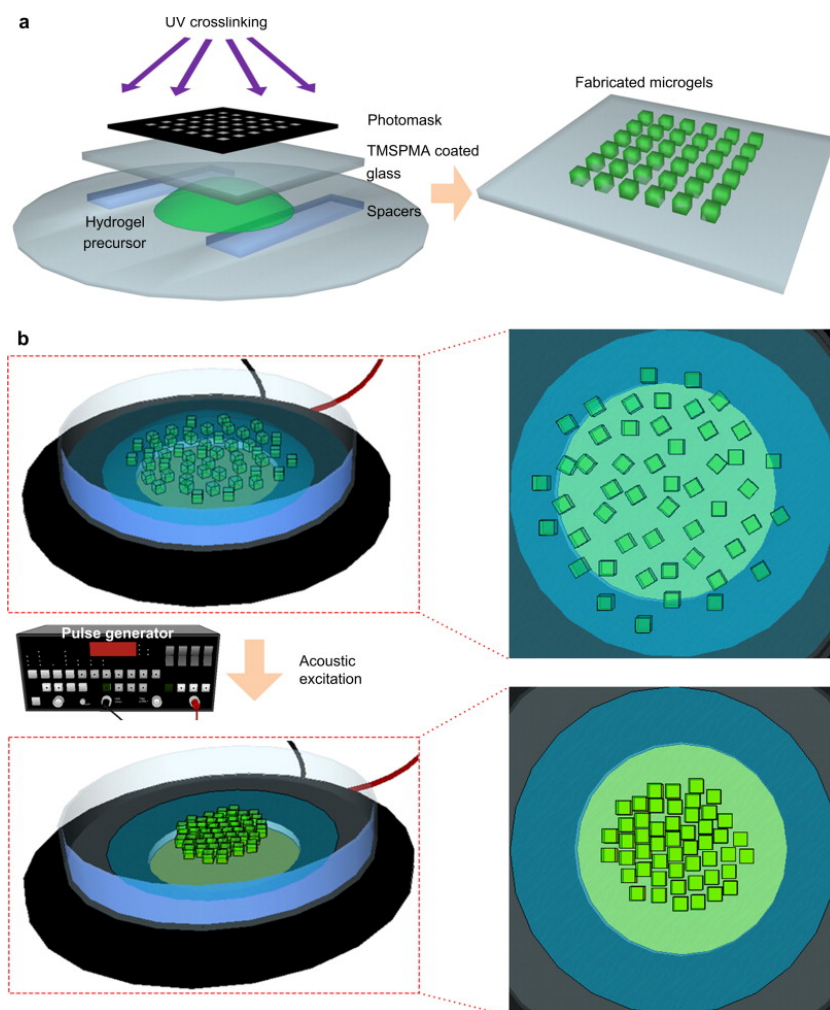


Figure 1.9, schematic of microgel assembly process, a) show the fabrication of microgels using photolithography, b) shows the assembly of microgels during acoustic excitation using acoustic assembler [216].

The cells were encapsulated in the PEG monomer prior to photolithography techniques and after UV exposure of 45sec the microgels were obtained in a droplet and using pulses the microgels were aggregated toward the centre of the droplet using acoustic pulse excitation.

However, this technique required pre-treatment of microgels, cells were not spatially aligned and involved photolithography procedures that led to direct exposure of cells under UV for a prolonged time.

Recently, surface acoustic wave (SAW) technology has been developed using piezoelectric substrates for the use in biotechnology, including microfluidic mixing, particle trapping, and biosensors in microfluidic devices [31-35]. Acoustic forces affect the suspended particles in an acoustic wave field. Acoustic waves generate pressure gradients and acoustic forces in a liquid, which can be used to manipulate suspended particles in a liquid medium [36-39]. Acoustic forces are non-contact forces and are usually “harmless” to biological objects such as cells. Unlike electrical, optical or magnetic methods [40-42], acoustic methods appear to be ideal for particle manipulation methods to build lab-on-a-chip devices as they are non-invasive, require no pre-treatment of the particles and work for nearly any type of micro-scale particles regardless of their optical or dielectric properties [41].

Surface acoustic waves are sound waves that propagate along the surface of an elastic material. As most of the energy of a SAW is confined in the superficial layer, usually within one to two wavelengths normal to the substrate surface, the energy density of a SAW is high. This makes it an effective way to manipulate particles and liquid droplets [43]. The safe use of ultrasound in its diverse diagnostic and therapeutic applications are widely acknowledged [44-46]. In the field of tissue engineering, ultrasound has predominantly been applied in the form of low intensity ultrasound to stimulate cells, and ultrasonic standing wave fields to generate acoustic traps, which can spatially manipulate cells, proteins and microbeads [47].

A SAW is like an earthquake wave propagating along the surface but with amplitude of a few tens of nanometres (Figure. 1.10). These waves are created by patterned interdigitated transducer (IDT) electrodes and have their wavelengths defined by the width of each individual finger of the electrode along the propagation direction of the wave and the gap between them [33].

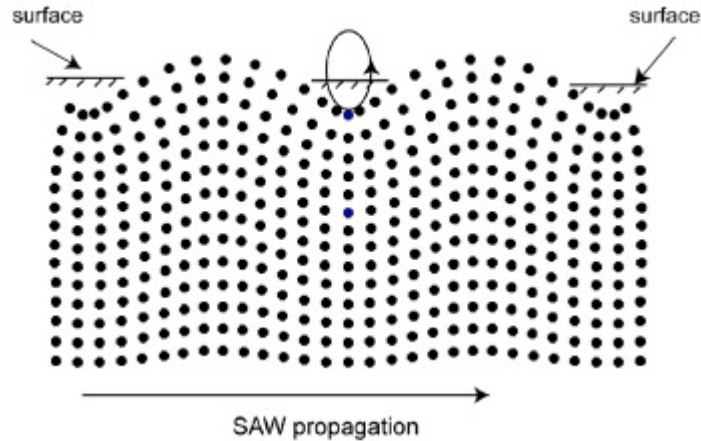


Figure 1.10, illustration of SAWs propagating and the particle motion on the surface is elliptical in a direction opposite to the wave propagation due to the transverse and longitudinal modes of rayleigh waves [41].

The ultrasonic wave is created by an interdigitated transducer (IDT) electrode designed on a piezoelectric substrate where as stated the wavelength is determined by width of the individual finger of the IDTs. When a fluid containing a suspension of cells is exposed to an standing wave in a chamber/trap, there is an acoustic radiation force arising from the scattering of the acoustic waves on the cells. The direct the motion (i.e. acoustophoresis) of cells typically to areas of minimum pressure, referred to as pressure nodes, facilitates their aggregation into multicellular clusters [27,48-89]. In cartilage tissue engineering, low intensity ultrasound devices have been used to enhance chondrogenic differentiation of bone marrow mesenchymal stem cells and chondrocytes in 3D environments [50-54]. Although acoustic waves or ultrasound are non-destructive and non-invasive cell manipulation techniques, they are relatively less exploited for applications in tissue engineering.

#### 1.4.4.1 SAW microfluidic advantages

SAW based microfluidics devices are an attractive platform for many lab-on-a-chip applications such as droplet microfluidics, particle manipulation and biosensing. The following are the advantages of SAW to demonstrate high throughput [49]:

- a. SAW allows control over excitation frequencies in a wider range compared to dielectrophoretic techniques for example, that makes SAW based devices more

versatile and flexible. This control over the device allows us to achieve more precise and controllable manipulation of particles and fluids [49].

- b. This platform does not require microfluidic channels or chambers to be made of acoustic reflective materials. This allows the use of materials made of polymers that have low acoustic reflection.
- c. SAWs require less power by confining their energy to the piezoelectric substrate.
- d. SAW devices can be easily fabricated through standard micro- or nano-fabrication processes on the same substrate as opposed to other microfluidic platforms.

## 1.5 Aim and Objectives

The main aim of this research is to investigate the feasibility of developing a novel highly adjustable platform using SAWs for making well-defined niches for three-dimensional (3D) cardiac cell tissue engineering and advance the understanding of effect of acoustics on cell morphology in hydrogel. In this work, SAW based devices will explore acoustic waves for quickly driving cells into 3D hydrogel scaffolds, Gelatin methacrylate (GelMA), in a uniform distribution using slanted-finger IDTs designed on a lithium niobate ( $\text{LiNbO}_3$ ) piezoelectric substrate was used for producing engineered 3D heart tissue constructs. The approach will follow a bottom-up tissue engineering approach to create cell sheets of aligned cells to be later formed into a larger module for creating a tissue for implantation purposes.

The objectives of this research were:

- Synthesising and characterizing rheological properties of GelMA hydrogel that can readily induce SAW for rapid cell manipulation prior to polymerization using UV radiation.
- Evaluation of cells encapsulated in the hydrogel scaffold and characterizing chamber design for integrating standing-SAW (SSAW).
- Understanding and analysing the cell viability morphology, proliferation, beating, action potential, calcium transient of the cardiac cells in GelMA when acoustically patterned and stimulated.

## 1.6 Thesis outline

This thesis comprises eight chapters, the contents of which are described below –

Chapter 1, an “Introduction” presenting an overview of tissue engineering, cardiac tissue engineering and microscale technologies that have been employed for manipulating cells in hydrogels. This Chapter gives a brief introduction of the project and outlines the main goals and objective of the thesis.

Chapter 2, a “Literature review” which aims to explore the development of research in the field of tissue engineering, cardiac tissue engineering, surface acoustic waves and dielectrophoresis in order to understand, design and develop a SAW device platform suitable to meet the objectives for designing slanted fingers IDTs to create 1D and 2D standing SAWs, draw a comparison between SAW and DEP platform devices.

Chapter 3 covers the material and methodology that discusses synthesising GelMA hydrogel, fabricating SAW and dielectrophoretic devices using microfabrication techniques, cell isolation methodologies, microscopy methodologies, cell-labelling and immunohistochemistry techniques.

Chapter 4, outlines the chemical and physical properties of gelatin methacrylate hydrogel for different concentrations necessary for mimicking natural ECM.

Chapter 5, outlines the characterization of microfabricated SAW devices on  $\text{LiNbO}_3$  substrate using slanted-finger design IDTs to generate multiple frequencies in the hydrogel GelMA, characterizing the chamber design to couple acoustic waves into the hydrogel for patterning cells and avoiding turbulence. It also discusses the experimental setup and analyses the forces exhibited on cells under acoustics and dielectrophoresis to draw a contrast between the two techniques. Finally it simulates the experimental data using acoustics, particle tracking and electrostatics module in COMSOL Multiphysics software 3.5/5.0.

Chapter 6, on “Cardiac tissue engineering using SAW” describes the experimental work for spatially patterning cardiomyocytes and cardiac fibroblasts in GelMA hydrogel under multiple frequency acoustic waves generated on the  $\text{LiNbO}_3$ . Furthermore, this chapter demonstrates the rheological measurements of different concentration of GelMA and quantifying patterned cells using cell-labelling techniques to investigate myofibers necessary for cell-cell communication.

Chapter 7, this chapter describes the analyses of cell-cell contact in gelatin methacrylate hydrogel to investigate beating, contraction, action potentials and calcium transients under three different control samples.

Chapter 8 on “Conclusion” describes the overall goals achieved in this work with reference to the objectives outlined in chapter one and draw main conclusions from the work. This Chapter also outlines future work that maybe undertaken based on the research using surface acoustic waves to manipulate the matrix of hydrogel under stimulations and co-patterning cells with nanomaterials encapsulated in hydrogel matrix to provide better structural and mechanical properties for creating 3D engineered tissue constructs.

## Chapter 2

### Literature review

#### 2.1 Introduction

This chapter gives literature background on tissue engineering, biomaterials, cardiac tissue engineering, surface acoustic waves and dielectrophoresis that are necessary to understand and develop a novel platform for creating 3D patterning of cells in a hydrogel to produce engineered tissue constructs.

#### 2.2 Tissue Engineering: An Engineering Feat

In the 21<sup>st</sup> century, cell based therapies have become one promising platform for major therapeutic modalities. Yet, a number of critical and important scientific and bioengineering challenges such as cell and development biology, bioengineering analysis and design, as well as clinical implementation have to be met [57]. The term tissue engineering has often been used to describe these efforts even though it is only one of the four options to repair a damaged tissue as shown below. Other approaches include pharmacological treatment, transplant replacement or artificial organ [58].

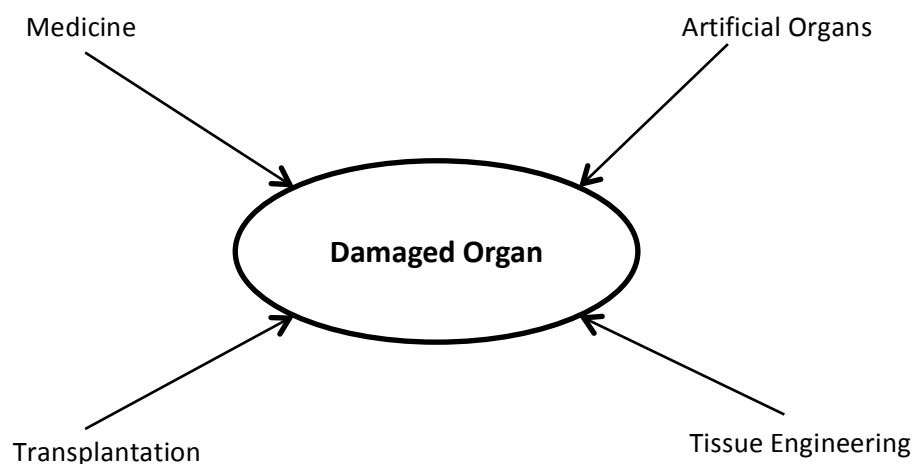


Figure 2.1, is a schematic representation of existing cell-based therapeutical approaches for tissue engineering and regeneration purpose to restore the function of the damaged tissue or organ.

According to Langer and Vacanti (1993) [59], tissue engineering is a combination of engineered materials and biology to induce tissue regeneration. The first symposium of tissue engineering was held in 1988 where the first working definition was proposed that,

“ The application of the principles and methods of engineering and life sciences toward the fundamental understanding of structure-function relationships in normal and pathological mammalian tissue and the development of biological substitute to restore, maintain or improve tissue function” [59].

This whole new field of reconstructive surgery has emerged to improve the quality of life by replacing the missing or lost functions of an organ by rebuilding the body’s structures. Organ and tissue transplantation from one individual to the recipient has been a breakthrough in scientific community and is considered as the most extreme form of reconstructive surgery [60]. Although molecular and cellular events of the immune response have been elucidated sufficiently in a clinical setting of transplantation new problems have emerged such as dislodgment, infection at the foreign body/tissue interface, fracture, and migration over time of implanted foreign body materials [60].

Although transplantation from one individual to another have been successful there have been severe constraints starting with the availability of tissue and organs for patients. As of 2015, a 120,000 men, women and children are awaiting kidney organ transplant in US alone [61]. About 8,500 transplants were donated from deceased donors and a 6,000 from living donors [61-62].

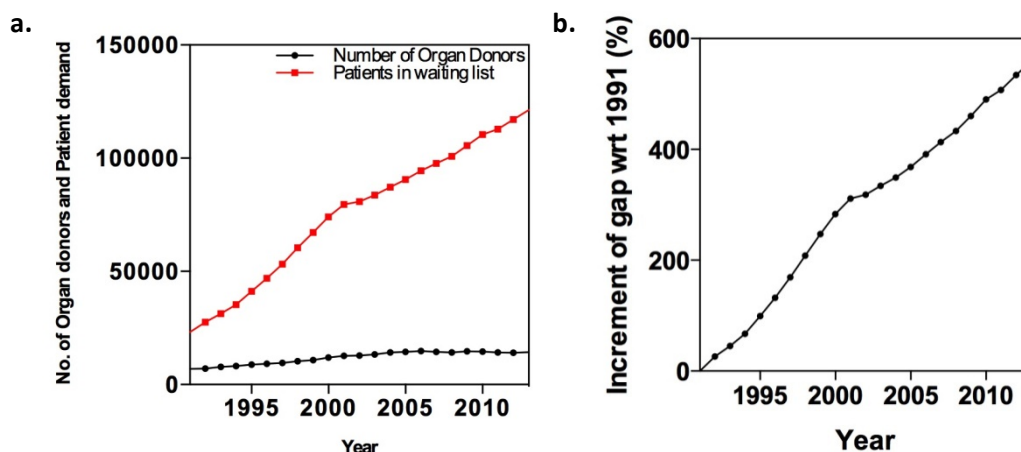


Figure 2.2, a) shows the widening gap between the number of people on the waiting list for kidney organ vs number of donors and b) shows steep increase in percentage of gap since 1991 [86].

After the transplantation, the immune system of the recipient produces chronic rejection and destruction over-time creating immunosuppression imbalance, which can cause tumor formation. Hence, these constraints have asked for new solutions to provide more biocompatible tissues. Tissue engineering fabricates living cells in a matrix or scaffolding that guides tissue development. In 2012, John B. Gurdon and Shinya Yamanaka were awarded Nobel Prize in Physiology and Medicine for re-programming cells to produce induced pluripotent stem cells (iPS cells). Since then the emergence of stem cell biology has created a new term called regenerative medicine [63]. Matrix or scaffold can be natural, man-made or composite of both to allow perfusion of cells introduced to form a tissue. After implantation, cells can migrate through the implant or matrix in cell culture prior to transplantation. This helps in the elimination of harmful tissue. The advantage of tissue engineering over cell transplantation alone is that tissue engineering provides a 3D functional tissue that is designed and developed using patient’s own cells [63]. Tissue engineering offers three main approaches to restore maintain or enhance tissue function – 1) use isolated cells as cellular replacement; 2) use cellular biomaterials capable of inducing tissue regrowth; and 3) use combination of cells and materials in the form of scaffolds, as shown below (Figure 2.3) [64].

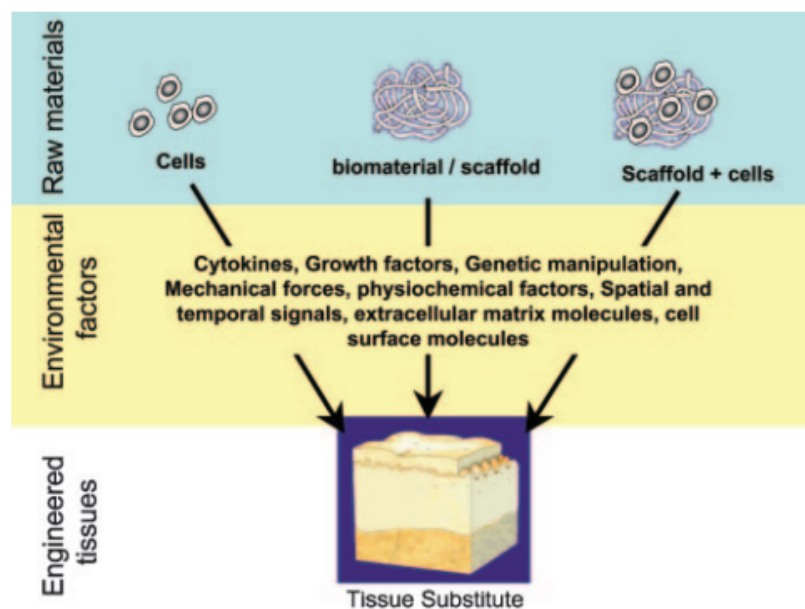


Figure 2.3, schematic representation of TE approaches in three stages, i) individual cells, ii) cells with scaffolds, iii) scaffolds alone, which enhance in-vitro microenvironmental factors before forming a tissue substitute [64]

### 2.3 Biomaterials and Scaffolds for Tissue Engineering

The aim of tissue engineering is to regenerate damaged tissues by combining cells from body with highly porous scaffold biomaterials that acts as templates for tissue regeneration for the formation of a new tissue. Over the past several decades, many tissue-engineered products are being used on clinical platform to address patients suffering from tissue loss or dysfunction in skin, bone or cartilage. The number of clinical trials have been increasing to treat more challenging diseases in nervous system and pancreatic tissues [65]. The role of biomaterials is to provide basic structural support (scaffolds) to promote cell adhesion and expansion during ex-vivo cultivation of cell to show that the cells isolated from donors could be co-injected with biomaterials such as fibrin or collagen into patients to prevent initial cell loss and improve graft survival rate [67].

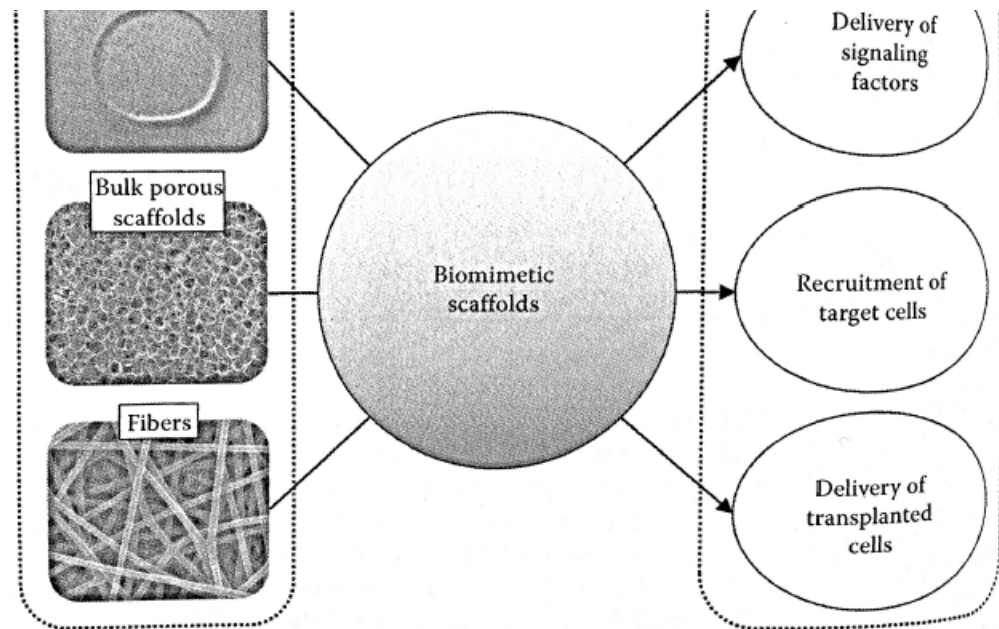


Figure 2.4, schematic representation of roles such as delivering signal factors, recruiting targeted cells and implanting the transplanted cells, and formats, such as gel, porous scaffolds and fibers, of biomimetic scaffolds in tissue engineering [65]

The materials from which tissue engineered products have been derived from include natural or synthetic origins, growth factors which stimulate tissue morphogenesis, differentiated or progenitor cells or a combination of these (Figure 2.4). In the natural state in a human body a tissue is composed of cells and extracellular matrix (ECM) that make it functionalized [67].

## 2.4 Extracellular Matrix

Under normal conditions in a human body, cells are intimately in contact with the neighbouring cells through mechanical binding of membrane bound proteins. This binding allows exchange of information of metabolic machinery interaction via soluble factors. A large portion of tissue is made up of interconnected network of macromolecules called extracellular matrix, which consists of proteins and polysaccharides [67]. ECM in different organ systems in the body has observed to differ in its constituents. Depending on the organ and tissue of that organ, ECM is synthesized, secreted, oriented and modified [68].

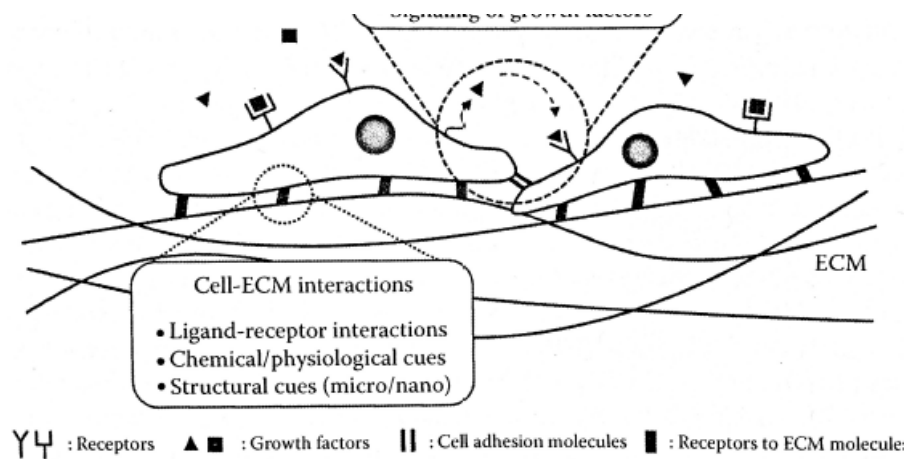


Figure 2.5, representation of main components of ECM and cells at cellular microenvironment illustrating different component involved cell-cell and cell-ECM interaction to provide cell adhesion, proliferation and differentiation in the ECM to mimic natively [68].

Figure 2.5 shows the interaction of cells at cellular level with ECM that provides supports to them and triggers biochemical signaling. ECM consists of biomacromolecules that are crosslinked and assembled as fibrous bundles that allow multiple binding of residing cells to control their diverse cellular activities [63]. One of the key components for this cell adhesion are proteins such as cadherins, selectins and integrins that are present on the cell surface [64]. Integrin is one class of the major glycoproteins that sense external signals through specific binding with numerous ligands such as laminin, collagen, thrombospondin, fibronectin [64].

For cell adhesion and proliferation on scaffolds, the arginine-glycine-aspartic acid (RGD) domain binds with the integrin. Studies have also shown that not only the chemical composition of the cellular microenvironment and conformation of proteins are important but also are the mechanical properties of the ECM, which help in regulating the cellular microenvironment [64].

## **2.5 Hydrogels in Tissue Engineering**

The objective of tissue engineered products on clinical platform is to provide an alternative to organ transplantation either by utilizing naturally existing biomaterial scaffolds such as ECM or by designing and developing synthetic materials such as hydrogels. Hydrogels are being used for regenerative and biomedical applications because of their ability to retain large amount of water, their low interfacial tension, their high biocompatibility and their minimal mechanical and frictional irritation [68]. The term hydrogel is derived from two words, 'hydro' means water and 'gel' means jelly. It is a polymer network, which is insoluble in water and swells to an equilibrium volume retaining its shape [69]. This insolubility is due to the 3D network of an existing equilibrium between dispersing hydrated chains and cohesive (preventing further penetration of water) forces exist. This hydrophilicity of the network is due to the presence of chemical residues as  $-OH$ ,  $-COOH$ ,  $-COHN-$  and  $-CONH_2$  for example [69].

The cohesive forces are generated by covalent bonds that exist between chains of polymer network or cooperative and associative forces such as van der Waals forces, Micellar packing, hydrogen bonding, ionic bonding, crystallizing segments or combinations of these [68].

A 3D organized structure of a hydrogel is shown below in Figure 2.6,

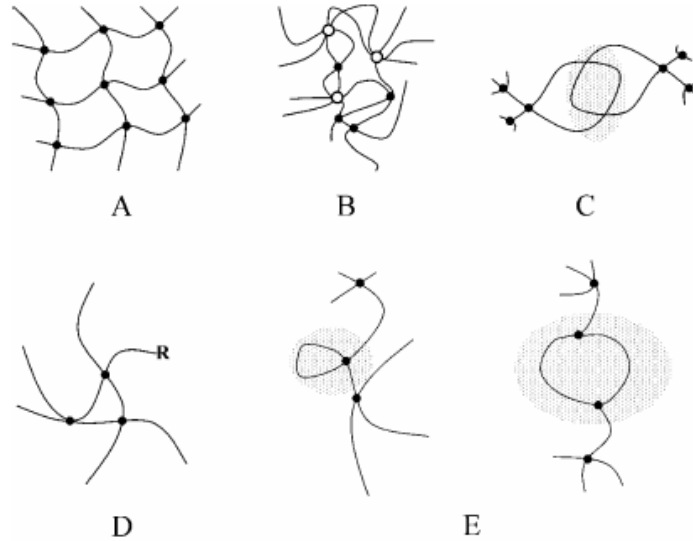


Figure 2.6 schematic representation of hydrogel structure, a) an organized tetra-branched network of covalent or non-covalent junctions (visualized as dots), B) random multi-branched network (clear and filled dots), C) a network of entangled chains (shaded), D) a network with defect R, E) two networks with loops in shaded region considered to be defects that do not provide mechanical strength to the hydrogel [69].

Hydrogels can be classified in several different classifications such as natural or synthetic, degradable or non-degradable; physical or chemical; Homopolymer, copolymer, block-copolymer or multipolymer hydrogels; Neutral, cationic, anionic, amphiphilic; Amorphous, semi-crystalline hydrogels; Matrix, film, membrane, microsphere or microcapsule hydrogels [70]. Hydrogels have the capability of swelling when not just in contact with water but also can be designed to swell at particular temperature ranges, pH, ionic strength, electric field, light and particular aqueous solution.

### 2.5.1 Swelling

Hydrogels have the ability to swell when in contact with water until equilibrium is reached. This osmotic swelling is counter balanced by the elasticity of the network, which generates a force known as swelling pressure ( $P_{sw}$ ). This pressure is equal to zero at equilibrium with pure water and is given by the following formula [69],

$$P_{sw} = k C^n \quad (2.1)$$

Where,  $k$  and  $n$  are constants and  $C$  is polymer concentration.

In terms of weight, volume or length, swelling can be described by the following formula,

$$W_w = \frac{WH_w - DH_w}{WH_w} \quad (2.2)$$

Where  $W_w$  is the weight of water taken up by the hydrogel,  $WH_w$  and  $DH_w$  are wet and dry hydrogel weights.

The degree of swelling is given by [69],

$$D_{sw} = \frac{WH_w}{DH_w}, D_{sw} > 1 \quad (2.3)$$

Where swelling ratio is given by,

$$R_{sw} = D_{sw} \frac{d_0}{d_{sw}} = \frac{WH_v}{DH_v} \quad (2.4)$$

Where  $d_0$  is density of hydrogel in dry state,  $d_{sw}$  is density of swollen gel;  $WH_v$  and  $DH_v$  are respectively the volumes of hydrogel in the wet and dry state.

When the hydrogel swells, the molecules trapped within the network are delivered outside the hydrogel according to Fick's Law that states the diffusion rate of liquid across the porous network of hydrogel is directly proportional to the difference in partial pressure, area of the porous network and inversely proportional to the thickness of the scaffold. In cases of drug delivery, this release can be exhaustive since it often comprises diffusion as well as polymer degradation and other physio-chemical parameters.

### 2.5.2 Scaffold Requirements

Tissue engineering relies on using porous 3D scaffolds that provide an appropriate cellular microenvironment for the growth of cells, regeneration of tissues and organs. Scaffold is a 3D biomaterial which the cells are seeded either into in-vitro or in-vivo [71]. These scaffolds are templates that contain cells, growth factors and are subjected to a bioreactor system (Figure 2.7).

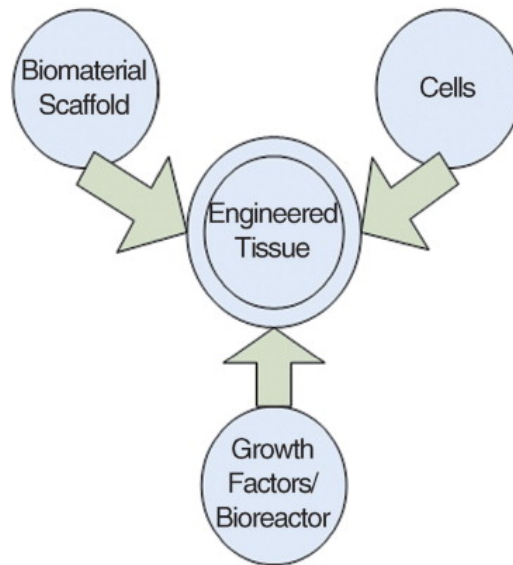


Figure 2.7, schematic illustration of triad of TE showing cells, signals, and scaffold that act as template from tissue formation by allowing cells to migrate, adhere and form tissue [4].

The cell seeded scaffolds can be either cultured in-vitro to synthesize tissues to be later implanted into an injured site or implanted directly on the injured site by inducing in-vivo body's own system for regeneration. Over the past decades numerous scaffolds have been designed from variety of biomaterials in an attempt to regenerate different tissues and organs in the body. There are key considerations that have to be taken into account when designing the suitability of a scaffold for use in tissue engineering are [70] –

**Biocompatibility** – this is first and most important criterion for any scaffold in tissue engineering. Cells must be able to adhere, function normally and migrate onto the surface to eventually begin proliferation in the matrix. After the implantation this engineered tissue must elicit negligible immune reaction to prevent severe inflammatory response that might hinder the healing or trigger rejection by the body;

**Biodegradability** – the purpose of tissue engineering is to allow the body's own cells to eventually replace the implanted tissue engineered scaffold. These scaffolds are not designed as permanent implants but as biodegradables that allow cells to produce their own ECM. During this degradation there should be no production of toxic by-products and any by-products should be able to easily exit the body without any interference with any organ. This gradual degradation occurs in tandem with tissue formation with controlled infusion of cells such as macrophages;

Mechanical properties – the tissue engineered matrix should have the mechanical properties consistent with the anatomical site to which it will be implanted in. It should be strong enough during surgical handling, however for special cases in cardiovascular and orthopedic applications the challenges are higher. Recently, too much focus has been put on developing scaffolds with mechanical properties similar to bone and cartilage but are detrimental of retaining high porosity due insufficient capacity for vascularization [70]. It is important to allow cell to infiltrate and vascularize by having scaffolds design with a balance of mechanical and porous architecture [70];

Scaffold architecture – having the correct architecture of the engineered tissue is critically important. The cells must be able to penetrate and nutrients be adequately be able to diffuse to cells through the interconnected pore structures and form an ECM. This porous structure also allows the transport of waste products and degradation by-products out of the scaffold without any interference with other organs and surrounding tissues. With respect to the porous structure, the pore size is also important. Naturally synthesized scaffold (e.g. collagen) ligands that cells primarily interact with in the form of RGD binding sequence (Figure 2.8). Integrins are the cell adhesion receptors that are responsible for development and pathological processes in the tissue. RGD is a cell adhesion motif that is found in numerous proteins. This cell adhesion sequence was discovered in fibronectin two decades back [211]. The RGD site can be easily reproduced with short peptides that mimic cell adhesion proteins in two ways: firstly when coated on a flat surface the cell adhesion is promoted and secondly in a solution they act as decoys and thus prevent adhesion [211]. In ECM molecules such as collagen, the RGD sequences are exposed upon denaturation. This allows cells to bind with the ligands using RGD-binding receptors. 8 out of 24 subset of integrins recognize the RGD sequence. RGD sequences are present in the triple helical fibrillary collagen sequence that become available in denatured collagen I [212]. Hydrogel scaffolds manufactured from collagen and glycosaminoglycan (GAG) possess qualities for tissue regeneration in the field of tissue engineering such as : scaffolds can be sterilized by chemical treatment, degradation rates can be controlled and scaffolds can be fabricated with different number of macromolecular constituents of variety of pore structures [213]. Synthetically made scaffolds require careful designing of these ligands by protein adsorption. The density of ligand is determined by the available surface within a pore to which cells can adhere to

that means the pore size should be large enough to accommodate cell migration into the structure to eventually allow them to bind to ligands.

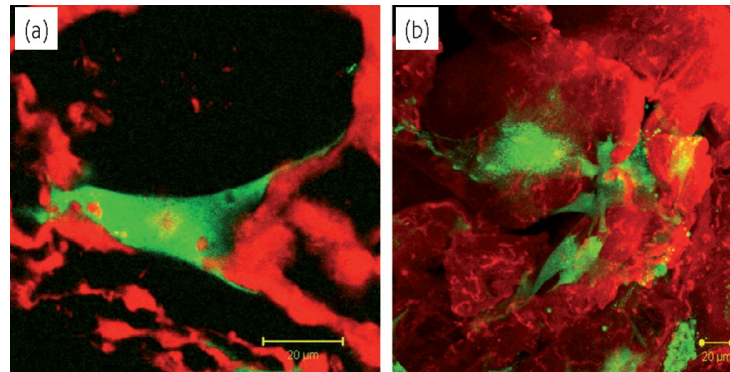


Figure 2.8, a, and b) shows confocal image of osteoblasts (green) attached to highly porous collagen-GAG scaffold (red) [71].

It is therefore critical to determine the range of pore size depending on the type of cell, tissue and organ.

Manufacturing technology – the engineered tissue must be cost effective and should be manufacturable in small batches for clinical and commercial use. The main aim of tissue engineering is provide an inexpensive alternative versus expensive artificial implant surgeries. By developing good manufacturing practice (GMP) for the engineered scaffold it should be possible to successfully translate these into clinical practice. In addition to this, it is important to be aware of how the scaffold will be stored, transported, delivered and made available to the clinician [68].

## 2.6 Cardiac Tissue Engineering

Tissue engineering has been an emerging field in the last two decade as a possible approach for producing engineered organs by using cells, matrix, biological active molecules and physiological stimuli. It is an interdisciplinary field that involves engineering, chemistry, biology and medicine. In cardiovascular medicine, cardiac tissue engineering is an alternative path that aims to regenerate injured myocardial ventricular wall or to repair congenital defects [70]. Coronary heart failure and coronary artery disease are the leading causes of high

morbidity and mortality in the western society, with numerous patients being diagnosed every year with CHF. According to British Heart Foundation in 2012, 29% deaths caused in men were related to coronary heart disease (Figure 2.9) [62]. Unfortunately, myocardium lacks the ability to regenerate the damaged tissue and as a result due to the development of non-contractile scar tissue, adverse heart remodeling takes place.

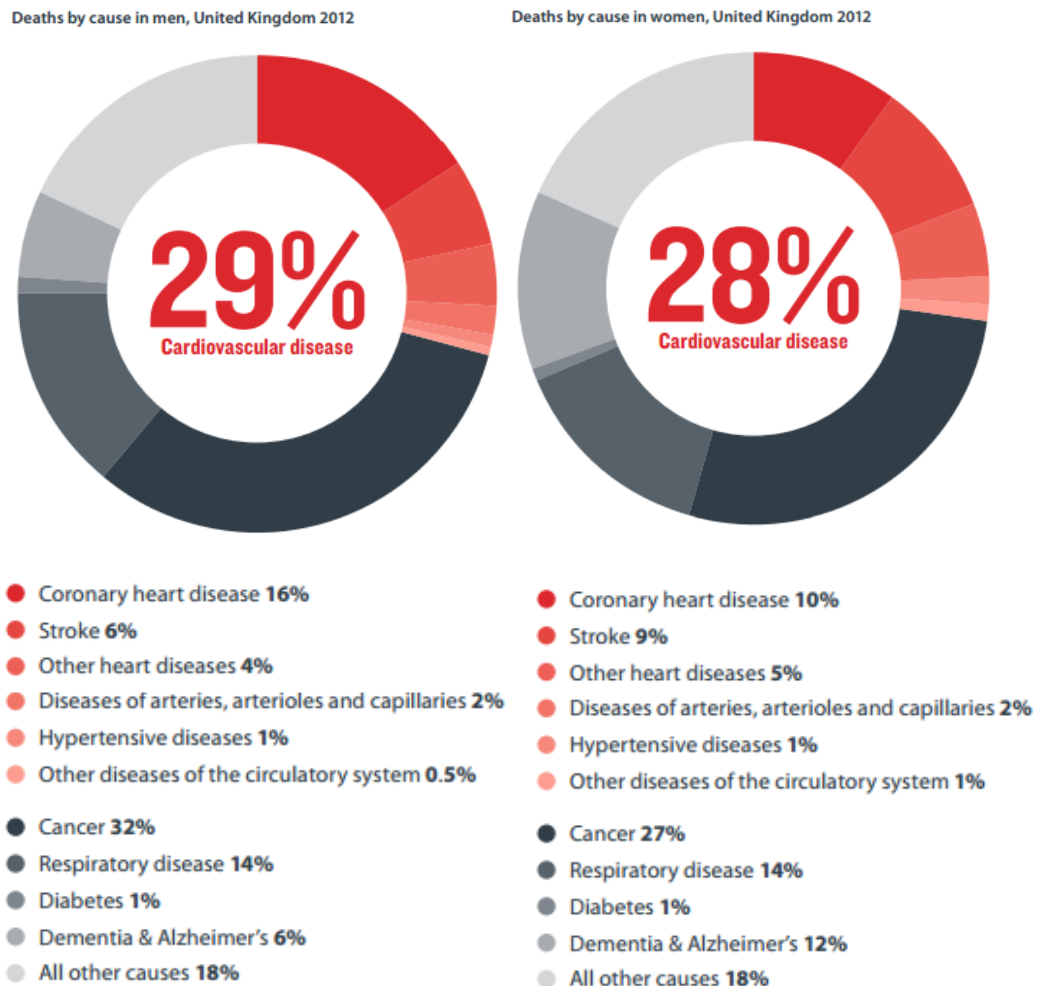


Figure 2.9 show statistics published by British Heart Foundation 2014 for Cardiovascular Disease in United Kingdom draw a comparison of deaths between men and women who suffered from majority of cardiovascular diseases as opposed to other diseases such as cancer, diabetes, Alzheimer's [61].

Although in the past decade, as a consequence of medical and surgical interventional therapies, the quality of life has improved for many patients, there are limited strategies available to prevent the development of heart failure related to the loss of cardiomyocytes. This is due to the myocardial contractile function [70]. At the end-stage of heart failure, patients are offered heart transplantation option but due to the severe shortage in organ donors

and possibility of rejection of the transplanted heart hinder the surgical approaches. Heart failure is one of the leading causes of death due to loss of cardiac tissue impairments of the left ventricular function.

Tissue engineered constructs promise to restore cardiac function after surgical therapy with the insertion of patches to correct the congenital heart defects in infants and congenital heart diseases in adults [5]. Cardiac tissue engineering has been combining scaffolds and cells in order to provide a regenerative approach to restore the myocardial tissue as shown below,

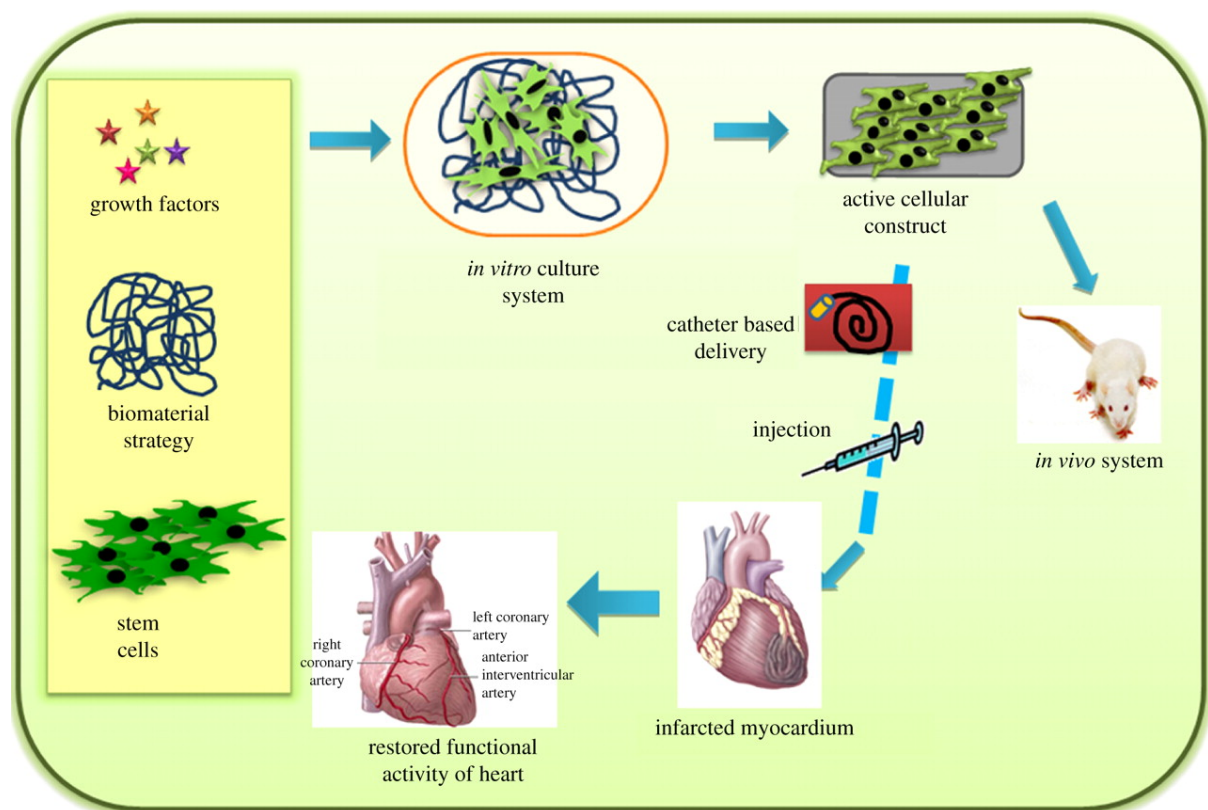


Figure 2.10, schematic representation of employing stem cells with scaffolds and growth factor to produce patches of heart tissue and inject into an infarcted myocardium heart to restore the functionality of a functioning heart [5].

The main aim of cardiac tissue engineering is to produce a biocompatible, non-immunogenic heart muscle with morphological and functional properties to repair myocardial infarction and restore to natural myocardium [71].

## 2.6.1 Regulating Cardiac Regeneration and Assembly

Recently, stem cell biology has allowed tissue engineers to produce high fidelity engineered cardiac tissue (Figure 2.11). In order to produce and develop an adult-like cardiac tissue in-vitro requires cues that will guide cell self-assembly to resemble native tissue morphology and function. Myocardium is an organized tissue, which allows anisotropic action potential propagation and contraction to pump the heart effectively [72]. The cues that are responsible for promoting the generation of in-vitro cardiac tissue include spatial environment around the cells. This environment makes an instructive structure that directs the cell adhesion and physiological levels of electrical and mechanical stimulation.

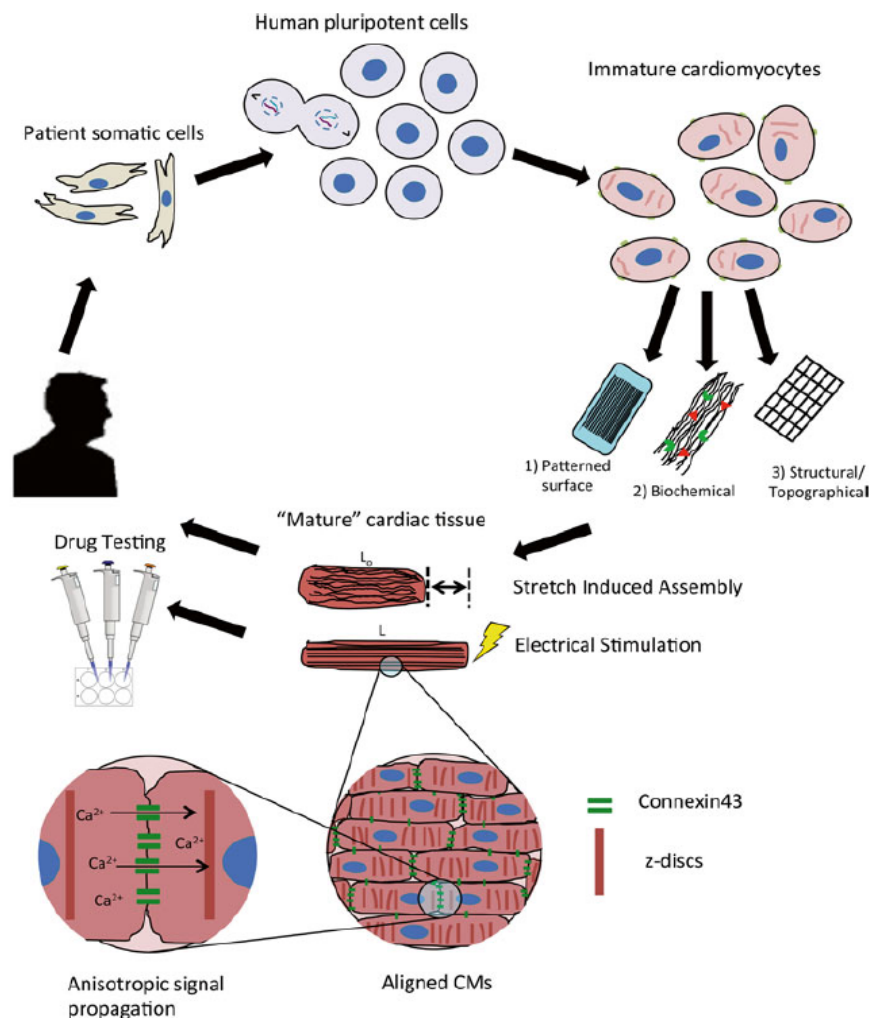


Figure 2.11, schematic of cardiac tissue engineering paradigm, patient’s somatic cells are reprogrammed to a pluripotent state and then differentiated towards an immature state of cardiomyocytes, which mature through specific electrical and mechanical cues. After the maturation the engineered cardiac tissue is implanted into the patient or used for drug testing applications [72].

Myocardium consists of a specific ratio of cardiomyocytes, fibroblasts, endothelial cells, pericytes, and smooth muscle cells [72]. In order to create high fidelity engineered cardiac tissue, it is important to obtain this ratio which will produce a supportive tissue environment for maintaining proper cardiomyocytes contraction. Fibroblasts form close connections with the cardiomyocytes that aid in its development and provide structural, biochemical and functional tissue properties [69]. In the heart, cardiac fibroblasts are primarily responsible for producing and regulating the ECM and are essential for creating a functional syncytium [4]. However, the ratio of cardiomyocytes to cardiac fibroblasts greatly influences the macroscopic tissue morphological properties and functional characteristics in a cardiac tissue. By encapsulating cells in a hydrogel the spatial orientation of cells can be controlled. These encapsulated cells interact with and remodel the surrounding fibres by using matrix metalloproteinases and other proteins to build an appropriate surround for their development. Since hydrogels consist of a high percentage of water, during remodeling the cells exert tractional forces on the matrix that makes the gel compact and releases water [68]. During this compaction process cells get closer and form functional connections with one another creating a tissue resembling native myocardium that conducts electric impulses and beat synchronously [73].

To resemble native architecture and function of the myocardium, cardiac tissue engineers use an array of biophysical cues which influence the assembly of organized mature cardiac tissue to generate aligned functional cardiac tissues. Researchers have implemented micro- and nano- scale technologies to replicate key feature of native heart [70]. Two aspects that play a critical role in recreating a functional tissue are – a) stretch activation (influences physical features such as increased size) and b) electrical stimulation (improves electrical maturation) [72]. This significantly improves the prospects of creating a high fidelity cardiac tissue.

## **2.7 Principles of Surface Acoustic Waves**

Recently acoustic waves devices have been gaining advances in wide range of applications such as resonators, filters, lab-on-a-chip (LOC), microfluidics and actuators. The family of acoustic wave devices consists of surface acoustic wave (SAW), shear horizontal surface acoustic wave (SH-SAW), shear horizontal acoustic plate mode (SH-APM), flexural plate wave (FPW) or Lamb wave mode (LWM) and thickness shear mode (TSM) devices [74]. The implementation of these devices requires knowledge of materials, acoustic wave properties,

device design, and sensing mechanisms for specific applications. To date, acoustic wave devices have been largely fabricated and manufactured for telecommunication systems, for example in the mobile phone industry. Acoustic wave devices are sensitive to a combination of parameters at any given time and to avoid this, overlaps of different fabrication material properties have been employed to generate acoustic waves such as anisotropic and piezoelectricity [74]. In this work piezoelectric materials such as lithium niobate ( $\text{LiNbO}_3$ ) have been used to generate acoustic waves.

### **2.7.1 Piezoelectricity and crystal symmetry**

Piezoelectricity is derived from the Greek translation word piezin, meaning pressure electricity, discovered by Jacques Curie and Pierre Curie in early 1880 [75]. They observed electrification on pyroelectric crystals when heated fluctuated under mechanical pressure. This behaviour was observed in crystals such as tourmaline, quartz, cane sugar and Rochelle salt [74]. Since it was observed for only certain type of crystal cuts and mostly pyroelectric materials it was understood that symmetry plays a decisive role in the piezoelectric effect particularly in the direction normal to polar axis. Lippmann in 1881 deduced mathematically from fundamental thermodynamic principle the converse piezoelectric effect, i.e., deformation or stress under applied electric field. J. Curie and P. Curie were quick to confirm this theory of Lippmann and since then piezoelectricity has been commonly used to describe materials that have the ability to develop electric displacement,  $D$ , which is proportional to the applied mechanical stress,  $\sigma$ , as shown in Figure 2.11,

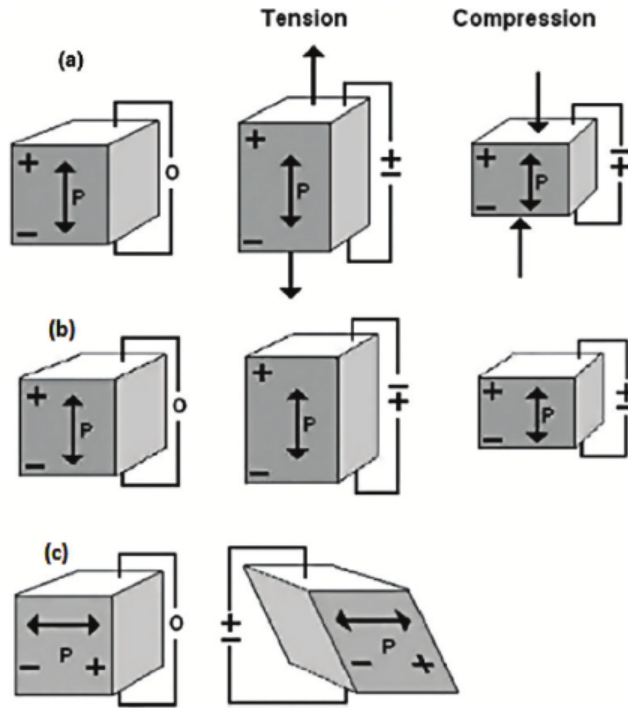


Figure 2.12, schematic representation of longitudinal, (a) direct, (b) converse, (c) shear piezoelectric effects on a piezoelectric substrate [73].

From the Figure 2.12, it can be understood that if the applied stress is changed from tensile to compressive then the electric charge that appears on the electrode reverses its sign. Hence all piezoelectric materials converse to piezoelectric effect which means they deform under applied electric field. In Figure 2.12 (c) shear piezoelectric effect occurs when it linearly couples shear mechanical stress or strain with the electric charge [74].

Table 2.1 Acoustic wave generations on different piezoelectric substrates [74].

	Rayleigh SAW	SH SAW	SH APM	Lamb wave FPW
Substrate	ST-quartz	Lithium tantalate	Lithium niobate ST-quartz	$\text{Si}_x\text{N}_y/\text{ZnO}$
$f_0$ (MHz)	160	110	160	1-6
$U^a$	transverse parallel	transverse	transverse	transverse parallel
$U_t^b$	normal	parallel	parallel	normal
Medium	gas	gas liquid	gas liquid	gas liquid

<sup>a</sup> Particle displacement relative to the wave propagation direction.

<sup>b</sup> Transverse component relative to the sensitive surface.

Different piezoelectric devices have been characterized in terms of material and particle displacement relative to the direction of wave propagation for operations in either gas or liquid medium. Table 2.1 shows a comparison of different modes of operation for various acoustic wave sensors. The principle mechanism behind these devices is primarily a function of parameter perturbation affecting the propagating wave on the surface of the sensor.

### **2.7.2 SAW transducers**

Surface acoustic waves (SAW) utilize mechanical or acoustic waves as a sensing mechanism. These waves propagate through the substrates made up of the piezoelectric crystals. In recent years, SAW based devices have gained momentum in the LOC and microfluidic community. Touch sensitive screens and biological/chemical sensing are just few of the established applications of SAW technology [76-80]. The characteristic of propagation path affects the velocity and the amplitude of the wave. The unique property of piezoelectric substrate is that when it undergoes mechanical stress it generates an electric field and when it experiences an electric field it will deform its shape, i.e., undergo mechanical stress [81].

One of the substrates used to generate acoustic waves is Lithium niobate ( $\text{LiNbO}_3$ ) [82,83]. This substrate made of quartz crystals has selective temperature dependence according to the cut-angle of crystals and the direction in which the waves propagate.  $\text{LiNbO}_3$  crystals are oriented according to three rotations - Y, Z and  $128^\circ$ . The crystals in the substrate used in this thesis have  $128^\circ$  rotation which exhibits velocity of waves of 3994m/s [84,85]. Gold-coated transducers are patterned on the substrate to generate SAW and the velocity of waves is taken into consideration when designing these inter-digitated transducers (IDTs).

### **2.7.3 Unique advantages of SAW-based biosensing devices**

SAW technology offers much useful and inimitable combination of features that attract a lot of application in the field of biomedical:

Simple, compact and inexpensive – SAW devices are being used widely in various commercially available electronics systems such as mobile phones. This demonstrates that the components and accessories that drive the SAW devices are compact,

inexpensive and highly reliable [86]. Microfluidic based SAW platforms offer easy to fabricate, integrate and produce microfluidic on-chip applications;

High biocompatibility – ultrasonic imaging has been predominantly used for monitoring health during different stages of pregnancy and has proven to be safe [87]. SAW devices operate in similar ranges in terms of acoustic power intensity and frequency. Therefore it is safe to assume that an ideally designed SAW based biochip will be safe and biocompatible with cells, molecules and other biological specimens. This assumption has been confirmed with cell viability and proliferation tests using available acoustofluidic devices [88-90];

Fast fluidic actuation – current LOC techniques find it difficult to generate fast fluidic actuation on particles. Due to this, their applications in medical diagnostics and biochemical studies have been limited. SAW devices can be designed to introduce chaotic advection in a microfluidic system to effectively manipulate fluids and particle [91]. From manipulating mm-scale object such as *C. elegans*, to separating um-scale biological cells and pumping fluids at 1-10 cm/s, SAW based devices have proven their achievements [92]. Neither of these features can be readily achieved by any other microfluidic technique [59].

Versatility – SAW based applications have enabled biological/chemical detection, fluid control such as mixing, translation, jetting and atomization, and particle manipulation such as focussing, patterning, separation, sorting, concentration and re-orientation [93]. Regardless of shape, electric or magnetic or optical properties, SAW devices can manipulate either a single particle or group of particles;

Contact free manipulation – this technology allows manipulation of particles and cells by means of acoustic radiation force applied by the surrounding fluid. This provides a platform that is contact-free thus eliminating any potential of damage to cells and prevents sample contamination;

Convenient on-chip integration with SAW based sensors – SAW based devices have recently been applied for sensitive detection and sensing by integrating with other microfluidic based sensors or with other SAW devices [94-96]. This characteristic makes this technology feasible for launching into practical clinical settings and fully integratable with LOC system.

## 2.8 Travelling Surface Acoustic Waves

Rayleigh waves are SAWs that are composed of longitudinal and a vertical polarized shear component [97] as shown below,

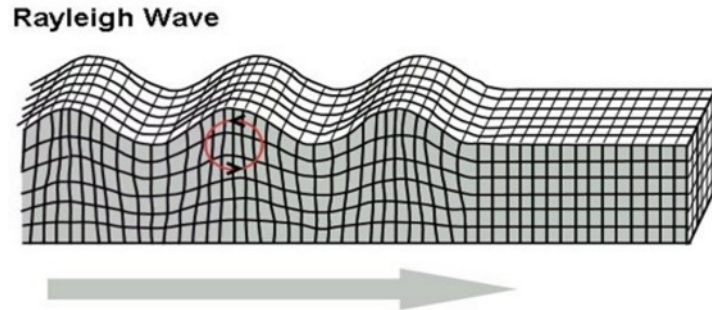


Figure 2.13, schematic representation of SAW travelling motion just like waves roll on the surface of lake or an ocean. Due to the rolling motion, the wave produces stress up and down the substrate and side to side in the same direction of propagation [97].

Rayleigh SAWs can strongly couple with the media on the substrate allowing sensing of mass perturbation and elastic properties of medium in the path of the wave propagation. Most SAW based LOC techniques employ Rayleigh SAWs for biomedical applications. Applying an electric field to a piezoelectric substrate induces a propagating mechanical stress that generates these waves. SAW based devices consist of at least one set of metallic interdigitated transducers (IDTs) that are fabricated on the surface of the piezoelectric substrate. An IDT consists of number of electrode fingers interspaced with an opposite set of connected fingers thus allowing an alternating current electrical signal (Figure 2.14).

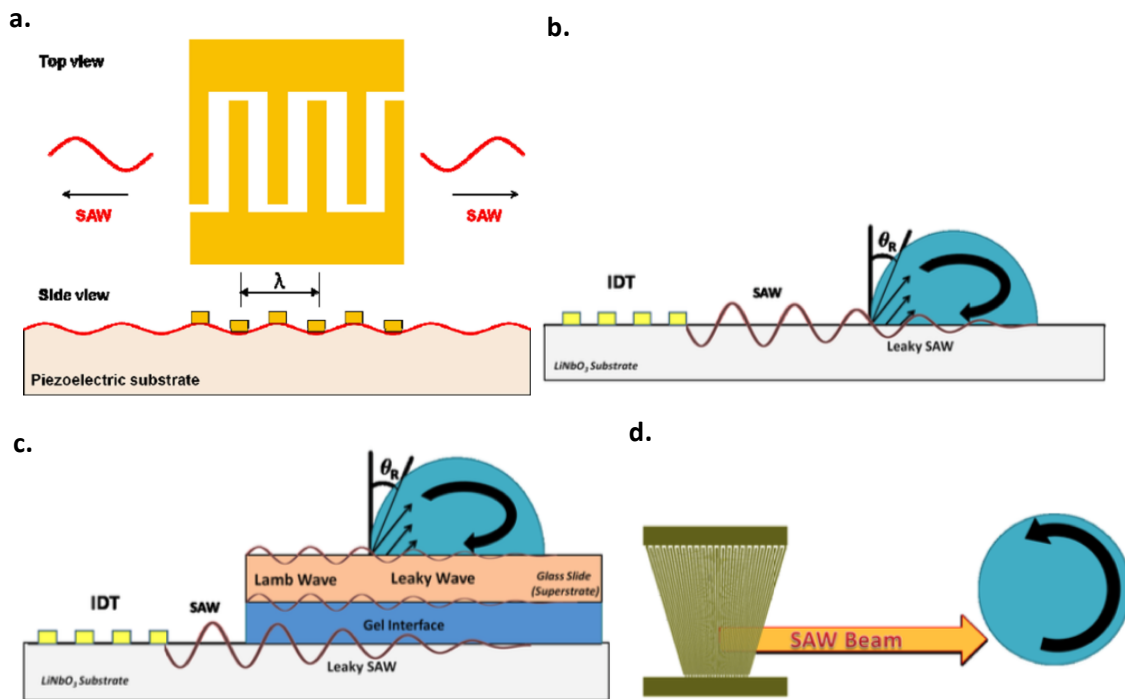


Figure 2.14, schematic representation of SAWs generated on piezoelectric substrate a) generation of waves propagating in both directions, b) represents the integration of acoustic wave into a droplet, c) shows wave integration onto a superstrate through a coupling layer of water or gel d) shows slanted-finger IDTs producing a narrow band of waves along with length of the IDTs [98].

SAW studies have shown to actuate droplet of liquid on bare piezoelectric substrates as well as integrating the waves onto a superstrate by using coupling layer such as water or gel. A slanted finger IDT has a gradient of electrode finger width perpendicular to the wave propagation direction that allows the IDTs to generate a narrow varying frequency along its finger length.

### 2.8.1 Acoustic streaming

When the SAWs come in contact with a stationary droplet of liquid, the liquid's increased viscosity relative to the air causes the part of SAW to refract into the liquid as a longitudinal wave called leaky or pseudo- SAW as shown in Figure 2.15 below [99] ,

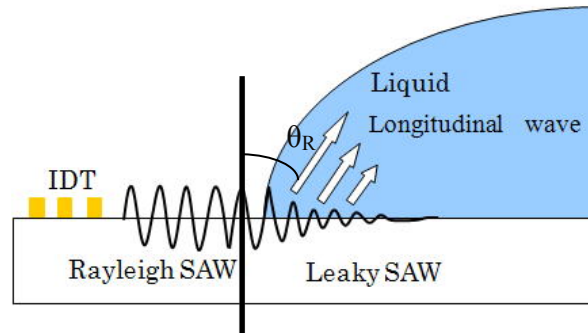


Figure 2.15, SAW induced acoustic streaming of Rayleigh SAW excited by IDTs. Upon contact with the liquid SAWs refract and convert to leaky SAW at an angle  $\theta_R$  into the fluid.

The travelling refracted wave moves in the direction of propagation defined by the refractive angle known as Rayleigh angle ( $\theta_R$ ), defined by Snell's law [100],

$$\theta_R = \sin^{-1} \left( \frac{c_l}{c_s} \right) \quad (2.5)$$

Where,  $c_s$  and  $c_l$  denote acoustic wave velocities of the piezoelectric substrate and fluid. Lithium niobate wafer that has a  $128^\circ$  Y-cut at room temperature has a wave travelling velocity 3994m/s [101]. The longitudinal waves upon interaction with the fluid induce the energy responsible for the fluid flow motion. This non-linear phenomenon that converts attenuated waver energy from SAW into a steady fluid flow is called SAW-induced acoustic streaming [102-108].

Acoustic streaming can be classified based on induced vortices and acoustic wavelength characteristics [109]. Firstly, Schlichting streaming, is the streaming that occurs at solid-liquid interface due vortex flow. Secondly, Rayleigh streaming occurs outside boundary layer due to vortex flow and thirdly, Eckart streaming which is the streaming of fluid occurring due to attenuation of travelling wave. Finally the streaming velocity magnitude depends on the Reynold's number [110-111].

SAW based manipulation of single cells have been the current focus of research due to its ability of being non-invasive. The standing surface acoustic waves (SSAW) are created in the sample by placing it between the identical IDTs on the piezoelectric substrate [112]. Bioparticles experiencing acoustic force are pushed to align in pressure and anti-pressure nodes of the standing wave, depending on medium and properties of the particle [113-114]. Shifting from regular-IDTs to slanted-IDTs has shown change in the controllable pattern of separation between particles [114]. Such control of particles has applications in tissue engineering and regenerative medicine [115]. Rogers et al. [116], studied two forces arising from acoustic streaming – radiation and drag forces, for particle manipulation in a micro-droplet. Smaller particles (6 $\mu\text{m}$ ) experienced dominant drag forces and larger particles (31 $\mu\text{m}$ ) experienced radiation forces at 10MHz.

SAW driven pumps offer diverse applications without being in contact with samples and affecting the electrodes. Acoustic streaming is the motion of fluid induced by acoustic wave propagation into the medium. This displacement of fluid originates either due to attenuation of the waves in the fluid over the length of the chamber or by boundary interaction with container walls [117]. The pressure gradient produces a force in the same direction of wave propagation and induces fluid flow. This is a non-linear phenomenon called acoustic streaming [118]. The state of fluid particles experiencing acoustic waves is described by pressure and velocity oscillations [119].

In an ideal fluid, time averages particle displacement, i.e., the net fluid flow is zero everywhere. However in real fluid, the viscous attenuation results in a net displacement of fluid particles during each cycle of oscillations [119]. This local effect leads to the global formation of streaming flow. This steady flow depends on velocity of flow, length scale of flow and geometry of flow along the channel [113].

Streaming flow patterns depend on the attenuation of the wave and the width of the microchannel. The magnitude of fluid velocity reported has been of orders of  $\mu\text{m/s}$  to  $\text{cm/s}$  [120]. Flow geometry of the fluid can be described in terms of vortices or jet patterns. During actuation of the fluid, vortices are created which develop pressure differences that pump the fluid [121]. However, it should be noted that the flow is only visible when wave propagation is comparable in size to acoustic wavelength [109] and if it becomes greater than Rayleigh streaming vortices the flow can become turbulent [122].

## 2.9 Standing surface acoustic waves (SSAW)

Conventional electrokinetic devices have previously dominated the development of micromanipulation in microfluidic devices. Manipulation of cells and droplets by mechanically driven pumps, optical tweezers [123], electrophoresis and electrowetting on dielectrics (EWOD) [124], have been proposed and each have their own advantages and disadvantages. The process of manipulation is critical for lab-on-a-chip devices and diagnostics. These conventional techniques have disadvantages such as complexities, bulky instrumentation, pre-treatment of bioparticles and lack of visual control on flow. Thus this calls for the development of simple, easily operated and convenient methods, which can be integrated with other lab-on-a-chip techniques. Surface Acoustic Waves recently have shown promising advances in micro-particle manipulation and mixing [115].

### 2.9.1 Formation of SSAW fields

SSAW are created by a pair of identical IDTs fabricated on piezoelectric materials by generating two or more identical travelling SAWs heading towards each other. The interference of these two waves will result in a one-dimensional SSAW as shown in Figure 2.16. In figure 2.16, the bright red region represents the negative pressure (region of lower pressure amplitude) and dark blue regions represent the large amplitude of pressure gradients. Standing surface acoustic waves create a wave pattern create points along the medium that appear to be still i.e. no displacement, these are known as nodes. However, there are other points that undergo large positive and negative displacement. These points are opposite of nodes called anti-nodes. Once an RF signal is applied to both the transducers, two series of SAWs propagate in opposite direction towards the sample medium. As a result, due to constructive interference of the two SAWs there is a periodic distribution of pressure nodes (minimum pressure amplitude fluctuation) and anti-nodes (maximum pressure amplitude fluctuation). The standing waves create fixed regions (nodes) due to lack of pressure fluctuations and alternating regions (anti-nodes) that exhibit alternating pressure maxima and minima. When these waves integrate in to the liquid medium, leakage waves in longitudinal mode are generated what cause pressure fluctuations in the medium. These pressure fluctuations result in acoustic radiation forces acting laterally in x-direction. As a result, the particles suspended in the liquid medium will either moved towards the pressure nodes or anti-nodes depending on the density and compressibility of particles and medium. The direction of the force is determined by the sign of the acoustic contrast factor ( $\phi$ ): a positive  $\phi$ -factor results in movement towards pressure nodes such as cells, polystyrene beads and a negative  $\phi$ -factor results in movements towards pressure

anti-node such as bubbles. Once the cells reach the pressure nodes, the acoustic forces resulting is nearly zero thus creating steady patterns of cells in the well due to lack of pressure fluctuations in the region. And ones the bubbles reach the pressure anti-nodes the acoustic force is exhibited on them due to the negative gradient of acoustic pressure exhibited in the region.

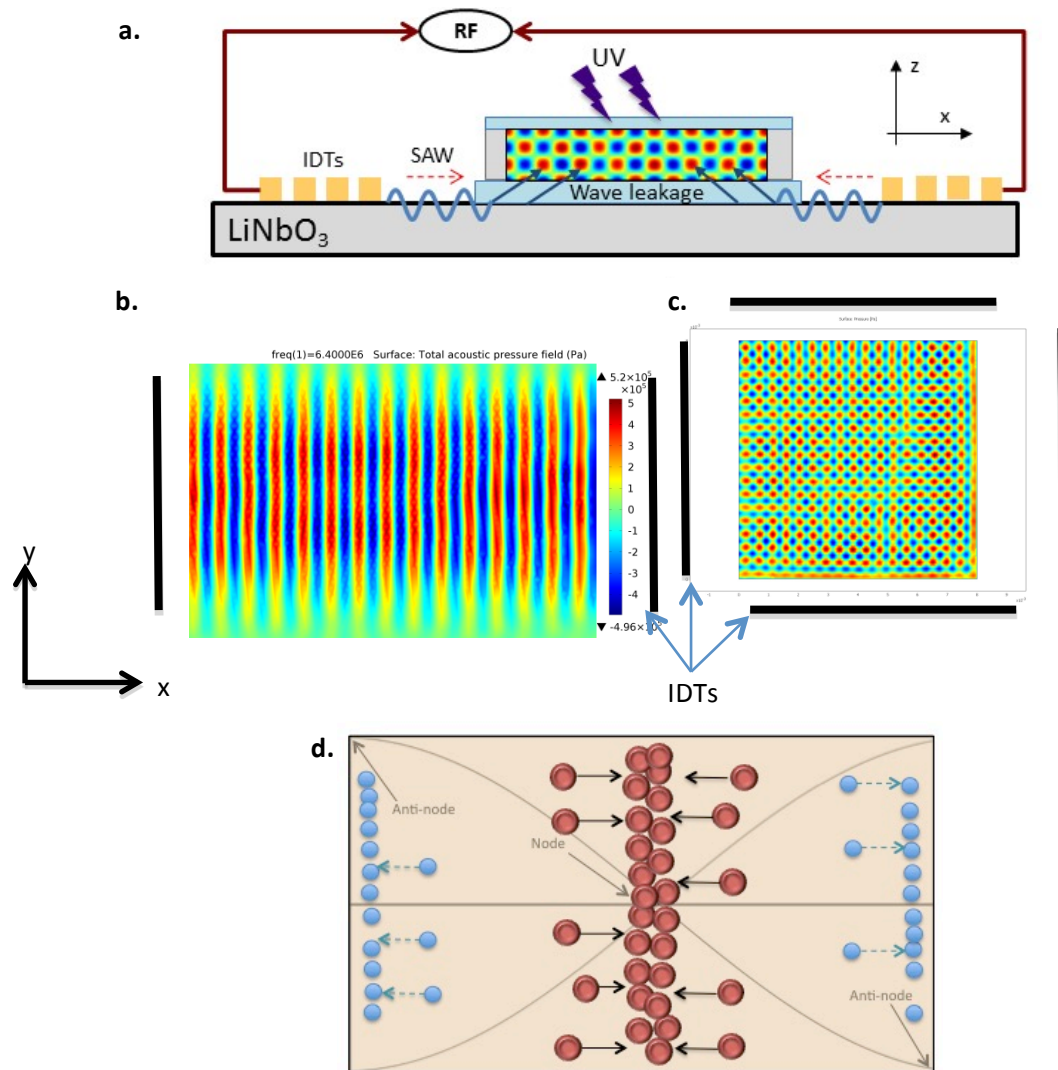


Figure 2.16, schematic representation of SSAW modelled in COMSOL Multiphysics software 5.0a, a) computational modelling of SSAW on lithium niobate substrate propagating towards each other, b) model of SSAWs from two opposing IDTs to create 1D patterning (top-view), c) model of SSAWs from subsequent four IDTs designed on the substrate to create 2D patterning (top-view), d) shows the movement of cells (red) moving towards the node on experiencing acoustic waves and bubble (blue) moving towards anti-nodes.

The light (red) and dark (blue) regions represent the small and large amplitudes of sound pressure waves in Figure 2.16. SSAWs demonstrate a series of nodes (minimum field) and

anti-nodes (maximum field) at fixed locations on the piezoelectric substrate. The distance of separation between adjacent pressure node (positive) and pressure anti-node (negative) is always half the wavelength of SAW generated. In Figure 2.16 (d), the spatial pressure distribution along the line X-Y is depicted by solid red line. This spatial pressure distribution is related to the time corresponding to the peak of the first half cycle of the wave. This peak is associated with a timing of  $t=1/(4f)$  where  $t$  refers to the time and  $f$  is the frequency. Similarly, the pressure distribution along the line X-Y in the negative peak of the second half-cycle of the wave is illustrated with the dotted blue line. This timing is associated with  $t=3/(4f)$ . Such plots can help us gain an understanding of not only the spatial patterning of the cells, but also further information regarding the cells localization. (e.g. higher amplitude pressure will result in faster organization of the cells).

Standing Surface acoustic waves (SSAW) can be used to control and manipulate bioparticles by a technique known as acoustophoresis. Standing SAWs generated by slanted-IDTs (SIDTs) have the advantage of knowing the lateral location of the waves generated by changing the input wave wavelength. SIDTs provide a control over the aperture of the transmitted waves. Recently studies have shown droplet manipulation [125], focussing microparticles with standing SAW [112,126-127], acoustic tweezers [112] and a SAW nano-pump [128].

Girardo et al. [114] discussed integrating LiNbO<sub>3</sub> substrate with polydimethylsiloxane (PDMS) for withdrawing water into PDMS channel by SAW. This process of withdrawal was related to the exponential decay of the wave power along the microchannel. Moreover, this model depends on liquid-air interface and droplet dynamics and states the dampness of power in liquid capillaries.

Y. Yeo et al., [129] demonstrated powerful actuation of fluid by SAW at megahertz frequencies. The study demonstrated fluid velocity starting from 1cm/s to 10cm/s in microchannels arising due to fluid-structural coupling. Furthermore, when SAW input power was held constant for increasing widths of channel, the flow of the fluid exhibited irregular patterns. These vortices arise due to sound wave reflection from the sidewalls [129]. A uniform flow was only observed when the width of the channel was less than the wavelength of the acoustic waves, which indicates that when the width of the channel is greater than the wavelength an oscillatory flow can be observed.

## 2.9.2 Primary acoustic radiation force

Theoretically and experimentally it has been established that for particles suspended in a fluid medium when exposed to SSAW, the primary acoustic radiation force will move the particles towards the pressure nodes or anti-nodes depending on the surrounding fluid and particle properties. SAW sensor electrodes are designed with same orientation as the crystals so that the IDTs can impart the maximum amplitude to the waves. The behavioural response of a SAW device coated with isotropic film is given as [130],

$$\Delta f = (k_1 + k_2)\rho h f_0^2 - k_2 h f_0^2 \left(\frac{4\mu}{V_R^2}\right) \left[\frac{\lambda + \mu}{\lambda + 2\mu}\right] \quad (2.6)$$

where,

$k_1$  and  $k_2$  are material constants for quartz substance

$V_R$  = Rayleigh wave velocity

$h$  = Film thickness

$\rho$  = Density

$\mu$  = Shear modulus of film material

$\lambda$  = Lamb constant

$f_0$  = Fundamental frequency of the device

The first half of the equation corresponds to the shift resulting from mass loading whereas the second half of the equation describes the effects of changes in elastic properties of the film on resonant frequency [130]. The time average acoustic radiation force is a gradient of a potential [217],

$$F_{rad} = -\nabla U \quad (2.7)$$

Where  $U$  is the acoustic force potential given by,

$$U = V \left[ \frac{f_1}{2\rho_m c_m^2} (p^2) - \frac{3f_2 \rho_m}{4} (|v|^2) \right] \quad (2.8)$$

Where  $p$  and  $v$  is the pressure and velocity field in the surrounding region of the particle,  $V$  is the volume of the particle and  $\rho_m$  and  $c_m$  are the density and speed of sound in liquid medium. The compressibility factor  $f_1$  and density factor  $f_2$  are given as [217],

$$f_1 = 1 - \frac{1}{\gamma\beta^2} \quad f_2 = \frac{2\gamma-2}{2\gamma+1} \quad (2.9)$$

Where  $\gamma$  and  $\beta$  are speed of sound ratio and density ratio of the particle and medium respectively,

$$\beta = \frac{c_p}{c_{pm}} \quad \gamma = \frac{\rho_p}{\rho_m} \quad (2.10)$$

In microfluidic systems, acoustic waves manipulate particles as a result of complex 3D resonance. One dimensional coupling effect of acoustic waves at a single frequency excitation can be observed commonly. Thus by assuming a chosen frequency a strong resonance field in 1D (axial) and wavelength being much longer than the radius of the particle the approximation of the acoustic radiation force is given by [218],

$$F_a = -\left(\frac{\pi P_o^2 V_p \beta_m}{2\lambda}\right) \emptyset(\beta, \rho) \sin(2kx) \quad (2.11)$$

$$\emptyset = \frac{5\rho_p - 2\rho_m}{2\rho_p + \rho_m} - \frac{\beta_p}{\beta_m} \quad (2.12)$$

where,

$P_o$  = Pressure amplitude

$V_p$  = Particle volume

$\lambda$  = Ultrasonic wavelength

$k$  = Wave factor

$x$  = Distance from a pressure node

$\emptyset$  = Acoustic constant factor

$\rho_p$  = Density of particles

$\rho_m$  = Density of medium

$\beta_p$  = Compressibility of medium

$\beta_m$  = Compressibility of particles

SSAW manipulation is suitable for handling large groups of suspended particles or cells. The equation (2.11) indicates that the acoustic force generated is directly proportional to the volume of the particle. The acoustic contrast factor (ACF) determines whether the particle moves to pressure node or anti-node depending on their elastic properties. The particles will aggregate at pressure nodes when ACF is positive and pressure anti-nodes when ACF is negative. Biological particles and cell have positive ACF whereas bubbles and lipids have negative ACF [132].

Due to the piezoelectric effect a spatially periodic field at the IDTs produces a corresponding periodic mechanical strain pattern as shown in Figure 2.17. This causes acoustic waves to propagate away from the IDTs in the direction perpendicular to the electrodes.

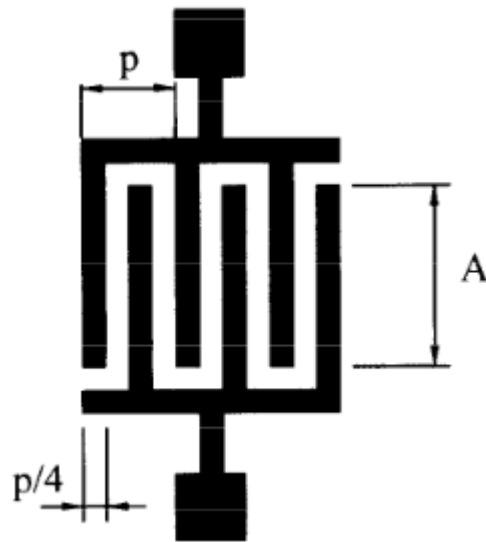


Figure 2.17, schematics illustrating a uniform IDT design with pitch (or period)  $p$  with equally spaced electrodes and a constant electrode overlap  $A$ .

The working wavelength of the device is determined by three parameters - width (also known as pitch), angled or compression shaped IDTs [8]. Period of the fingers is given by [131],

$$D = \lambda = \frac{c}{f} \quad (2.13)$$

Where,

$\lambda$  = wavelength of SAW excitation

$c$  = wave velocity

$f$  = resonant frequency of sub-channel

The transducer pitch determines the wavelength of SAW,

$$\lambda = 2d \quad (2.14)$$

When a sinusoidal voltage is applied with frequency  $f$  ( $=1/T$ ) the vibrations interfere constructively only if the distance  $p/2$  between the adjacent electrodes is equal to half of the wavelength. This frequency  $f$ ,

$$f = \frac{v}{p} \quad (2.15)$$

where  $v$  is the phase velocity of the acoustic wave, corresponds to cumulative effect called synchronous frequency or resonance frequency.

The RF pulsed excitation signal generated from the IDT has a power level enough to cause droplet displacement and fluid streaming [133]. At lower excitation power the induced streaming motion inside the droplet causes internal circulation (generation of vortices). For high power ultrasonic excitation, the induced streaming motions impart momentum to the fluid giving acoustic streaming jets or atomization [134]. However, at higher excitation powers but below the frequency range that would cause jetting or atomization, the entire droplet translates along the direction of SAW propagation due to net force arising from leaky SAW [134-135]. Hence when the wavelength of the SAW decreases, the acoustic force increases over the viscous force [136].

When a standing SAW (SSAW) is created and interfaced in a liquid medium inside a channel, longitudinal-mode leakage waves are generated causing pressure fluctuations [136]. These pressure fluctuations (according to pressure node and anti-pressure node) can be calculated by finding the absolute node locations to which the bioparticles will be pushed when experiencing the force according to their density and/or compression variations [137-138],

$$x_n = \frac{n\lambda}{2} \quad (2.16)$$

for  $n^{\text{th}}$  order pressure node.

And the node displacement can be calculated by [138],

$$\Delta x_n = \frac{c(\lambda_1 - \lambda_2)}{2} \quad (2.17)$$

Standard SAW IDTs are designed to generate one specific frequency, compressed IDTs (CIDTs) give a wide range of frequencies and Slanted-IDTs (SIDTs) generate frequencies over a range defined when designing [137]. This bandwidth of SIDT translates into a wide spectrum of accessible standing SAW wavelength that defines large manipulation range of the device. By varying the input RF signal, the shift in location of pressure nodes created by interference of SSAW can be seen [138].

## 2.10 Patterning in stagnant fluid using SSAW

SSAW based technologies provide an invaluable platform for non-invasively arranging particles or cells in a stagnant fluid medium into desired patterns that are highly desirable for many biomedical applications including microarrays, tissue engineering and regenerative medicine. This non-invasive and non-contact acoustic force generated by SSAW serves as an excellent enabler of cell patterning techniques. Shi et al. [95] have demonstrated linear arrangement of particles by developing acoustic tweezers to effectively manipulate cells in PDMS microfluidic channels as shown below,

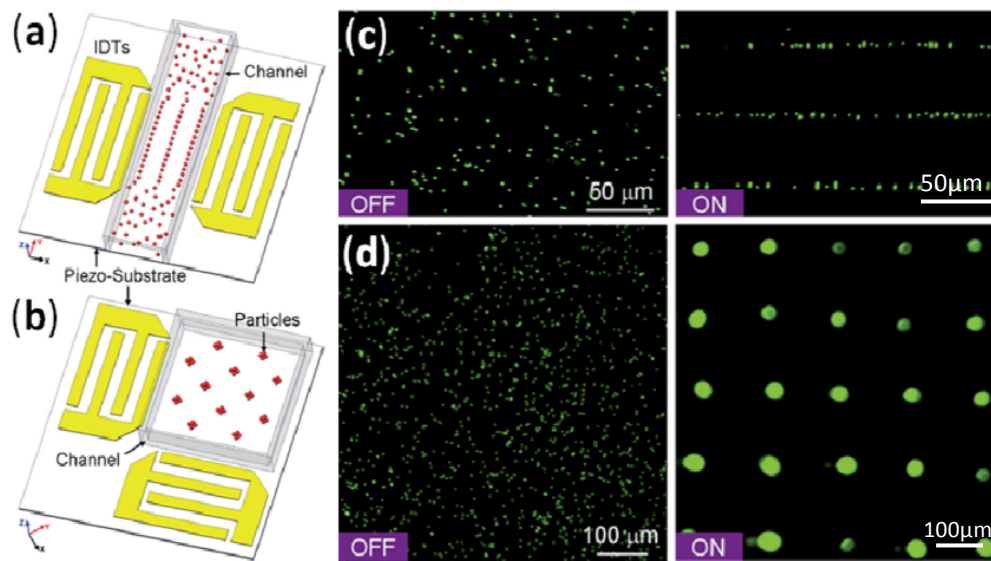


Figure 2.18, schematic representation of SSAW based patterning of group of particles in a stagnant fluid, a) using 1D patterning through two parallel IDTs, b) 2D patterning using two orthogonal IDTs, c) distribution of fluorescent microbeads before and after 1D SSAW is applied, d) demonstrates distribution of fluorescent microbeads before and after 2D SSAW is applied. The aforementioned devices have a narrow frequency patterning range due to design of regular IDTs. By designing slanted-finger IDTs a broader range of frequencies is available allowing dynamic control of particle patterning [95].

## 2.11 Dielectrophoresis

Particles of biological origin exhibit electric properties with respect to their shape, size and materials when exposed to electric fields, resulting in particles to experience forces and torques. This phenomenon is named particle electromechanics [139] and these forces and torques that arise are from the interaction of dipole and higher order moments with the field.

DEP is a type of imposed field interaction acting on a cell in presence of external field created by electrodes. The starting point to understand DEP will be to study the force acting on an infinitesimal electric dipole in a non-uniform electrostatic field [140]. An electric dipole is a system of two equal and opposite charges separated by a distance, as shown below,

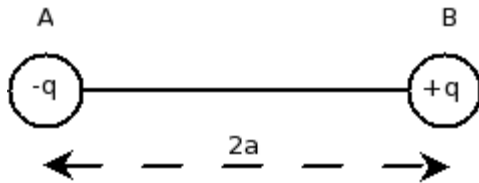


Figure 2.19: An electric dipole consisting of two charges  $+q$  and  $-q$ , separated by vector distance  $2a$  which is called length of the dipole.

Following the definition of electric dipole, electric dipole moment can be defined as, product of charge and length of electric dipole ( $C \cdot m$ ) [141],

$$\vec{m} = q \vec{d} \quad (2.17)$$

where,  $q$  is electric charge and  $d$  ( $=2a$ ) is the length of the dipole.

In a non-uniform electric field the representation of force and torque exerted upon a dipole is represented as given in Figure 2.20 [142],

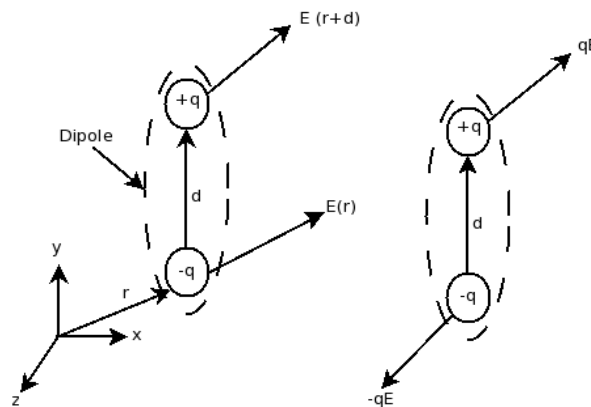


Figure 2.20: (a) The net force acting on the dipole of strength, (b) Coulombic forces creating net torque [142].

Therefore in a non-uniform electric field  $E$ , the net force acting on the dipole is [142],

$$F = qE(r + d) - qE(r) \quad (2.18)$$

However, for an infinitesimal dipole the length can be assumed as  $|d| \rightarrow 0$  and still be calculated as a finite dipole moment. Then the force acting on dipole of finite size will be represented as [141],

$$F = m \cdot \nabla E \quad (2.19)$$

where,  $m$  is the dipole moment and  $\nabla E$  is the field gradient (often stated as  $\text{grad } E$ ). This will give an adequate field interaction at smaller scales due to the large dimensions of the electrodes used compared to particle dimensions. This approximation is important in DEP because it explains that in a uniform field, i.e. when  $\nabla E = 0$ , the DEP force is zero.

If a particle is suspended in a fluid with uniform electric field it will cause the particle to polarize and induce a moment. This moment is said to be effective moment which is important for calculating the forces and torques exerted by electric field on biological particles as shown in Figure 2.21 [143],

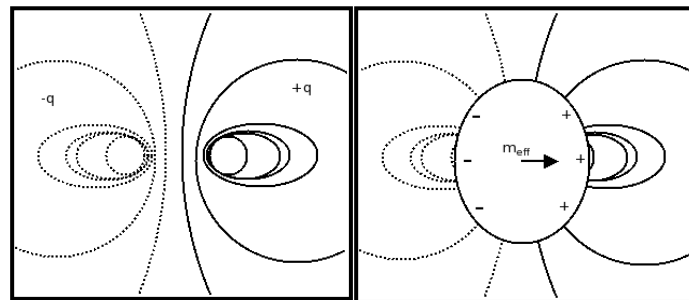


Figure 2.21: (a) Potential distribution of Point-Dipole, (b) Similar potential distribution as a Point-Dipole due to an assumption of formation of effective dipole moment

The electric field around the dipole is given by,

$$E = - \nabla \phi \quad (2.20)$$

where,  $\nabla$  is del operator and  $E$  is a vector quantity with unit Volts/m,  $\phi$  is electrostatic potential with units of Volts.

For a homogeneous dielectric sphere, effective dipole moment is given as [141],

$$m_{\text{eff}} = 4\pi \epsilon_1 C M R^3 E_0 \quad (2.21)$$

where, CM is known as Clausius-Mossotti (CM) function and can also be written as  $f(\epsilon)$  which is known as effective polarizability of the particle (per unit volume)[139].

$$f(\epsilon) = \frac{\epsilon_2 - \epsilon_1}{\epsilon_2 + 2\epsilon_1} \text{ or } \text{CM} = \frac{\epsilon_2 - \epsilon_1}{\epsilon_2 + 2\epsilon_1} \quad (2.22)$$

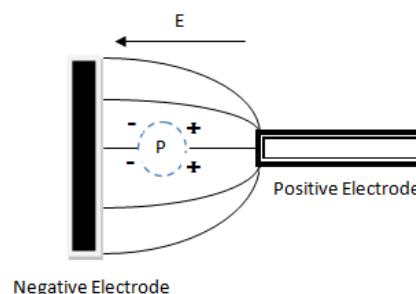
If  $\epsilon_2 > \epsilon_1$ , CM will be greater than 0 and the effective moment will be collinear with imposed electric field. If  $\epsilon_2 < \epsilon_1$ , CM will be less than 0 and  $m_{\text{eff}}$  and  $E_0$  will be antiparallel to each other. The Clausius-Mossotti factor is limited in limits of  $-0.5 \leq \text{CM} \leq 1$ , depending on the relative permittivity of particle and medium. And yet the effective moment is limited even if  $\epsilon_2 \rightarrow \infty$ . For the purpose of this research and convenience the permittivities are re-written as  $\epsilon_1 = \epsilon_p$  and  $\epsilon_2 = \epsilon_m$ , where  $\epsilon_p$  is permittivity of the particle and  $\epsilon_m$  is permittivity of the medium [129].

Biological particles exhibit conductivity due to the presence of ions on their structures that makes their surrounding medium, a state of conducting electrolyte [144]. Therefore any conduction loss is compensated by complex permittivity when an AC field is applied that has an imaginary part associated with the permittivity of the particle.

### 2.11.1 Dielectrophoretic force

DEP is a label free technique that can characterize and sort particles based on their dielectric properties, distinctively. It can also be defined as the force exerted on an induced moment of uncharged dielectric and/or conductive particle in presence of non-uniform electric field. It is defined as translational motion of electrically neutral matter in a non-uniform electric field which can be AC or DC [143]. The particle becomes polarized and can be thought of as a dipole experiencing a net force. Hence, dipole approximations describe DEP force acting on a particle. The effect of polarity is shown below in Figure 2.22,

Figure 2.22: The particle will experience a greater force of repulsion because of high Electric field near the positive electrode (due to nDEP) and if the particle had reversed polarity it would experience a strong force of attraction (due to pDEP).



The time-average DEP force acting on a spherically shaped particle in the form as,

$$F = (m_{\text{eff}} \nabla) E \quad (2.23)$$

and combining with equation (2.23),

$$F_{DEP} = 4 \pi \varepsilon_0 \varepsilon_m R^3 f(\varepsilon) (E \cdot \nabla) E \quad (2.24)$$

This equation can be re-written as,

$$F_{DEP} = 2 \pi \varepsilon_0 \varepsilon_m R^3 \text{Re}[f(\varepsilon)] \nabla E_{\text{rms}}^2 \quad (2.25)$$

where,

$\varepsilon_m$  : absolute permittivity ( $\varepsilon_r \varepsilon_0$ )

R : Radius of particle

Clausius-Mossotti factor or effective polarizability,  $f(\varepsilon)$  is given by,

$$\text{CM (or } f(\varepsilon)) = \frac{\varepsilon_p^* - \varepsilon_m^*}{\varepsilon_p^* + 2\varepsilon_m^*}$$

$\varepsilon_p^*$  : complex relative permittivity of the particle which in this case will be a cell.

$\varepsilon_m^*$  : complex relative permittivity of the medium.

E = amplitude (rms) of electric field.

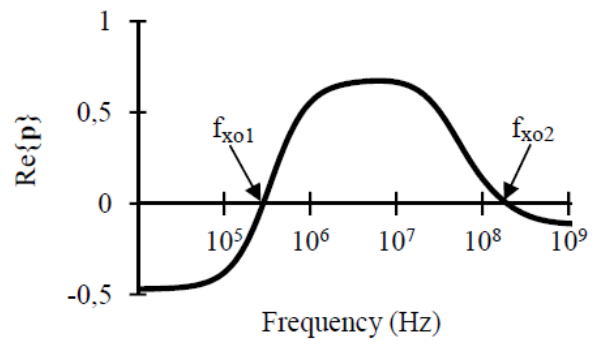
$\nabla$  = gradient operator.

Equation (2.25) reveals following important facts about DEP force [129], it depends on square of applied electric field, volume of particle and electrode geometry which are essential to study particle concentrations; and the separation and rotation.

The characteristics of  $F_{DEP}$  equated from equation (2.25) suggest that in a uniform field (i.e. for  $\nabla E = 0$ ), DEP force is zero, the larger the particle volume the greater will be the DEP force acting on it, if the particle's permittivity is greater or less compared to the surrounding medium, the induced dipole moment will align with or against the applied field respectively, giving rise to positive or negative DEP, where positive DEP can attract and negative DEP can repel in region of high electric field strength, DEP can be applied as either DC or AC field because the equation uses square of applied field magnitude and the factor  $(E \cdot \nabla E)$ , determines the electrode geometry and is an important parameter with units  $V^2/m^3$ . It reveals that reducing the dimensions of the electrode can increase the magnitude of FDEP acting on a particle [129, 143].

$E^2$  indicates whether AC or DC field is applied the force direction remains independent of polarity of electric field,  $E$  [129,142]. If CM factor is positive then work is required to withdraw particle from highest field region and if it is negative then work is required to push particle from a low to high field region.  $R^3$  dependence indicates DEP is particle-volume dependent. Induced dipole moment is either aligned with or directed against the applied field, depending on whether the particle's permittivity is greater or less than that of surrounding medium respectively. This corresponds to positive or negative DEP. In positive-DEP (pDEP), particle moves towards the region of high field strength where as in negative DEP particles moves towards the low field region [145]. This movement depends on the driving frequency and the dielectric nature of the particle and medium.

Figure 2.23 [145]: Frequency variation of the real part of the CM function for lymphocytes. The DEP force is proportional to this function and shows two cross-over frequencies,  $f_{x01}$  and  $f_{x02}$ .



At low frequencies ( $\omega \rightarrow 0$ ) the dielectric displacement current dominates and the particle acts like a capacitor, i.e., like an electrically insulating particle and the DEP force depends on conductive properties of the particle and suspending medium exhibiting negative DEP. At intermediate frequencies both conductive and dielectric properties of the medium and the particle enable the particle to be more polarisable than the medium. The electric field will penetrate through the cell creating a positive DEP effect. At high frequencies the permittivity values are important. A transition occurs from negative to positive DEP occurs at well-defined frequency  $f_{x01}$ . The second cross-over frequency  $f_{x02}$ , occurs approximately at 100MHz irrespective of the cell size as shown in Figure 2.23, depending on the conductivity of the medium [145].

Collins et.al. (2014) [146] demonstrated a virtual Deterministic Lateral Displacement (vDLD) method. According to this technique, travelling acoustic waves/dielectrophoretic forces are generated on a lithium niobate substrate which generate pressure nodes on particles enclosed in a PDMS chamber. However, since the IDTs are designed on a piezoelectric substrate, they will generate acoustic forces rather than electric forces.

Wiklund et al. [147], have presented an integrated ultrasonic wave technique with dielectrophoretic microelectrodes used as deflectors. This is the first paper, published in 2006, that discussed the combined application of DEP and ultrasonic waves.

## 2.12 Similarities between SAW and DEP

Equations (2.11) and (2.25), show that both the surface acoustic wave technology and dielectrophoresis have some similarities such as - Both are directly proportional to volume of biological cell, DEP is proportional to square of electric field gradient and SAW is directly proportional to acoustic pressure, which is dependent on applied voltage and DEP is dependent on CM factor, whereas SAW is dependent on ACF (Acoustic contrast factor) [147].

## 2.13 COMSOL Multiphysics modeling

### 2.13.1 Finite element modeling of Surface Acoustic Waves

SAWs are mechanical waves that are generated on piezoelectric substrates such as lithium niobate and propagate on the surface of the substrate either in Rayleigh mode or shear wave mode. The velocity of these waves is determined by the substrate properties such as elasticity, crystal orientation, density and quality of piezoelectric wafer. SAWs are very sensitive to changes in ambient environments and defects on wafers [148]

Acoustic-piezoelectric interaction module was used to simulate SAW propagation and acoustic pressure field generated on the device. The lithium niobate substrate is governed by linear piezoelectric equations consisting of Maxwell's equations for electric field and stress-strain equations for mechanical motion [149],

$$T = C_E \cdot S - e^{tr} \cdot E \quad (2.26)$$

$$D = e \cdot S + \varepsilon \cdot E \quad (2.27)$$

Where, T is mechanical stress vector,  $C_E$  is elasticity matrix, S is strain vector, e is piezoelectric stress matrix coupling the electric field and mechanical motions between the two equations, E is electric field vector, D is electric displacement,  $\varepsilon$  is dielectric matrix and 'tr' represents transpose of a matrix [149]. Helmholtz wave equation governs the harmonic acoustic field in the fluid and microfluidic chamber,

$$\frac{1}{\rho_i^*} \nabla^2 p - \frac{\omega^2 p}{\rho_i c_i^2} = 0 \quad (2.28)$$

$$\text{where, } \rho_i^* = \frac{\rho_i c_i^2}{\omega^2} \left( \frac{\omega}{c_i} - j \ln(10) \frac{\alpha_i}{20} \right)^2 \quad (2.29)$$

$\rho_i, c_i$  and  $\alpha_i$  are density, speed of sound and acoustic attenuation coefficient in the corresponding domain. SSAWs are generated in the fluid by applying sinusoidal AC signal applied to the electrodes on the piezoelectric substrate and the outer boundaries of the lithium niobate substrate are electrically insulated. The boundaries surrounding the IDTs on the wafer are set at stress free boundary condition except for the boundaries in contact with the fluid and PMMA [149]. This allows the no force loads or constraints to be applied on the two regions. The remaining region of the lithium niobate substrate is set at zero normal displacement. The acoustic pressure field generated in contact with medium and PMMA is represented as,

$$T \cdot n = -pn \quad (2.30)$$

The acoustic pressure wave is determined by setting the acceleration boundary condition at the interface of the chamber and fluid side [150],

$$n \cdot \left( -\frac{\nabla p}{\rho_i^*} \right) = a_n \quad (2.31)$$

Where  $n$  is the unit vector and  $a_n$  is normal acceleration.

To study the effect of acoustophoresis on driving particles at pressure and anti-pressure nodes, a certain number of particles were allocated in the fluid domain for particle tracing. This allows determination of acoustic radiation force on the suspended particles by employing Newton's second law on the  $k$ th particle [148],

$$m_{p,k} \frac{dv_k}{dt} = \langle F_{ac} \rangle_k + F_{Drag,k} + F_{G,k} \quad (2.32)$$

$$\text{Where } F_{Drag,k} = -6\pi\eta a v_k \left[ 1 + 1.08 \left( \frac{a}{d_k} \right) + 1.4 \left( \frac{a}{d_k} \right)^2 \right] \quad (2.33)$$

$F_{Drag,k}$  is the drag force of the  $k$ th particle which considers the wall effect during motion,  $\eta$  is fluid dynamic viscosity,  $d_k$  is distance between centre of  $k$ th particle and wall,  $m_{p,k}$  is mass of the  $k$ th particle,  $t$  is the time,  $v_k$  is velocity vector of  $k$ th particle,  $F_{ac}$  is the acoustic radiation force on the  $k$ th particle [149].

### 2.13.2 Electrostatics Module for modelling dielectrophoresis

An electric field is created in a material even if it is a non-conducting material, i.e., dielectric. This field interacts with bound charges in the material, distorting the molecules in the dielectric as these charges face the force exerted by electric field. Although (on interaction with electric field) these charges move very slowly, they do not contribute to charge flow or current flow. This creates a balance between positive and negative charges locally distributed creating the material to be polarized. This distribution of electric voltage through a dielectric medium can be calculated by Poisson's equation. To begin with, force of attraction or repulsion is demonstrated by Coulombs Law [140],

$$F = \frac{Q_1 Q_2}{4\pi\epsilon_0 R^2} \quad (2.34)$$

where,  $Q_1$  and  $Q_2$  are the charges,  $R$  is the distance between the two charges and  $\epsilon_0$  is the permittivity of free space. The electric field intensity is defined as Force per unit charge, therefore,

$$E = \frac{Q_1}{4\pi\epsilon_0 R^2} \quad (2.35)$$

The electric field extends radially from the centre of a charge which Faraday's experiments led to the concept of electric flux. From this, the electric flux density,  $D$  can be determined from the amount of electric flux crossing an imaginary sphere away from the charge as,

$$D = \epsilon_0 E \quad (2.36)$$

whose unit is Coulomb per meter square ( $\text{Cm}^{-2}$ )

Polarization,  $P$  can be derived from dipole moment per unit volume of the dielectric material and contributes to electric flux density, then

$$D = \epsilon_0 E + P \quad (2.37)$$

Gauss's Law states the total electric flux through a closed surface is equal to the charge enclosed within it [140],

$$Q = \int_s D \cdot ds \quad (2.38)$$

With the inclusion of surface charge density over the entire volume, the enclosed charge will be,

$$Q = \int_v \rho dV \quad (2.39)$$

The surface integral in equation (2.38) can be converted to volume integral by divergence theorem. By reducing the volume to infinitesimally small the integral form will convert to a differential form to exhibit point form of Gauss's Law,

$$\nabla \cdot D = \rho \quad (2.40)$$

Therefore equation (2.40) can be re-written as,

$$\nabla \cdot (\epsilon_0 E + P) = \rho \quad (2.41)$$

The electric field strength is equal to applied voltage over separation distance between the parallel plates of the electrode. However, as the distance becomes infinitesimally small then the electric field strength will be,

$$E = -\frac{dV}{dx} \quad (2.42)$$

This synopsis can be expanded to 3D [151],

$$E = \left( -\frac{\partial V}{\partial x}, -\frac{\partial V}{\partial y}, -\frac{\partial V}{\partial z} \right) \quad (2.43)$$

which can be simplified by using del operator as follows,

$$E = -\nabla V \quad (2.44)$$

Substituting in equation (2.44) will give Poisson's equation,

$$-\nabla \cdot (\epsilon_0 \nabla V + P) = \rho \quad (2.45)$$

which can be simplified to,

$$\nabla^2 V = -\frac{\rho}{\epsilon} \quad (2.46)$$

where,  $\epsilon$  is permittivity of the medium.

Table 2.2: Boundary Conditions for Electrostatics implemented in COMSOL Multiphysics software,

<i>Condition</i>	<i>Equation</i>
Electric Potential	$V = V_0$
Ground	$V = 0$
Electric Displacement	$n \cdot D = n \cdot D_0$
Surface Charge density	$-n \cdot J = \rho_s$
Electric Insulation	$n \cdot D = 0$

The acoustic model was simulated for a 6.4MHz using a one pair of IDTs for creating standing waves since the structure of the IDTs is periodic. The models simulated in this work have assumed particle diameter to be  $7\mu\text{m}$  and the effect of the field variable on the particle is considered. The acoustic and field variables were first computed and then using particle tracing physics the field variables were used to simulate the trajectories of the particles. The following assumptions such as thermophysical properties of the liquid was kept constant so that there would be no thermal effect on the medium and particle. The model walls were kept as non-porous structure that would not react with the surrounding medium. The boundary condition for the elastic field on lithium niobate surface was selected as stress-free that would allow zero displacement at the boundaries. This also allowed to avoid a mismatch of the standing waves radiated into the medium. The wall boundaries were selected to be have no-slip condition which meant that the viscous liquid medium is simulated to have zero velocity relative to the boundary. At the solid-liquid interface there is no fluid-surface friction occurring. This selection was made to represent the stagnant liquid medium in the chamber that during the SSAW excitation. The SSAWs were generated to create pattern of cells in the liquid medium therefor this required the boundary layer condition to have zero velocity (no-slip) conditions. The Eigen frequency analysis of the model demonstrated visual understanding of the standing waves created for patterning cells in alignments.

For simulating the dielectrophoretic model a pair of IDTs were employed to demonstrate the DEP field region due to the uniformity and periodic structure of the electrodes. This allowed to study the force at different heights in the channel that would be exhibited in experimental cases.

## Chapter 3

### Materials and methods

#### 3.1 Introduction

This chapter describes the principles behind the methodologies used throughout the entire project. These methods include microfabrication of SAW and DEP devices, synthesis of GelMA hydrogel, agarose preparation, rheological techniques, microscopy techniques, cell isolation, cell culture, and immunohistochemistry methodologies to investigate cell growth, proliferation cell, beating, action potentials and calcium transients.

#### 3.2 Microfabrication techniques

##### 3.2.1 Photolithography

Aloys Senefelder invented the process called lithography in 1796 [152]. The word lithography comes from the Greek, *lithos* means stones, and *graphein* mean to write. Nowadays, the lithography is known as the technique used to transfer copies of a master pattern onto the surface of solid material is usually silicon wafer or glass wafer [152]. The most widely used form of lithography is photolithography which is basically the use of light to pattern the substrates. Photolithography generally involves a set of basic processing steps: preparation of the wafer or substrate, photoresist application, soft baking, exposure, post exposure treatment and development.

##### 3.2.2 Preparation of lithium niobate wafers

The most important step in lithography process is the substrate cleaning. There are two types of contaminants that can disturb the uniformity of the substrate leading to poor adhesion of resist. Physical contaminants such as dust particles can prevent the adhesion of resist on to the substrate and/or disturb the surface uniformity of a coated photoresist. Whereas, chemical contaminants can also react with various materials used in the photolithography process and generate non-uniformity. Newly opened wafers do not need additional cleaning, because they are cleaned before shipping and are kept in a contamination free container. Several cleaning techniques can be used to remove the contaminants depending on the substrate and the types

of contaminant. Wet immersion cleaning, for example, might be carried out using diluted hydrofluoric acid, Piranha (3:1 mixture of concentrated sulphuric acid ( $\text{H}_2\text{SO}_4$ ) with hydrogen peroxide ( $\text{H}_2\text{O}_2$ )) or DI water rinsing followed by solvent rinse. Other methods include ultrasonic agitation, polishing with abrasive compounds, and vapour cleaning can also be used [152].

### **3.2.3 Photoresist application and soft baking**

The principal components of a photoresist are the polymer that gives the resist its structural properties, a photoactive compound (PAC), which is the light-sensitive component, and a solvent. The PAC in a resist controls the chemical reactions in the polymeric phase and is usually sensitive to a narrow band of ultraviolet (UV) light radiation that changes the structure of the polymer in the resist.

Photoresists are classified into two groups, positive resists and negative resists. A positive photoresist is more soluble in a developer solution when it is exposed to UV. The unexposed regions of the positive resist remain after development which develops the resist pattern identical to the mask. The photochemical reaction during the exposure of a positive resist weakens the polymer by rupturing the main and side chains. This allows the resin to become readily soluble in developers such as alkaline solutions, for example, KOH, tetramethylammonium hydroxide (TMAH) or acetates.

A negative resist is insoluble in the developer when it is exposed to UV radiation. The unexposed regions of the negative resist are dissolved by the developer, which makes the developed resist pattern the negative of the mask pattern [152]. The insolubility of exposed negative resist is a consequence of either an increase in molecular weight of the resist through UV included crosslinking, or by a photochemical transformation of the resist to form new insoluble products. Often the increase in molecular weight is accomplished through photo-initiators that generate free radicals which facilitate photo-polymerization of the monomer or oligomers. The photochemical transformation of the resist may also generate hydrophobic or hydrophilic groups inducing preferential solubility between the exposed and unexposed resist [152].

Most commonly, photoresists are deposited on the surface of substrates is through spin coating. The photoresist is dispensed onto a substrate that is held by a vacuum chuck in a

resist spinner. As a result the centrifugal forces push the photoresist toward the edge of the wafer where excess resist is flung off. The frictional force of viscosity opposes this centrifugal force and as the film thins the centrifugal force which is proportional to the mass of the resist on the wafer decreases and evaporation of solvent while spinning leads to dramatic increases in the viscosity of the resist as the film dries. Eventually the increasing viscous force exceeds the decreasing centrifugal force and the resist stops flowing. However, at the edge of the wafer, the third force called surface tension becomes significant. The surface tension at the resist-air interface results in a force pointing inward toward the centre of the wafer. The extra force adding to the viscous force will stop the flow of resist sooner at the edge than over the central portion of the wafer, resulting in an accumulation of resist at the edge. This accumulation is called an edge bead, which might require an additional removal process prior to subsequent processing steps [152,153]. The resulting thickness of the film depends on the viscosity of the resist ( $\eta$ ), the polymer concentration in the resist (C), and the angular spin speed ( $\omega$ ). An empirical relation often used to predict the film thickness is given by

$$T = KC^\beta \eta^\gamma / \omega^\alpha \quad (3.1)$$

Where,

T is the film thickness and K,  $\alpha$ ,  $\beta$ , and  $\gamma$  are experimentally determined constants that vary from system to system. Typical values of  $\alpha$ ,  $\beta$ , and  $\gamma$  are 0.5, 1 and 1, respectively [152-154].

After resist coating, the resist still contains solvent and may contain built-in stresses. Thus soft baking which is a critical step in photolithography is typically performed at 95°C for approximately 3min on a hot plate which is faster and more controllable and does not trap any solvent as may occur when using a convection oven. This step effectively removes the majority of remaining solvent, relieves any stress resulting from the spinning process and also promotes adhesion of the resist layer to the substrate [155]. Failure to sufficiently remove the solvent will affect the resist profile while excessive baking destroys the photoactive compound and reduces sensitivity. There are several methods that can be used to bake photoresists. [155].

### 3.2.4 Exposure and post-exposure treatment

The photoresist-coated substrates are transferred to an UV illumination device where they are aligned with the patterned mask. The patterns are transferred into the photoresist on the substrate by shining UV light through the mask. Each photoresist is manufactured to absorb specific wavelength of ultraviolet light (UV). The UV is usually divided into four regions based on wavelength, namely; near UV, UV, deep UV, and extreme UV (Table 3.1).

Table 3.1 – UV Light illumination regions

Region name	Wavelength (nm)
Near UV	330-450
UV	260-330
Deep UV	200-260
Extreme UV	10-14

The emitted radiation from mercury (Hg) or mercury-xenon (Hg-Xe) lamps are most commonly used due to certain peak wavelengths that are in the spectrum. These peaks are commonly referred to as spectral lines including the I-line (365nm), the H-line (405nm), the G-line (436nm) and the E-line (546nm) (Figure 3.1).

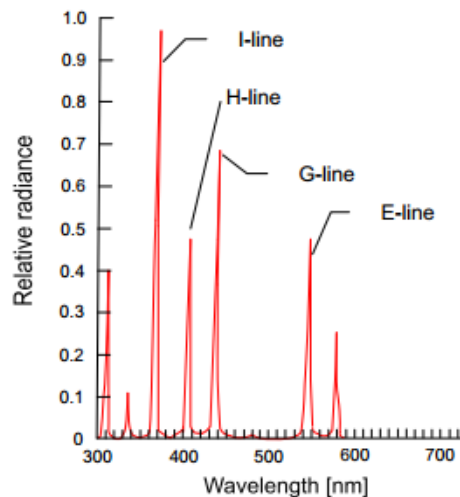


Figure 3.1: Emission spectrum for Hg-Xe source

The I-line is widely used in most applications in which small feature sizes are needed since it provides smaller wavelength that give better resolution.

In order to develop the photoresist completely a minimum amount of optical energy or dose is required (D). Therefore, the actual amount of energy per unit surface area exposed to a wafer

can be calculated by multiplying the light intensity by the exposure time (Equation (3.2)) [152].

$$D = I * t_{\text{exposure}} \quad (3.2)$$

Where,

D is the incident dose ( $\text{J cm}^{-2}$ ),

I is the incident light intensity ( $\text{W cm}^{-2}$ ) and

$t_{\text{exposure}}$  is the exposure time (sec) [153]. In practice, typical doses are on the order of 10-100  $\text{mJ cm}^{-2}$ .

The two most common and simple techniques of exposing a photoresist through a photo mask are contact (or hard) and proximity exposures. In contact exposure the mask is physically strongly pressed in contact with the photoresist layer. This technique offers reasonably high resolution. It transfers patterns quickly and fairly true to the original mask with a disadvantage of damaging the mask when in contact with the photoresist on the substrate.

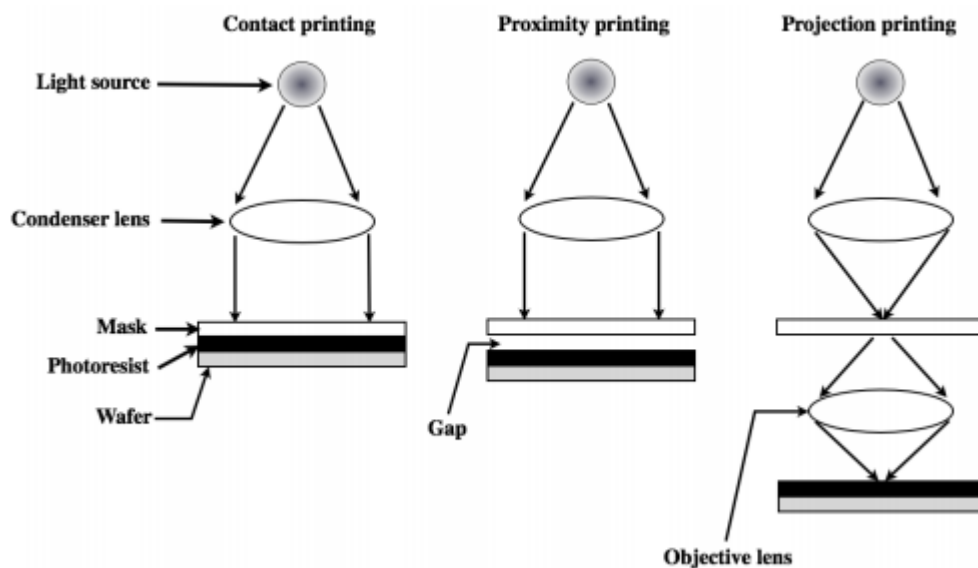


Figure 3.2: Different types of lithographic exposures. Contact printing-masks make direct contact with the substrate. Proximity printing- masks are slightly raised above the substrate. Projection printing- the photomask is projected image through a high-resolution lens system onto the substrate [152].

Proximity exposure method reduces the damage to the mask since the mask is not pressed against the substrate (Figure 3.2). There is a small gap of 10 to 50  $\mu\text{m}$  between the mask and

the substrate however this reduces the resolution of the printing the pattern on the photoresist. Contact and proximity exposures are called shadow printing methods because both rely on opaque and transparent regions of the mask to directly transfer the mask pattern to the resist.

Another method of exposure called projection lithography where the mask is imaged by a high-resolution lens system onto the resist-coated substrate. As a result the mask is never in contact with the substrate and also this techniques allows to change the size of the image through the lenses built-in the system [153].

Following the exposure a post-exposure treatment is often desired to halt the reactions or to induce new ones as the reactions initiated in the resist during exposure might not have run to completion. Generally, a post-exposure bake at 100-120°C is one of the post-exposure treatments mostly frequently performed which improves resist adhesion, toughens the resist, prevents undercutting during development and reduces striations caused by standing waves.

### **3.2.5 Pattern transfer**

After the patterns have been lithographically printed in photoresist, if the photoresist is a permanent part of the final device, further processing may not be necessary. In a subtractive process, the resist acts as a protective barrier to the etching agent. When the etching is complete, the resist is stripped leaving the desired pattern etched into the deposited layer. Similarly, the lithographic pattern is used as a protective barrier in additive process. The material to be patterned is deposited on the unprotected areas of substrate by either chemical vapour deposition or e-beam evaporation. Stripping of the resist then leaves the new material on the substrate [152].

### **3.2.6 Metal evaporation and lift-off**

The metal evaporation over the substrates are carried out in an automated e-beam evaporation system at low pressure of  $3 \times 10^{-7}$  Torr. This reduces the chamber contamination in the system guaranteeing both the quality and reproducibility of the resultant metal layer. The most commonly used metal crucibles used are titanium (Ti), gold (Au), palladium (Pd) and chromium (Cr). The lift-off process follows on after the metal deposition and involves dissolving the resist pattern in lift-off solution to leave behind metal layer. Poor lift-off can be

due to a non-ideal resist profile and resulting in rough electrode edges which short circuit closely spaced features. Therefore it is important to carefully wash the substrate in the lift-off solution to ensure metal particles in non-defined pattern regions do not re-adhere to the substrate.

### **3.3 SAW Device fabrication**

Polymer-emulsion film masks were used to fabricate SAW devices. The layout of the mask was designed using L-Edit (tanner Research Inc., USA). The printing of the masks were performed by JD Photo-Tool (Photo Data Ltd., UK). The super-high resolution option with 128,000 dpi offered by JD Photo is suitable for a minimum feature of size 10 $\mu$ m.

SAW IDTs are designed on an acetate photomask using L-Edit software and fabricated at James Watt Nanofabrication Centre (JWNC) (Glasgow, UK). SAW devices used in this research are slanted finger interdigitated transducers (SFIDTs) fabricated on 0.5mm thick, 128° Y- cut, X-propagating double polished lithium niobate substrate (Precision Micro-optics, MA, USA) using a S1818 positive photoresist, spun at 4000rpm for 30 secs and UV (i-line, 365nm, Mask aligner MA 6, SUSS MicroTec AG, Germany) exposed for 5secs, as shown in Figure 3.3. The exposed was resist developed in 1:1 Microdev (Microposit, Shipley, UK) and pure deionised water for 1 min. Bilayer of metals Titanium/Gold were deposited at 20nm and 100nm using metal sputtering machine (Plassys II, PLASSYS-BESTEK, France) to form electrodes. Titanium acted as an adhesion layer between the substrate and glass. The process was completed by lift-off technique, where the substrate was kept in hot bath of 50°C submerged in a beaker containing acetone for 30 mins to 60 mins.

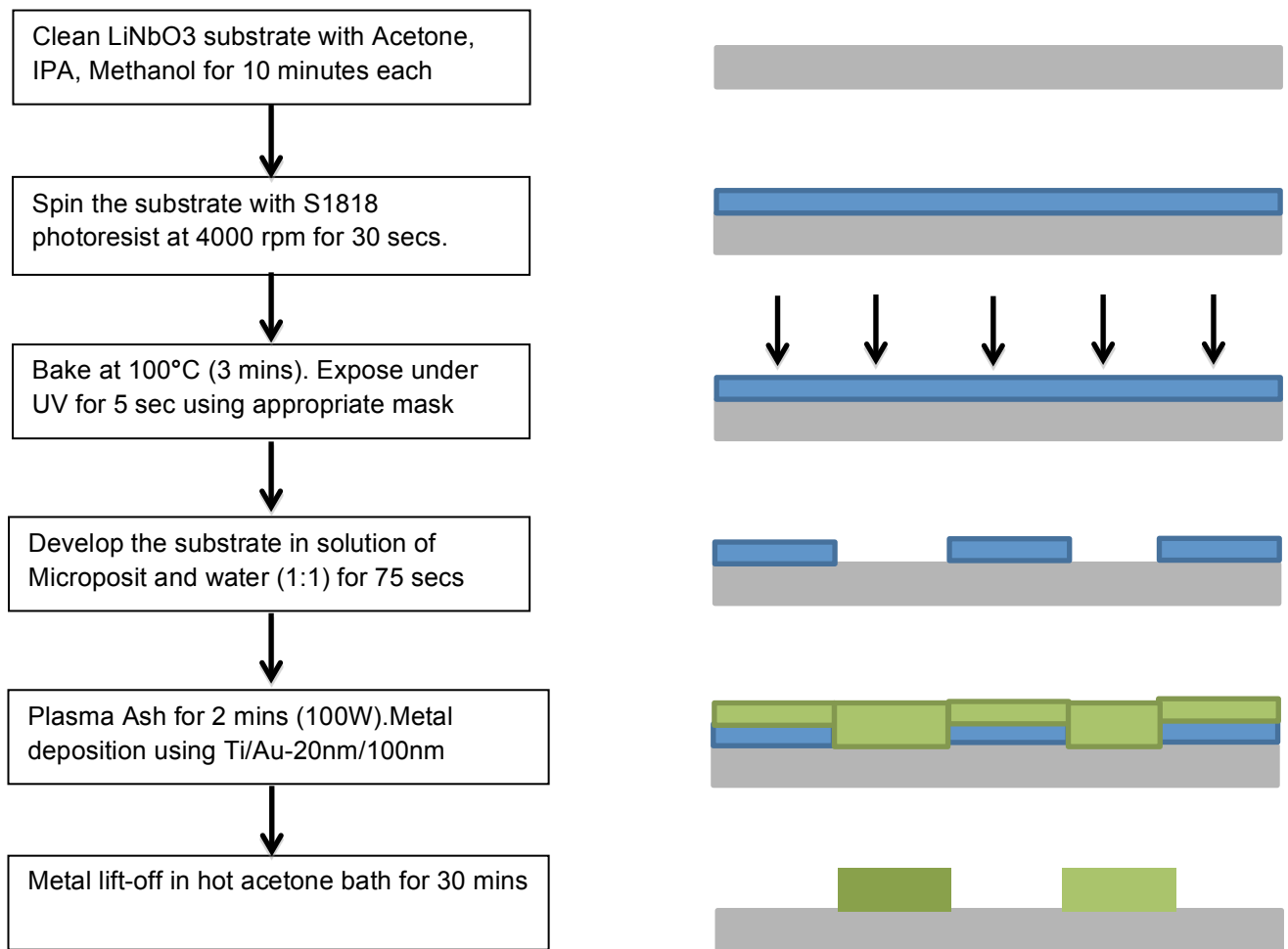


Figure 3.3, shows the fabrication protocol followed for fabricating the IDTs on lithium niobate substrate.

The connection pads were connected to electrical wires using silver metallic paste. The input power was supplied to the SAW device by a signal generator (TTi 50MHz Function generator) and amplifier (Mini circuits 15542), and measured using a digital oscilloscope (Agilent Technologies, E5071C 9KHz-3GHz Network Analyzer).

### 3.4 Dielectrophoretic device fabrication

The experiments to determine cross-over frequencies for n-DEP and p-DEP were performed with metal electrodes patterned on glass slides. These electrodes were fabricated using standard microfabrication protocols briefly presented here. The protocol steps are shown in Figure 3.4. The glass substrates were cleaned with Decon-90, acetone, IPA, methanol and water each for five minutes and dehydrated baked at 180°C for 30 mins. After which the substrates were given a brisk nitrogen blow dry.

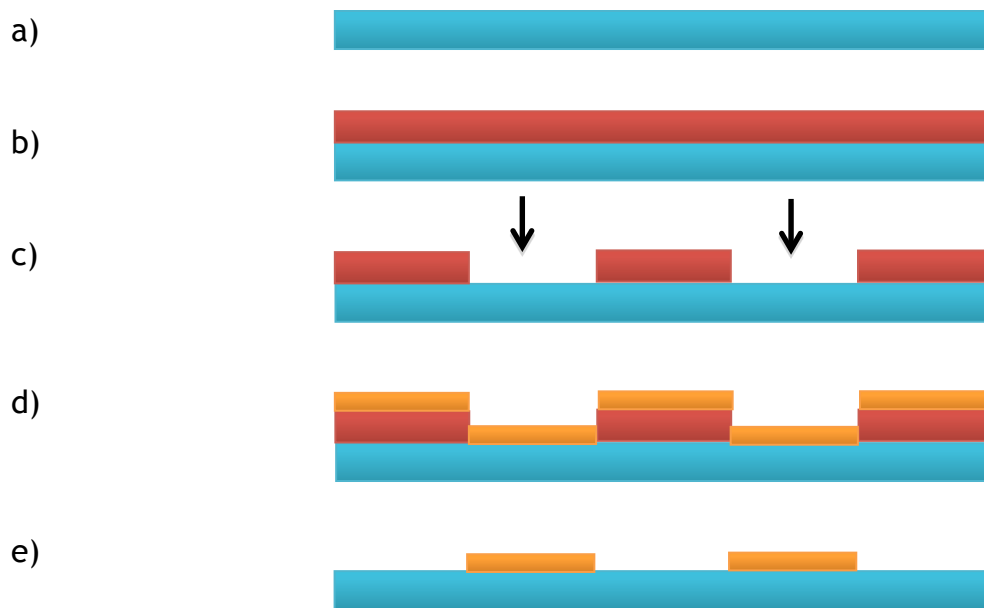


Figure 3.4, a) a cleaned glass substrate, b) spin coat S1818 photo resist, c) exposure under UV light and developed, d) deposition of Ti/Au layer on the substrate, e) lift-off process

The substrates were then placed in plasma asher for 3 mins at 100W. A positive photoresist S1818 (Shipley) was deposited at the rate of 4000 rpm for 30 secs to create 2 $\mu$ m thick layer. The substrates were then baked at 95°C for 3 mins before flood exposing the substrate using acetate masks. The exposure time of under the UV light was 5 secs (Suss Microtec MA6 mask aligner). The substrates were then developed in 1:1 ratio of Micro Dev developer and water for 60 secs and washed under slow running RO water for 1 min. After checking the development of the patterns in the microscope the next step was deposition of gold on the substrates. A 20nm thickness of Titanium was deposited initially and then 100nm of Gold was deposited on the substrate (Plassys Electron Beam Evaporator). The metal lift-off process was carried out by placing the substrates in a beaker containing acetone and placed in hot water

bath for 15 mins. If upon required the left-over resist between the IDTs were removed by sonication for 3 mins.

The layout of the patterned mask was designed using L-Edit (Tanner Research Inc., USA). The printing of the masks were performed by JD Photo-Tool (Photo Data Ltd., UK). The super-high resolution option with 128,000 dpi offered by JD Photo is suitable for a minimum feature of size 10 $\mu$ m. Before using the device, wires were connected with silver paint applied to the connection pad of the IDTs.

### 3.5 Cardiac cell isolation Protocol

In this work, anisotropic scaffolds were produced in order to seed neonatal rat cardiomyocytes. Isolation refers to the process in which cellular components of a tissue are separated from the surrounding ECM. In this study, cardiomyocytes were isolated from neonatal rat hearts (Figure 3.5). Enzymatic digestion was performed using 0.1% w/v Collagenase type II (44C14823A, Worthington) in Hank's Balanced Salt Solution (HBSS, Life Technologies).

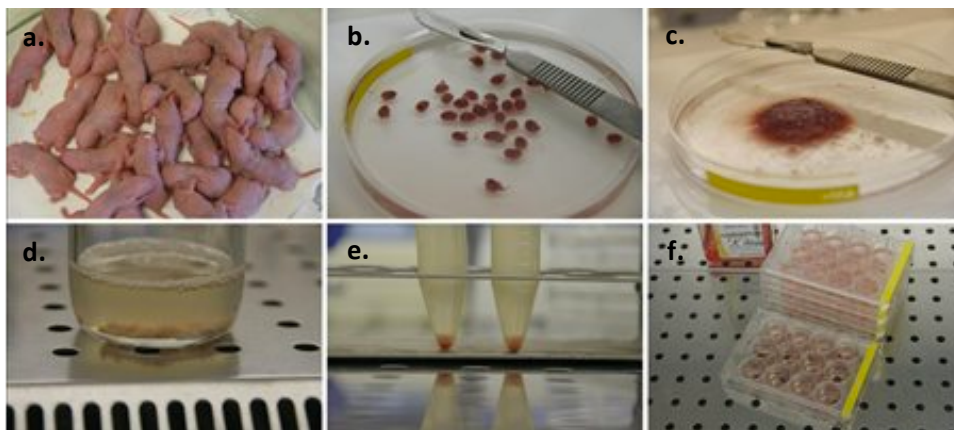


Figure 3.5, schematic representing isolation of cardiomyocytes and cardiac fibroblasts from hearts of neonatal rat pups, a) neonatal rat pups were ordered for surgery procedures to isolate hearts, b) hearts from the neonatal rat pups were surgically removed and placed in trypsin, c) the hearts were sliced into thinner pieces using surgical knife under the cell culture hood, d) the heart pieces were exposed to enzymatic digestion using Collagenase type II, e) centrifuged cells (cardiomyocytes and cardiac fibroblasts) settled at the bottom of the Eppendorf tubes, f) plating of cardiac fibroblasts in the experimental samples in 12-well cell culture plate.

The day before the surgery the following steps were followed – in an ice bucket 30ml of HBSS was added in a 50ml Falcon tube under the hood and covered with a parafilm. In addition, 9ml of HBSS was added in the 10ml Falcon tube containing 0.05% trypsin and sealed with parafilm. During the time of heart isolation surgery, the surgical metal container consisted of one medium petri dish, two autoclaved envelopes containing surgical long scissor, tweezer, a small scissor and 70% ethanol in a small container. The isolated heart pieces are stored in trypsin in between two petri-dishes and placed in cold room for overnight slow swirling.

The day after the surgery the following steps were followed - 300ml of media (DMEM + 1% P/S + 10% FBS) was warmed. The water bath was cleaned and sterile water poured with one drop of antibiotic. Ethanol was sprayed all around the bath and the water temperature was set to 37°C. The collagenase solution Type 2 (305 u/mg) 0.1%wt (50 mg in 50ml HBSS) was prepared and stored in water bath. A fresh pack of 50mL Falcon tubes was prepared on standby inside the cell culture hood. The cell culture was cleaned with ethanol and the UV light switched ON for 2hrs minimum.

### **3.5.1 Neutralise Trypsin**

10ml media was prepared in 50mL Falcon tube and the heart pieces with trypsin from the cold room were removed and collected with a 25ml pipette by pipetting at the surface surface of the solution, and minimising the amount of trypsin collected. The pieces were gently deposited suspending drop wise into the 50ml falcon tube with 10ml of cardiac media. Any remaining heart pieces attached to the wall of the pipette were detached from the surface by pipetting some media with the pipette. The pieces were then gently swirled in water bath for 5 min (by hand, around 80 rpm). In the meantime the collagenase was put under the hood and the media was collected carefully from tube with a 10ml pipette and pieces left in the tube. .

### **3.5.2 Collagenase treatment**

7ml (for 1l) or 12ml (for 2l: if the heart pieces are big) of collagenase was added to the pieces and swirled slowly in a 37°C water bath for 10 min (making sure there is no turbidity in supernatant) and rotated at around 80 rpm. In the meantime 15 ml media was added to a big flask (1 flask for 1l; 2 flasks for 2l) and placed inside an incubator to warm. To disrupt heart

pieces the mixture was pipetted up and down 10 times avoiding bubbles at all times. If after 5-7 times turbidity was seen then the process was halted because the presence of turbidity means that there are too many cells in the liquid which was to be removed. Using a pipette gun, the liquid was removed from the tube as much as possible; a 1ml pipette was used to avoid taking up the pieces or the mucous components. 15ml was added for 2l collagenase and vortexed by hand really fast for 10 min in the warm water bath and regularly checked to see if the pieces were being dissolved.

If larger pieces were found the collagenase process was performed again for the remaining pieces. The cell mixture was pipetted with a 10ml pipette up and down 10 times fast (to break the pieces as much as possible) and repeated with a 1ml pipette up to six times. The Falcon tube was placed vertically for 1-2 min and a cell strainer (70 $\mu$ m) was placed in the correct position on a new falcon tube. The solution was pipetted 1ml at a time on the strainer avoiding aspiration of the mucous (which would block the tip).

The falcon tube was washed with 2ml media to release the media from the sides of the Falcon tube and pipetted back again into the strainer. The strainer was tilted at 45° and the media flowing through the surface of the tube was recirculated through the strainer. To the collected suspension under strainer 10ml of media (for 2l collagenase solution) was added to re-suspend remaining components and shaken for 10min in water bath and pass the remaining liquid through the cell strainer.

### **3.5.3 Preplating**

The cells were centrifuged at 1000rpm for 5min at 37°C. After centrifugation without disturbing the pellet and surrounding layer the supernatant was carefully removed with a 25ml pipette and then a 1ml pipette. The supernatant was not thrown away but put it into another Falcon tube to be re-centrifuged. The cells were re-suspended using fresh 2ml of cardiac media and gently mixed with a 1ml pipette so as not to break the cardiomyocytes, as they are weak. The cells were seeded into 75ml culture flask (T75) drop wise tilted. The 50ml tube was washed with 2ml media and solution was added to flask and tilted few times to homogenize the solution.

The flask was then placed in the cell culture incubator for 1hr to allow cardiac fibroblasts to attach. The cardiomyocytes that did not attach to the surface were used for experimentation.

The surface was washed several times with 25ml pipette and transferred to 50ml tube. 10ml media was added to the flask and washed again and added to the same Falcon tube. The cardiac fibroblasts attached to the surface of the flask were given 20ml of warm media and placed in incubator.

The cardiomyocyte solution was collected in the falcon tube was mixed with 25ml pipette and the population of cells were counted using standard cell counting plate. The cells were then centrifuged at 1200rpm for 5min and prepared for appropriate experiments.

### **3.6 Freezing**

The T75 flask containing the cardiac culture was rinsed with 5ml of 0.05% trypsin/EDTA warmed to 37°C and removed by aspiration. 3ml of trypsin/EDTA was added into the flask and incubated at 37°C for 2 min. The trypsin/EDTA was removed and replaced with 3ml of fresh trypsin/EDTA and incubated again for 2-3 min. The flask was checked under a microscope to determine whether cells were dislodged and if not dislodged the flask was tapped few times to dislodge any adherent cells. 3ml of soybean trypsin inhibitor was added to the flask and contents transferred into a 15ml centrifuge tube. The empty flasks were rinsed with 8ml medium and added to the cells already in the 15ml centrifuge tube to have now a total volume of 14ml. The tube was centrifuged for 5 min at 500xg and the medium aspirated. The pellet was re-suspended gently in 1.5ml freezing medium (98% FBS/5% DMSO) in to a Nalgene freezing jar containing room temperature isopropanol. The jar was immediately placed into -80°C freezer and freeze cells at the rate of 1°C/min for six to twelve hours before transferring the vial in to liquid nitrogen storage.

### **3.7 Cell thawing**

The cells were thawed in a 37°C water bath (about 2 min), and transferred into 15ml centrifuge tube containing the pre-warmed cell media. The tube was centrifuged at 500xg for 5min and the media aspirated. The pellet was resuspended in 5ml warm cardiac media and added to 10ml media already present in the preprepared T75 cell culture flask to avoid giving thermal shock to the cells and increase their viability. The media was replaced after 4hrs with fresh culture media after the cells have attached and discard the non-adherent cells to promote increased viability and avoid contaminations.

### 3.8 Cardiac fibroblast cell culture

The cell culture T75 flask was taken out from the incubator and the media was discarded using the vacuum glass pipette. 5ml of DPBS was added to the flask and shaken to remove any media and aspirated through the vacuum suction. 3.5ml of trypsin was added into the flask and incubated for 5mins to allow cells to detach from the flask and start floating. The flask was checked under the microscope for detachment of cells. 5ml of cell culture media was added and pipetted 15 times in the flask to dislodge any adhered cells from the surface and the cell mixture solution was added to the 15ml centrifuge tube.

The solution was centrifuged at 1200 rpm for 5 min and the liquid discarded leaving behind just the pellet of cells. The cells were re-suspended in the tube by adding 2ml of media. The solution was divided into two tubes of 1ml each. The first 1ml was added to the culture flask containing 4ml of media and incubated for future experiments. The second 1ml of cell solution was centrifuged at same speed and time. The media was discarded and pre-determined concentration of prepared GelMA hydrogel was added to re-suspend the pellet by pipetting 15 times.

### 3.9 Cardiomyocytes seeding & encapsulation

After isolation, cardiomyocytes were suspended and mixed in a ratio of 1:1 in DMEM along with cardiac fibroblasts in order to obtain a final concentration of  $3 \times 10^6$  cells/ml (Figure 3.6). These cells were then centrifuged at 1200rpm to obtain a pellet of cells.

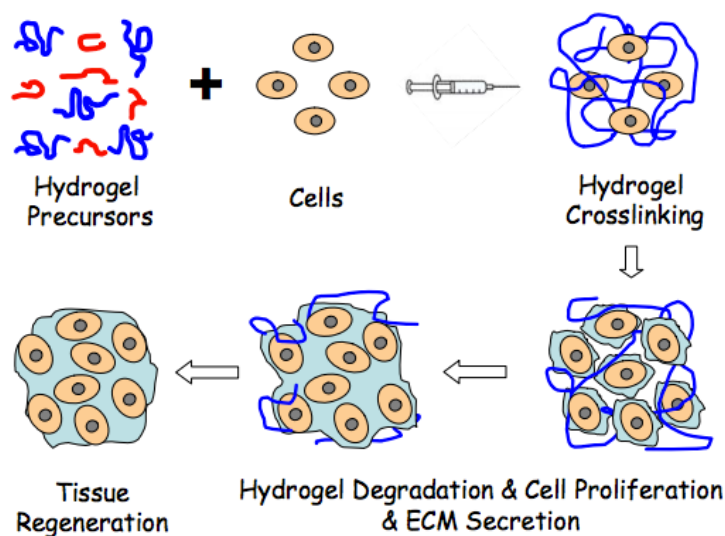


Figure 3.6, Schematics of encapsulating cells in a hydrogel matrix and crosslinking the fibres to promote cell proliferation to generate an engineered tissue

The DMEM media was discarded and GelMA solution was poured into the falcon tube. The cells were re-suspended in the GelMA carefully and slowly in order to avoid bubble formation. To reduce the risk of contamination, the medium was changed 24 and 48 hours after seeding.

### **3.10 Beating analysis**

Cardiomyocytes contraction was monitored in a Zeiss light microscope (Axio Observer Z1) starting from day 5 of culture. Thirty seconds videos with 10x magnification were recorded in different scaffolds areas and then loaded into an automated MATLAB code to obtain the beating frequency and the pattern of the beating signal. The software interprets the images properly when the scaffold is securely held on to the bottom of the well. When the scaffold was floating, movements can be misinterpreted as cellular contractions. As a consequence, beating frequency was manually recorded for floating samples.

Monitoring of the beating behaviour was performed every day until contraction was no longer observed. Frequency was then plotted as a function of time (i.e. days after seeding). To evaluate the regularity of cell beating, standard deviation of peak-to-peak distances in the beating pattern was calculated.

### **3.11 TMSPMA coating**

A 3-(Trimethoxysilyl)propyl methacrylate (TMSPMA) treated glass slide was used to form the superstrate of the chamber design and allow integration of acoustic waves into the hydrogel. The methodology for preparing TMSPMA is described as follows – a glass beaker was submerged in a bucket of ice (*Caution:* this was a very exothermic reaction releasing a lot of heat) and 50g of NaOH pellets (10% (w/v) solution (Sigma Cat# S5881-1KG)) was weighed. 450ml of distilled water was slowly added to allow all pellets to be dissolved. Glass slides were placed in the same beaker in a staggered manner to allow contact with NaOH solution from all directions.

The beaker was then covered with a Pyrex dish, since aluminium foil reacts with NaOH producing gaseous products, and allowed to sit under a fume hood overnight. The NaOH

solution was appropriately discarded in to the waste bottle and gloves thoroughly rinsed and rubbed under flowing distilled water. Each side of the glass slide was dipped in 3 distinct 100% reagent alcohol (Fisher Cat # A962P-4) baths and allowed to air dry under the hood. The glass slides were then wrapped in aluminium foil and baked for 1hr at 80°C. The TMSPMA (Aldrich 440159-100ML) treatment was given under the fume hood. The glass slides were stacked vertically and 3ml of TMSPMA was poured on top of the stacks using a syringe. After 30min the stacks were flipped upside down to allow an even coating. The beaker was then covered with aluminium foil and baked overnight at 80°C. The following day the glass slides were cleaned with reagent grade alcohol three times and air-dried. The TMSPMA coated glass slides were wrapped in aluminium foil and stored at room temperature for future use.

### 3.12 Agarose preparation

Agarose is a neutral linear polysaccharide purified from agar-agar of red algae. It is composed of alternating residues of D-galactose and 3,6-anhydro-L-galactose joined by  $\alpha$ -(1 $\rightarrow$ 3) and  $\beta$ -(1 $\rightarrow$ 4) glycosidic linkages (Figure 3.7).

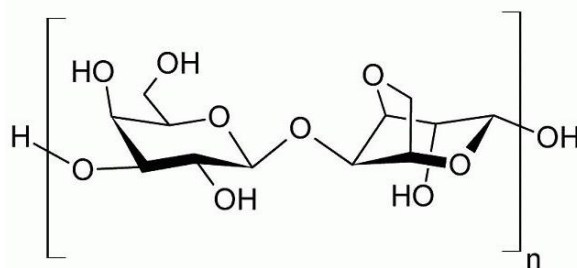


Figure 3.7: Chemical structure of agarose [210]

Agarose chains form helical fibres that aggregate into supercoiled structures with a radius of 20-30nm [210]. Agarose is soluble in hot water and once it cools, forms a gel through the crosslinking of the agarose polymer chains by hydrogen bonds. Gelation of agarose results in a three-dimensional mesh of channels whose diameters range from 50 nm to >200 nm [210].

### 3.13 Gelatin methacrylate preparation

The degree of methacrylation can be tuned during the process of synthesizing it depending upon the amount of methacrylic anhydride as shown in the Table below –

Table 3.2, degree of methacrylation of GelMA

<i>Degree of Methacrylation</i>	<i>Volume of methacrylic anhydride per g of gelatin (mL)</i>	<i>Concentration (w/v %)</i>	<i>Require UV exposure time(s)</i>
1 (low)	0.025	5	30
2	0.075	-	30
3	0.125	5	30
4	0.4	-	25
5 (high)	0.8	5	25

The protocol of preparing gelatin methacrylate (GelMA) described in this work consists of 10g of gelatin. To make the GelMA mix in an Erlenmeyer flask 10g Gelatin Porcine Skin (Sigma G2500-500G) and 100ml of PBS (Gibco 14190) was added and rotated with a magnetic stirrer at 60°C until gelatin was dissolved (avoiding the formation of foam or bubbles).

For each gram of gelatin added the appropriate amount of methacrylic anhydride (8ml) 94% (Sigma 27,668-5) was added dropwise for high methacrylation. And the emulsion was allowed to rotate at 60°C for 3 hours using a magnetic stirrer on a hot plate. The Gel-MA solution was diluted with pre-heated 20ml PBS/g to stop methacrylation reaction and stirred at 60°C temperature for additional 115 minutes.

The GelMA solution was then transferred into four dialysis membrane tubings (SpectrumLabs through Fisher S432706, 08-667E) through the help of a funnel. The tubings were submerged into distilled water at 40°C to 50°C for about 1 week in order to remove the toxic methacrylic anhydride. The dialysis was allowed to run at 500rpm while changing water every 12 hours and each time reversing the membranes. Preheated 200mL ultrapure water was added to the solution after dialysis and temperature was increased until 60°C to facilitate the successive filtering step. On day 8, an adequate number of 50ml Falcon tubes were prepared, each containing 25ml of the solution. The next steps were performed rapidly to maintain the liquid at 40°C. The first filtration step of GelMA was carried out through coffee filter

followed by second filtration that was filtered through a vacuum Express Plus (0.22 $\mu$ m pore size) filtration cup. The sterilized polymer was transferred into 50ml-Falcons (25 to 30ml in each). The falcons were stored at -80°C for at least 2 days. Falcon tubes opening were covered with Kimwips and secured with rubber bands and then put into freeze-dryer for 5 days. Falcon tubes were stored horizontal while freezing in order to have an optimal repartition in tube when gel will be lyophilized. The frozen GelMA was freeze-dried for 5 days at vacuum pressure of  $\sim 130 \times 10^{-3}$  Mbar.

### **3.14 Prepolymer preparation**

GelMA prepolymer (5, 7% (w/v)) was combined with cardiac cell media and 0.25% photoinitiator (Irgacure 2959) and incubated at 37°C for 30min before mixing with cells or microparticles.

For DEP experiments, GelMA prepolymer of similar concentrations was combined with sucrose buffer and 0.25% photoinitiator and kept at 37°C for 1hr until the experiments. The sucrose buffer was made from 0.25M Sucrose, 0.06M D-glucose,  $1 \times 10^{-3}$ M CaCl<sub>2</sub>,  $2 \times 10^{-3}$ M NaCl, 0.1mM KCl,  $2 \times 10^{-5}$ M MgSO<sub>4</sub> and  $2 \times 10^{-5}$ M NaH<sub>2</sub>PO<sub>4</sub> at pH 7.2.

TopVision (Thermo Scientific), Low gelling Agarose was dissolved in buffer solution to give a 2% (wt/vol.) concentration. The agar solution cured between temperatures of 27°C – 30°C. Hence during the experimentation the agarose solution was maintained at 37°C by placing in hot water bath.

### **3.15 Photoinitiator and UV device**

The pre-hydrogel solutions were crosslinked using photoinitiator (PI) (Irgacure 2959) (0.5w/v%, CIBA Chemicals). PI was mixed in DPBS or culture media at 80° C before adding the necessary quantity of GelMA. Photo crosslinking was achieved by exposing the GelMA prepolymer to  $6.7 \text{mW cm}^{-2}$  UV light (360 – 480nm; using an OmniCure S2000 UV lamp (Lumen Dynamics)) between 12-15 secs at 37°C temperature.

### **3.16 Viscosity measurement**

The viscosity of hydrogel samples was measured on an Anton-Paar 301 rheometer. The upper geometry was an aluminum cone (1° angle, 25mm diameter) while the bottom plate was Peltier-controlled to keep sample temperatures between 25-37°C for viscosity measurements. After loading, the edge of the geometry was sealed with oil to prevent evaporation. Shear rates were acquired from 0.01-100s<sup>-1</sup> at 25°C. After completing this measurement, a 10 minute equilibration was allowed at 37 °C prior to performing a shear rate sweep from 0.01-100s<sup>-1</sup> at 37°C.

### **3.17 Swelling characteristics**

The swelling characteristics of a network are important in various applications as it affects solute diffusion, surface properties, mechanical properties, and surface mobility [34]. The degree of swelling of gels is dependent on the pore size of the polymer network and the interaction between the polymer and the solvent [15]. As hydration can have a substantial effect on the physical properties of the resultant hydrogel and fidelity of the desired micro-pattern, the change in mass swelling ratio of GelMA was investigated relative to the hydrogel concentration and degree of methacrylation. Hydrogels were made as described previously at 5%, 10%, or 15% (w/v) GelMA of low, medium, or high degree of methacrylation. Hydrogels were allowed to reach equilibrium over 24hr incubation in DPBS at room temperature, and then the mass-swelling ratio of the swollen mass to the dry mass of polymer was calculated and compared.

### **3.18 Cell Imaging techniques**

#### **3.18.1 Bright field microscopy**

The simplest methodology of imaging is using bright field microscopy technique which relies on light absorption. In this technique light travels from a light source through the condenser that contains an aperture diaphragm. This aperture diaphragm is used for controlling and focussing the light on the specimen [156]. When the light that passes through the specimen, it is collected by an objective lens and then relayed to an eyepiece lens. In bright field microscopy, an image is projected as either a dark or highly coloured pattern against a bright

background. The features of an image are caused by light that is being absorbed by stains, pigmentation, or dense areas of the sample. Most commonly this technique is employed for fixed, stained specimens, specimens having an intrinsic colour or specimens that naturally absorb significant amounts of transmitted light. This technique is commonly used for cell counting on haemocytometer. Using bright field microscopy alone to observe some biological samples such as living organism can be very difficult due to the small contrast between the sample and surrounding media or solution [156].

### 3.18.2 Phase contrast microscopy

Phase contrast microscopy (PCM) is a technique that uses an optical mechanism which converts tiny variations of light phase passing through a transparent specimen (or phase shifts which are invisible) to corresponding changes in amplitude in the image which can be visualised as differences in image contrast. PCM can be used for examining living organisms in their natural state without previously being killed, fixed, and stained [156].

In PCM, phase shift occurs between light wave fronts travelling through different portions of the specimen. The difference in location of emerging wave front between the specimen and surrounding medium is called the phase shift [156]. When the light waves pass through different media such as cell nuclei, cytoplasm, or water, their velocity is altered proportionally to the refractive index differences (Figure 3.8). If the refractive index of the specimen is greater than the surrounding medium, the traveling wave's velocity is reduced through the specimen.

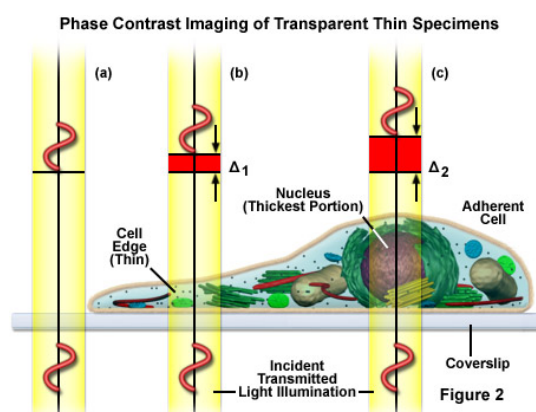


Figure 3.8: Schematic illustration of the phase shifts in a cell. There are very small differences in phase shift between surrounding medium and cell cytoplasm (b) and the cell nucleus (c) while there is no phase shift in the surrounding medium (a) [158].

If the refractive index of the specimen is less than the surrounding medium, the wave passing through the specimen is advanced in phase upon exiting the specimen. In PCM, light travels from the light source through the annular ring and forms a hollow cone because due to the annular ring's shape. This hollow cone of light is then focused onto the specimen by the condenser lens as shown in the Figure 3.9 –

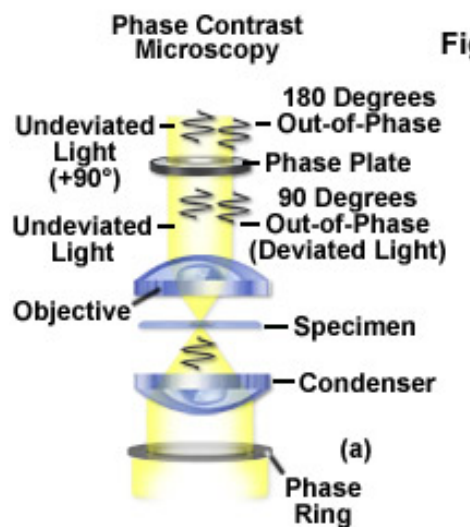


Figure 3.9: Schematic illustration of the phase contrast microscope [158]

On passing through the specimen, some portions of the illuminating light usually experience a phase change due to different refractive indices from surrounding medium and are diffracted to the inside or outside of the hollow cone light. The portions of light that pass through the surrounding medium are not affected and retain their phase. The diffracted and unaffected light is collected by the objective and is segregated at the rear focal plane by a phase plate which is aligned with the annular ring in the condenser lens. Whereas, the unaffected light from the regions surrounding the specimen will hit the phase plate which shifts the surrounding light. This increases the phase difference between light that was phase-shifted by the specimen and light that was phase-shifted by the phase plate. Finally, the light is focused at the intermediate image plane to form the final phase contrast image observed through the eyepiece lens [152,158].

### 3.18.3 Fluorescence microscopy

Most biological studies especially in living cells are highly dynamic, with molecules in the living cells changing their interactions and spatial organisation in response to signals. Recent advances in optics, probe design, and photon detection, fluorescence microscopy have provided a number of possibilities for investigating dynamic events in living cells and intercellular communications between cells can be measured [152].

Fluorescence is a process in which light is emitted from the molecules after photons are absorbed. The molecules that exhibit fluorescence are called fluorophores. Each fluorophore has a specific excitation and emission spectrum with distinct maxima. When a fluorophore absorbs light of a specific wavelength (10 – 15 s), the molecule is raised to an excited state as a result of electron transfer to a higher energy orbit. After absorption the molecule returns to the original ground state which is accompanied by emission of light (Figure 3.10).

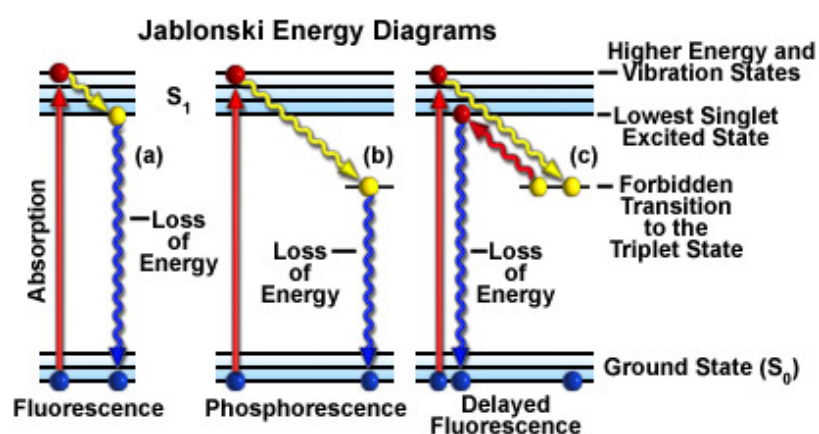


Figure 3.10, Jablonski diagram illustrates absorption and emission mechanisms of fluorescence, phosphorescence, or delayed fluorescence. A) When a fluorophore absorbs light energy, it is usually excited to a higher vibrational energy level in the first excited state ( $S_1$ ) before rapidly relaxing to the lowest energy level. B) Phosphorescence decay is similar to fluorescence, except the electron undergoes a spin conversion into a forbidden triplet state ( $T_1$ ) instead of the lowest singlet excited state. Emission from the triplet state occurs with lower energy relative to fluorescence, hence emitted photons have longer wavelengths. C) With delayed fluorescence, the electron first decays into the triplet state, and then crosses back over into the lowest singlet excited state before returning to the ground state ( $S_0$ ) [158].

The delay between absorption and emission of photons called the fluorescence lifetime is in the order of  $10^{-8}$ s or less (If the fluorescence lifetime is about  $10^{-6}$ s, it is called delayed

fluorescence while the lifetime is longer than  $10^{-6}$ s results in phosphorescence). Absorption and emission of light take place at different regions of the light spectrum, known as the Stokes shift. According to Stokes's law the wavelength of emission is almost always longer than the wavelength of excitation [153]. A fluorescence microscope provides an optimal collection of the fluorescence signal from the specimen whilst minimising signals coming from scattering and reflection of excitation light and auto-fluorescence. The unique advantage of fluorescence microscope is that it takes difference of wavelength between exciting and emitted light. Epifluorescence microscopes are commonly used in biological laboratories that illuminate the object from above (or below for an inverted microscope) with the illumination light being guided into the objective lens by a reflecting mirror [152].

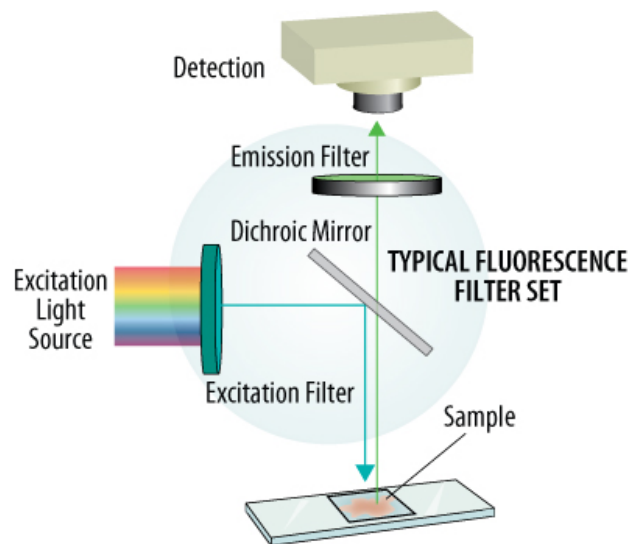


Figure 3.11: Schematic diagram of a microscope for fluorescence microscopy [157]

The light from the source which is placed perpendicular to optical path passes through an excitation filter and hits a special type of mirror called a chromatic beam-splitter which also known as a dichroic mirror (Figure 3.11). This mirror is positioned above the objective oriented at  $45^\circ$  to direction of the light beam. The dichroic mirror has a special interference coating that reflects light with wavelengths shorter than a certain wavelength and transmits light of longer wavelengths. Therefore dichroic mirror will reflect the shorter wavelengths of the exciting light to the objective and ultimately onto the specimen. The longer wavelengths of the emitted fluorescence from the irradiated specimen are collected by the objective lens and transmitted through the dichroic mirror. This emitted light is further filtered through a

barrier or emission filter (to eliminate any residual unwanted excitation light) before reaching the eyepiece or camera [152].

### 3.18.4 Confocal image analysis

Confocal microscopy offers several advantages over other conventional microscopy techniques such as shallow depth of field, elimination of out-of-focus glare and ability to collect serial optical section from thick specimens [209]. Confocal microscopy has been widely used to image either fixed or live cells in different mediums that have been tagged with one or more fluorescent probes.

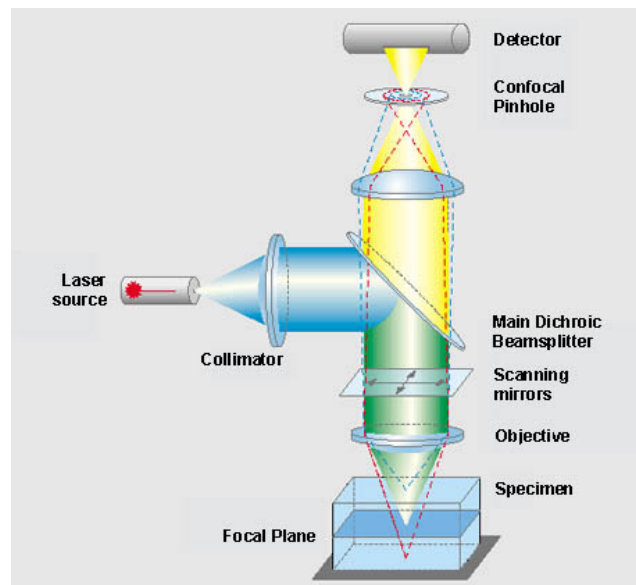


Figure 3.13, the path of laser beam travelling on the specimen in a confocal laser microscope [210].

A laser is used to provide light which hits two mirrors that scan the laser across the sample (Figure 3.13). A microscope objective is used to focus the laser onto the specimen where it excites the fluorescence. The light from the fluorescence labels in the sample and emitted light get descanned by the same mirrors to focus the light through the pinhole that is measured by a detector, photomultiplier tube. The emission filter only allows a selective range of fluorescence spectrum that is selected [210]. The detector is attached to display unit that builds up the image one pixel at a time. Pin hole explanation – in confocal microscopy laser light is reflected off the dichroic mirror which further strikes two mirrors that scan this laser across the sample. In a sample that has been fluorescently stained, and emits light gets

descanned by the scanning mirrors that also scan the excitation light from the laser. This emitted light then passes through the dichroic beamsplitter and is focussed onto a confocal pinhole. The light that passes this pinhole is measured by a detector called photomultiplier tube. Confocal Pinhole efficiently rejects out of focus fluorescent light. Due to this, a small depth of field is established for thin section of samples. Therefore by scanning multiple thin sections, a 3D image can be built up.

### 3.18.5 Scanning electron microscopy

Scanning electron microscope (SEM) is used for observing specimen surfaces. Upon irradiating the specimen with a fine electron beam called electron probe, secondary electrons are emitted from the specimen surface [207]. These emissions of secondary electrons allow image acquisition of the topography by 2D scanning of electron probe over the specimen surface (Figure 3.12).

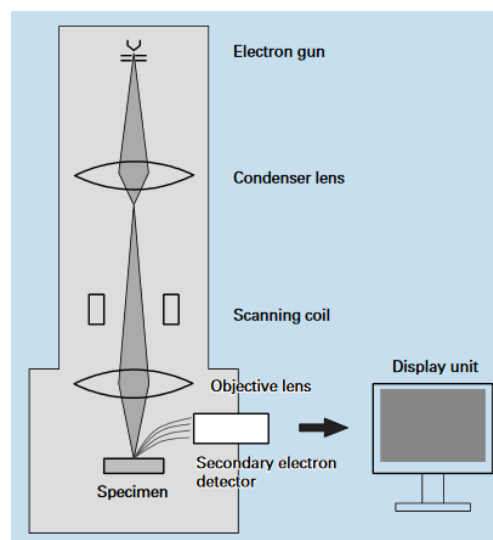


Figure 3.12 shows basic construction of SEM [207].

The SEM consists of a vacuum chamber to avoid any obstruction to the electron beam as it passes through the body of the microscope. When the electron beam strikes the specimen it emits incident beam (X-rays) and three types of electrons – primary backscattered, secondary and auger electrons [208]. The SEM uses primary backscattered and secondary electrons that are picked up electron recorder and records their imprints. This information is then translated onto a display screen that allows generation of 3D images.

SEM samples need to be prepared carefully in order to properly scan and image specimens. Specimens containing metal require no preparation since the metal layer will conduct electricity and respond to bombarding electrons. However samples that do not contain metal layer are coated with a sputter coater that deposits a thin layer of conductive materials (usually gold) on the specimen.

### **3.19 Cell alignment evaluation**

In order to evaluate alignment of cardiac fibroblasts and cardiomyocytes that were seeded on scaffolds, fixation and immunostaining were performed as soon as contraction was no longer observed. Samples were observed under an inverted laser scanning confocal fluorescence microscope (Leica SP5 X MP).

#### **3.19.1 Cell Counting**

Cell counting and viability was performed using Neubauer Haemocytometer (Fisher Scientific UK) by mixing 1:1 trypan blue with cell suspension. The resulting solution was pipetted (10 $\mu$ L) into the first chamber; cells were counted within the centre 5x5 grid (0.1mm<sup>3</sup>) which was repeated in the other chamber.

#### **3.19.2 Cell viability - Live/dead assay**

Live/dead is a two-colour dye-based cytotoxicity assay that induces a green-fluorescent staining of living cells and a red-fluorescent staining of dead or damaged cells. The probe for living cell is calcein acetoxymethyl (AM). Living cells are distinguished by the presence of ubiquitous intracellular esterase activity, determined by the enzymatic conversion of the virtually non-fluorescent cell-permeant calcein AM to the intensely fluorescent calcein. The poly-anionic dye calcein is well retained within living cells, producing an intense uniform green fluorescence. The probe for dead cells is ethidium homodimer-1 (EthD-1), that enters cells with damaged membranes and undergoes a 40-fold enhancement upon binding to nucleic acids, thereby producing a bright red fluorescence in dead cells. EthD-1 is excluded by the

intact plasma membrane of living cells. Fluorescence microscopy data on samples treated with live/dead staining assay can be analysed to quantify the rate of cell survival. A mixed solution of red colour with concentration of 2 $\mu$ l/ml and green colour with concentration of 0.5 $\mu$ l/ml was prepared. After washing with Dulbecco's Phosphate Buffered Saline (DPBS) (Sigma Aldrich, Modified without calcium chloride and magnesium chloride) buffer the prepared solution was added and samples were put in the incubator for 15 minutes wrapped in aluminium foil. After washing with DPBS buffer, red and green fluorescence pictures were taken and living and dead cells were counted. Viability was measured as number of viable cells on the total. Calcein is excited by 494nm light and emits 517nm light, while ethidium homodimer-1 is by 528nm light and emits 617nm light.

### **3.19.3 Immunostaining cardiac cells**

First, the samples were fixed for 1hr at room temperature using 4% (v/v) paraformaldehyde in DPBS. Cells have been permeabilised soaking the samples in 0.1% (v/v) Triton 100x in DPBS buffer for 30min, and non-specific binding was inhibited using 10% v/v bovine serum albumin (BSA, Sigma-Aldrich) solution in 0.1% (v/v) Triton 100x in DPBS buffer for 1hr at room temperature. Samples were then soaked overnight at 4°C in a solution containing the primary antibodies with 1:200 (v/v) dilution in 10% (v/v) BSA in 0.1% (v/v) Triton 100x. In particular, mouse monoclonal to sarcomeric alpha actinin (ab9465, abcam) and rabbit polyclonal to connexin-43 (ab11370, abcam) antibodies have been used. Anti-sarcomeric alpha actinin antibody stains Z lines and dots in stress fibres of myotubes in cardiac muscle, while anti-connexin 43 antibody stains the gap junctions (i.e. transmembrane channels) through which materials of low molecular weight diffuse from one cell to a neighbouring cell.

After washing with DPBS buffer, the secondary antibodies were added with 1:200 (v/v) dilution in 10% (v/v) BSA in 0.1% (v/v) Triton 100x and samples were incubated for 6 hours at 4°C wrapped in aluminium foil. Goat anti-rabbit IgG secondary antibody was conjugated with Alexa Fluor 488 (A11008, Life Technologies), while goat anti- mouse IgG secondary antibody was conjugated with Alexa Fluor 594 (A11005, Life Technologies). Samples were washed in DPBS buffer and 1 $\mu$ l/ml solution of DAPI (Sigma-Aldrich) in DPBS buffer was added for 15 minutes. After washing with de-ionized water, samples were kept protected from light at 4°C in DPBS buffer before visualization with confocal fluorescence microscope.

### **3.19.4 F-actin and DAPI staining**

F-actin and DAPI staining were used to quantify the cellular attachment and alignment at the pressure nodes in the GelMA for a period of time after the initial culture. For F-actin staining cell-seeded scaffolds were first fixed in 4% paraformaldehyde (15710, Electron Microscopy Sciences, Hartfield, PA) in DPBS buffer for 30min and then permeabilised in 0.1% (w/v) Triton X-100 (T9284, Sigma-Aldrich) solution in DPMS for 20 min and blocked in 1% (w/v) bovine serum albumin (BSA) for 1hr. The scaffolds were then incubated in a solution containing 1:40 Alexa Fluor-594 Phalloidin (A12381, Life Technologies, Grand Island, NY) in 0.1% BSA for 45 min at room temperature to stain the actin cytoskeleton. The scaffolds were then perfused with PBS buffer and visualised under a fluorescent microscope. For DAPI (D8417, Sigma-Aldrich) staining, cell alignment was quantified by fixing in 4% paraformaldehyde solution in DPBS buffer for 30min. In order to stain the cell nuclei the scaffolds were then incubated in 0.1% (w/v) DAPI solution in PBS buffer for 10min at 37°C and then perfused with PBS for visualization under a fluorescent microscope.

### **3.20 Stimulation construct preparation**

hiPSc cardiomyocytes (GE Cytiva) ( $0.5 \times 10^6$  cells) were encapsulated into 5% GelMA (45 $\mu$ l) and 0.25% PI (Irgacure 2529) and seeded onto PMMA chamber (6mmx4mmx0.8mm). Constructs were placed on TMSPMA coated glass slide and cultured without mechanical stimulations on day 0 , 1 , 2 and day 3 in six-well plates (1 construct per well in 2ml of culture medium in 37°C 5% CO<sub>2</sub> humidified incubator) to allow cells to attach to scaffold.

### **3.21 Beating analysis**

Cardiomyocytes contraction was monitored from day 6 onwards using video camera (Sony XD-X710) attached on an inverted optical microscope (Nikon Eclipse TE 200U, Japan) with temperature maintained at 37°C at the time of recording using temperature controller. 30s videos with 10x magnification were recorded in different scaffolds areas and then loaded into an automated MATLAB code to obtain the beating frequency and the pattern of the beating signal. The software works properly when the overall scaffold was stable at the bottom of the well. When the scaffold was floating, beating frequency was manually recorded for floating samples.

Monitoring of the beating behaviour was performed every day following day 5 onwards until contraction was no longer observed. The beat frequency (number of beats/min) was quantified from videos taken from at least 5 different samples of micro-patterned co-cultured cells in 5% GelMA concentration. To evaluate the regularity of cell beating, standard deviation of peak-to-peak distances in the beating pattern was calculated.

### 3.22 Mechanical stimulation using surface acoustic waves

After pre-culture, constructs were transferred onto the LiNbO<sub>3</sub> substrate patterned with SFIDTs at a distance of approximately 1cm and connected to a TTi TG2512A 2Ch 25MHz Function/Arbitrary/Pulse Generator through copper wires. During the stimulated period, SAW was turned on at 3.4MHz (180mW) and periodically applied for 30 secs every minute for total of 6mins of one cycle for up to 2 cycles a day on days 3, 5, 7, 9 and 11 (Figure 7.4). Constructs cultured without mechanical stimulation under otherwise identical conditions served as non-stimulated controls. After stimulations all the 6-well plates were filled with fresh cell media.

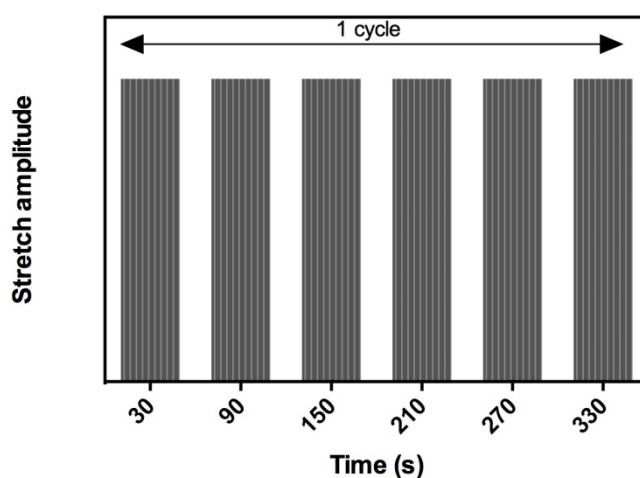


Figure 7.4, representation of 1 cycle of mechanical stimulation applied every 30 sec activation and 30 sec relaxation period using SFIDTs at 3.4MHz and 180mW.

### 3.23 Action potential and Calcium imaging

In order to measure calcium transients modified Tyrode solution was prepared consisting of 140mM NaOH, 10mM glucose, 10mM HEPES, 4mM KCl, 1mM MgCl<sub>2</sub> and 1.8mM CaCl<sub>2</sub> at pH 7.4. 6μM Fura-2 AM (Invitrogen, USA) dye containing 0.1% pluronic F-127 (Invitrogen) was added to the cell seeded hydrogel samples. The cells were then washed with tyrode

solution and incubated for 15 min at room temperature for allow full acetoxymethyl (AM) ester cleavage.

Action potential generated by the cardiomyocytes can be analysed by using potentiometric dyes that are based on response time and mechanism of voltage sensitivity. The most commonly used aminonaphthylethenylpyridinium (ANEP) dye was used. 7.5 $\mu$ M di-4-ANEPPS (Invitrogen, UK) was used to stain the 3D hydrogel scaffolds seeded with cells and dissolved in Tyrode's solution at 1ml/min at 37°C.

Imaging was performed at 37°C incubator chamber built-in the fluorescent microscope (LSM 510 scanning system, Zeiss GmbH, Germany) equipped with x40 objective lens (numerical aperture (NA) = 1.4). Fura-2 was excited by 488nm line of an argon laser and emission signals over 505nm was collected and the fluorescence signal was measured to represent the relative level of intracellular  $[Ca^{2+}]_i$ . The detector gain was set around 700 and line scan images were acquired at sampling rate of 1.54ms per line along the longitudinal axis of the cells. The action potentials (AP) were recorded in the same microscope setup using a single excitation wavelength (530nm) and single emission wavelength (590nm) at 125 fps. The AP was then calculated and plotted using a custom developed and designed application (ClydeBiosciences, Glasgow, UK), by calculating the time of maximal rise in membrane potential to the time of 90% repolarization for each beating from three beatings for each cluster. A 2D image of 512x512 lines were generated and stored for offline analysis using NIH ImageJ custom built-in application.

### **3.23.1 Image processing algorithm**

Cell contraction was observed and documented using fluorescent microscope (LSM 510 scanning system, Zeiss GmbH, Germany) with a capture rate of 10 frames  $s^{-1}$ . Clyde Biosciences (Glasgow, UK) developed a confidential video processing algorithm that was based on block-matching methodology written in Matlab using image processing toolbox and later called in as an ImageJ plugin. The algorithm measures local displacement of cell from sequential frames in the contraction video where each image of 880x880 pixels was divided equally into 16x16pixels and analysed using algorithm that determined the x- and y-axis displacement of each block between sequential frames. Each pixel in the image frame was 5 $\mu$ m and each contraction cycle was represented by displacement vector map and amplitude

contour map. Each image was divided into 25 equal regions and autocorrelation was used to compute displacement vector and plot as a function of time. The autocorrelation curves belonging to each region of interest and its four neighbouring regions were compared by calculating coefficient correlation between them.

Imaging was performed at 37°C incubator chamber built-in the fluorescent microscope (LSM 510 scanning system, Zeiss GmbH, Germany) equipped with x40 objective lens (numerical aperture (NA) = 1.4). Fura-2 was excited by 488nm line of an argon laser and emission signals over 505nm was collected and the fluorescence signal was measured to represent the relative level of intracellular  $[Ca^{2+}]_i$ . The detector gain was set around 700 and line scan images were acquired at sampling rate of 1.54 ms per line along the longitudinal axis of the cells. The action potentials (AP) were recorded in the same microscope setup using a single excitation wavelength (530nm) and single emission wavelength (590nm) at 125 fps. The AP was then calculated and plotted using an custom designed application (Clyde Biosciences, Glasgow, UK), by calculating the time of maximal rise in membrane potential to the time of 90% repolarization for each beating from three beatings for each cluster. A 2D image of 512x512 lines were generated and stored for offline analysis using NIH ImageJ custom built-in application.

### **3.24 Buffer solution - Osmolarity, conductivity and pH measurements**

The osmolarity of buffer solutions prepared for dielectrophoretic experiments were measured using Advanced Micro Osmometer 3300 calibrated using standard solution of 850, 290, and 50 mOsm/kg supplied by Advanced Instruments, UK. The conductivity was measured using Jenway 4071 conductivity meter (288-8199) from RS, UK. Finally the pH measurements were conducted using Hanna Instruments pH meter and calibrated using solutions of 4, 7 and 10pH.

### **3.25 Thermal Camera Imaging**

Thermal images were taken using Ti-25 Fluke Thermal Camera (Fluke, Norwich, UK).

### 3.26 Hydrogel and Scaffold mechanical properties

To evaluate the mechanical properties of the hydrogel and strength of scaffold various compressive stress-strain measurements were conducted on Instron model 5943 as shown in Figure 3.14,

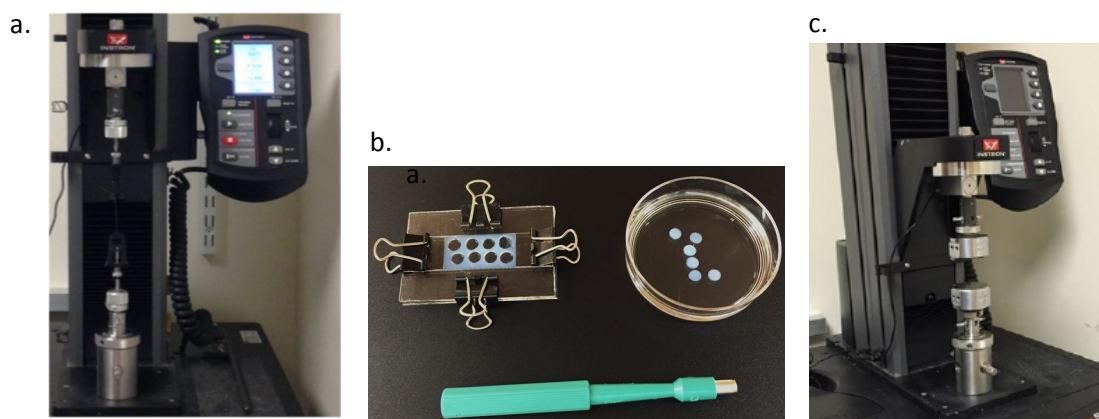


Figure 3.14, a) setup of Instron (Instron 5943) instrumentation for measuring mechanical properties of hydrogel scaffolds, b) Mold with 1 mm depth and cylindrical samples obtained using a 5mm diameter puncher, c) shows the cylindrical plates attached to the Instron, where samples are placed at bottom plate and the top plate is vertical positioned at the surface of the scaffold without collapsing it.

Pre-hydrogel solution was poured into a 1mm thick rectangular mold and crosslinked under the UV light for 30s. From this crosslinked scaffold cylindrical samples with 5mm diameter and 1mm height were obtained using a 5mm diameter biopsy puncher as shown in Figure 3.14.

These scaffolds were allowed to swell in DPBS for 6 hours before testing on the Instron. The Instron model 5943 is a mechanical tester that can be used to measure material properties in tension and compression at room temperature. Maximum loads capable of measuring are 10N and 100N for the two load cells we have.

The samples were placed on the lower plate at the centre of the 10N load cell by carefully scooping it out from the DPBS solution. Samples were then compressed at a strain rate of 1mm/min to 70% deformation by the upper plate which was connected to the load cell. Elastic moduli of the scaffolds were derived from the regression of the first linear portion of stress-strain curves (i.e. the second linear portion is referred to the material itself, when the porosity is fully compressed).

Experimental elastic moduli of the scaffolds were compared with theoretical values that can be obtained from the following formula [5]:

$$E = E_0(1 - \phi)^2 \quad (3.3)$$

where:

- E is the Young's modulus of the scaffold;
- $E_0$  is the Young's modulus of the material (i.e. when the porosity is zero);
- $\phi$  is the porosity.

In particular the following equation was used:

$$\phi = \frac{V_{app} - V_{eff}}{V_{app}} \quad (3.4)$$

where:

- $\phi$  is the porosity;
- $V_{app}$  is the apparent volume calculated from the overall dimensions of the scaffold
- $V_{eff}$  is the effective volume of the scaffold and it is calculated knowing the number of deposited fibres, their length and diameter.

### 3.27 Numerical modelling of SAW in COMSOL Multiphysics software

In order to evaluate the theoretical principles of the working of SAW based device, finite element simulations were conducted to determine the mathematical characteristics of the cells for manipulation and patterning. In this work Acoustic Radiation Force ( $F_{rad}$ ) exhibited due to the scattering of SAWs on the cells manipulated the position of the cells. The time-average acoustic radiation force as a gradient of a potential function ( $U_{rad}$ ) on a single small spherical cell of radius  $a$ , density  $\rho_c$ , and compressibility  $k_c$  in a viscous fluid placed in a standing wave is given by [144]:

$$F_{rad} = -\nabla U_{rad} \quad (3.5)$$

$$U_{rad} = \frac{4}{3} \pi a^3 \left[ \left( \frac{f_1}{2\rho_g c_g^2} \right) p^2 - \left( 3 \frac{f_2 \rho_g}{4} \right) v^2 \right] \quad (3.6)$$

$$f_1 = 1 - \frac{k_g}{k_c} \text{ and } f_2 = 2 \frac{(\rho_c - \rho_g)}{(2\rho_c + \rho_g)} \quad (3.7)$$

where,

$\rho_g$  and  $\rho_c$  are the density of the fluid (GelMA) and cell respectively,

$c_g$ , speed of sound in fluid,

$k_g$  and  $k_c$  are compressibility of the fluid and cell and

$p$  and  $v$  represent pressure and velocity fields, respectively

Simulation were carried on COMSOL Multiphysics 5.0a by considering uniform electrode in the design on a cross sectional plane (x-z plane) of GelMA by including piezoelectric substrate, glass slide and GelMA in the parameters.

Material properties of LiNbO<sub>3</sub> used in our simulations are characterized in previous studies [37]. Also, material parameters correspond to GelMA and cells are tabulated on Table 3.3. By making use of the CFD Eigen frequency module, the resonance frequency of the device was obtained and subsequently, the generated acoustic pressure field was modeled using frequency domain approach. Finally, particle-tracing module was utilized in order to simulate the influence of the pressure field on the cells within the GelMA. In top view model simulations the modeled GelMA fluid was excited by defining acceleration on the walls in frequency domain and subsequently used particle tracing for evaluation of the cells manipulation.

Table 3.3. Simulation Model Parameters at 37°C

GelMA 5%			
Speed of sound	1534	m/s	$c_g$
Viscosity	0.0025	Pa.s	$\eta_g$
Density	1020	Kg/m <sup>3</sup>	$\rho_g$
Boundary layer thickness	0.35	$\mu\text{m}$	$\delta_g$
Bulk module	2.4	GPa	$k_g$
Cell			
Speed of sound	1525	m/s	$c_c$
Poisson ratio	0.5	-	$\nu_c$
Density	1060	Kg/m <sup>3</sup>	$\rho_c$
Bulk module	2.46	GPa	$k_c$
Cell diameter	10	$\mu\text{m}$	$d_c$

### 3.27.1 Finite Element Method

Most commercial modelling software is based around the finite element method (FEM) to solve and simulate models. The technique divides the geometry of the object into simple manageable blocks that can be calculated by the software. Usually there are two widely used fluid dynamic methods for simulating fluid properties – Finite Difference Method (FDM) and Finite Element Method (FEM). The advantage of using FEM is that it can solve complicated flows such as electric current flow for simple boundaries [13].

The geometry space is divided into multiple subdivisions called elements. The created mesh contains the properties of the structure and thus depending on the distribution of mesh it defines the response, like electric field, electric potential etc. and accordingly plots the results whether as sub-domain plot, iso-surface plot, contour plot and so on. Usually the mesh is dense near the point or object of interest and coarse far away, to give maximum accuracy and fast computation. It calculates the equations of unknown variables in each distributed element to create a set of system equations to describe the entire space of the structure in a general format [14]. This process can easily be calculated by computing software. It was also noted that the size and number of elements are inversely related. As the number of element increases the size decreases which increases the accuracy to solve the problem. Therefore it is essential to define mesh very densely near the point of interest to get the best possible results.

### 3.28 Laser Doppler vibrometer

Laser Doppler vibrometry (LDV) is a technique that allows non-contact direct measurement of vibrations of test objects using the Doppler Effect (Figure 3.15).

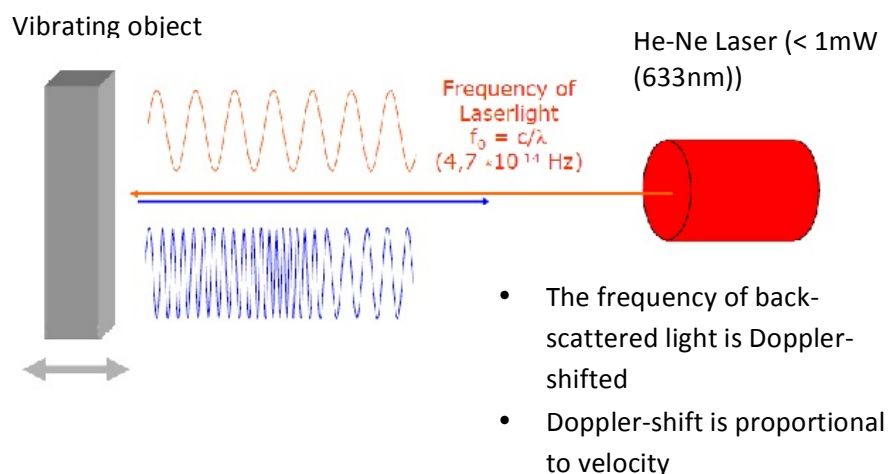


Figure 3.15, illustration of a LDV setup used for determining vibration velocity and displacement at a fixed point over a defined region using Doppler effect by sensing the frequency shift of back scattered light from the vibrating piezoelectric surface [159].

In this work LDV (Polytec Inc) was employed to quantify the displacement of acoustic waves on the surface of  $\text{LiNbO}_3$  in the z-direction. To generate acoustic waves, a sinusoidal signal was applied to the set up. The aperture and amplitudes of the vibration were noted ranging in pm or nm over the predetermined region of interest on the surface of the piezoelectric wafer.

## **Chapter 4**

### **Gelatin Methacrylate synthesis**

#### **4.1 Introduction**

This chapter discusses gelatin methacrylate (GelMA) as an inexpensive, cell-responsive hydrogel for creating cell-laden micro-tissues compatible with surface acoustic wave devices. The hydration and mechanical properties of GelMA are demonstrated by tuning different gel concentration to create cellular micro-patterns for in-vitro cell studies in 3D tissue constructs.

#### **4.2 Material and methods**

##### **4.2.1 GelMA scaffold preparation**

GelMA hydrogels were prepared for different concentration (5, 7, 10% (w/v)) in cardiac cell media containing 2-hydroxy-1-(4-hydroxyethoxy)phenyl)-2-methyl-1-propanone (0.25% (w/v)), Irgacure 2959, (CIBA chemicals) photoinitiator. Then the solution was preheated in incubator at 37°C for 30mins before encapsulating the cells obtained from cell isolation process.

##### **4.2.2 GelMA swelling analysis**

Polymerization was performed as described for mechanical testing. After the photo crosslinking the pre-polymer solution of GelMA, a hydrogel cylinder disc was formed of height 1mm and incubated in DPBS for 24hrs prior to recording the swollen weight of the scaffold. Samples were then lyophilized and weighed again to determine the dry weight of the polymer. As a result, the mass swelling ratio was then calculated as the ratio of swollen hydrogel mass to mass of dry polymer.

##### **4.2.3 GelMA porosity analysis**

Porosity of GelMA hydrogels was determined using variable pressure (environmental) scanning electron microscopy (SEM) (Hitachi S-3400N). Hydrogel samples with 5%, 10% and 15% (w/v) GelMA macromer concentration and 0.5% (w/v) photo- initiator were prepared in the form of 20 mL droplets on coverslips. Prior to imaging, the samples were

frozen in liquid nitrogen and fractured to reveal the sample cross-section. Specimens were mounted on a cold stage covered in double-sided carbon tape for imaging. Pore diameters of the gels were calculated from the SEM images using NIH ImageJ software.

#### **4.3 Gelatin Methacrylate (GelMA) hydrogel synthesis**

Cellular environment plays an important role in controlling cell behaviour and function. Recent studies have shown cell morphological behaviour such as shape, cell-cell interaction and signalling can be controlled by controlling the microenvironment [172-174]. Currently available dry gels suffer from poor mechanical properties, cell binding and viability due to inability to control the microarchitecture. Native ECM matrix such as collagen has been used to create cell-laden micro-gels. However due to insufficient mechanical robustness the ability to create lasting micro-patterns is limited [175-176]. Polyethylene glycol (PEG) or hyaluronic acid have stronger mechanical properties and excellent cell viability however cells typically cannot bind in the matrix and degrade the materials. Thus cells are unable to proliferate, elongate, migrate and organize in the gel [173].

Gelatin methacrylate (GelMA) is a photo-polymerizable hydrogel that consists of modified natural ECM components which make it attractive for tissue engineering applications. Gelatin is an inexpensive material and is a denatured collagen that can be derived from various sources that could retain cell-binding motifs such as RGD as well as matrix metalloproteinase (MMP) suitable for sensitive degradation sites (Figure 4.1) [176-180]. It offers the advantage of better solubility and low antigenicity [173]. By the addition of methacrylate group to the gelatin for photo-crosslinking under the assistance of photoinitiator and UV light, 3D structures can be fabricated to control cellular behaviour and study cell-biomaterial interactions. The chemical modification of gelatin by the addition of methacrylic anhydride involves less than 5% amino acid residues in molar ratio, which means that functional RGD motifs and MMP-degradable motifs are not significantly influenced [181-183]. This ensures good cell adhesive properties of GelMA. Gelatin forms the backbone of GelMA that provides cell responsive characteristics such as provision for cell adhesion and proteolytic degradability.

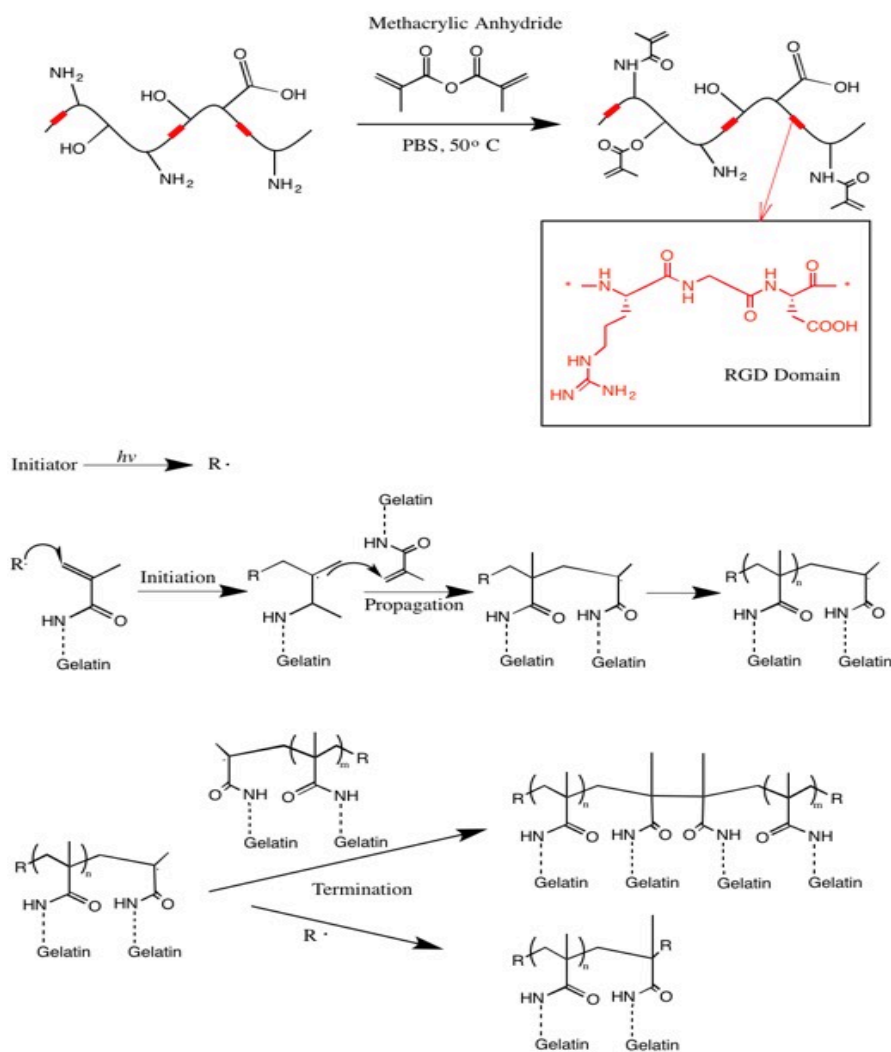


Figure 4.1, schematic representation of preparation of photocrosslinked GelMA hydrogel, a) shows the reaction of gelatin with methacrylic anhydride at  $50^\circ\text{C}$  for grafting methacryloyl substitution groups. This modification occurs at the site of primary amine and hydroxyl groups. The RGD domain is highlighted in red along with their chemical structure in the GelMA chains [185-187]. B) Shows the reaction during the photocrosslinking of GelMA to form hydrogel network. The free radicals generated from photoinitiator that initiate the chain polymerization of methacryloyl substitution cause for the propagation to occur on same chain and on different chains. The termination step occurs between two of these propagating chains or between one propagating chain and a second radical [188-190]

The GelMA hydrogel was photocrosslinked using water-soluble photoinitiator (2-hydroxy-1[4-(2-hydroxyethoxy)phenyl]-2-methyl-1-propanone) (Irgacure 2959) which is commercially available and has a solubility of at least  $5\text{mg/ml}$  sufficient enough for photo-polymerization in aqueous medium. The degree of GelMA concentration, initiator concentration and UV exposure allow tuning the physical properties of the resulting hydrogel that is suitable for conducting cardiac cell experiments.

## 4.4 Rheological measurements of GelMA

In order to determine the suitability of GelMA hydrogel for tissue engineering and micro-patterning application using SAWs, different physical and chemical properties such as hydrogel network pore size, gel compressive moduli, viscosity, elastic and loss modulus, and swelling ratios were studied.

### 4.4.1 Pore Size

In order to determine the porous network of the hydrogel, scanning electron microscopy (SEM) was used to analyse the pore size for 5%, 10% GelMA concentration in the 3D scaffolds which were fixed with glutaraldehyde and dehydrated in series of ethanol baths (Figure 4.2). GelMA has an advantageous physical structure that promotes cell behaviour such as the ability to migrate through pore walls, remodel the pore structures and replace gel material with secreted ECM.

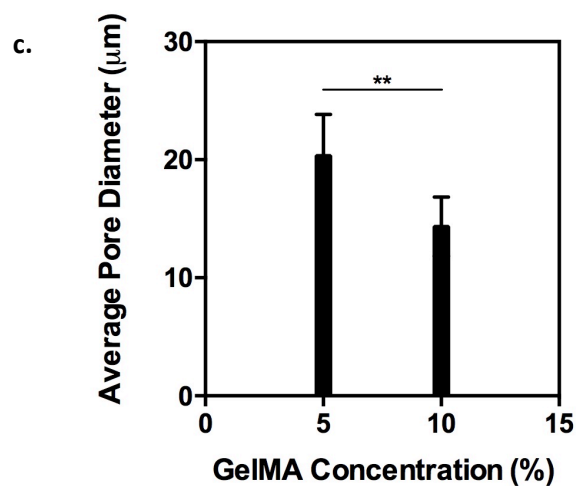
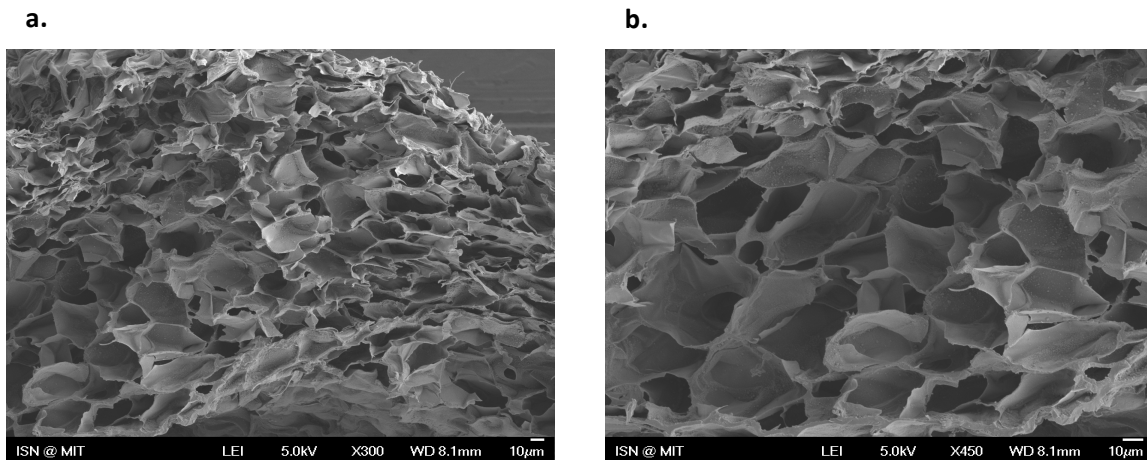


Figure 4.2, a) SEM images of 10% and b) 5% concentration of GelMA photocrosslinked with 0.25%(w/v) I2959 photoinitiator. Sample mounted on studs and sputter coated with 8nm Iridium layer using Emitech K575X and examined in SEM (FEI XL30 ESEM FEG) operated at 5kV in vacuum mode. Porosity was determined using the projected area of the pores for multiple pores using NIH ImageJ software. c) The largest pores were achieved with lower concentration of GelMA for the same amount of photoinitiator at same UV exposure rate of 12 secs (n=3) (p<0.05).

It was found that the average pore size was inversely related to the concentration of GelMA hydrogel. In order to promote cell migration and spreading, nutrient exchange and cell by-product transfers the pore diameter of 5% GelMA concentration,  $20\mu\text{m} \pm 5\mu\text{m}$ , was found to be suitable.

#### 4.4.2 GelMA swelling characteristics

When in contact with aqueous medium such water or cell media hydrogels have the ability to swell up until equilibrium is reached. The swelling characteristics are important for solute diffusion, surface properties, and surface mobility. The swelling depends upon the pore size of the polymer network and the interaction between polymer and solute. In addition the chemical and diffusion properties depend on the chemical composition and structure of the internal network of the hydrogel (Table 3.2).

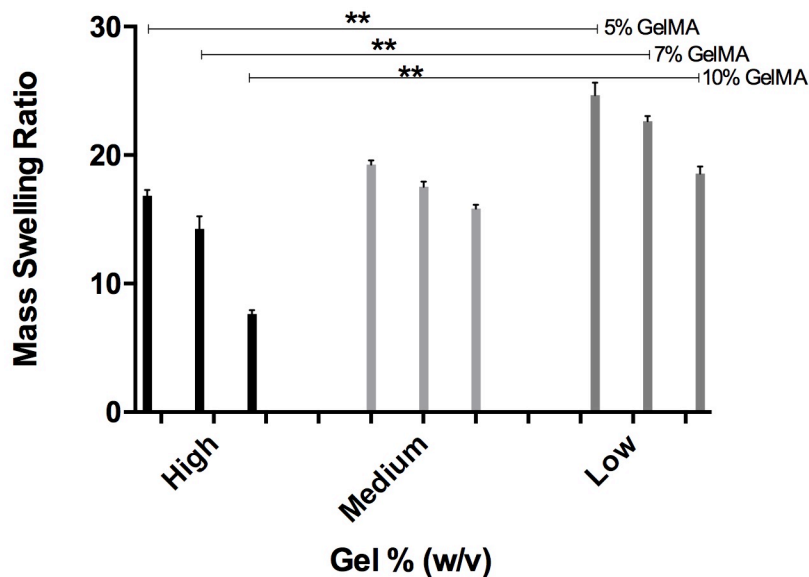


Figure 4.3, swelling properties of methacrylated gelatin hydrogel for different concentration and degree of methacrylation as mentioned in table 3.2. The mass swelling ratio of GelMA at

different % (w/v) and degree of methacrylation have shown significant differences, as the swelling ratio increases the degree of methacrylation decreases ( $n=3$ )( $p<0.05$ ).

GelMA concentration of 5%, 7% and 10% (w/v) were synthesized for making GelMA matrices of low, medium and high acrylation (Figure 4.3). Before use they were allowed to reach an equilibrium by soaking for 24hrs in DPBS at room temperature. Then according to the mass swelling ratio of swollen mass to dry mass of polymer the swelling characteristics were determined as shown in Figure 4.3. The mass swelling ratio increased with decreasing degree of methacrylation for the three different concentration of GelMA. This demonstrated that the degree of methacrylation has an effect on the matrix's ability to attract and store water in the polymer network. This is important since the effect of hydration on the physical properties of hydrogel and the fidelity of micropattern can change with the mass swelling ratio and with respect to degree of methacrylation as well as the hydrogel concentration. Since swelling can have a profound effect on the overall shape, by increasing the degree of methacrylation and hydrogel percentage the pattern fidelity could be improved.

#### **4.4.3 Compressive modulus of GelMA**

Surface properties of hydrogel are important for cell adhesion and biocompatibility. A great amount of water is trapped inside the 3D scaffold of hydrogel which is an advantageous criteria for biocompatibility. This is important to ensure the access of nutrients and cell products through the porous structure created with a suitable concentration of synthesized hydrogel. Hence, compressive tests were performed on the 3D scaffold in the perpendicular direction with respect to the deposition plane. It was found that the mechanical properties strongly correlated with the porosity of different concentration of GelMA.

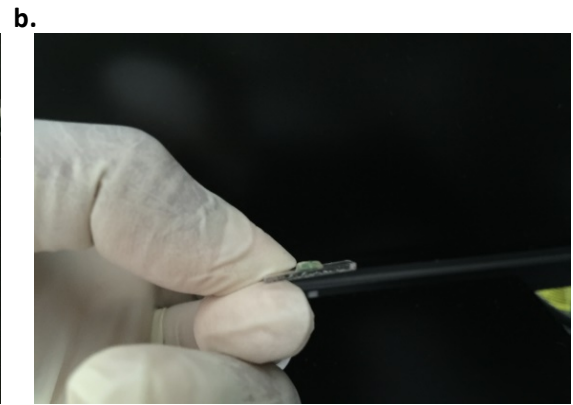
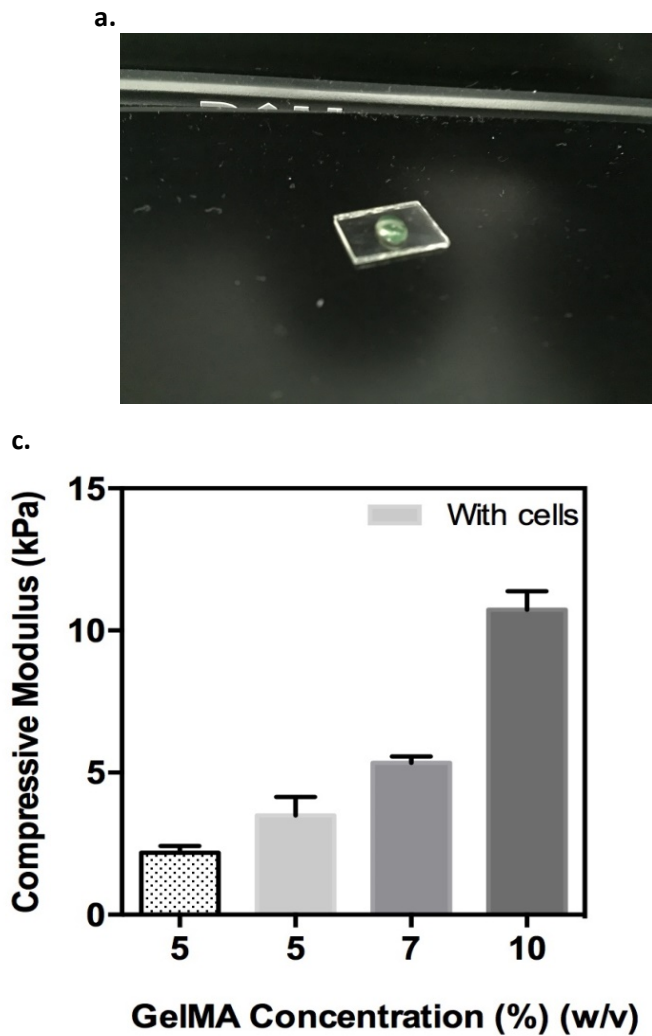


Figure 4.4, a,b) shows cylindrical 3D scaffold of 5% GelMA (w/v) prepared for quadruplicate compressive mechanical testing (Instron 5542) using 0.25% photoinitiator exposed to UV light (360-480nm) for 12 secs at 800mW, c) characterization of GelMA hydrogels with different concentrations to measure compressive modulus. It was noted that the compressive modulus of 5% GelMA scaffold seeded with cells was higher than 5% GelMA without cells indicating the cells being adhered into the matrix due to the porous network (n=3).

Upon compression, the stiffness of the scaffold increased and the compressive modulus of each synthesized GelMA increased with increasing degree of concentration,  $2 \pm 0.18 \text{ kPa}$  for 5% to  $11 \pm 0.33 \text{ kPa}$  for 10% GelMA (Figure 4.4). This analysis proved that when the porosity of the hydrogel fibres increase the compressive modulus consequently decreased and also indicated that the compressive modulus is directly proportional to mass/volume fraction of GelMA.

#### 4.4.4 Shear elastic (storage) vs shear viscous (loss) Modulus

By varying the concentration, degree of methacrylation and temperature, the shear yield stress and elastic moduli of GelMA can be studied. Dynamic mechanical analysis were performed on the cured hydrogel scaffolds to provide quantitative information on the viscoelastic and

rheological properties of the matrix by measuring the mechanical response of the samples as they are deformed under periodic strain. The shear elastic (or storage) modulus  $G'$  and the shear viscous (or loss) modulus  $G''$  are presented in the Figure 4.5.

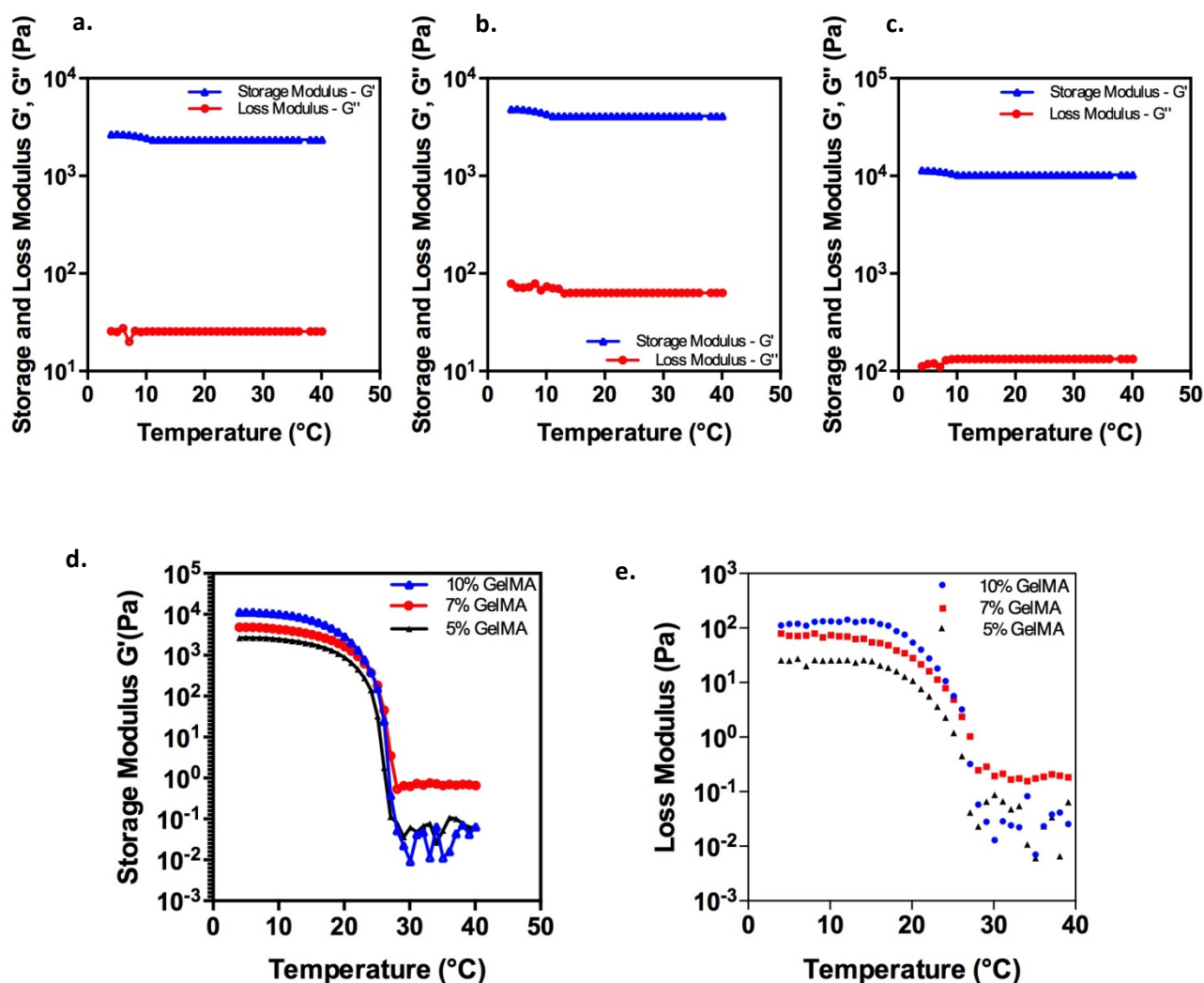


Figure 4.5, shows the dynamical rheological observations of crosslinked and non-crosslinked GelMA of different concentrations stored at 4°C, a,b,c) shows the effect of different degree of concentration of GelMA (5%, 7%, 10% respectively) with increase in temperature in presence of 0.25% (w/v) photoinitiator. The samples were brought to room temperature and then immediately exposed to UV light. d,e) show the effect on storage and loss modulus in absence of photoinitiator (n=3).

For the purpose of comparison, different concentration of GelMA was prepared to allow distinction between the respective contribution of physical and chemical crosslinking in presence and absence of photoinitiator. Figure 4.5 represents the mechanical spectrum exhibited a pronounced plateau in the temperature range invested with loss modulus ( $G''$ )

considerably smaller than storage modulus. The UV treatment for photo-crosslinking of hydrogel led to high storage moduli both above and below the melting point which indicates the presence of photo-initiator inducing chemical crosslinking. The loss modulus for different concentrations was observed to be low in magnitude and steady as the temperature increased. In Figure 4.5 (d,e) high value of  $G'$  is obtained at lower temperature but as the temperature rises the elastic and viscous modulus decrease indicating the transition from elastic network to a solution. Therefore, as the concentration of GelMA hydrogel increases the matrix network becomes denser due to high elastic modulus. However, a high w/v percentage of concentrated GelMA hydrogel prevents the formation of strong physical network of cell growth through the denser pores therefore giving rise to poor mechanical properties, compatibility and a weaker hydrogel is formed.

#### 4.4.5 Viscosity of GelMA hydrogel

Micro-patterning techniques using surface acoustic waves in GelMA based 3D scaffolds depend on the viscosity of the hydrogel and temperature. Different concentrations of GelMA were tested for viscosity measurements under different temperature ranges with constant 0.25% photoinitiator concentration and 12 secs UV irradiance (Figure 4.6).

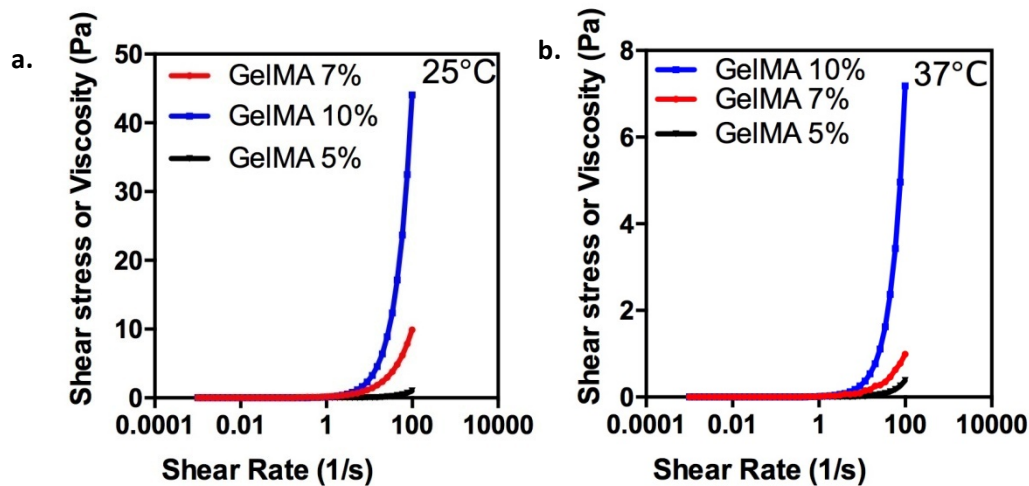


Figure 4.6, a,b) shows the increase of viscosity as the temperature decreases for different concentration of GelMA with 0.25% (w/v) photoinitiator (I2959) (n=3)

The kinematic viscosity of 5% GelMA was found to be  $0.09 \text{ cm}^2 \text{ s}^{-1}$  at  $37^\circ\text{C}$ . This degree of concentration of GelMA hydrogel scaffold allowed dispersion of SAWs for patterning cells at  $37^\circ\text{C}$  in the chamber of dimension  $6.0 \times 4.0 \times 0.8 \text{ mm}$  as described later. The GelMA hydrogel

scaffolds designed in PMMA channels for 3D architecture patterning of cells would provide high aspect ratio as it is feasible to attain high cellular alignment and elongation in the whole engineered scaffold with long term viability.

In summary, GelMA hydrogel possess properties that promote cell survival and differentiation in 3D by combining synthetic and natural macromers to provide controllability over mechanical architecture as shown in later chapters. GelMA hydrogel scaffolds provide a very cytocompatible environment that can maintain a relatively constant proportion of viable live cells throughout the experiments. These data suggest that a wide range of scaffolds can be produced using GelMA by varying the degree of methacrylation, initiator concentration, UV exposure time and hydrogel concentration to alter the mechanical properties of matrix for different applications in tissue engineering.

#### **4.5 Conclusion**

This chapter has demonstrated the use of GelMA for micro-scale tissue engineering applications. The physical properties of GelMA were controllable by varying different concentration of the gel yielding tunable mechanical and swelling properties for different applications.

## Chapter 5

### SAW Device characterization

#### 5.1 Introduction

In recent decades, SAW devices have been employed for applications ranging from radio frequency (RF) communication [160], chemical and biochemical sensors [161], optical modulators [162], droplet microfluidics [166], continuous flow microfluidics [163] and particle separation [166]. This chapter discusses with the design and characterization of slanted-finger IDTs SAW device, poly methyl methacrylate (PMMA) gasket chamber characterization, quantifying forces on cells and COMSOL Multiphysics simulations for SAW and DEP based devices.

#### 5.2 Material and Methods

##### 5.2.1 Device and experimental setup

The SAW devices were fabricated on a double side polished 128° Y-cut X-propagating 3inch LiNbO<sub>3</sub> wafer. The slanted finger interdigitated transducer (SFIDT) consisted of 18 pairs of fingers. The width of the tapered fingers and space between them varied linearly from 124.69μm to 332.5μm along the aperture to yield working frequencies between 3MHz and 8MHz. The LiNbO<sub>3</sub> wafer was coated by spinning S1818 photoresist before transferring the pattern using standard photolithography protocols and developed using Microdeveloper. A 20nm titanium adhesion layer was evaporated prior to the deposition of 100nm of gold and lift-off was then performed using acetone.

The DEP devices were fabricated on 1mm thick glass slides. The IDT design on the photomask had dimension of 50μm thickness and 50μm gap between each electrode. The electrodes were patterned on the glass slide using conventional photolithography procedure as stated above. S1818 was poured onto the glass slide and baked at 90°C for 30min. The samples were then irradiated by UV light through a mask aligner (MA-6; Mikasa Co. Ltd, Japan) and developed with MF CD-26. A 20nm titanium adhesion layer was deposited followed by 100nm of gold layer. The electrode design was then revealed by the lift-off technique using acetone in warm water bath at 37°C.

The SAW device was characterized by using Network Analyzer (Agilent Technologies E5071C ENA series) and vibrometer (Polytec) as demonstrated earlier. The SFIDTs were connected to TGR1040 – 1GHz RF Generator (Thurlby Thandar Instruments) in conjunction with a Mini Circuit ZHL-5W-1, 5-500 MHz amplifier and a 3A, 24V dc power supply to generate SAWs.

### 5.2.2 Data analysis

Acoustic radiation forces were analysed for polystyrene beads, cardiac fibroblasts and myocytes and MCF-7 cells suspended in different media, after being pushed towards the pressure nodes by acoustic radiation force. During this process, the induced Stokes drag forces counteract with the acting acoustic force so that the acoustic radiation force can be determined by examining the velocity of the particles. The movement of particles were investigated under different input power level in order to obtain parallel alignment of cells and avoid turbulence and fluid mixing and motion. The velocity of each single particle was examined using ParticleTracker software and ImageJ plugin called MTrackJ. The velocity obtained for each particle corresponds to the peak of acoustic radiation force along the trajectory. Therefore, the acoustic radiation force can be calculated using the formula,

$$F_{ARF} = 6\pi\mu r v \quad (5.1)$$

Where, ARF is the acoustic radiation force,

$r$  is radius of the particle,

$\mu$  is the dynamic viscosity of the medium

$v$  is the velocity of the particle

### 5.3 SAW Device - Slanted Finger IDTs (SFIDTs)

Precise manipulation of cells in three-dimensions offers many applications in regenerative medicine, tissue engineering and biophysics. SAW based devices manipulate biological cells using sound waves offering many unique advantages such as non-invasive and scalable manipulation. These waves created by the vibrations of piezoelectric crystals on the lithium

niobate substrate do not alter the cell characteristics. In this work, a SAW device consisting of slanted finger-IDTs was patterned on a piezoelectric substrate as shown in Figure 5.1 using the standard UV photolithography protocol mentioned earlier. On applying an RF signal at the IDTs the lithium niobate wafer contracts and expands due to the redistribution of charges which causes deformations that lead to formation of SAWs. These SAWs have both longitudinal and transverse vibrations along the direction of propagation of waves. SFIDTs allow positioning the waves from one end to the other. SSAWs at different wavelengths have been created using the same design for cell patterning applications. The SAW device was tested with  $S_{11}$  reflection test using a network analyser (E5071C ENA, Agilent Technologies) to detect its response at a range of frequencies. The SAW devices fabricated in this study have been designed for a frequency range of 3 MHz to 8 MHz (Figure 5.1). The network analyser sends a range of frequency signals and compares with the reflected signal and displays the difference signal at resonance frequency sent to SAW device.

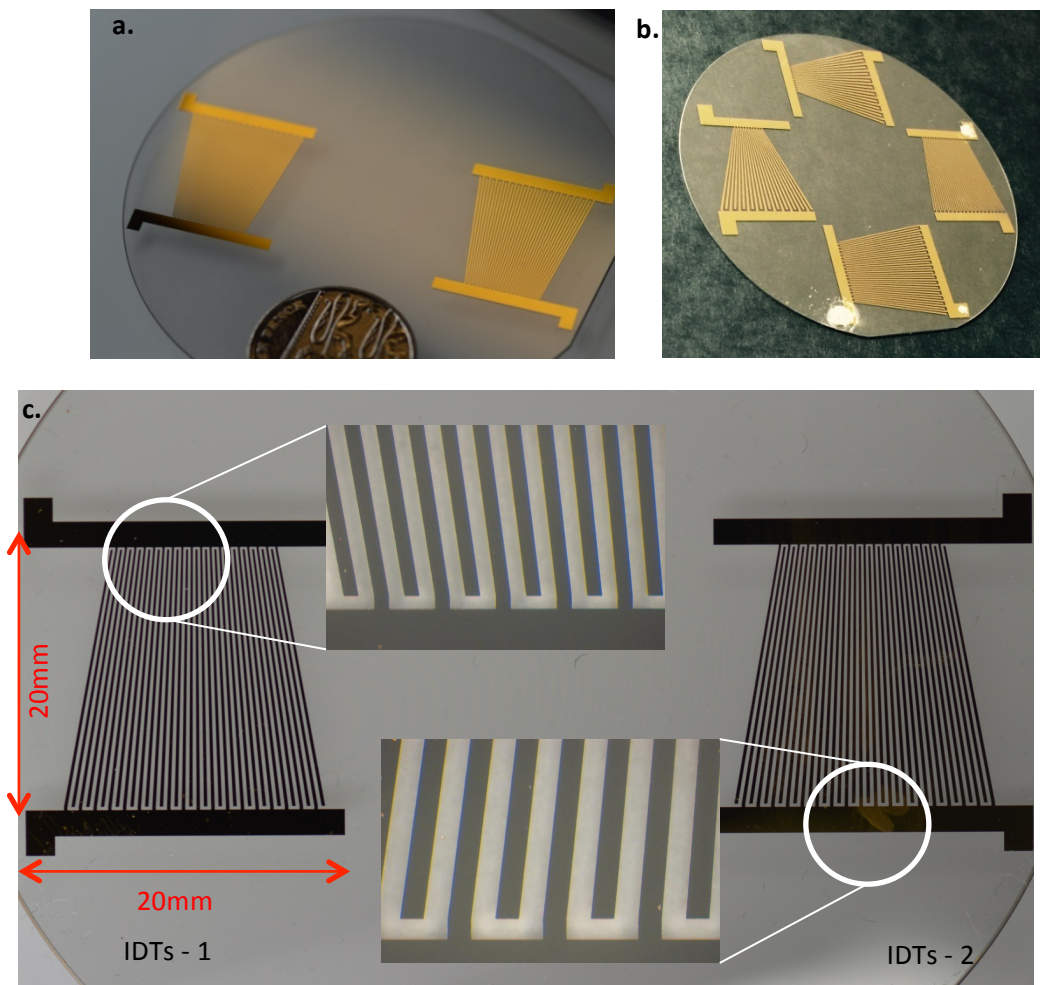


Figure 5.1, schematic of SAW Device microfabricated IDTs patterned on LiNbO<sub>3</sub> 128° Y-X

cut double polished substrate, a) parallel identical SFIDTs designed at opposite ends of the wafer to create 1D patterning at centre region of interest b) four identical SFIDTs orthogonal IDTs designed to create 2D patterning of bioparticles, c) shows varying thickness width of the SFIDTs with magnified image of either ends of the IDTs ( $124.69\mu\text{m}$  and  $332.5\mu\text{m}$ , respectively).

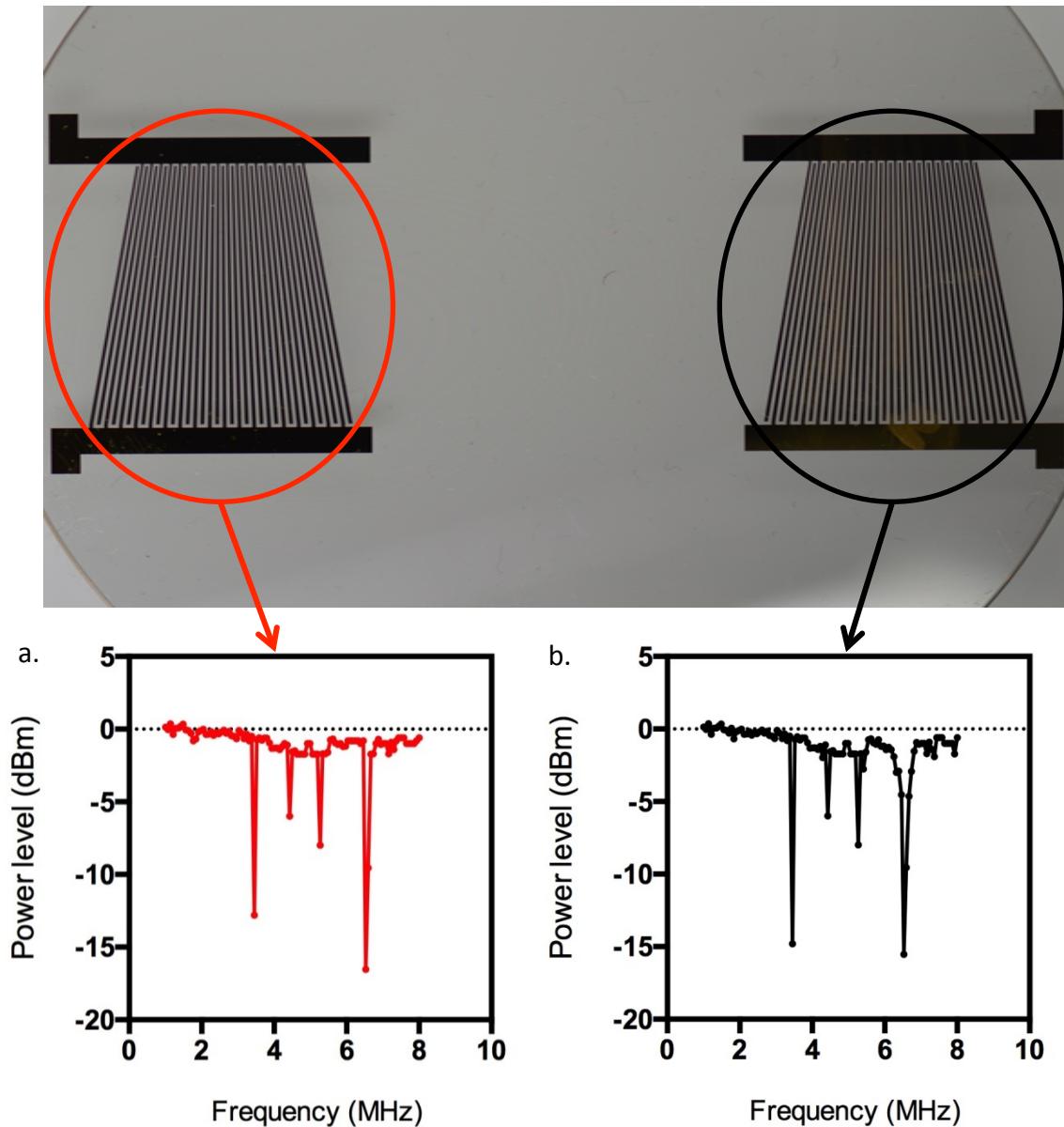


Figure 5.2, shows the resonance frequencies observed from the excitation of SFIDTs at frequency range of 3MHz-8MHz, a) for one end of SFIDTs, b) for opposite designed SFIDTs at the other end showing a resemblance of resonance frequencies measured that is important for creating phase match at creating acoustic waves. The measurements show the resonance performance of the SAW transducer at four frequencies 3.4MHz, 4.6MHz, 5.34MHz and 6.4MHz respectively using network analyser (n=3).

In this work, the resonance frequency occurred at 3.4MHz, 4.6MHz, 5.34MHz and 6.4MHz respectively as shown in Figure 5.2 for the both the two opposite designed SFIDTs have significant prominent  $S_{11}$  measurements with significant range or power levels. The reasons for variation in power levels include design transfer error on the acetate mask and over etching of the photoresists that can cause the finger edges to change in width. This variation can also be due to the manufacturing defects in the wafer that cause mismatch of crystal charge and orientation at the time of excitation.

#### 5.4 Temperature effect on lithium niobate wafer

128° Y-X cut LiNbO<sub>3</sub> substrates have excellent material properties such as large piezoelectric coupling constant (5.36%) and high SAW velocity (3994m/s). However, it has poor temperature stability. SAW devices are capable of working at high temperatures up to approximately 550°C on LiNbO<sub>3</sub> [8]. Hence they are being employed for high temperature applications such as in wireless communication systems. The thermal measurements made in this work were at two working frequencies (3.4MHz and 6.4MHz) at varying SAW power level ranging from -20dBm to -10dBm (Figure 5.3).

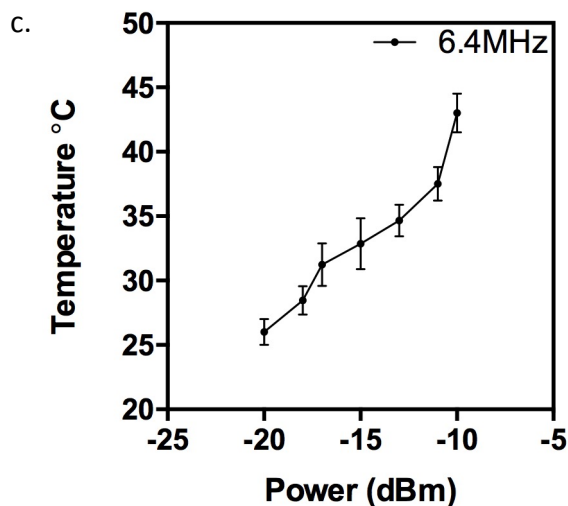
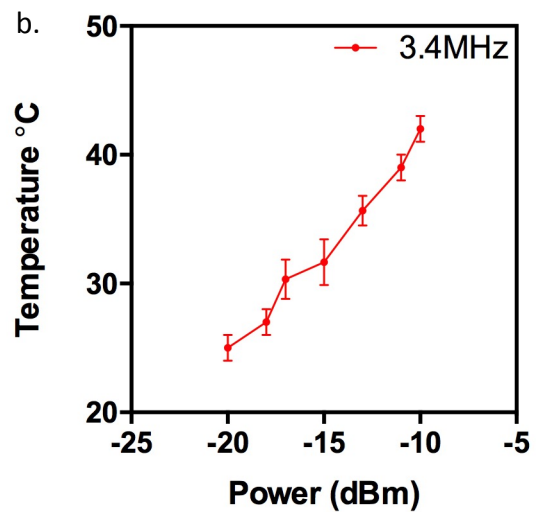


Figure 5.3, a) shows infrared image (IR) of an orthogonally active SFIDTs SAW device using an IR camera (Fluke Ti-25), b) temperature changes on the surface of the wafer during the application of 3.4MHz frequency and c) temperature changes on the surface of piezoelectric wafer on applying 6.4MHz. At least three measurements were taken (n=3).

It was observed by increasing the input power the temperature increased over time over the region of interest. Therefore the input parameters were optimized to have the ideal conditions for patterning cells and reducing heating effect on the 3D scaffold. Since the biological cells were cultured *in vitro* at 37°C it was necessary to maintain a temperature of the substrate at approximately 40°C ( $\pm 5^\circ\text{C}$ ) (Figure 5.3). A power level of approximately -10dBm was found to keep the cells at the incubation temperatures throughout the duration of the experiments. Once the adequate temperature range (37-42°C) for both the SFIDTs was achieved, the power levels were noted and maintained throughout for all the experiments.

### 5.5 Quantifying Laser Doppler Vibrometry

Laser Doppler vibrometry (LDV) from Polytec was used to investigate the behaviour of waves in the z-direction and quantify the displacement on the surface in the region of interest where the superstrate was to be placed (Figure 5.4).

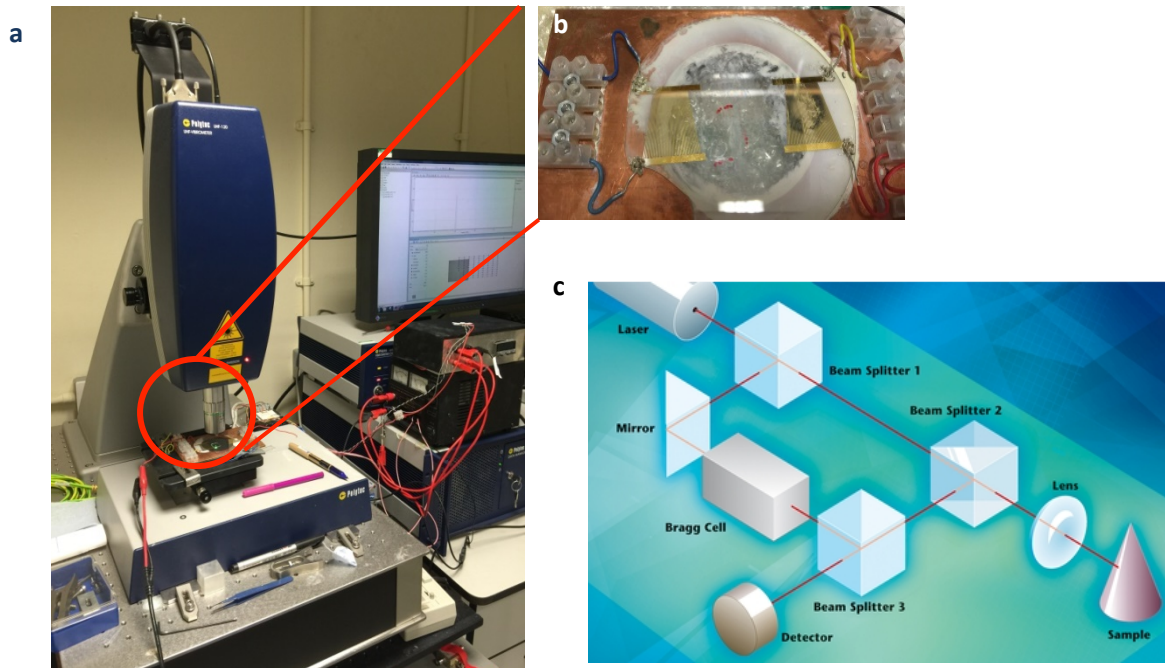


Figure 5.4, a) shows the setup of the Laser Doppler Vibrometry (Polytec UHF-120) to investigate the surface displacement on two opposite SFIDTs for SSAWs, b) transducer being used to investigate the displacement at the centre of the SFIDTs over an area of  $1\text{cm}^2$ , c) schematic representation of a Polytec vibrometer system used for determining the displacement at fixed region. Using Doppler-effect principle the system senses the frequency shift of reflected scattered signal from the source.

The transducer device was connected to a Synthesized RF Generator (TGR1040-1GHz, Thurlby Thandar Instrument) in conjunction with a 5-500 MHz amplifier (Mini Circuits ZHL-5W-1) and a 3A 24V<sub>DC</sub> power supply, to generate the SAW. The effective aperture ( $Ap_{eff}$ ) of an excited SAW from the SFIDT can be calculated through [168],

$$Ap_{eff} = \frac{1}{n} \frac{f_c}{f_h - f_l} A_0 \quad (5.2)$$

where,

$n$  is the number of pairs of IDTs,

$f_c$ ,  $f_h$  and  $f_l$  are centre, highest and lowest frequency,

$A_0$  is the horizontal length of the IDTs.

The width of the SFIDTs varied linearly from 332.5 $\mu$ m to 124.7 $\mu$ m along the aperture corresponding to wavelengths of 1330 $\mu$ m and 498.75 $\mu$ m respectively and range of frequencies from 3MHz to 8MHz on LiNbO<sub>3</sub> wafer, where  $c = 3994\text{ms}^{-1}$ . 18 pairs of fingers were designed with an horizontal length of 20mm and according to the equation 5.2, this would yield the effective aperture to be 1.33mm. Figure 5.5a, shows a schematic representation of SAW propagation generated from SFIDTs with a selected input frequency of 3.4MHz and 6.4MHz at one given time. The part of the IDTs that supports the resonance frequency condition at that region resulted in the propagation of SAW with an aperture of 1.33mm ( $\pm 0.5\text{mm}$  found experimentally). SFIDTs allow tuning of frequencies to control the lateral position of the excited waves and an aperture region can be characterized from varying input frequencies. The aperture was characterized by setting input frequency at 3.4MHz and 6.4MHz as shown by the resonance peaks in network analyser using LDV and an IR imaging camera.

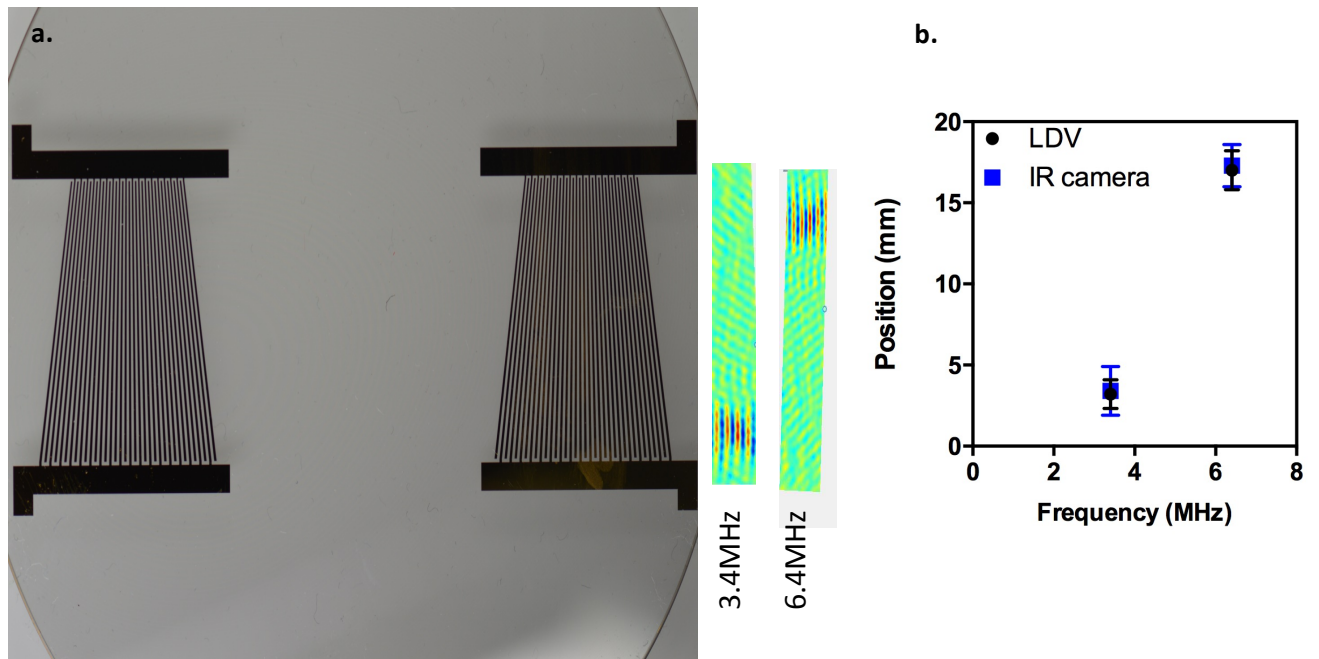


Figure 5.5, schematic of working principle of SAW beam generated by SFIDTs, a) shows the excitation of SAW waves at 3.4MHz and 6.4MHz through surface displacement on the LiNbO<sub>3</sub> 0.5mm thick wafer obtained by LDV, b) shows the graph of working frequency (3.4MHz and 6.4MHz) over a aperture of 1.33mm ( $\pm 0.5$ mm) using the results from LDV and IR camera (n=3).

The same controls of the SAW as used in the LDV was extended to measure the displacements on the LiNbO<sub>3</sub> substrate using a 1 cm<sup>2</sup> glass slide of 1mm thickness as a superstrate. The superstrate was coupled with water and then with gel to investigate the damping of the amplitude of the displacement.

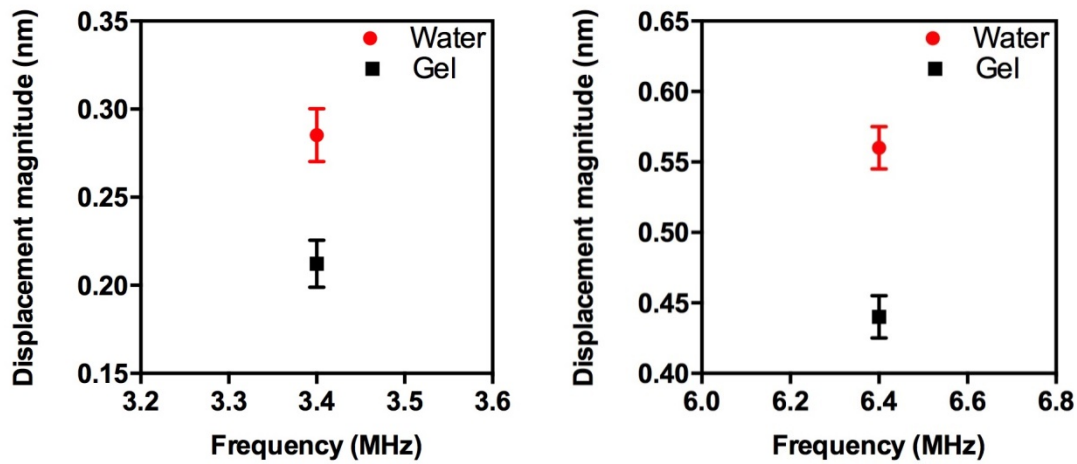


Figure 5.6, shows the surface displacement magnitude measured by LDV (Polytec UHF-120) using water as coupling layer and gel as a coupling layer at a) 3.4MHz and b) 6.4MHz at 180mW (n=3).

It was found that the waves were 21% ( $\pm 10\%$ ) less damped at 3.4MHz and 24% ( $\pm 10\%$ ) less damped at 6.4MHz when comparing the use of water as a coupling layer and when gel was used instead (Figure 5.6). This was due to the low viscosity property of water leading to better diffraction of waves involved in coupling into the superstrate.

## 5.6 Chamber design & characterization

The chamber designed for this application consisted of a 0.8 mm thick PMMA sheet that was cut using a laser cutting machine (K2030 YL 40W). The following design requirements were taken into account considerations, namely: the chamber material and dimension should be able to couple the SAWs into the hydrogel to create SSAWs and avoid streaming effects; the dimension and position of the chamber on the wafer should phase match the position of the acoustic pressure nodes in the chamber; the resonator should be efficiently able to transmit acoustic power from  $\text{LiNbO}_3$  into the fluid filled chamber with low losses and high Q-value and display good acoustic reflection properties to create 1D patterning; the device was set up to allow rapid localization of cells in multiple samples at a faster rate which meant using a superstrate that was a  $1\text{cm}^2$  TMSPMA coated slide. A  $2\mu\text{l}$  droplet of water was used to properly align and bond the chamber with the base slide; in order to form a sealed device the top of the chamber was covered with a  $0.8\text{cm}^2$  cut glass piece that would allow the waves to reflect and bounce back into the medium for patterning cells; the chamber should be designed

so that the turbulent or stagnation zones can be avoided; assembling and disassembling needs to be simple, fast, biocompatible and preserve sterility so that cell culture protocols can be carried without contamination; upon submerging the device in the cell media after excitation of waves, there should be exchange of nutrients and gas to allow the hydrogel reach the equilibrium with the media and incubator atmosphere; the chamber should allow easy handling when changing media and visualizing under the microscope causing little to less disturbance to the cells.

The chamber consists of three parts – first is the base (superstrate) which is a TMSPMA coated glass slide. The coating allows the hydrogel to attach to the slide after photo polymerization effect under UV light. The second part is the chamber that housed 45 $\mu$ l of 5% GelMA hydrogel (w/v) containing encapsulated cells. And finally the third part is cover glass that is used to seal the device (Figure 5.7) and allow the SAWs to reflect and bounce back in to the medium.

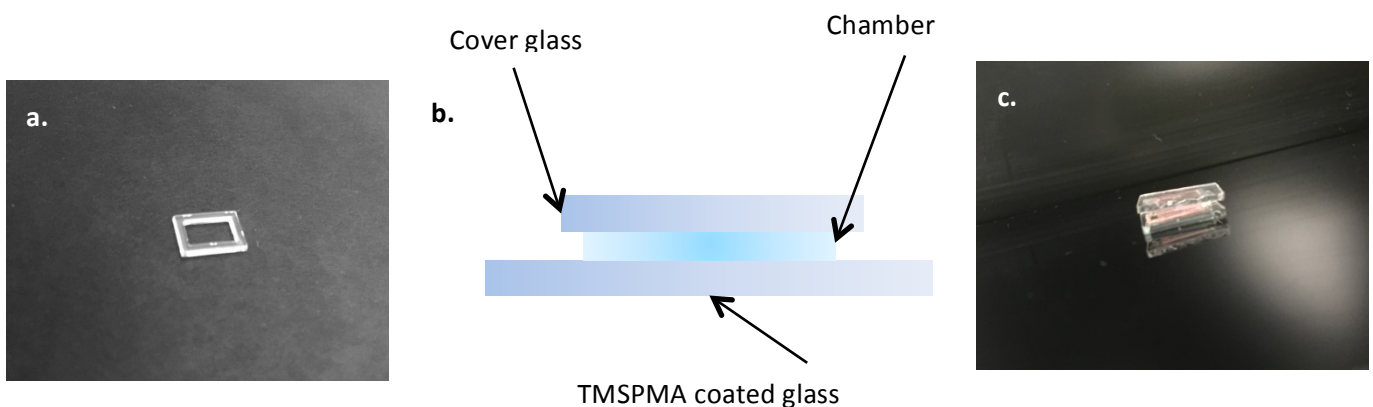


Figure 5.7, a) shows the rectangular gasket chamber of 0.8 x 0.6 cm dimension and depth of 0.8 mm. The internal hollow dimensions were 0.6 x 0.4 cm, b) schematic representation of the sandwiched superstrate chamber, c) experimental setup of the superstrate used with sterilized water as a coupling agent with LiNbO<sub>3</sub> wafer.

One of the important phenomena to pay attention to is the acoustic streaming. Acoustic streaming is the fluid motion that is created by high amplitude waves propagating through the fluid medium. This work focuses on creating cell alignments at pressure nodes of the SSAWs, which meant designing chambers of different inner length and width. The starting dimension for the chamber was set at 1.5 x 1.0 cm and investigated for creating standing waves using 6 $\mu$ m fluorescent beads suspended in the 5% GelMA (w/v). It was observed that turbulence

and streaming effects were significantly higher even by varying the level of input power (Figures 5.8, 5.9, 5.10). Upon, further experiments and trials it was revealed that the dimensions of 0.6x0.4cm were ideal to create just enough patterns at the two different working frequencies, 3.4MHz and 6.4MHz.

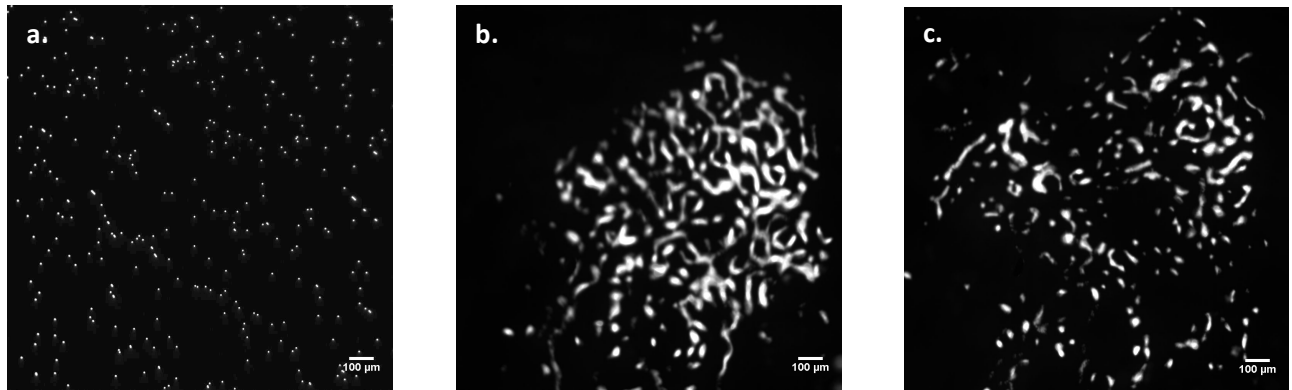


Figure 5.8, schematic representation of characterizing the SAWs to generate patterns in the chamber by adjusting the power level at input frequencies of 6.4MHz, -5dBm. a) shows the random distribution of fluorescent beads (6 $\mu$ m) in 5% GelMA (w/v), b) The acoustic streaming patterns were observed when on excitation of SSAWs at high power (220mW) and large inner perimeter of chamber, c) fluorescent beads were forming aggregates due to formation of streaming vortex.

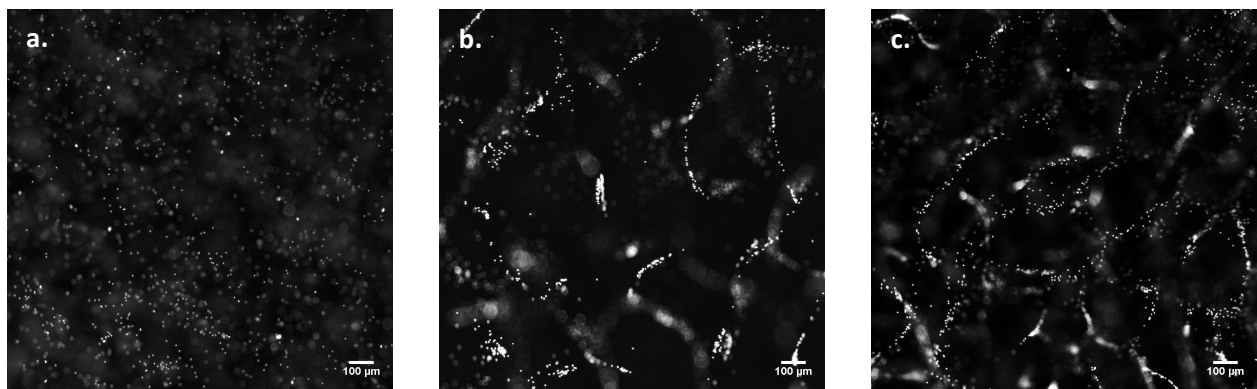


Figure 5.9, schematic representation of characterizing the SAWs to generate patterns in the chamber by adjusting the power level at input frequencies of 6.4MHz, -14dBm. a) shows the randomly distributed fluorescent beads in 5% GelMA (w/v), b) The acoustic wavy distorted patterns were observed when on excitation of SSAWs, c) the wavy and distorted patterning of beads was observed and the yet parallel arrangement of beads were not observed.

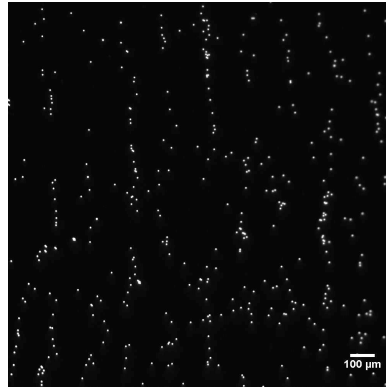


Figure 5.10, schematic representation of cell alignment due to SSAWs to generate patterns in the chamber by adjusting input frequency at 6.4MHz, -10dBm. The acoustic 1D patterns were observed when on excitation of SSAWs without creating fluid turbulence or vortex formations in the medium using a phase contrast microscope at magnification (5x).

Acoustic streaming is the motion of fluid induced by acoustic wave propagation into the medium. This displacement of fluid originates either due to attenuation of the waves in the fluid over the length of the chamber or by boundary interaction with container walls [117]. The pressure gradient produces a force in the same direction of wave propagation and induces fluid flow. This is a non-linear phenomenon is called acoustic streaming [118].

In an ideal fluid, time averages particle displacement, i.e., the net fluid flow is zero everywhere. However in a real fluid, the viscous attenuation results in net displacement of fluid particles during each cycle of oscillations becoming non-zero [119]. This local effect leads to global formation of streaming flow. This steady flow depends on the velocity of flow, length scale of flow and geometry of flow along the channel [113].

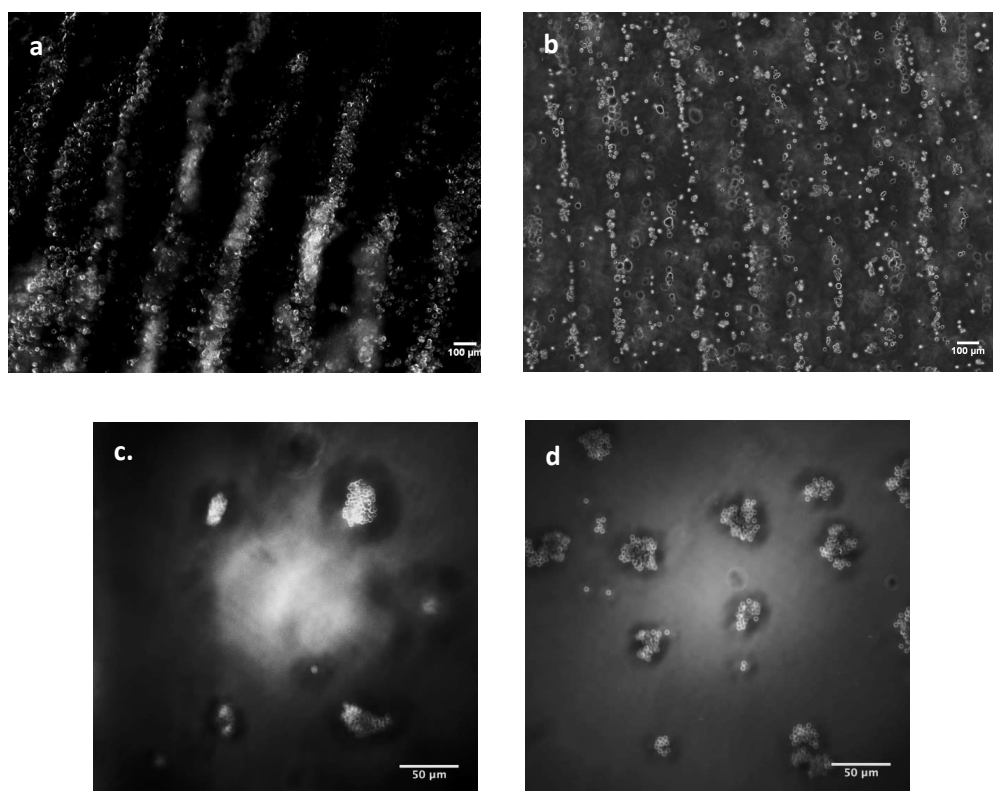


Figure 5.11, show 1D patterning of cardiac fibroblasts in 5% GelMA (w/v) before photocrosslinking and polymerization of the hydrogel with UV at 12sec. 1D patterning at a) frequency 3.4MHz, b) frequency 6.4MHz sat 180mW by oppositely paired IDTs on the  $\text{LiNbO}_3$ . c and d) show formation of cell aggregates due to 2D patterning of cells at 4.6MHz using the orthogonally excited SFIDTs at 220mW.

The SFIDTs based SAW device has been experimentally characterized for 3.4MHz, 6.4MHz for rapid 1D patterning using SSAWs and 4.6MHz using orthogonal SSAWs on the lithium niobate substrate as shown in Figure 5.11. The input power levels were investigated for each of the resonant frequencies to avoid fluid motion, streaming and turbulence in the designed chamber.

### 5.7 SAW Device setup and quantifying acoustic forces

Acoustic waves have proven to be safe to manipulate biological samples and are widely used in LOC applications and diagnostics. SSAWs field region can be created to manipulate and manoeuvre cells or other bio-particles in a programmed manner. SAW devices provide a novel platform that is compact and non-invasive technique as opposed to other LOC

techniques. Previous studies have confirmed the non-invasive nature of using SSAWs on cell membranes before and after exposing them to excited waves. In this research, SSAWs have been employed to spatially localize cells encapsulated in GelMA hydrogel (Figure 5.12).

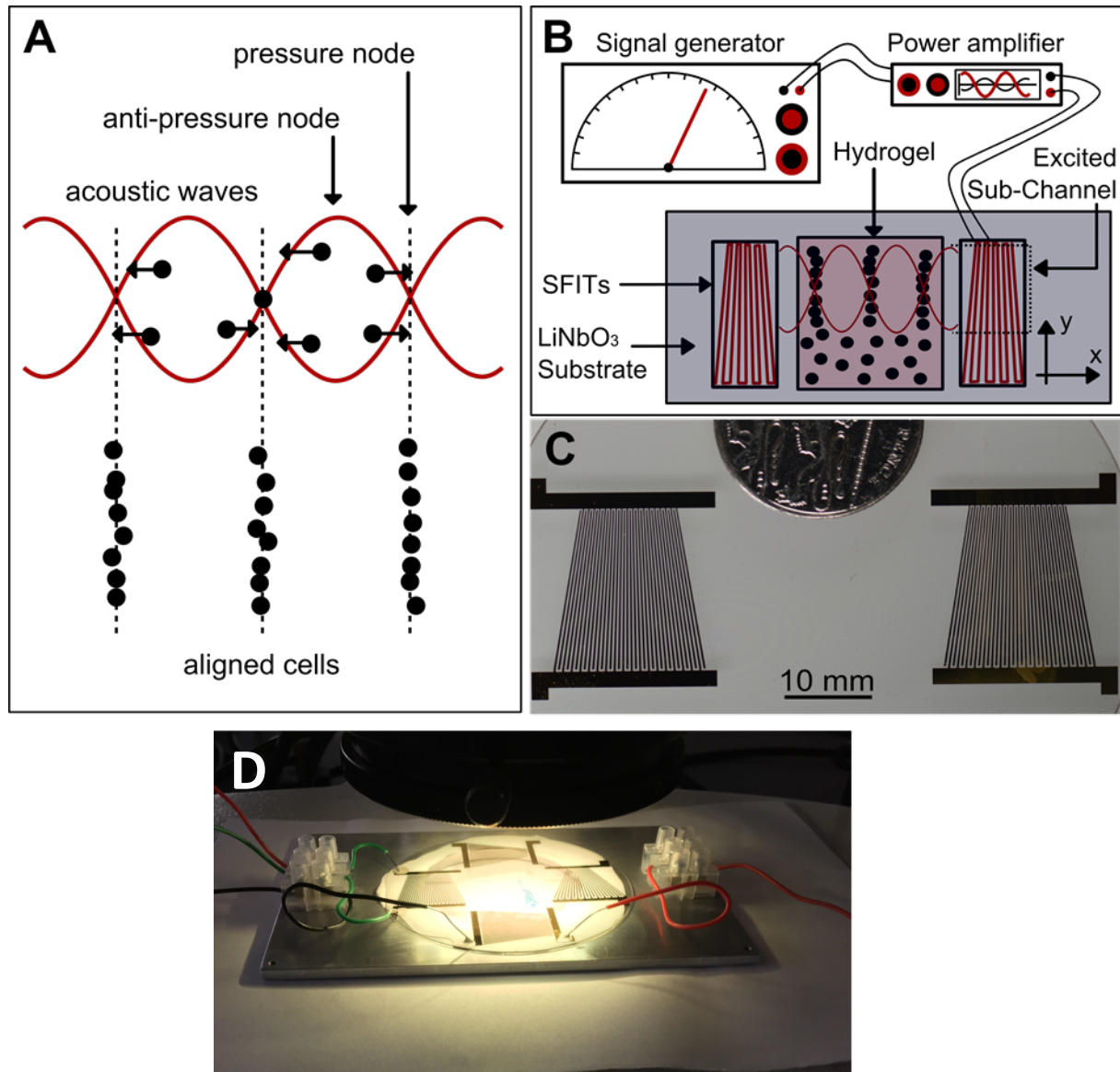


Figure 5.12, a) schematic representation of SSAWs exhibited on the particles that push them towards the pressure nodes and pattern cells in lines corresponding to the wavelength, b) schematics of the setup employed to generate SSAWs on LiNbO<sub>3</sub> wafer using one dimensional waves created by SFITs, c) top-view of the microfabricated SAW device, D) image of the experimental setup including the transducers on piezoelectric wafer placed on heat sink.

The primary forces involved in patterning cells using SSAW are Acoustic radiation forces ( $F_{ARF}$ ), gravitational forces ( $F_G$ ), buoyant forces ( $F_B$ ) and viscous forces ( $F_v$ ) as shown in

Figure 5.13(a). The gravitational and buoyant forces are typically balanced since they are of similar magnitude and act in opposite direction [9]. The cells trapped at the pressure nodes face minimal value of acoustic radiation force (ARF). Figure 5.13 (b,c) shows the cardiac fibroblasts moving towards closer pressure nodes. As the cells approach the pressure node, ARF decreases and consequently the velocity decreases (Figure 5.14).

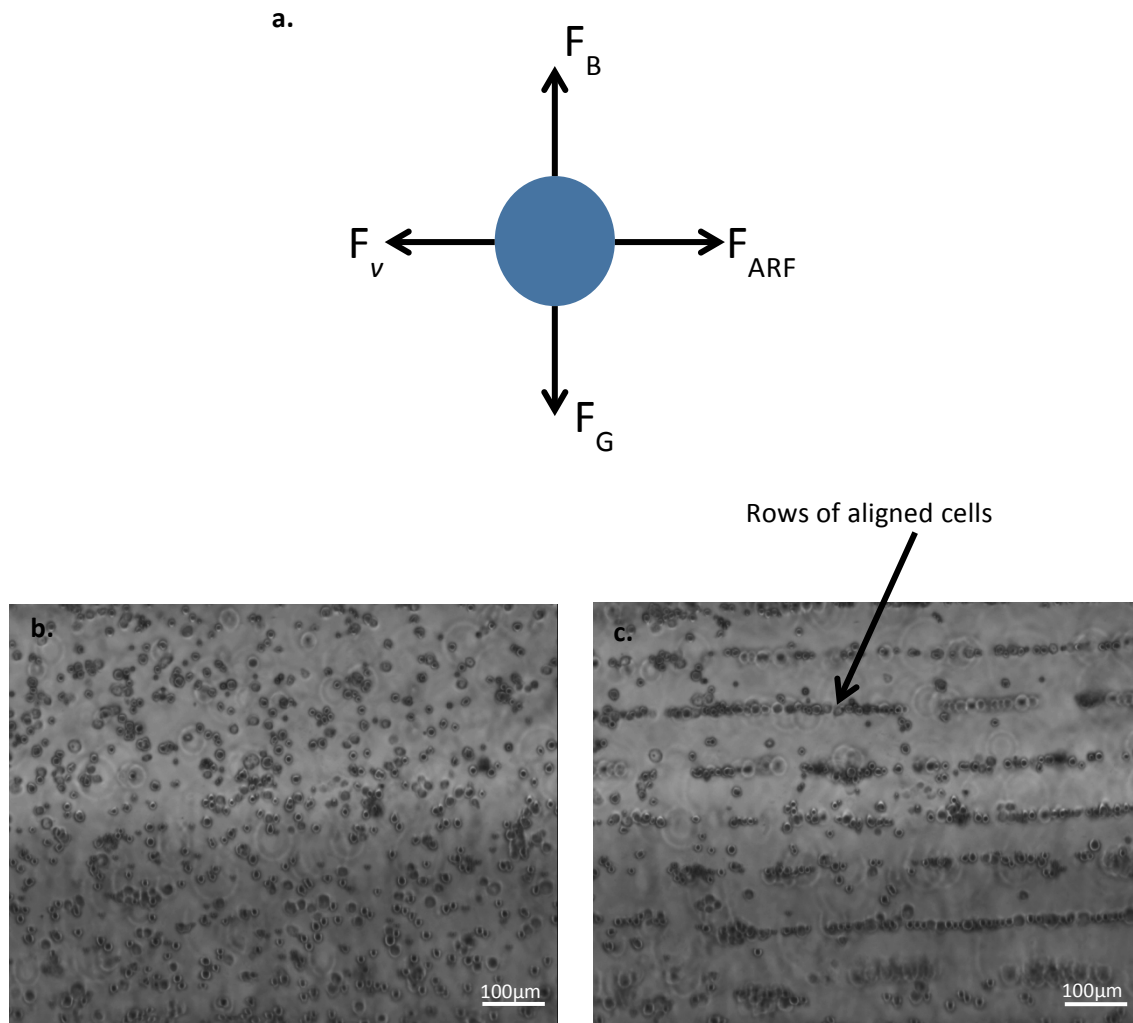


Figure 5.13, a) schematic representation of forces acting on a particle before experiencing acoustic force causing it to move towards the pressure node, b) experimental image of cells dispersed randomly in 5% GelMA medium in the chamber, c) shows the 1D alignment of cardiac fibroblast cells when exposed to SSAWs at 6.4MHz at 180mW.

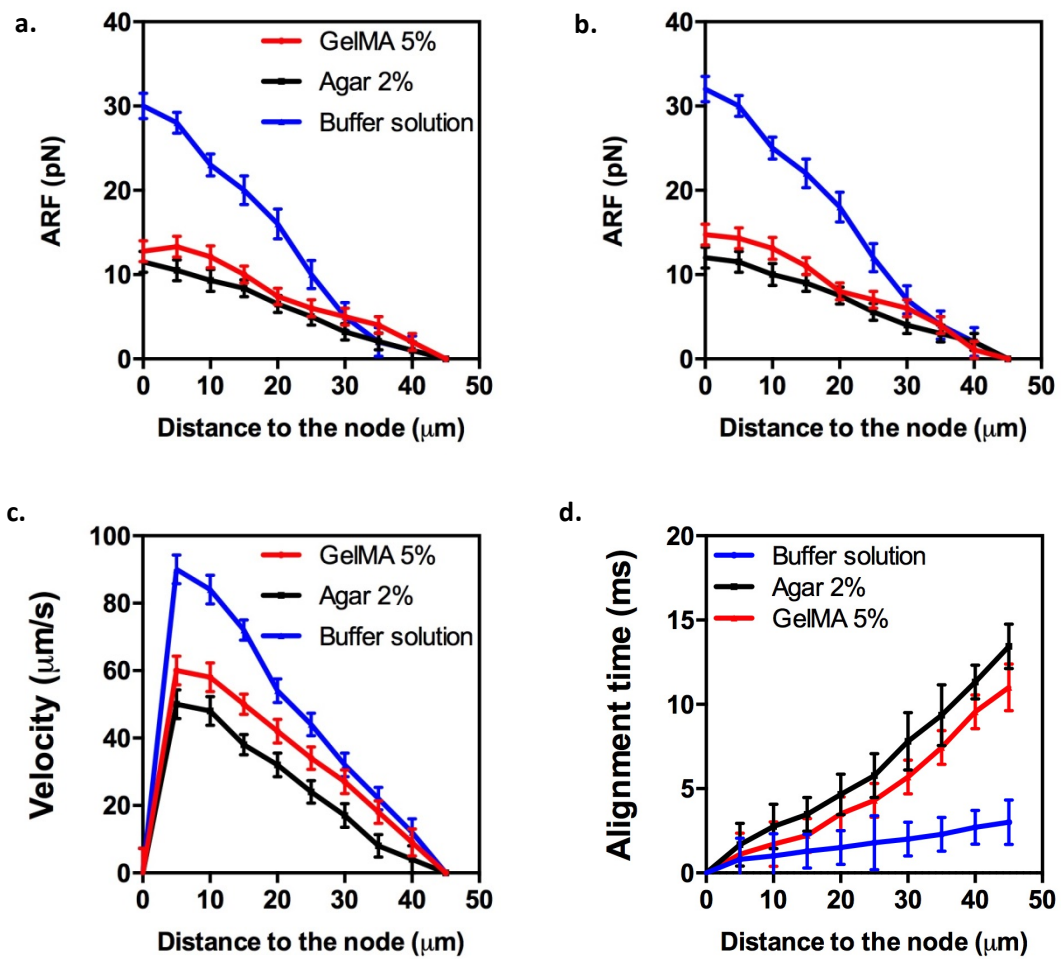
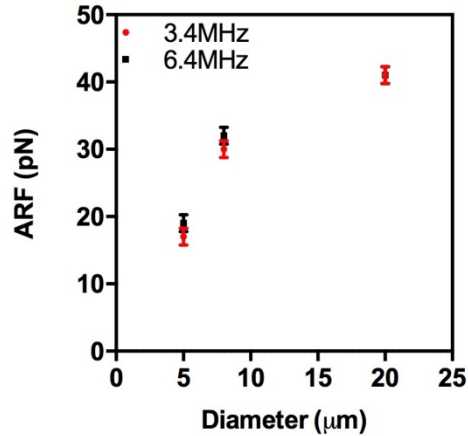


Figure 5.14, a) shows the distribution of ARF acting on cardiac fibroblasts pushing them towards the pressure node trap at 3.4MHz and b) 6.4MHz respectively. It can be seen that at higher frequency higher ARF was experienced by the cells, c) shows the motion of particles in SSAW field at 3.4MHz in different mediums, d) represents the alignment time of the cells at 3.4MHz SSAW in different mediums. The alignment time was faster for beads in buffer medium as opposed to beads suspended in GelMA or agar (n=3).



Figure, 5.15, shows the dependence of ARF with respect to particle size, fluorescent beads (6μm), cardiac fibroblasts (10μm), MCF-7 (17μm) cells, as the dimension of the particle increases the larger the force it will experience. As the diameter of the particle increased the acoustic forces increased in 5% GelMA (w/v) at different frequencies (3.4MHz and 6.4MHz)

When a SSAW field is generated across the chamber the acoustic radiation force (ARF) pushes the bioparticles towards the closest pressure nodes. The viscous drag forces counter the acoustic forces. Therefore by examining the particle velocity the ARF acting on the particle can be revealed (Figure 5.14) and dependence on the size of the particle (Figure 5.15). The movement of cardiac fibroblasts in different mediums in 1D SSAW field was calculated for frequencies at 3.4MHz and 6.4MHz using MATLAB code, NIH ImageJ cell tracking add-on (MTrackJ) and ParticleTracker software. It was observed that ARF was much higher in the buffer solution with low viscosity (0.89mm<sup>2</sup>/s) of the medium as opposed to 5% GelMA (w/v) hydrogel to push the cells towards the pressure nodes. However, it was also noted that the acoustic forces were weak when patterning cells in agar (2%) gel. This was observed repeatedly due to the curing of agar in the chamber caused by temperature variations on the platform and atmosphere. When the cells reached the pressure nodes, the velocity decreased gradually with decrease in ARF, thereby creating traps for cells. This procedure allows fast and continuous on-chip measurements of acoustic forces under bright field microscopy. It was noted that the difference of acoustic force exerted on particles with different dimensions resulted in higher forces with particles of higher diameters. SFIDTs allow to tune the wavelength and position of the excited waves which is beneficial to control the position and distance between the aligned patterns (Figure 5.16).

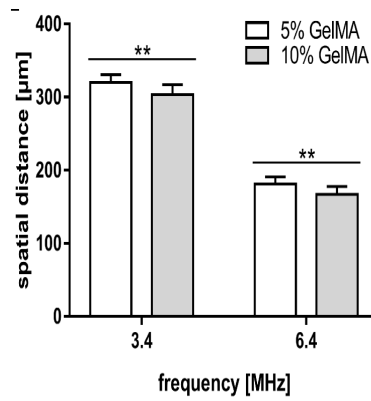


Figure 5.16, shows spatial patterning of cells in SSAW region at 3.4MHz and 6.4MHz in the chamber on LiNbO<sub>3</sub> substrate (n=5) (\*\*p<0.05)

This tuneable feature of SFIDTs allowed creating spatial patterns at 3.4MHz and 6.4MHz respectively in 5% GelMA concentration for 1D patterning and at 4.6MHz 2D patterning without the assistance of any fluid flow and turbulence. Hence this feature of non-invasive manipulation of cells using acoustics has been used for cardiac tissue engineering application.

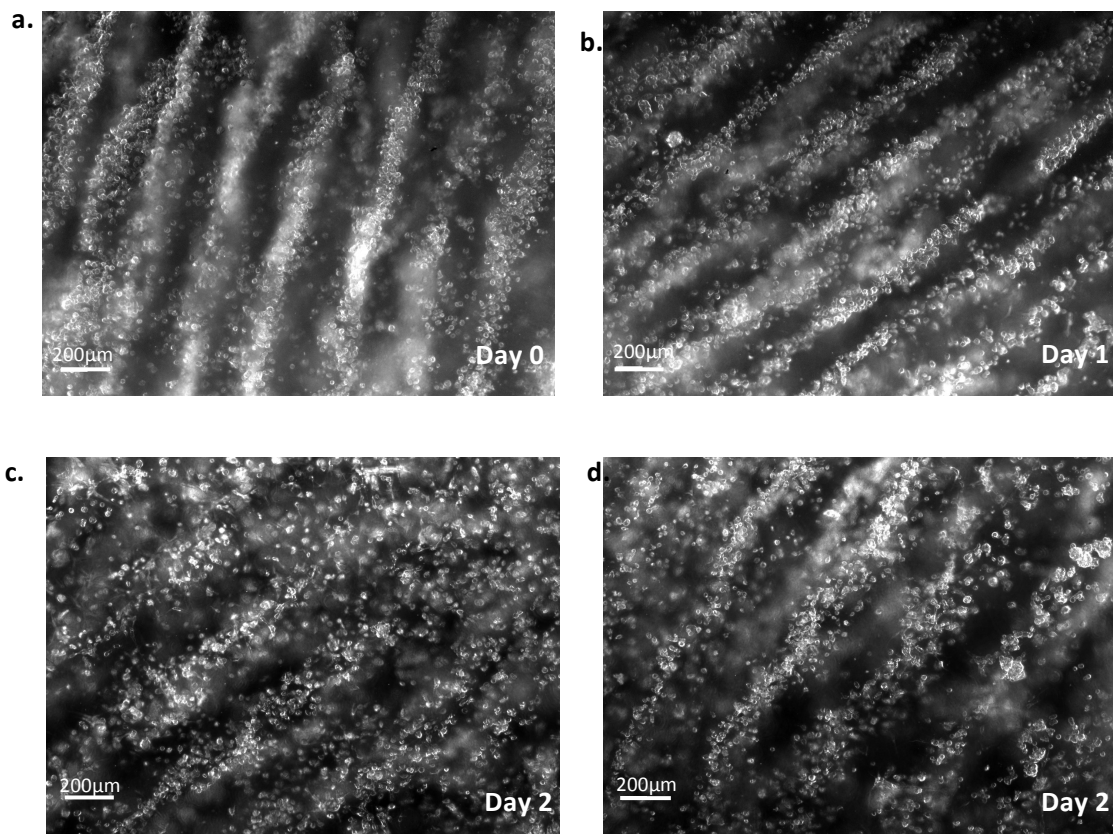


Figure 5.17, shows the phase contrast images of the patterned co-cultured cardiac fibroblasts and cardiomyocytes in 5% GelMA concentration at frequency 3.4MHz 180mW in the photo crosslinked hydrogel. a) patterning on day 0 of experiments, b) patterning on day 1 on post

culture, c, d) show the dislodgement of cells from the alignment positions on day 2 of the culture. (Scale bar 200 $\mu$ m)

In order to obtain a network of cardiac myofibers that promote cell-cell communication and exhibit synchronous and uniform contractions the cells must retain their position of alignment in the post culture period, i.e. the patterning must have high long term fidelity. It was noted that cells that were patterned at 3.4MHz in 5% GelMA scaffold displaced from the original node location to random locations by day 2. However this was not observed when cells aligned using SSAWs with input frequency of 3.4MHz (Figure 5.17). The spatial alignment thickness and gaps for waves traveling at 6.4MHz was lower than the 3.4MHz therefore resulting in more number of alignment nodes at the standing wavelength pressure nodes. This allowed rapid movement of cells to the closest node that created thinner alignment of cells and therefore retained the position of the alignment in the photo crosslinked polymer even on day 3 of the culture (Figure 5.18).

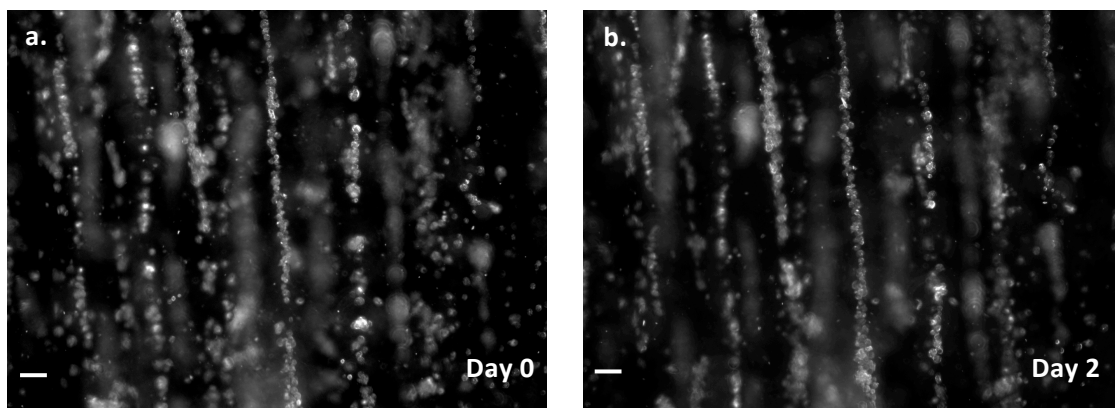


Figure 5.18, shows the maintained alignment of cardiomyocytes and cardiac fibroblasts cells in 3D scaffold of 5% GelMA at 6.4MHz even on, a) day 0, b) day 2 of the cell culture. (Scale bar 200 $\mu$ m)

## 5.8 SAW compared with DEP technique

Lab-on-a-chip techniques have emerged as useful tools in tissue engineering and biological applications. Surface acoustic waves can be used in conjunction with competing or complementary force-fields. A number of different applications combining acoustic waves with gravitational fields, hydrodynamic forces, electric field, magnetic and optical forces have been mentioned [169]. Dielectrophoresis technique has been largely exploited for manipulating particles such as cells, DNA and proteins in microfluidic system. Under dielectrophoresis particles suspended in the medium experience induced polarization due to different dielectric characteristics of the cell membrane, when an AC electric field is applied (Figure 5.19). The work mentioned here discusses employing the conventional DEP platform where if particles become more polarized than surrounding medium the induced dipole will align them with the electric field and hence particles move towards region of high field strength, due to positive DEP (p-DEP). On the other hand, if particles are less polarizable than the surrounding medium the induced dipoles will align against the applied field and the particles will move towards region of lower field strength due to negative DEP (n-DEP).

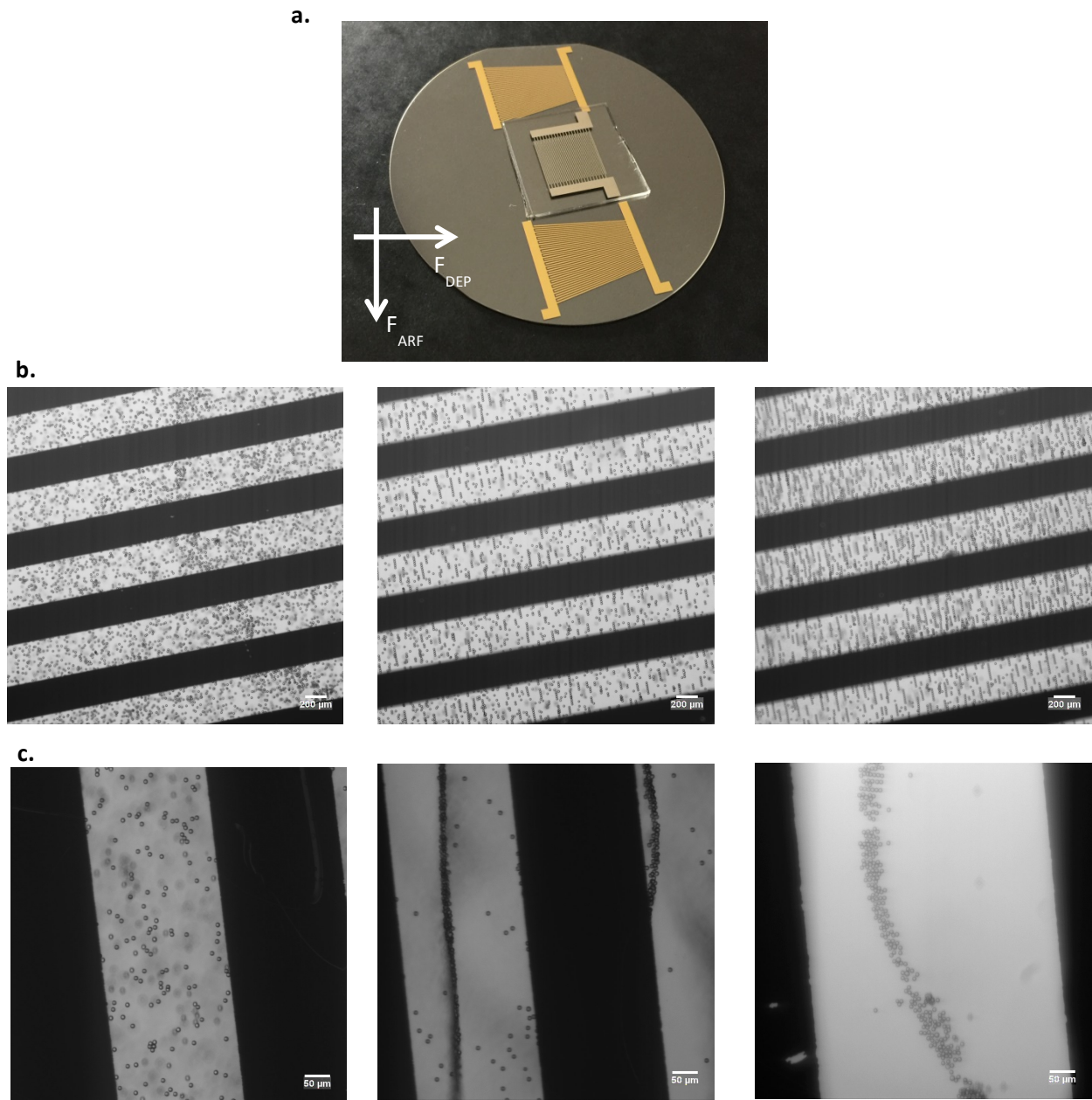


Figure 5.19 a) shows microfabricated gold SFIDTs on LiNbO<sub>3</sub> substrate and titanium deposited DEP IDTs on a glass slide (1mm) which acts as a superstrate on the piezoelectric substrate when coupled using an ultrasonic gel. The SAWs excited at complementary to the DEP in the region of interest. Both the DEP and ARF depend on the radius of the particle, b) shows random dispersion of polystyrene beads in the buffer medium of 8mS/m conductivity at pH 7.2. When the SAWs are generated at 3.4MHz beads align at the closest pressure nodes. Upon turning ON the DEP device at 10Vp-p, 3.8MHz the beads exhibited n-DEP .c) When the SAWs are generated at 3.4MHz the beads align at the pressure nodes as shown and when an AC voltage of 10Vp-p at 60KHz is applied the beads were aligned orthogonal to the IDTs exhibiting p-DEP.

The work described here using this arrangement of two different transducers employing mechanical and electrical forces can be used for investigating single cell properties and micro-patterning cells. However, certain hurdles were faced when integrating DEP technique for patterning cells. Firstly, DEP forces tend to be invasive forces travelling and polarizing the cell membrane. Secondly, this technique depends on the conductivity of the medium unlike SAWs which do not depend on the medium constituents and are non-invasive. Finally, to pattern the cells with high fidelity and preserve the alignments, the cells in hydrogel scaffold were placed in direct contact with the electrodes this caused the degradation of hydrogel due to a heating effect and also caused the cells that settled towards the bottom of scaffold to adopt a pattern. The objective of this work was to develop a novel platform for cardiac tissue engineering that would allow quick and efficient micro-patterning of cells in a small succession of time without any pre-treatment of either the substrate or scaffolds. Although the DEP technique can be used for alignment cells by manipulating medium conductivity, input AC signal, and width of the IDTs, it was noticed that by using SFIDTs there is more control over spatial cell manipulation regardless of the medium only by tuning wavelength of the waves generated on the piezoelectric substrate. This platform provides a clean and efficient method for manipulating cells in 3D hydrogel scaffolds without altering the native state of the cells. The implementation of this device allowed precise transport of cells with controllable spatial distances that facilitated investigations to develop engineered cardiac tissue construct by addressing problems such as spatial regulation of cells in 3D microenvironments.

## 5.9 COMSOL Multiphysics Simulations for SAW and DEP forces

### 5.9.1 Modelling SAW forces

The area between the SFIDTs on the piezoelectric substrate is very sensitive to surface perturbation. To understand underlying mechanism of wave propagation theoretical models have been developed to analyse SAW devices [170]. Acoustic wave sensors are categorized as bulk acoustic wave sensors (BAWs) and surface acoustic waves sensors (SAWs). SAWs have the ability to generate cell patterns in 3D space unlike BAWs. COMSOL Multiphysics version 5.0 was employed to model and simulate the pressure nodes of the acoustic waves in the hydrogel for all the simulations using frequency domain approach (Figure 5.20). The material properties of  $\text{LiNbO}_3$  used are characterized in previous studies [171]. The material parameters corresponding to the structures defined in the model have been tabulated in chapter 3. By using particle tracing module, cell movements were simulated under the influence of acoustic pressure waves in the GelMA hydrogel in x-z axis (Figure 5.21). For top-view simulations (x-y axis) and side-view simulations (x-z axis), the hydrogel was excited by defining acceleration on the walls in frequency domain and particles were subsequently traced to track motion of cells to visualize and study the force and velocity acting on them at the corresponding pressure node (Figures 5.20, 5.21, 5.22). When a standing ultrasound waves is established in the chamber the cells are subjected to two opposing forces : the acoustic radiation force from the scattering of sound waves on the cells and the Stokes drag force from the induced acoustic streaming flow.

Figure 5.20 displays numerical modeling in a cross section of GelMA demonstrating cell manipulation by ARF in the described setup. Due to boundaries of the PMMA channel, the transferred waves reflect off the boundaries, creating rectangular standing waves. These pressure fields lead into the creation of the nodes and anti-nodes as shown in figure 5.20.

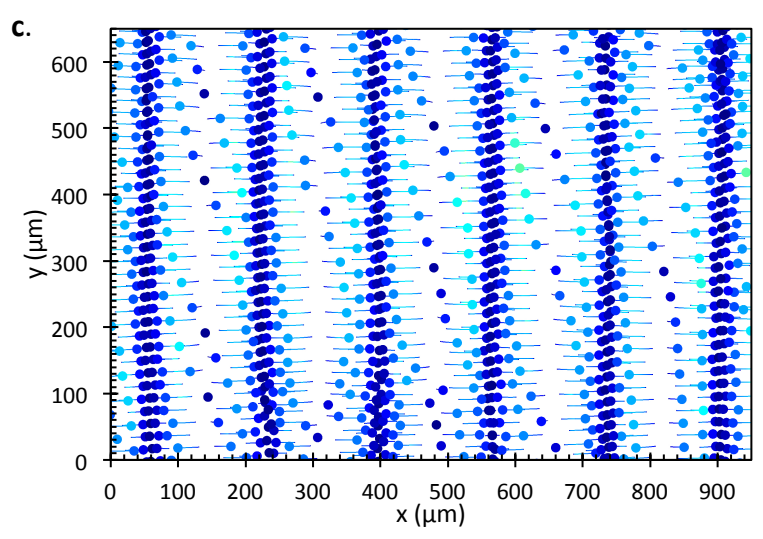
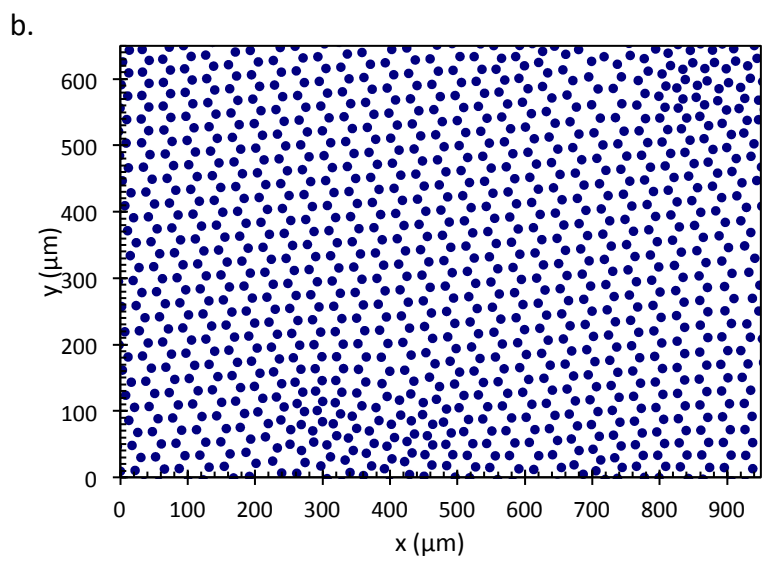
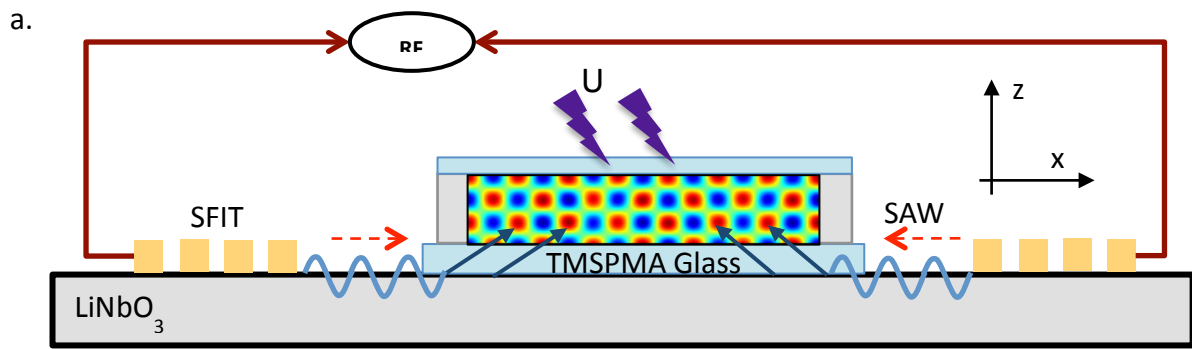


Figure 5.20, schematic representation of numerical modelling of ARF at 6.4MHz on  $\text{LiNbO}_3$  showing the dark and bright field regions of pressure and anti-pressure nodes, a) cross-sectional view of acoustic wave device setup used for patterning cells encapsulated in GelMA in the chamber, b) shows the random distribution of particles at  $t=0$  sec, c) shows the particle movement towards pressure nodes upon experiencing acoustic forces ( $t = 0.05\text{ms}$ )

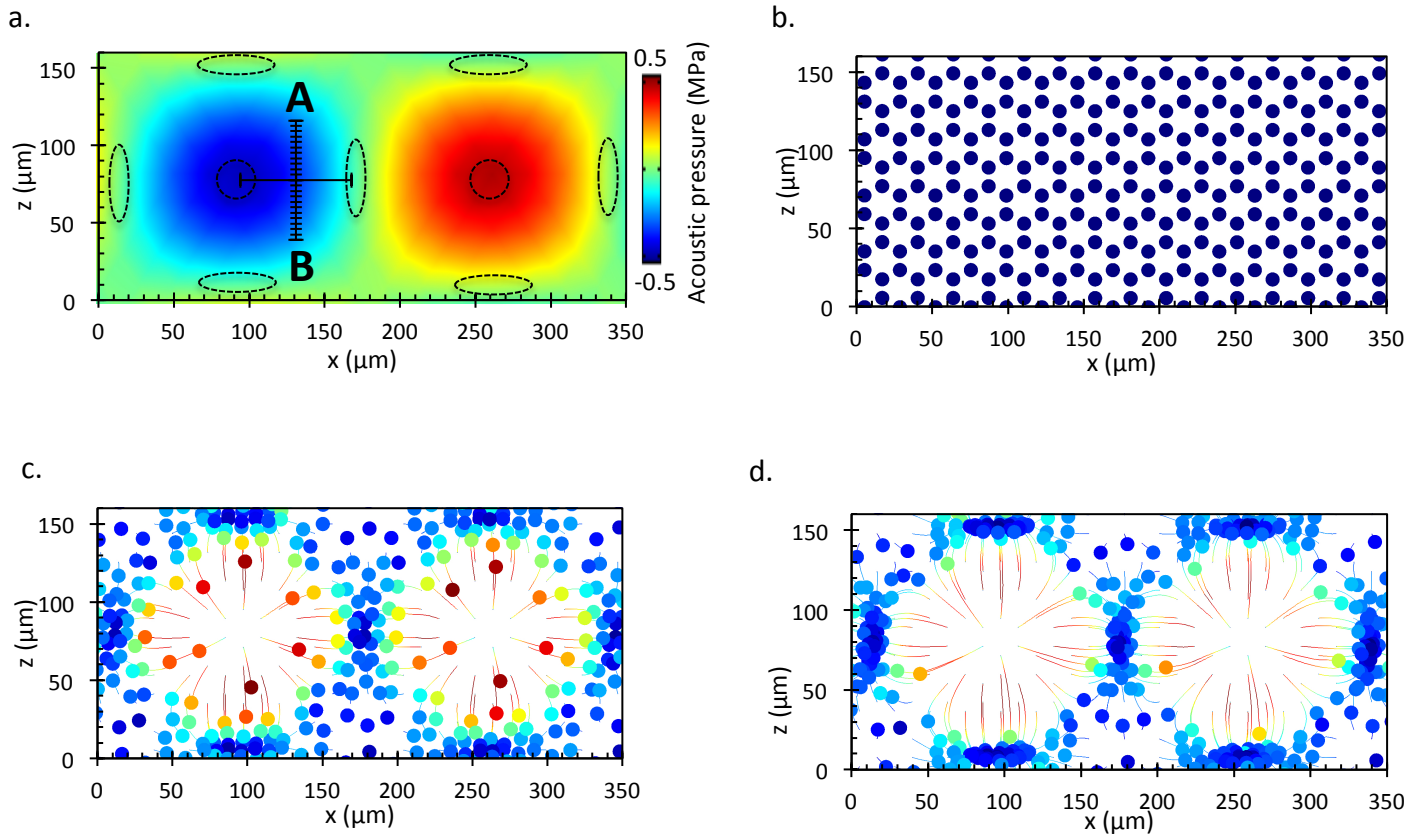
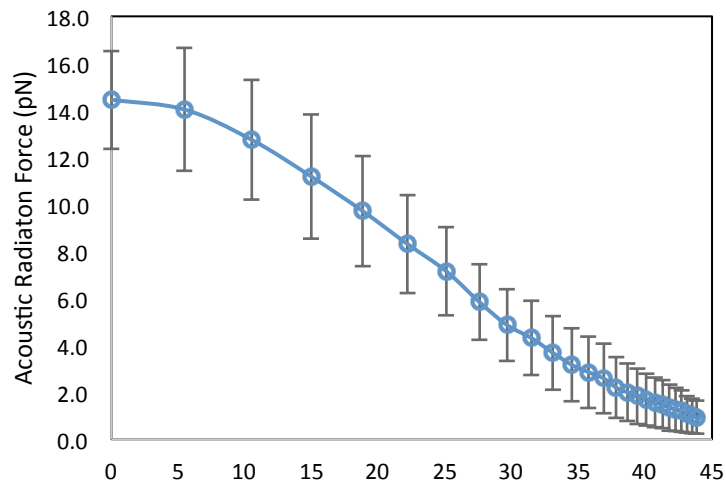


Figure 5.21, a) shows the z-axis of the acoustic pressure field creating pressure and anti-pressure nodes as demonstrated by elliptical and circular lines respectively which causes cells to move from one region to another as shown by midline A-B, b) shows the random dispersion of cells at time  $t=0$ secs, c, d) show the movement of particles toward the pressure nodes in 0.02 and 0.05 msec.

a.



b.

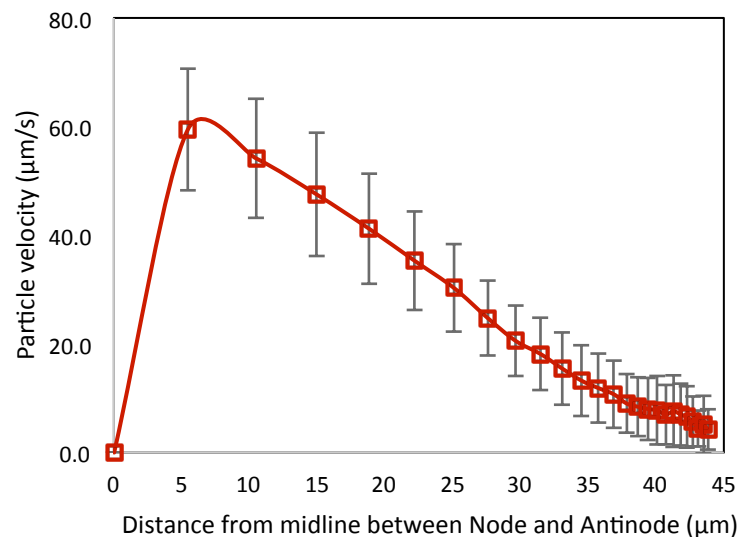


Figure 5.22, a) graph represent the acoustic force decreases as the cells approach the pressure node which is in similar terms with experimental data, b) represents velocity of the cells travelling towards the pressure and decreases in magnitude as it gets closer to it.

The cell alignment simulations from top-view have shown similar pressure and anti-pressure node distribution and by using particle tracing the particles moved to the pressure node under the same simulation parameters (Figure 5.23). In addition to investigating the capability of acoustic forces in 2D (Figure 5.24) using orthogonal transducers, simulations were carried out to model the complex experiments images on Multiphysics module.

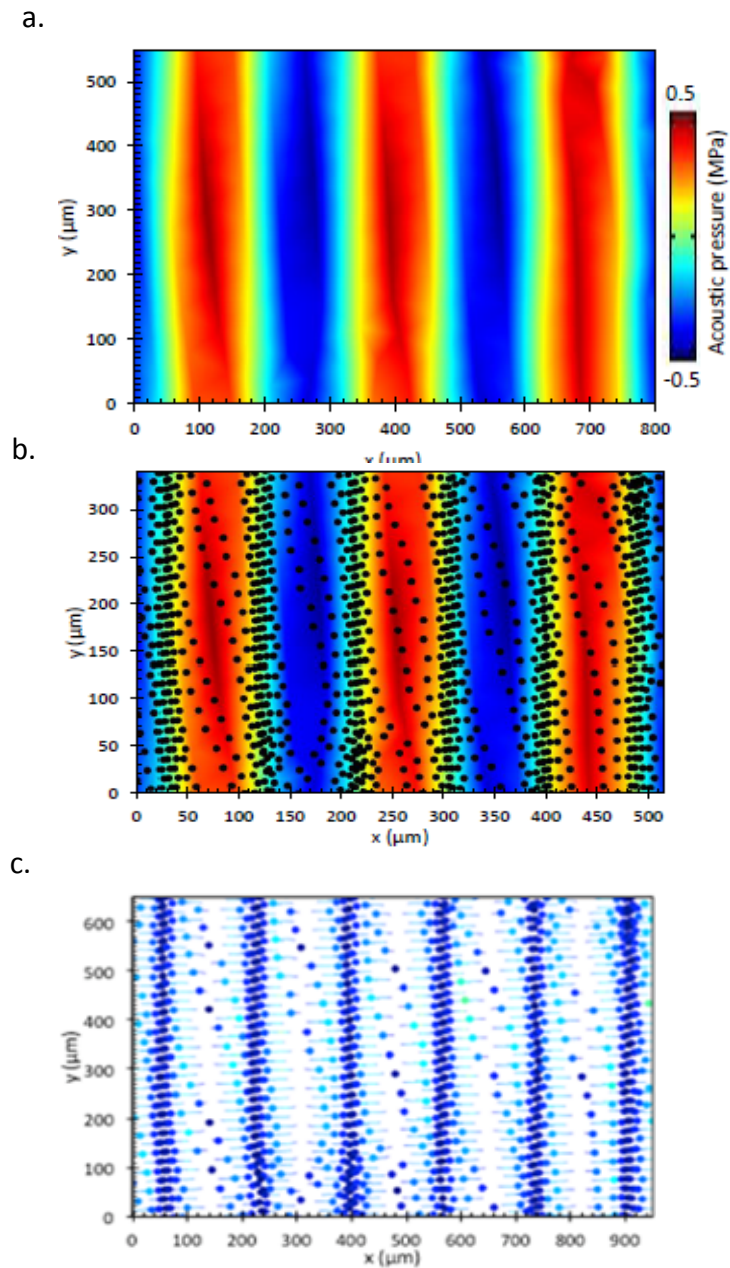


Figure 5.23, a) shows the pressure (red) and anti-pressure (blue) fields corresponding to SSAWs to create patterning of cells in the x-y axis and the movement of particles away from the anti-pressure nodes towards the pressure nodes at frequency 6.4MHz, b) shows the movement of particles moving to adjacent pressure fields, c) show the particles symmetrically aligning at the pressure fields as observed in a x-y axis plane.

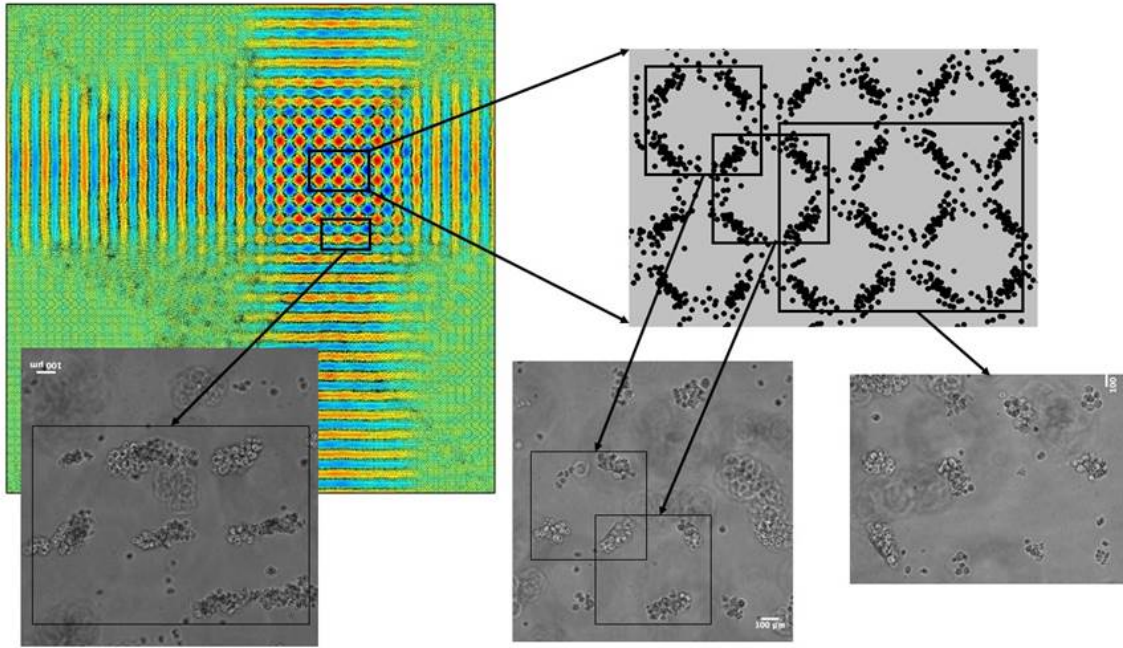


Figure 5.24, schematic representation of the simulation of 2D orthogonal acoustic waves generated at 4.6MHz and creating a 2D patterning due to standing waves which is corresponded with the complex patterns achieved during experimental visualizations using cardiac fibroblasts in 5% GelMA pre-polymer solution.

As hypothesized, the simulations confirmed that the cells encapsulated in the gel medium should be driven to the pressure node leaving behind empty space in the anti-pressure node region therefore creating spatial patterns. These data associated with 1D and 2D patterning serve as a strong proof of evidence that surface acoustic wave devices can be used to localize cells and create spatial patterns in hydrogel.

### 5.9.2 Modelling DEP forces

To simulate the DEP forces exhibited on particles a finite element model was designed in 3D using electrostatics module in COMSOL Multiphysics software 5.0a. This design simulates DEP forces spanning the height of the channel. The dimension of the chamber was set at  $500\mu\text{m} \times 150\mu\text{m} \times 50\mu\text{m}$  and input AC voltage of  $10V_{p-p}$  and frequency of 3MHz. The two electrodes are sufficient to analyse the DEP forces exhibited in the chamber. These standard IDT design have shown in previous studies to be highly efficient in selective separation of particles from a heterogeneous mixture using negative DEP ( $\text{Re}(CM) < 0$ ).

Using COMSOL Multiphysics software, the DEP force and gradient electric field ( $\nabla E^2$ ) is calculated by measuring the force at different heights in the chamber, 40 $\mu\text{m}$ , 20 $\mu\text{m}$  and 10 $\mu\text{m}$ . The design of the 3D geometry electrodes were spaced at 50  $\mu\text{m}$ , had width of 50 $\mu\text{m}$  and thickness of 120nm. The following Table shows the constants and equations used in the electrostatics module,

Table 5.1: Constants and Equations used in Electrostatics Module in COMSOL Multiphysics

<i>Description</i>	<i>Abbreviation</i>	<i>Value</i>	<i>Unit</i>
Radius	R	5e-6[m]	m
Free space permittivity	Ep	8.854e-12[F/m]	F/m
Cell permittivity	Ec	60*Ep[F/m]	F/m
Claussius-Mossotti Factor	Cm	-0.5	
Applied voltage	V	10[V]	V
Frequency of the electric field	F	3[MHz]	MHz
DEPForce-x-axis	DEPX	$2*3.14*Ep*Ec*R^3*Cm*d(\text{normE\_es}^2,x)$	N
DEPForce-y-axis	DEPY	$2*3.14*Ep*Ec*R^3*Cm*d(\text{normE\_es}^2,y)$	N
DEPForce-z-axis	DEPZ	$2*3.14*Ep*Ec*R^3*Cm*d(\text{normE\_es}^2,z)$	N
DEPForce	DEP	$\text{sqrt}((\text{DEPX}^2)+(\text{DEPY}^2)+(\text{DEPZ}^2))$	N
GradE <sup>2</sup> -x-axis	GradE2X	$d(\text{normE\_es}^2,x)$	V <sup>2</sup> /m <sup>3</sup>
GradE <sup>2</sup> -y-axis	GradE2Y	$d(\text{normE\_es}^2,y)$	V <sup>2</sup> /m <sup>3</sup>
GradE <sup>2</sup> -z-axis	GradE2Z	$d(\text{normE\_es}^2,z)$	V <sup>2</sup> /m <sup>3</sup>
GradE <sup>2</sup>	delE2	$\text{sqrt}(\text{GradE2X}^2+\text{GradE2Y}^2+\text{GradE2Z}^2)$	V <sup>2</sup> /m <sup>3</sup>

The simulated model shown in Figure 5.25 shows the DEP force produced in the chamber on a log scale in order to amplify the very small scale of the force. The number of mesh elements exceeded 250,000 due to the 120nm thickness of the electrodes which caused the simulation times to run longer than 150mins.

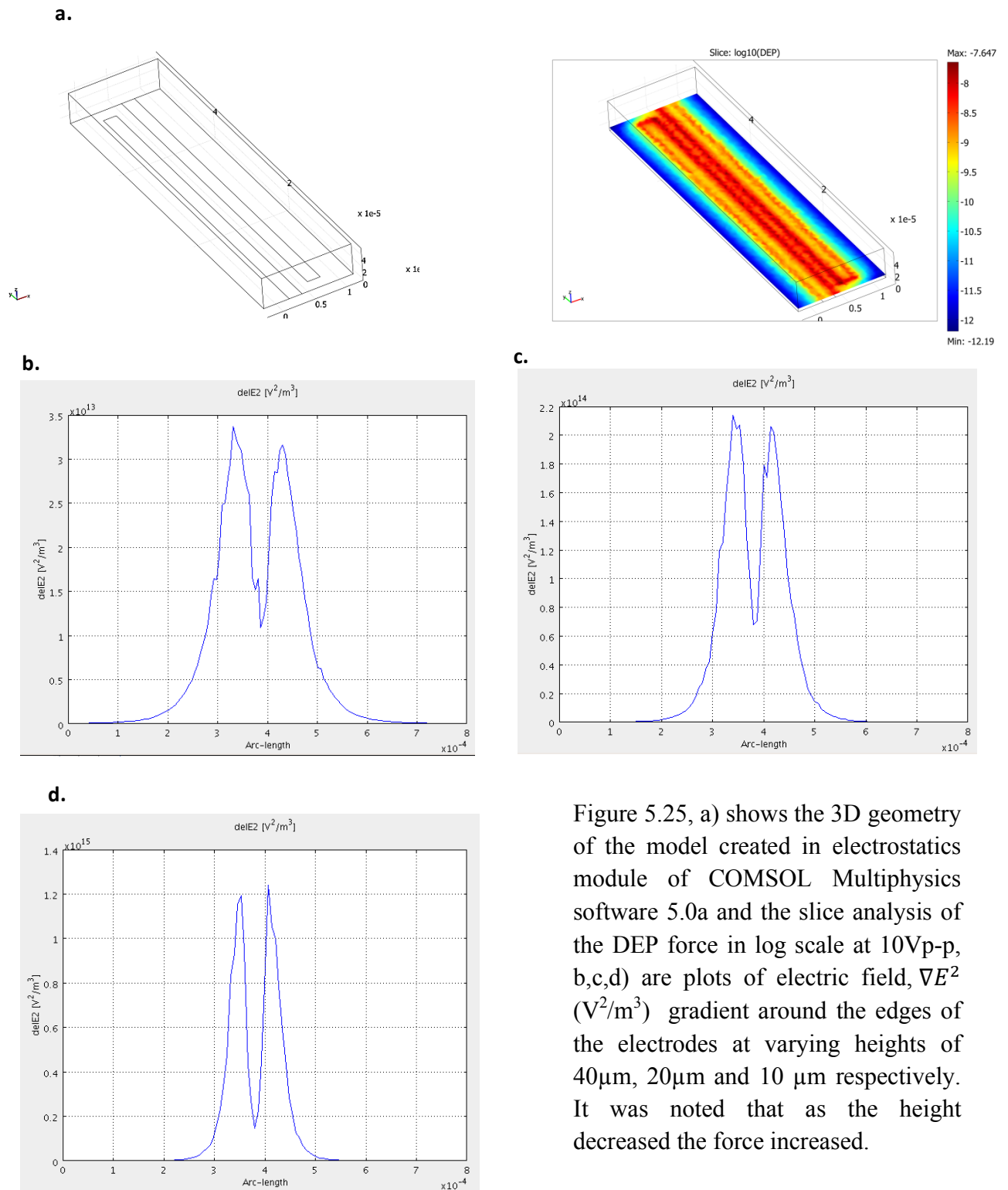


Figure 5.25, a) shows the 3D geometry of the model created in electrostatics module of COMSOL Multiphysics software 5.0a and the slice analysis of the DEP force in log scale at 10Vp-p, b,c,d) are plots of electric field,  $\nabla E^2$  ( $V^2/m^3$ ) gradient around the edges of the electrodes at varying heights of 40 $\mu$ m, 20 $\mu$ m and 10  $\mu$ m respectively. It was noted that as the height decreased the force increased.

These DEP IDTs produce non-uniform electric field through the length of the chamber. The approximate electric field gradient was calculated to  $77.14 \times 10^{15} (\text{V}^2/\text{m}^3)$ . The DEP force was found to be in the range of  $10^{-11}$  to  $10^{-12}$  N. These forces are comparably higher than ARF and are invasive to the cell due to sinking of cells in hydrogel because of gravity closer to the IDTs. DEP patterning is strong when the cells are closer to the electric field region with high intensity which is nearer to the IDT electrodes. As a result ARFs provide a platform that does not depend on conductivity of the medium or require for the cells to be in close proximity with the electrodes in order to create spatial patterns.

## 5.10 Conclusion

This Chapter has demonstrated the development of microfabricated SAW devices using SFIDTs patterns on  $\text{LiNbO}_3$  according to the standard cleanroom protocols. This platform has been shown to be a tuneable non-invasive technology for organizing cells in engineered hydrogel, GelMA. Under appropriate conditions, 3.4MHz and 6.4MHz were used to create SSAWs using two identical oppositely designed pair of electrodes. These were then tested and measured using network analyser, IR camera and LDV to determine the working resonance frequency, power, and aperture of the beam. The Chapter also shows the setup used to carry out the experiments by creating SSAWs to pattern cells and quantifies the forces acting on the cells. The design of the chamber was critical in this work since SAWs can generate turbulence and streaming effects. Thus, by designing and testing the device at different frequencies and power levels measured using a network analyser, it was concluded that 3.4MHz and 6.4MHz waves generated from the pair of identical SFIDTs at 180mW created parallel cell alignment patterns. In order to employ complex 2D patterning, 4.6MHz was used by orthogonal SFIDTs at 220mW. The waves exhibited larger forces in less viscous fluids like buffer solution as compared to GelMA hydrogel which satisfies the theoretical formulae.

In addition the acoustic forces also depend on the properties of the particle that come in contact with it such as density and diameter. It was noted that the larger sized particles felt higher acoustic waves than smaller sized particles. Out of many advantages of SAW based devices, one unique advantage is the controllability of the spatial pattern over cells. By tuning the frequency using SFIDTs, the results have shown spatial patterning of cells corresponding to the input wavelength generated at 3.4MHz and 6.4MHz. However, to maintain the high

fidelity, 6.4MHz acoustic waves were preferred to create standing 1D patterning. Moreover, a comparative study was conducted by employing another LOC technique called dielectrophoresis that has been widely used for particle manipulation. Although both the techniques depend on the dimension of the particle, there are lots of differences in experimental conditions.

In particular, the DEP technique requires a specific medium conductivity, width and geometry of electrodes and requires a settling time for the particles to reach the bottom of the substrate before applying an input AC signal. This causes the cells to be in close vicinity of the electrodes which can be harmful. It already known that DEP forces are invasive forces so this gives another advantage of using SAW based device that provides more controllability to manoeuvre particles spatially to create patterns.

Finally using COMSOL Multiphysics software, this chapter has shown numerical models of SAW and DEP devices that generate forces to manipulate particles under experimental conditions and represent experimental data. Thus, SSAWs created on the LiNbO<sub>3</sub> wafer were specifically designed to pattern cells spatially without creating turbulence and streaming to meet and address the current challenges faced in tissue engineering.

## **Chapter 6**

### **Cardiac Tissue Engineering using SAWs**

#### **6.1 Introduction**

Tissue engineering provides an approach for creating functional cardiac patch for the purpose of healing scars after myocardial infarction since the heart is a non-regenerating organ. Cardiac cells are seeded into scaffolds that provide artificial biomechanical support. Cell micro-patterning using surface acoustic wave is a powerful technique to control cell position in a hydrogel scaffold. In this chapter, gelatin methacrylate (GelMA) hydrogel has been synthesized as an inexpensive, cell-responsive matrix to create cell-laden 3D engineered tissue constructs that mimics the natural behaviour of tissues and ultimately allows the heart to beat in a synchronous manner. Cardiac fibroblasts and cardiac myocytes isolate from neonatal rats were encapsulated in different concentrations of GelMA before patterning them at 3.4MHz and 6.4MHz to create spatial alignments before UV light photo polymerization. The responsive behaviour of cells such as beating of the network of patterned cells was investigated analysed over the consecutive culturing days. Finally, the cell morphology was investigated to visualize the formation of cardiac myofibers to promote cell to cell communication through gap junctions and sarcomeres for excitation-contraction using immunostaining techniques.

#### **6.2 Micropatterned 3D heart constructs in GelMA using standing-surface acoustic waves**

Cell fate such as proliferation, migration, differentiation and apoptosis are important things to be determined when establishing a 3D microscale patterned scaffold in making functional tissue constructs. The patterning approach followed here is the use of SAWs. This technique has characteristics for manipulating cells with high accuracy, efficiency, speed, scalability and ability to handle adherent and non-adherent cells. 3D cardiac micro-tissues scaffolds were created by cardiomyocytes and cardiac fibroblasts which are the main cellular constituents of a native myocardium. To successfully use micropatterned cells in GelMA hydrogel suitable for cardiac tissue engineering applications, encapsulated cardiac fibroblasts and cardiomyocytes in a 1:1 ratio were investigated in high methacrylation degree GelMA matrix prepared under different concentrations. The geometries of the construct was precisely

controlled and assessed for their role on synchronous contraction of cells in 3D culture. As compared to monoculture cardiomyocytes, those here exhibit a native like phenotype when co-cultured with cardiac fibroblasts. Figure 6.1, illustrates the device setup from micro-patterning the cells using SSAWs, to photo-crosslinking to culturing the 3D scaffolds in cell culture media.

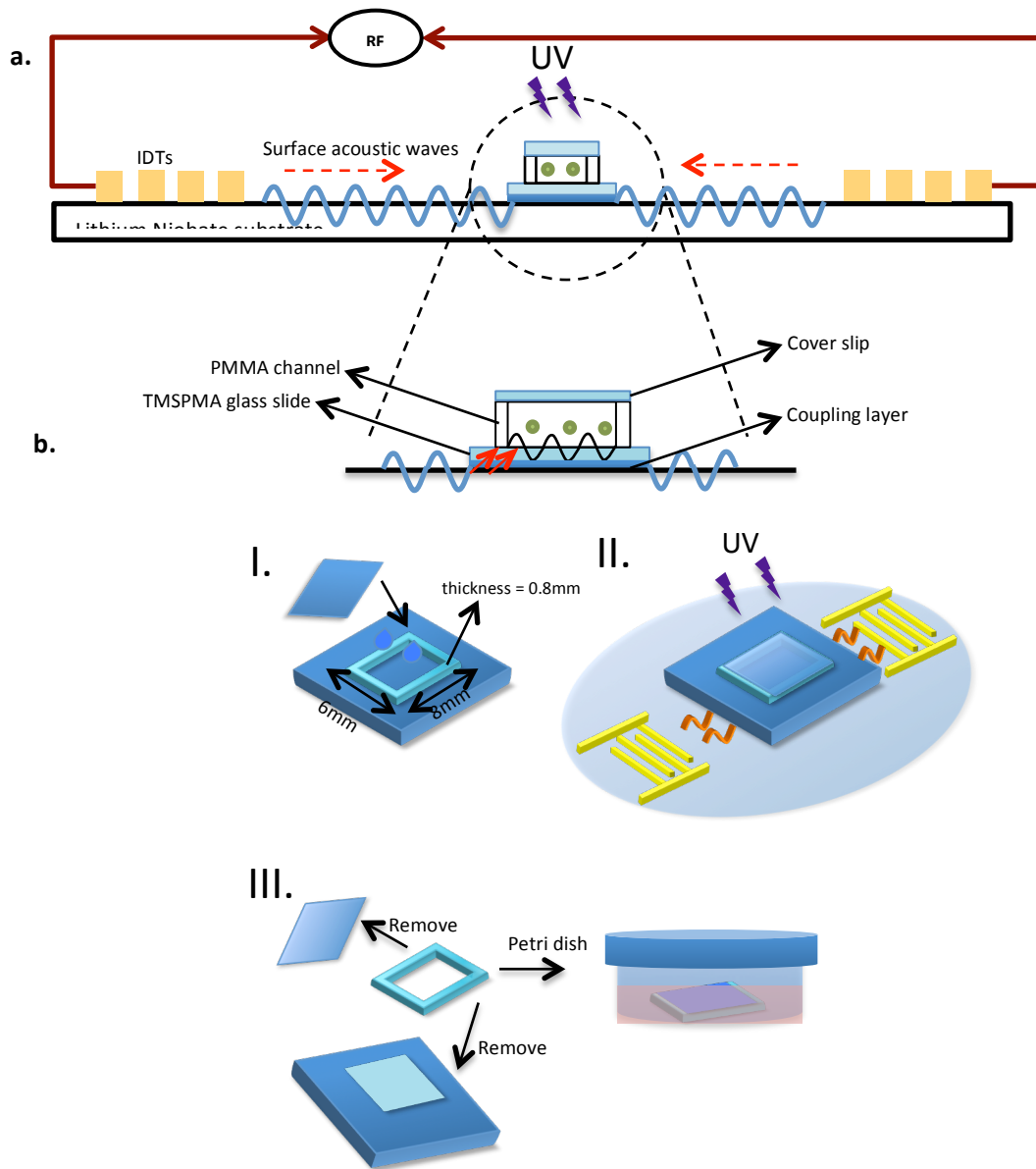


Figure 6.1, schematic representation of the experimental setup, a) shows the generation of SSAWs on  $\text{LiNbO}_3$  substrate by SFIDTs. The input frequencies applied in this work are 3.4MHz and 6.4MHz at 180mW. The SSAWs integrate in to the PMMA chamber of 0.8mm thick on top of 1mm thick TMSPPMA glass slide (superstrate) filled with cell encapsulated in the hydrogel

The SSAWs travel in to the GelMA scaffold held between a PMMA chamber through a coupling layer of water. The waves are reflected back into the hydrogel after bouncing from the cover glass to create standing waves in the matrix. Figure 6.1 shows step by step representation of plating one hydrogel scaffold in cell culture media after patterning. Figure 6.1 (a) show the dimensions of the chamber placed on TMSPPMA coated glass slide of 1cmx1cm and 45 $\mu$ l droplet of cell encapsulated GelMA was added before placing the cover glass on top. The chambers were then placed on the LiNbO<sub>3</sub> substrate and coupled using a 2 $\mu$ l of water at the centre region from the opposite of SFIDTs. An input RF signal was applied to generate the SSAWs to pattern the cells at different frequencies and then the hydrogel was photo-crosslinked under UV light for 15 secs to polymerize the chains. Figure 6.1 (c) shows the after UV illumination step were the cover slip and PMMA structure are carefully removed to expose the 3D hydrogel scaffold directly in contact with the cell media. The standing structure of the rectangular construct of the hydrogel after UV photo-crosslinking is shown in Figure 6.2.

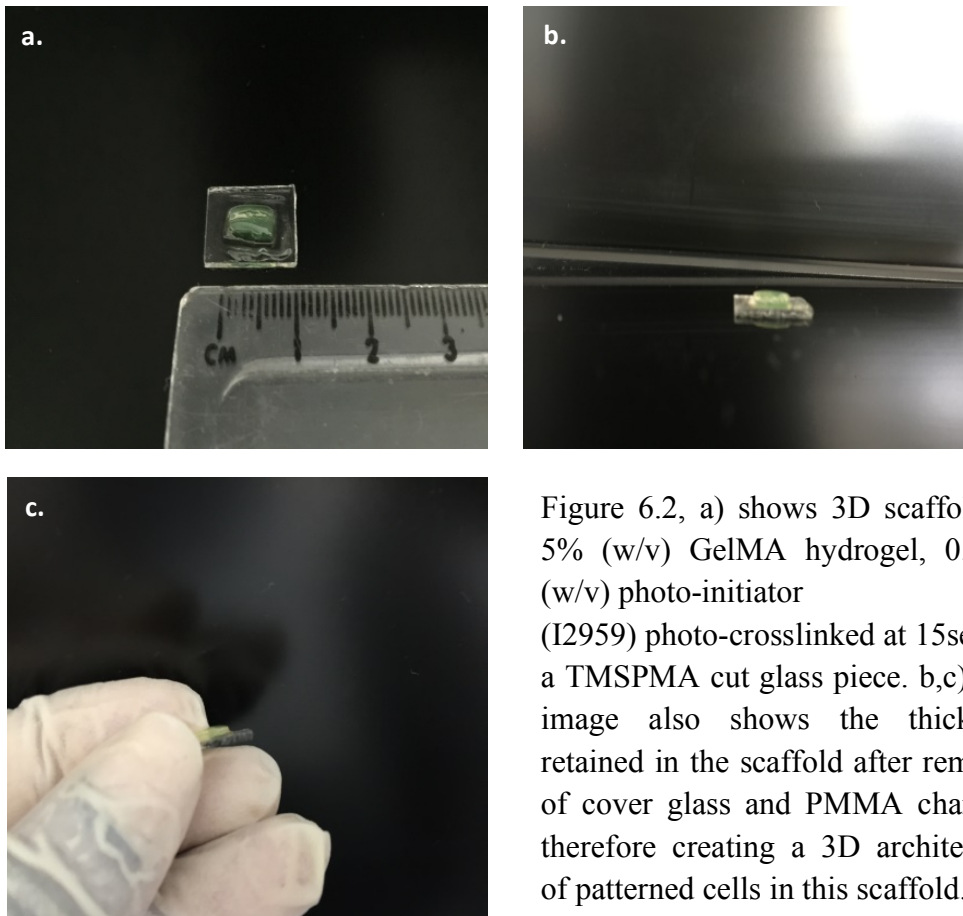


Figure 6.2, a) shows 3D scaffold of 5% (w/v) GelMA hydrogel, 0.25% (w/v) photo-initiator (I2959) photo-crosslinked at 15sec on a TMSPPMA cut glass piece. b,c) The image also shows the thickness retained in the scaffold after removal of cover glass and PMMA chamber therefore creating a 3D architecture of patterned cells in this scaffold.

For each scaffold prepared, 45 $\mu$ l of un-polymerized GelMA hydrogel encapsulating cardiac fibroblasts and cardiomyocytes was added to the PMMA chamber on the superstrate. The population of cells used was 1-1.5million cells/ml of cardiac fibroblasts to 1-1.5million cells/ml of cardiomyocytes to total of 2-3million cells/ml. The samples were then exposed to SSAWs at 3.4MHz and 6.4MHz at 180mW which created different spatial patterning distance between the alignments with respect to the wavelengths generated. No pre-treatments of cells, PMMA chamber, LiNbO<sub>3</sub> was required and all the experiments were conducted at 37°C incubation chamber attached to the Zeiss light microscopy (Axio Observer Z1). The same microscopy equipment was used for live-imaging of cells in the 12-well cell culture plate. Due to the low viscosity (0.09cm<sup>2</sup>s<sup>-1</sup>), pore size and elasticity 5% GelMA concentration easily integrated standing surface acoustic waves at the two wavelengths and preserved cell pattern with high fidelity (Figure 6.3).

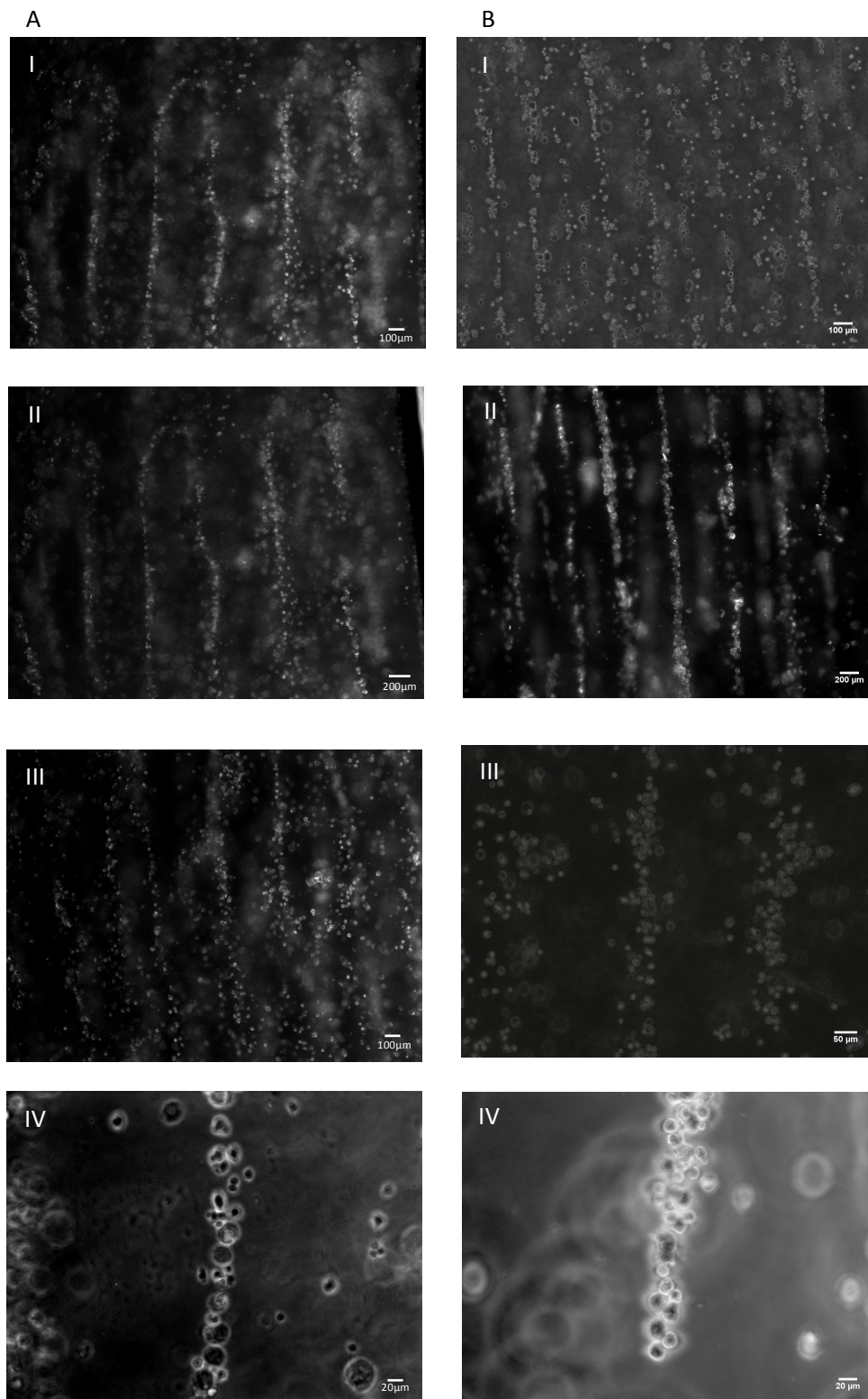


Figure 6.3, phase contrast images of cardiac fibroblasts. Column A shows the patterning of cardiac fibroblasts cells at 3.4MHz (180mW) in 5% GelMA (w/v) 3D hydrogel scaffold. The spatial distance corresponded with the theoretical wavelength of  $320\mu\text{m} \pm 10\mu\text{m}$  with assembling time of 1.5 secs (I) Alignment of cells before UV irradiance, (II) and (III) show alignment of cells after UV treatment, (IV) shows magnified image of single cell alignment. Column B shows patterning of cells at 6.4MHz at the input power show closer alignment of

cells due to the shorter wavelength of the generated waves. (I) alignment of cells before UV treatment, (II) show cardiac fibroblasts aligned at the pressure nodes of the waves before UV, (III) shows the single cell alignment between three pressure nodes, (IV) show magnified image of single cell alignment. Post exposure has shown increased fidelity of cells in the hydrogel.

Upon applying input RF signal to generate SSAWs on the LiNbO<sub>3</sub> substrate the acoustic energy is radiated into the hydrogel enclosed in PMMA chamber through a coupling layer of water resulting in pressure fluctuations that position the cells according to the wavelength of the waves generated. The entire assembly time from setting the sample on the substrate to patterning to UV exposure took approximately 3 mins for each sample. Figure 6.2 shows the optical microscope images of patterned cardiac fibroblasts and cardiomyocytes cells before and after UV exposure and quantified in Figure 6.4. The cardiac fibroblasts and cardiomyocytes aligned at the resonant frequencies of 3.4MHz and 6.4MHz respectively as shown. After turning off the SSAWs device and UV exposure, the assembled cell alignment patterns still remain intact and stable as shown (Figure 6.5).

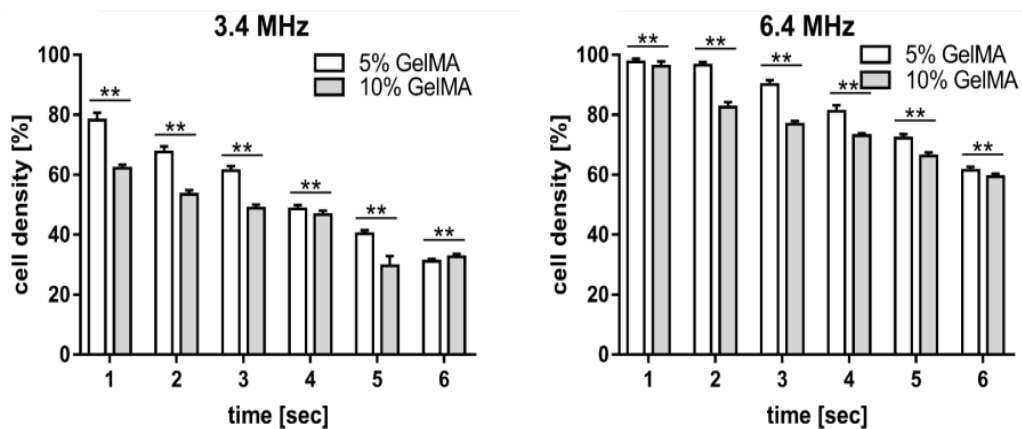


Figure 6.4 shows the cardiac cell density dependence on two different frequencies, 3.4MHz and 6.4MHz in 5% and 10% GelMA concentration hydrogel. a) The alignment time shows the dispersion of aligned cells after switching off the SAW device but without UV crosslinking in pre-polymer solution of 5% GelMA (n=5) (\*\*p<0.02)

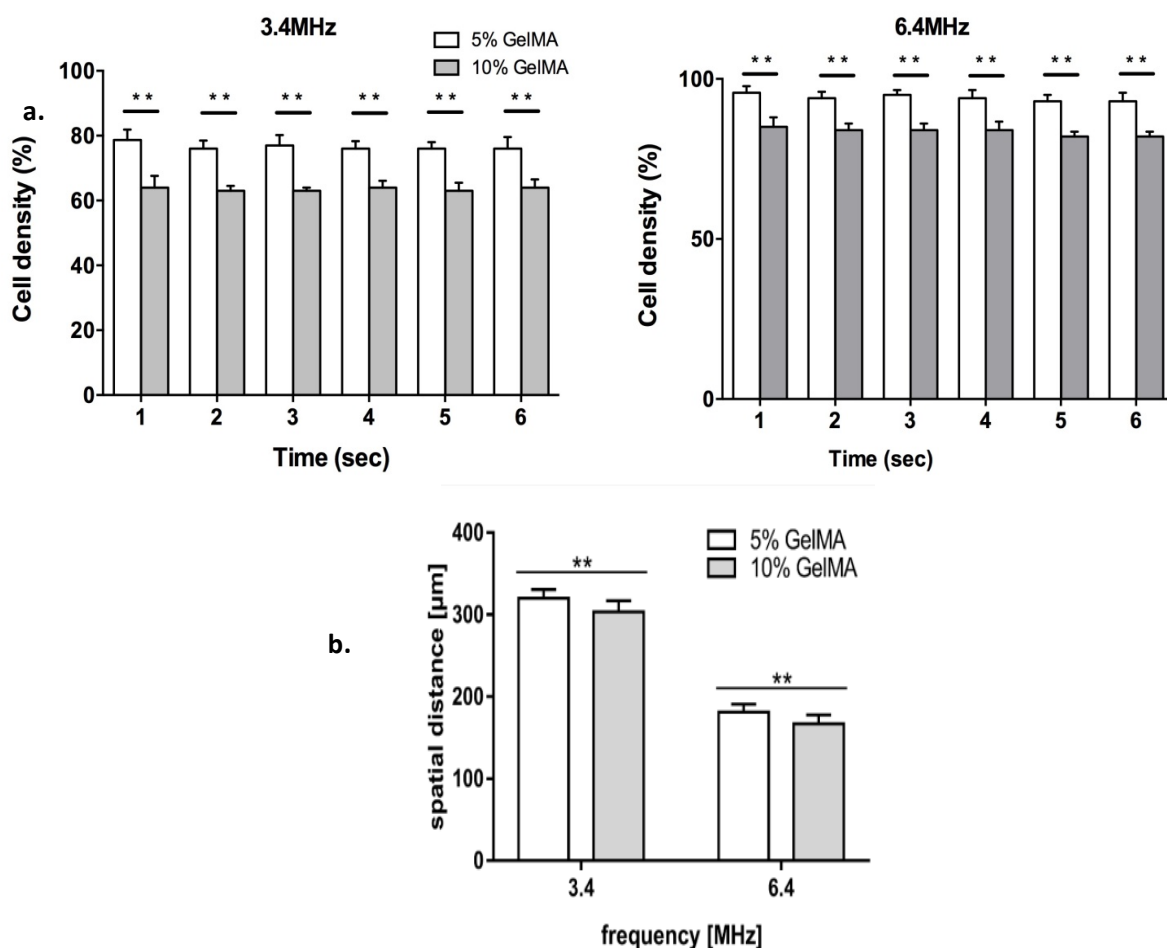


Figure 6.5 a) shows the intactness of the patterned cells after switching off the SAW device (3.4MHz and 6.4MHz) and crosslinked under a UV chamber for 12s, b) Shows the spatial distance of alignment of co-cultured cells in the hydrogel scaffold at different wavelengths of the acoustic waves generated using SFIDTs on the piezoelectric substrate in the pre-polymer solution of 5% GelMA (w/v) containing cardiac fibroblasts and myocytes (n=5) ( $p < 0.05$ ).

The percentage of cell density patterning with respect to applied frequencies were quantified using NIH ImageJ software and plotted in Figures 6.4, 6.5 for different concentrations of GelMA. SSAWs have shown better cell alignment in 5% GelMA as opposed to the 10% GelMA under the same conditions. This is due to the high viscosity of 10% GelMA, which has a denser network, smaller pore size and larger interconnected network of fibres that dampen the acoustic waves travelling into the medium. Also with 10% GelMA the efficiency of patterning for 3.4MHz waves was approximately 60% lower when opposed to the same concentration and patterning at a higher frequency of 6.4MHz. This frequency showed higher efficiency of cell density both before and after the UV treatment. After patterning the co-cultured cells encapsulated in different concentrations of GelMA, the scaffolds were exposed to UV light (360-480nm) for 12 – 15 sec to photo-crosslink the hydrogel. Due to the photo-

initiation effect the hydrogel fibres crosslinked causing the cells to remain intact in their aligned position during the culture period, as evident from the graphs above.

### 6.3 Live/Dead Analysis

After seeding the cells in the scaffold, the cardiac cell behaviour was inspected for days 1, 3, 5 and 7 in 5% GelMA concentration under different UV exposure rates (Figure 6.6).

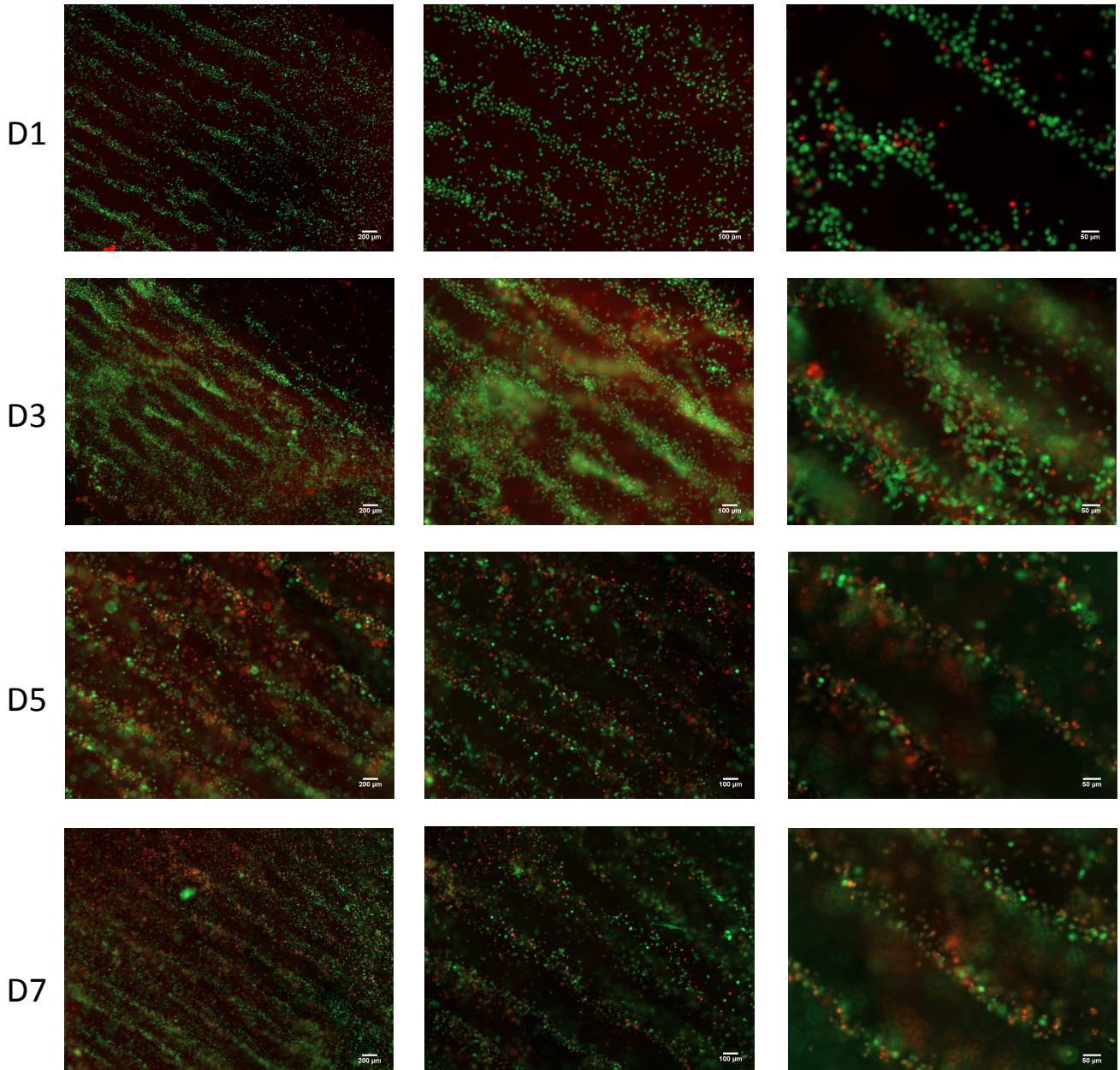


Figure 6.6, Show the viability of cardiac fibroblasts in the 3D construct of 5% (w/v) GelMA with 0.25% (w/v) photo-initiator (I2959) on consecutive days of cell culture in cardiac media. Live cells were stained with Calcein AM (green) and dead cells stained with ethidium homodimer (red). The hydrogel scaffold photo-crosslinked at 12sec under UV light.

In order to generate a functionalized engineered cardiac tissue it is necessary to encapsulate cells in the 3D micro-environment that promotes both viability and functionality.

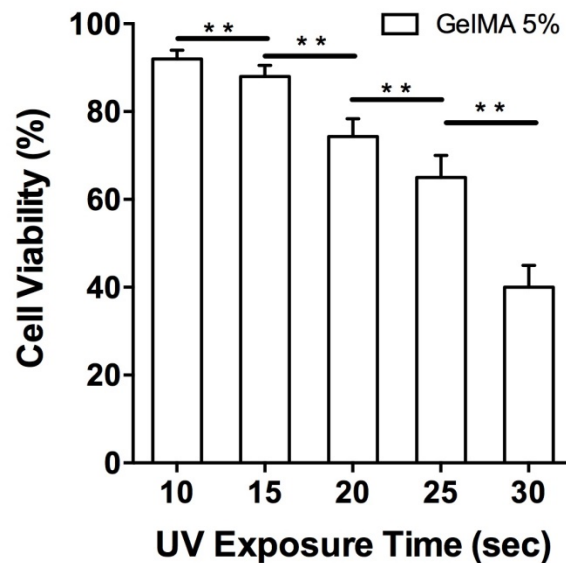


Figure 6.7 , shows quantification of percentage of viability of co-cultured cardiac fibroblasts and cardiomyocytes in 5% GelMA at different UV exposure rates for a period of 7 culturing days (n=5)(\*\*p<0.05)

The cellular viability in the engineered constructs in monoculture condition for seven consecutive days was assessed. Viability images shown in Figure 6.6 for 5% GelMA scaffold polymerized using 12-15 secs irradiation show higher viability than when exposed to 30s of UV light to photo-crosslink the hydrogel after culturing for five days. The overall cell viability quantified for 12-15 secs UV exposure was  $89.46\% \pm 2.83$  (n=3) within all the constructs (Figure 6.7). Cell proliferation of cardiac fibroblast cells in constructs were observed on day 5 under 15 secs UV exposure. It was envisioned that this would assist cardiomyocytes in establishing interconnected networks leading to formation of functional 3D microtissues. Cell viability also depends on the depth of the scaffold produced here in order to allow diffusion of oxygen and nutrients into the construct. The scaffolds had a height of approximately 800 $\mu$ m that allowed cells to be patterned at different heights within the scaffold and also allow transfer of necessary nutrients and oxygen when submerged in 1ml of cardiac cell media in a 12 well-plate.

## 6.4 Actin cytoskeleton Organization

Cellular alignments in the GelMA constructs were investigated by using F-actin and DAPI stained fluorescent images. As shown in Figure 6.8, cardiac fibroblasts and cardiomyocytes proliferated facilitating the alignments and formation of cardiac myofibers. The cells elongated along the alignments and created a strong network of micro-patterned cardiac fibers inside the hydrogel construct.

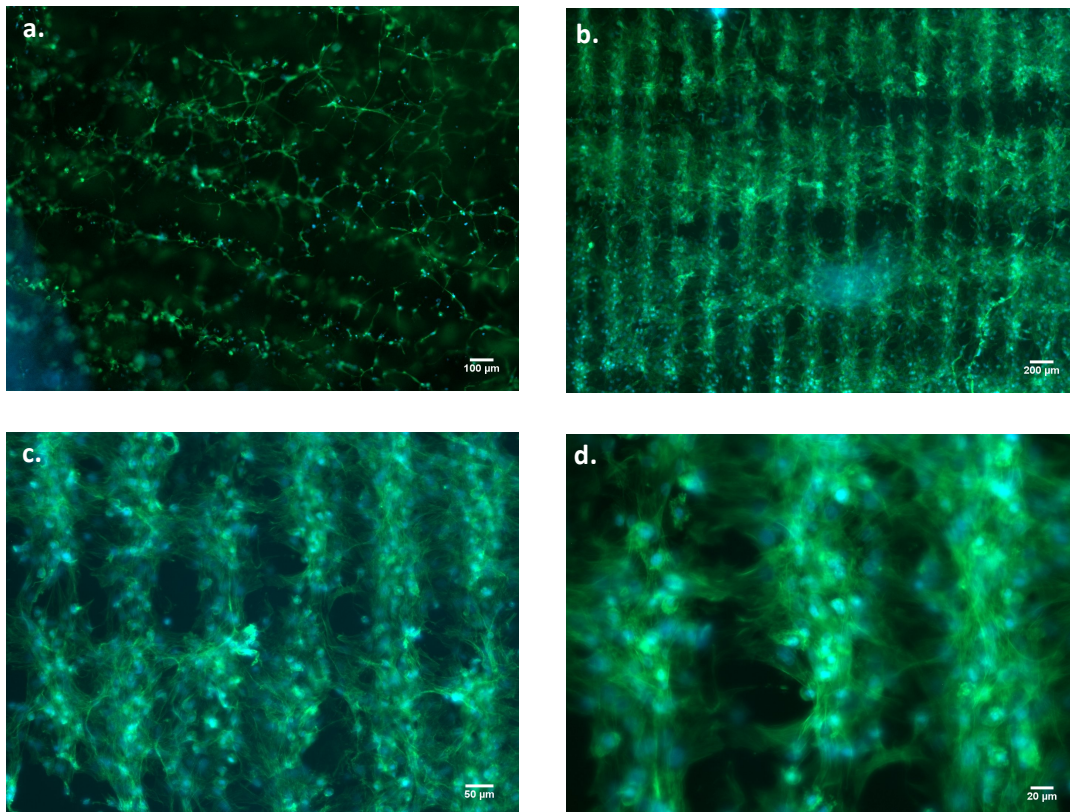


Figure 6.8, co-culture of cardiac fibroblasts and cardiomyocytes marked with F-actin and DAPI stains in 5% GelMA 3D scaffold micro-patterned at 6.4MHz, a) image of patterned stretching myofibers on day 5, b) cell alignment and proliferation can be visually seen on day 7 of culture along the patterns created, c) on day 9 cell expansion and adherence was observed with alignments intact, d) magnified image showing cell nucleus and f-actin fibre stretching and elongating along the patterns and spreading in the scaffold

Fluorescent images of the stained samples taken on day 9 of the co-culture have shown enhanced cell-hydrogel interaction. The cardiac fibres formed in the 5% GelMA concentration scaffold mimic the morphology of the native myofibers as in native heart tissue.

The expression of cardiac differentiation markers such as troponin I, sarcomeric  $\alpha$ -actinin and connexin 43 inside the GelMA constructs were evaluated on day 9 of the maturation period of

the cells. As shown in Figures 6.9, 6.10, 6.11, 5% GelMA (w/v) concentration 3D scaffold promoted the expression of troponin I in addition to connexin 43 and sarcomeric  $\alpha$ -actinin. Cardiac troponin T and I are regulatory proteins with high specificity of cardiac injury released immediately into the bloodstream. They are the preferred markers of myocardial injury. Troponin is a protein that is released from cardiac myocytes in an event of myocardial infarction, when the heart muscles face an irreversible damage.

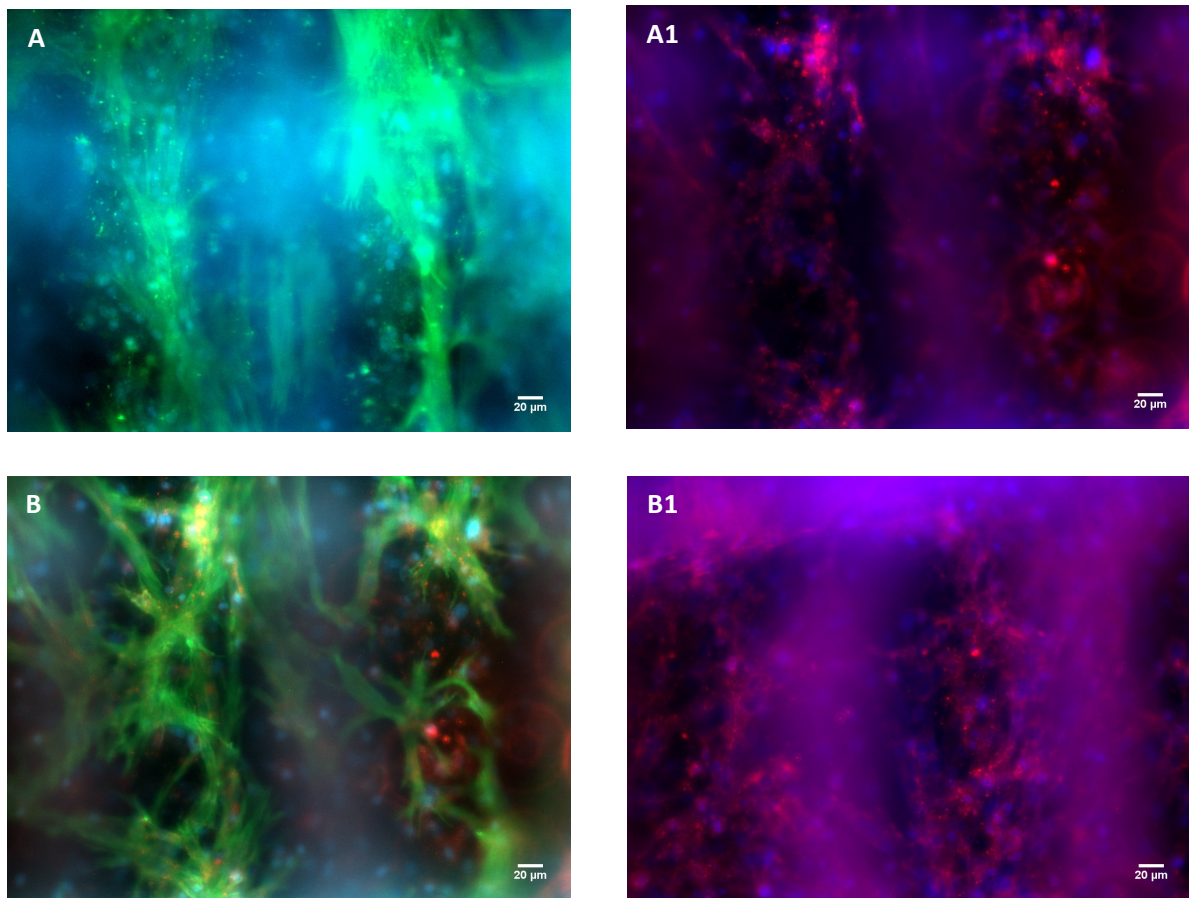


Figure 6.9 A, B) shows immunohistochemical staining to analyse protein expression of differentiating cardiac cells fixed with paraformaldehyde and permeabilised with 0.5% Triton X-100 in 3% paraformaldehyde and stained with Troponin I (green), Connexin43 (CX43) (red), Sarcomeric  $\alpha$ -actinin (green) and nucleus stained with DAPI (blue). These images show the expansion of cardiac myofibers necessary for cell-cell communication between each aligned pattern. A1 and B1 images show the staining of connexin43.

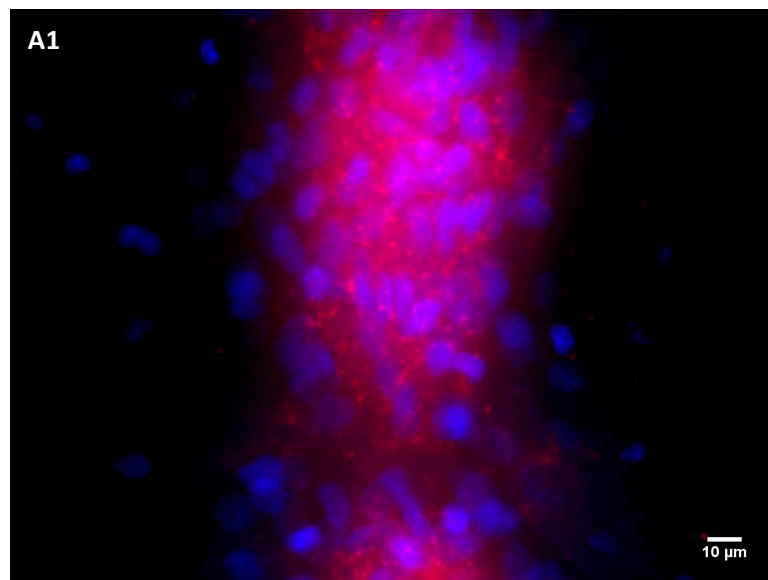
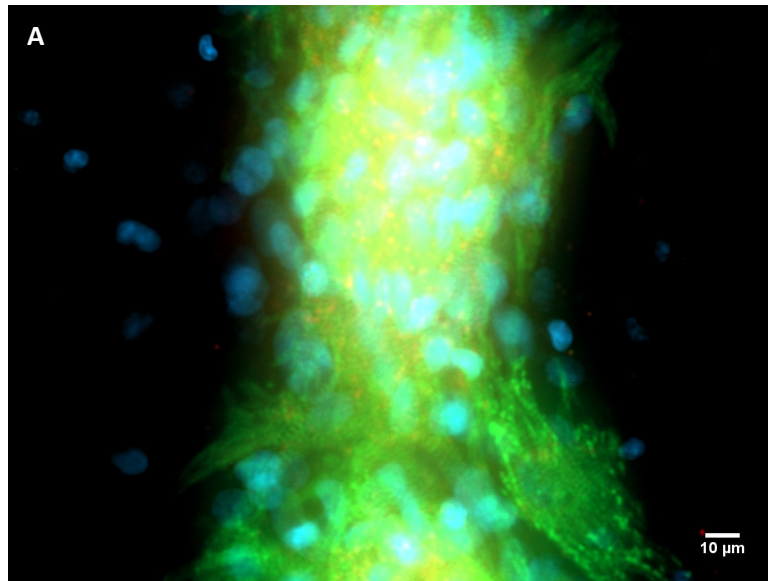


Figure 6.10 shows immunohistochemical staining to analyse protein expression of differentiating cardiac cells fixed with paraformaldehyde and permeabilised with 0.5% Triton X-100 in 3% paraformaldehyde and stained with, A) cardiac troponin I (labelled secondary antibody, green), A1) Connexin-43 (red) and nucleus stained with DAPI. These images show the formation of cell and clonal expansion of cardiac cells.

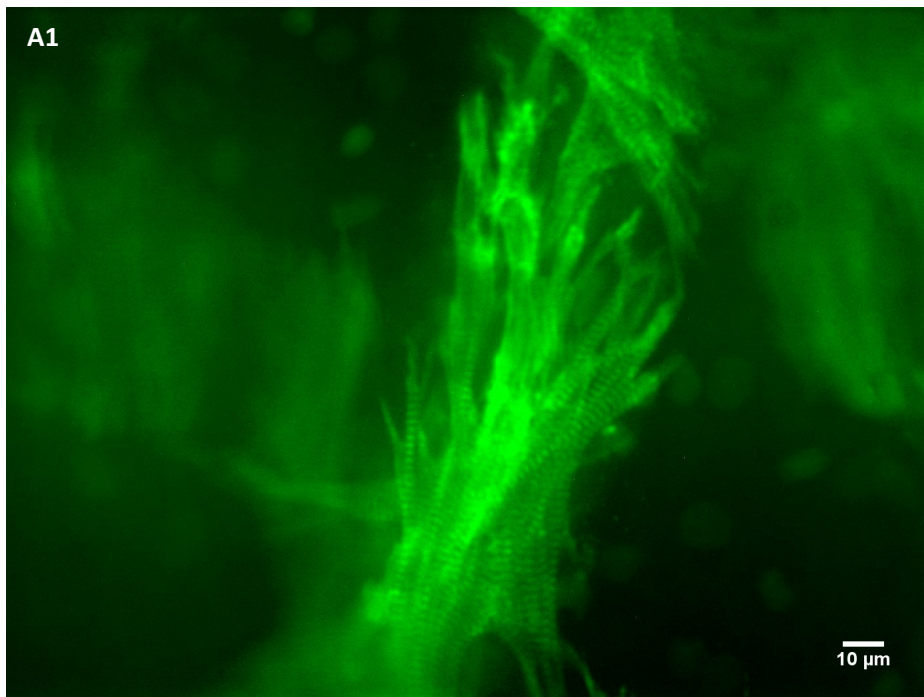
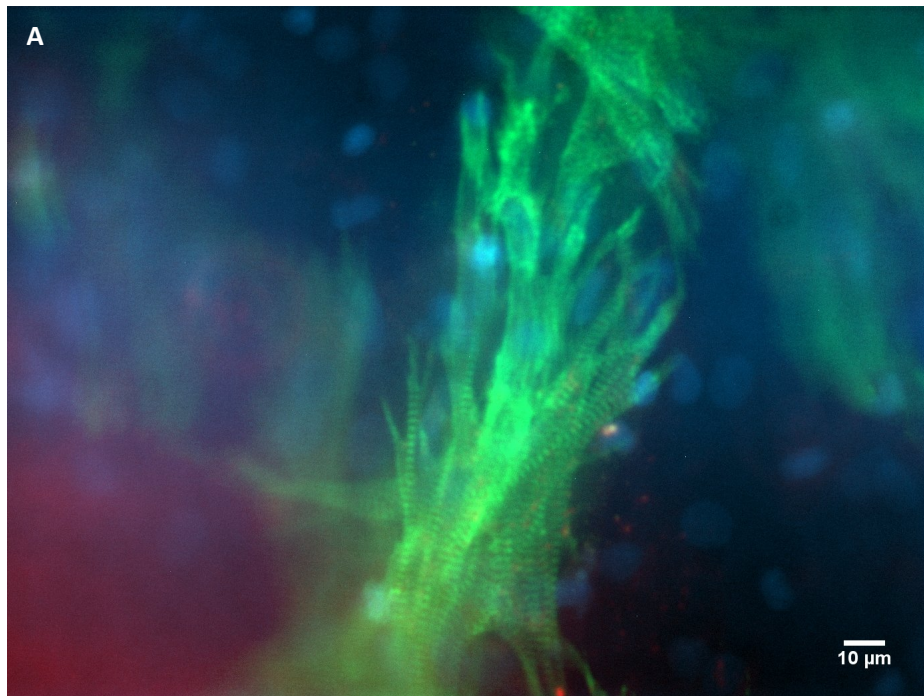


Figure 6.11, A and A1 shows staining of cells to show gap junction formation in the hydrogel and striations of sarcomeric organization observed in the scaffold (scale bar 10μm)

The hydrogel promoted and facilitated the formation of elongated, well-defined, cross-striated sarcomeric layers inside the scaffold that resemble to those of native rat ventricular myocardium. The presence of connexin 43 staining indicated the development of intercalated disk and gap junction between the myocytes that are responsible for excitation-contraction and generation of action potentials (Figure 6.11, 6.12). Accurately and rapidly detecting troponin allows early diagnosis of myocardial damage which is important for treatment of cardiovascular diseases to improve the prognosis for patients.

Troponin proteins are part of a complex (Troponin C and Binary I-C complex), which are responsible for muscle contraction. This complex is located within the myocyte contractile apparatus that regulates calcium-mediated contraction of myosin and actin filaments. Gap junctions, which are known to play an important role in impulse conduction, are membrane channels that allow cell-cell movements of ions and metabolites localized at left ventricle (LV). A multigene family known as connexins encodes them. In this work connexin 43 (Cx43) was used to express the working of a neonatal myocardium and conducting velocity. Cardiomyocytes are composed of bundles of myofibrils that have distinct repeating micro-anatomical units called sarcomeres. Sarcomeres are basically the contractile units of myocytes define the region of myofilament structure between two Z-lines consisting of thick and thin filaments – myosin and actin. Figure 6.12, shows clear sarcomeric organization on day 9 of the culture in 5% GelMA.

The presence of gap junctions on the surface of cardiomyocytes plays an important role in native heart tissue for providing cellular linking and electrical coupling. This study has shown a well-developed network of gap junctions and sarcomeres inside the GelMA hydrogel that mimic the structures of native myocardium by promoting cardiac fibroblasts and cardiomyocytes spreading and maturation.

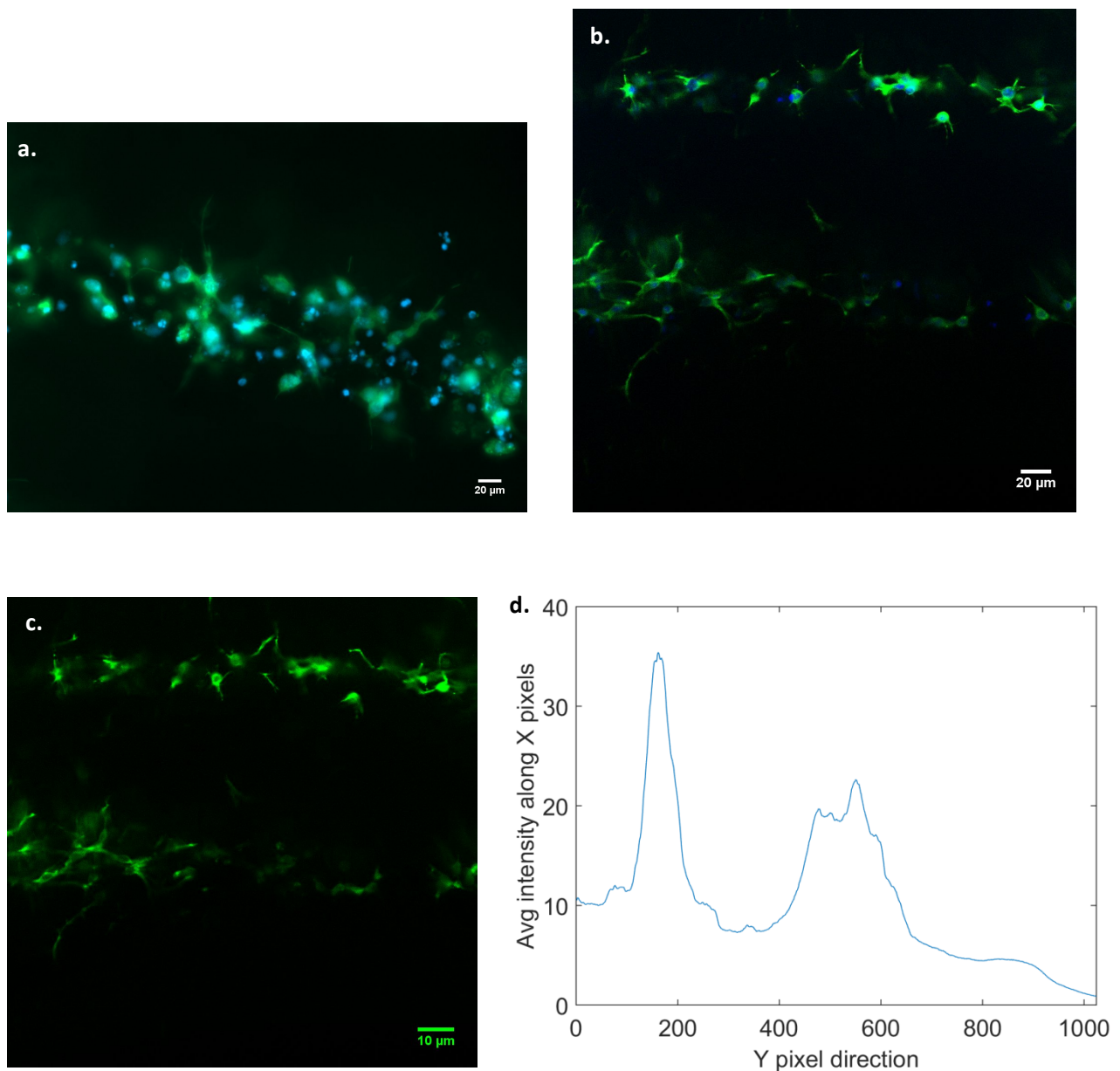


Figure 6.12, a) shows 20X image showing cardiac fibroblasts and cardiomyocytes stained with F-actin and DAPI at the pressure of standing wave at 6.4MHz elongating in the direction of alignment on day 5, b,c) show confocal images of cardiac fibroblasts and cardiomyocytes cells in the 3D scaffold. The image analysed consisted of 20 Z-stacks in order to show the alignment and development of cell growth 3-dimensionally. In this image the alignments are different heights and growing x-, y-, and z- axis, d) characterizing the layer of patterns by measuring the pixel density of the alignment using the MATLAB code to indicate the presence of alignments at different heights of the 3D scaffold.

The cells were aligned at pressure nodes generated by 6.4MHz frequency standing waves. Cell patterning was visually noticed using optical microscope at different heights of the 3D scaffold. Using confocal imaging, Z-stack images clearly showed that alignments at different

position of the scaffold. The Figure 6.13 shows the F-actin (green) pixel density being higher for alignment at higher position than at lower in the scaffold. The alignments have also shown orientation of cell growth and F-actin fibres along the patterns within the 3D scaffold of GelMA demonstrating the formation of 3D micro-tissues. The images have shown clearly sarcomeric  $\alpha$ -actinin, connexin-43 and troponin-1 penetrating the cellular network inside the GelMA hydrogel matrix with well-defined cardiac markers expression. These observations suggest that cardiomyocytes and cardiac fibroblasts of neonatal rats were highly interconnected across the patterned alignments and at different structural heights of the scaffold leading to development of superior structural and tissue-level functionalities such as beating.

## 6.5 Conclusion

This Chapter has demonstrated synthesis of GelMA and quantified rheological characteristics to explore different degrees of concentration of hydrogel to produce a viable and biocompatible 3D scaffold. The integration of acoustic waves in the 3D constructs has allowed the creation of different spatial patterns by tuning the input wavelength of the generated waves. 6.4MHz SSAWs provided higher cell density concentration at alignments in 5% GelMA than when compared to 3.4MHz. It was also seen that the higher the time required to photo-crosslink the hydrogel with UV light the cell viability decreased. The optimal UV exposure was set between 12-15 secs for all the experiments. 5% GelMA hydrogel provided a cell-compatible and elastic substrate with tuneable mechanical and physical properties that can readily integrated with surface acoustic waves. Moreover, no pre-treatment of SAW based device and PMMA structure was needed.

This Chapter has shown neonatal rat cardiac fibroblasts and cardiomyocytes preferentially align at the pressure nodes of standing acoustic waves and proliferate. F-Actin and DAPI staining allowed visualization of cardiomyofibers of the cardiomyocytes and fibroblasts during the culture period. The immunostaining technique applied allowed fluorescent visualization of the gap junctions and sarcomeres by staining with commercially available primary and secondary antibody proteins. The optimized GelMA concentration, UV intensity and time, photo-initiator concentration and acoustic wave frequency and power have rendered a novel platform compatible for cell encapsulation and manipulating to create a single cell

sheet technology. This allows to potentially mimicking the in-vivo structure of native heart muscle in several sheets of GelMA layers *in vitro* and culturing them over an extended period of time.

## **Chapter 7**

### **Electrophysiology of cardiac cells**

#### **7.1 Introduction**

The aim of this chapter is to explore the use of surface acoustic wave based devices to provide mechanical stimulations as a non-invasive technique to study the effects on cardiomyocyte morphology and conduction in 3D scaffolds and so understand the cardiac electrophysiology properties such as beating, contraction, action potential and calcium transient characteristics.

#### **7.2 Theory**

##### **7.2.1 Mechanical stretching of cells using SAW**

The complicated phenomenon of cell interaction with the surface in the microenvironment has been studied from different angles with respect to relevant biology, chemistry, physics and engineering fields. The mechanism of how cells interact through different physical and chemical properties is important for understanding human health, developing biomaterials and tissue engineering.

The heart has mechanosensitive capabilities that allow response of the organ to increase its growth life. Cardiomyocytes have the functionality to stretch and react to stretching by changing their function and increasing in size [65]. Integrin, stretch-sensitive ion channels, sarcomeric proteins and cell-surface receptors are responsible for the mechanosensor behaviour. These striated muscle contractions due to the cardiac muscle cells keep the heart actively mechanically stimulated. Studies have shown the contribution of mechanical stimulation on cells and tissue by using mechanical stress in the form of stretch and fluid flow shear stress (Figure 7.1). Uniaxial stretching of cells during the 2D culturing has been shown to create functionalized cardiac tissue [65]. The stretching promoted improved organization of cardiomyocytes, lengthening of myofilaments and contractual forces behaving similar to native myocardium. cardiomyocytes make up a total of 70% of total heart mass and function with the proper provision of cellular and extracellular components in addition to sufficient oxygen and nutrient supply. Stretch-stimulated grafts have been produced and implanted into heart infarctions as a solution to repair infarctions in rat [199]. These studies have shown

improved signs of repair and strengthen of the tissue upon implantation and monitoring post-surgery. Studies have also shown the effect of stretching on arterial smooth muscle cell orientation in 3D collagen matrix to exhibit hybrid tissue characteristics that were similar to natural arterial membrane wall [200].

Current conventional therapies have been limited due to the inability of regeneration of myocardium due to injury and shortage of organ transplantation. In the work of this thesis and elsewhere, surface acoustic waves have shown to have the ability to align cells and allow cell differentiation and growth without any invasive techniques using a non-bulky platform. SAWs can be employed to apply cyclic mechanical stimulations that cause mechanical stretching and improved cardiac physiological responses in hydrogels (Figure 7.2). SAW therefore can induce the required mechanical stimulus to obtain functional syncytium.

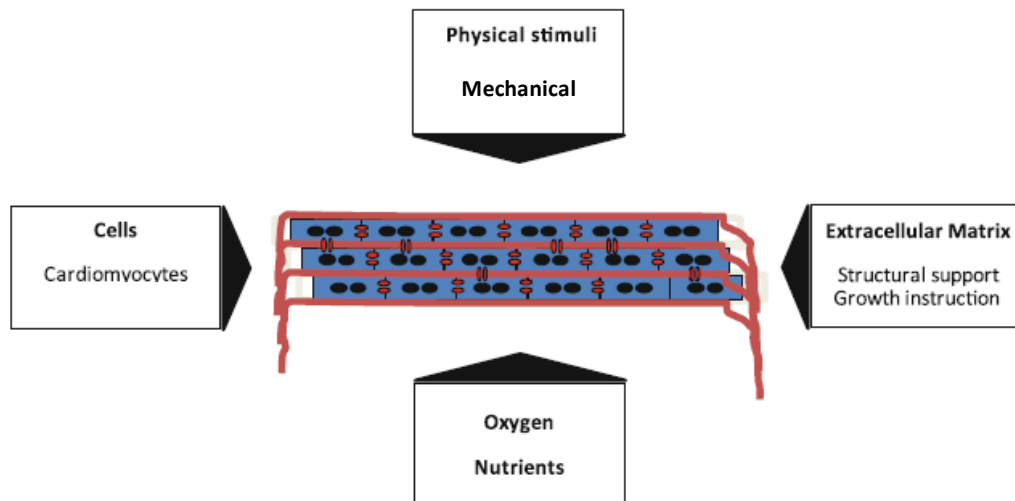


Figure 7.1, schematic representation of in-vitro assembly of cardiomyocytes in hydrogel being exposed to physical stimuli using SAW based platform to create a functional syncytium.

Cardiomyocytes are the natural key for generating functional myocardium due to their ability to provide appropriate contractile machinery. The 3D scaffold when placed in the region of travelling SAWs experience longitudinal stimulation in which the cells stay roughly in the same pressure nodes.

## Longitudinal

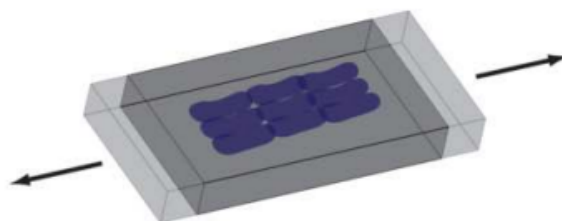


Figure 7.2, schematic representation of uniform longitudinal stretching of the scaffold in perpendicular direction of patterned cells.

### 7.2.2 Electrophysiological responses of cardiac cells

#### 7.2.2.1 Beating and contraction characteristics

Tissue engineering provides an alternative to produce a cardiac patch with myocardial features. Injectable polymers such as fibrin glue, matrigel and self-assembling peptide hydrogels have been employed to study cell survival and cardiac function [201]. The studies have shown encouraging results however there is a question about how the composition and structure of these biomaterials affect the cardiomyocyte remodelling and its function in the gel. By encapsulating cardiomyocytes in GelMA hydrogel using in-vitro culture techniques it would be beneficial to answer clinical question surrounding cell and tissue contraction. GelMA consists of the natural biomaterial collagen in the form of liquid precursor. This liquid precursor forms a 3D scaffold upon excitation of UV light with the aid of photo-initiator.

The frequency of heartbeats can range from 0.05 to 20Hz [204]. A whale's heart beats at a slow rate of 3 to 4 beats/min (0.05 – 0.07Hz) during deep dives whereas human heart beat at 60 to 70 beats/min (1–1.1Hz). Rat hearts beat at 360 beats/min (6Hz) and humming birds have a beating rate of 1200 beats/min (20Hz) during flight [204]. In order to promote cellular linking and electrical coupling, a well-developed network of gap junction and sarcomeres have to be present on the cardiomyocytes in the GelMA hydrogel. Previous chapters have shown that cardiac fibroblasts and cardiac myocytes have expressed a range of cardiac markers in GelMA hydrogel that prove the presence of ECM proteins needed for promoting cardiomyocytes spreading and maturing through the provision of appropriate cellular cues. To mimic a functional native heart, high levels of cell-junctions are required on micro-patterned cells in the 3D micro-architecture. These would lead to improved cell-cell coupling

accompanied by enhanced overall contractile properties of the engineered tissue constructs and facilitate synchronous beating.

The contraction of hiPSC-cardiomyocytes cells in 2D and 3D culture were investigated to study the contraction behaviour using video analysis algorithm developed by Clyde Biosciences (Glasgow, UK). 2D culture systems provide a simple approach to identify and assess parameters that influence cell responses however they fail to mimic most of the cell niches in the body consisting of 3D hydrated network of natural biomaterials. GelMA hydrogel allows the tuning of the crosslinking density by varying different concentration, UV curing time and concentration of PI that affects the matrix stiffness without altering cell-adhesion properties. Hence this elastin-like hydrogel is suitable for tenability, strength and extensibility. On a 2D surface cardiomyocytes lose their phenotype or contractility ability [201]. Therefore, having a 3D micro-environment improves the morphological and functional responses of cardiomyocytes that could provide scientific insight into the modulation behaviour and function of them.

#### **7.2.2.2 Action potential and calcium transients**

Myocardium primarily comprises of cardiomyocytes that create complex electromechanical dynamics. Starting the heart's pacemaker node electrical signals travel through myocardium via purkinje fibers (conductive regions of specialized cardiomyocytes) propagating via electrochemical cell-cell connections in the intercalated discs (Figure 7.3).

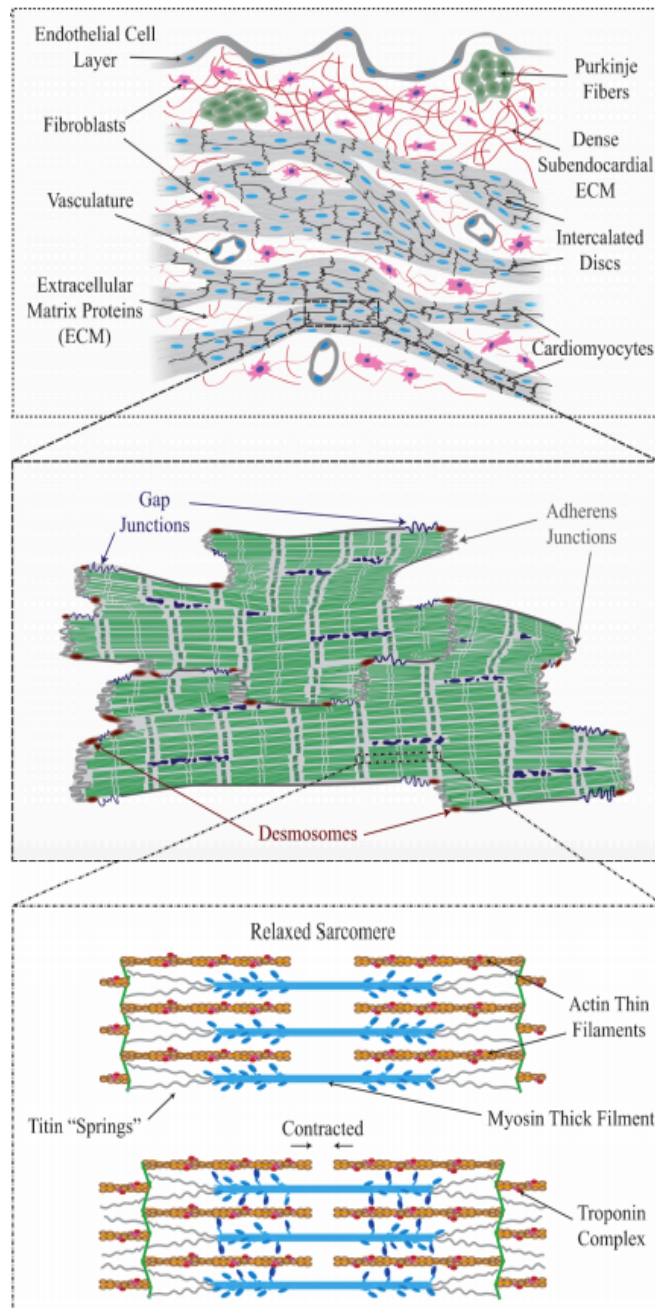


Figure 7.3, schematic representation of different layers in myocardium, showing cardiomyocytes and sarcomeres [203].

The action potential (AP) generated, comprised of electrochemical signals at cellular level, are observable due to changes in sodium, calcium and potassium concentrations. Once an action potential is triggered cell-cell junctions traverse and excite electrically coupled cardiomyocytes in a simultaneous fashion. Optical techniques provide a non-invasive measurement methodology to monitor cell membrane depolarization and cardiac action potentials. By the use of voltage sensitive dyes embedded in cardiomyocytes cell membrane allow optical measurements of transmembrane potential can be made as a change in

fluorescence intensity. Therefore, this non-invasive approach offers greater spatial resolution and opportunity to visualize the responses of multiple cells simultaneously [203]. Calcium ( $\text{Ca}^{2+}$ ) concentration sensitive dyes allow spatial and temporal changes in intracellular  $\text{Ca}^{2+}$  during excitation of cardiomyocytes when optically recorded. Calcium indicators that have low affinity and allow rapid response of  $\text{Ca}^{2+}$  are ideal to characterize cardiac action potential rapidly and allow measuring significant changes in intracellular calcium concentration [203].

### 7.3 Beating characteristics of co-cultured cardiac fibroblasts and myocytes in GelMA

The beating behaviour of co-cultured cardiac fibroblasts and cardiomyocytes (1:1) inside the 3D GelMA scaffold was investigated from day 6 onwards when the contractions began to be observed. The spontaneous and synchronous beating (BPM) of the co-cultured cells in 3D architecture of 5% GelMA concentration as a function of cell- was observed from day 6 onwards with the peak at day 9 and measured until day 12 till the beating stopped (Figure 7.5). The scaffolds were found to be beating showing evidence of the presence of connexin-43 protein that is responsible for cell-cell gap junction interactions. The communication between adjacent myocytes occurs through this gap junction proteins that allow the passage of ions and solutes between the cells.

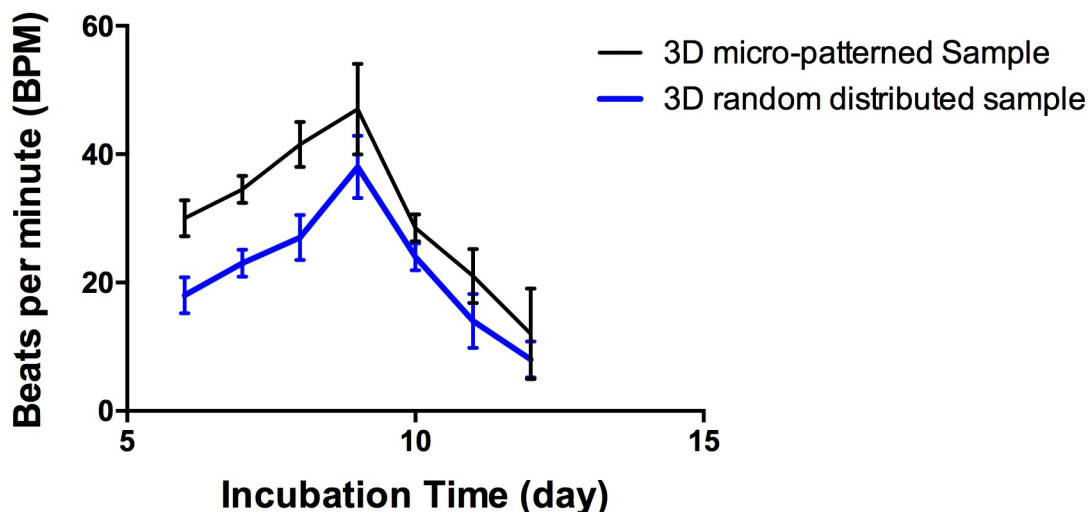


Figure 7.5, Co-cultured cardiac fibroblasts and cardiomyocytes beating characteristics in 5% GelMA which was photo-polymerized for 12sec using UV light. The quantitative analysis of synchronous beats per minute (BPM) of different samples (n=3) from day 6 to day 12 demonstrating an increase in beating, with peak reaching at day 9, when cells have matured

and decreased as the culturing days increased. The beating frequency was higher for cells that were patterned by standing surface acoustic waves than the cells were randomly distributed in the GelMA hydrogel scaffold.

The observation showed that the co-cultured cells seeded in the 3D GelMA hydrogel scaffold adhered within the matrix promoting spontaneous beating rates. The gap junctions formed ensure synchronous contraction of cells and play a prominent role in generating tissue level syncytium. This time frame of *in vitro* cardiac construct of beating cells between days 7 and 10 was found to be consistent with 5 samples. As seen from Figure 7.5, the beating rates increased with the cell culture days and peaking on day 9 after which it declined. The beating rate varied from 12 beats/min to 49 beats/min ( $\pm 10$  beats/min) (0.2 – 0.82 Hz ( $\pm 0.2$  Hz)). The beating observed in the initial period of culture exhibited strong uniform beating but the rate decreased post maturation day with the culturing time, demonstrating elastic properties of GelMA that can support expansion-contraction of cells during beating. Thus, the SAW based device has shown that SAWs are capable of patterning cells at different wavelengths and also allowing cells to remain viable over several culture days to grow in functional constructs that demonstrate beating.

#### **7.4 Effects of mechanical stimulation on cell orientation and contraction**

To further investigate the effect of SAWs on cells in hydrogel, mechanical stimulations were carried on in 3D scaffolds of encapsulated cells using acoustic waves. Scaffolds allow the release of signal molecules and ingress of nutrients and oxygen to keep the seeded cells alive. It has been shown that the 3D architecture of hydrogel transmits mechanical stimulation post alignment and culturing. To study the effect of mechanical stimulations on 3D cultured cells, traditional methodologies of 2D platform were employed to draw a comparison between the samples.

hiPSc-cardiomyocytes (GE Cytiva) started contracting after 5 days of culturing in both control and 3D scaffold samples. The cardiomyocytes were seeded at density of  $5 \times 10^5$  cells per ml into each of the sample. After 5 days of culturing, cardiomyocytes spread on the flat 2D control sample well coated with fibronectin to provide cell adhesion and in 3D stimulated samples the cells responded to patterning and mechanical stimulation showing elongation and alignment along the direction of wave propagation (Figure 7.6). The cell morphology on flat substrate reveal circular, sphere and triangle growth, where the morphology of cells in stimulated samples reveal elongated and spindle shape.

The contraction of cardiomyocytes that was observed from day 5 onwards was anisotropic and parallel to alignments in contrast to the isotropic on the flat 2D surface in the well plate. The synchronous beating of cardiomyocytes was observed from day 9 onwards where the cells were visualized to be beating and contracting along the direction of the standing acoustic waves that created cells alignments.

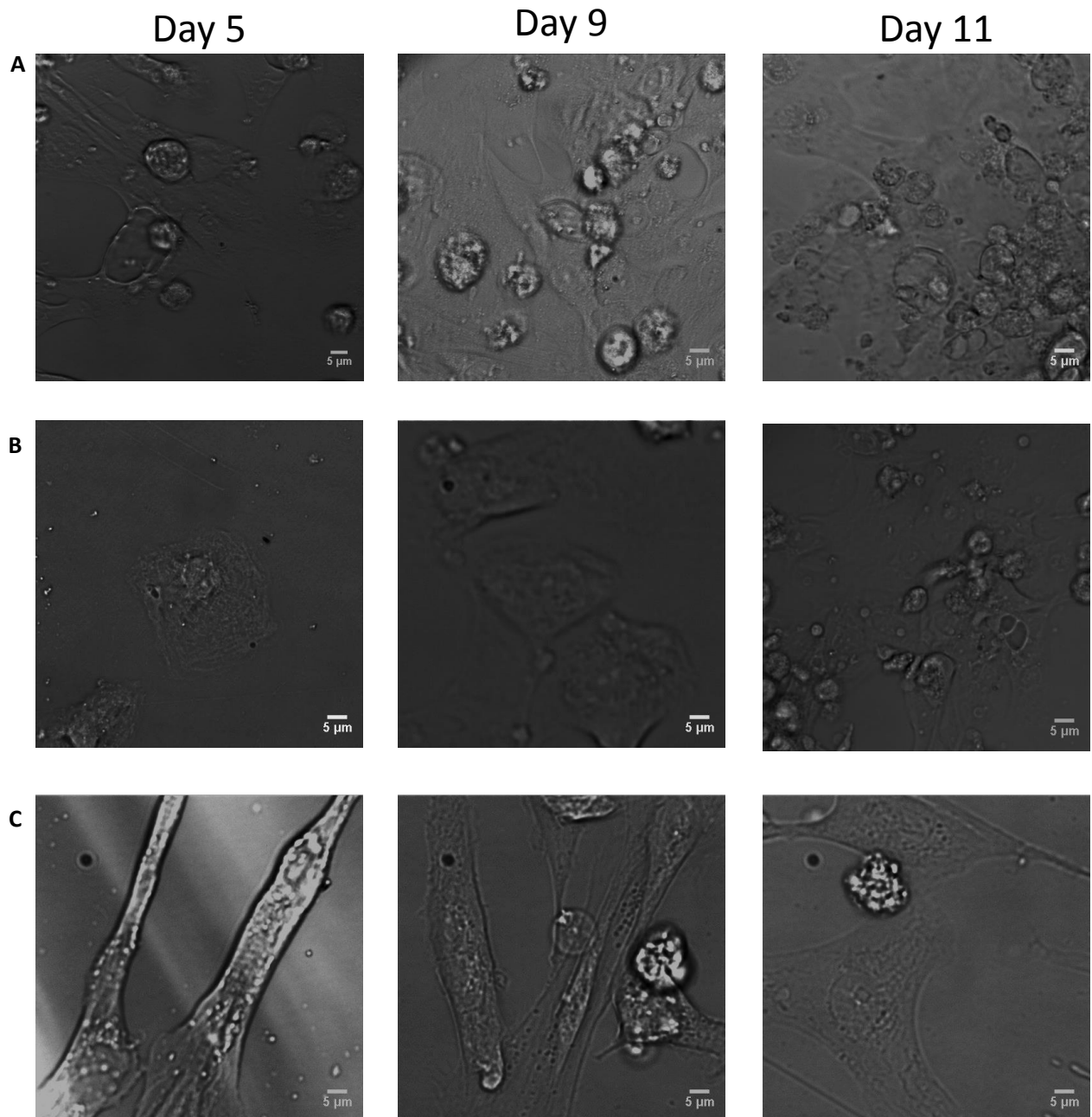


Figure 7.6, A) shows hiPSC-cardiomyocytes (GE Cytiva Cardiomyocytes) seeded on well plated coated with Fibronectin providing a 2D platform, B) shows cardiomyocytes encapsulated on a TMSPPMA glass slide coated with fibronectin but not exposed to SAWs, C)

show clear elongation growth of cardiomyocytes in 3D scaffolds when stimulated mechanically with SAWs at 3.4MHz, 180mW for 3mins during consecutive cell culture days. SAWs control and align the cell nucleus and actin in the direction of propagation that affects the cell migration as shown.

As it is visible from Figure 7.6, SAWs can align and orientate the cell morphology on the pressure nodes showing an elongation and two directional protruding extensions of the end of cell membranes. Therefore it is possible to control the cell migration behaviour. This polarity of alignment translated down to the cytoskeleton as well as the migration machinery of the cell thus causing the cell to grow in an elongated manner. This concept can therefore have important implications for creating 3D cardiac tissue patches that may improve the guidance of regeneration of cells across the damaged gaps.

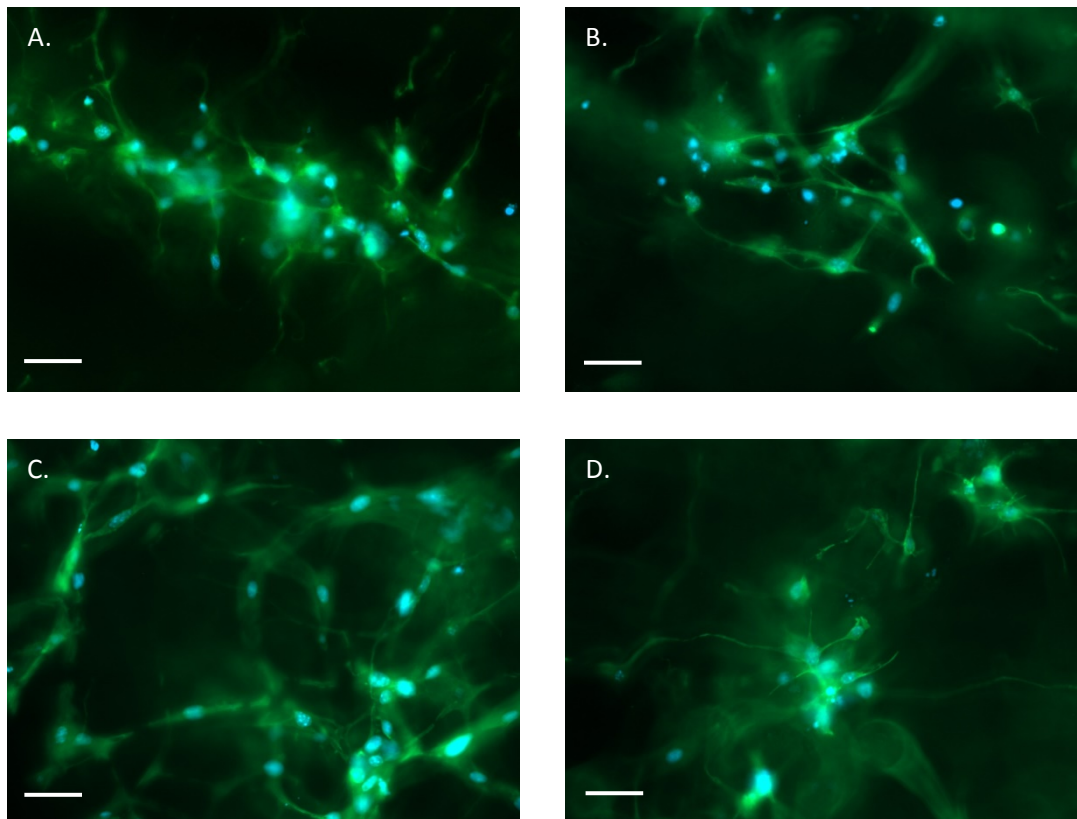


Figure 7.7, hiPSC-cardiomyocytes alignment, stretching and elongation of cardiomyofibers on day 7 inside the GelMA hydrogel. Representative images of F-actin and DAPI stained cells in 5% GelMA (Scale bar: A-20µm, B, C, D - 10µm)

The formation of cardiomyofibers in 5% GelMA hydrogel exhibit promotion of cell-cell communication and allow cell synchronous excitation-contraction of cardiomyocytes (Figure 7.7). Contractility was measured visually using the optical microscope setup at Clyde

Biosciences and the onset of spontaneous contraction in the 3D matrix of 5% GelMA was recorded. The contracting cell in the hydrogel was quantified at each time point using an ImageJ plugin that was developed by the company. By analysing the contractility activity of cells in control samples and SAW stimulated hydrogel samples, it can be ensured that potential of retaining the contraction was higher in elongated cells present in GelMA. Figure 7.8 shows the contractility displacement of cardiomyocytes in 5% GelMA after analysing the recorded video through ImageJ plugin (Clyde Bioscience, UK).

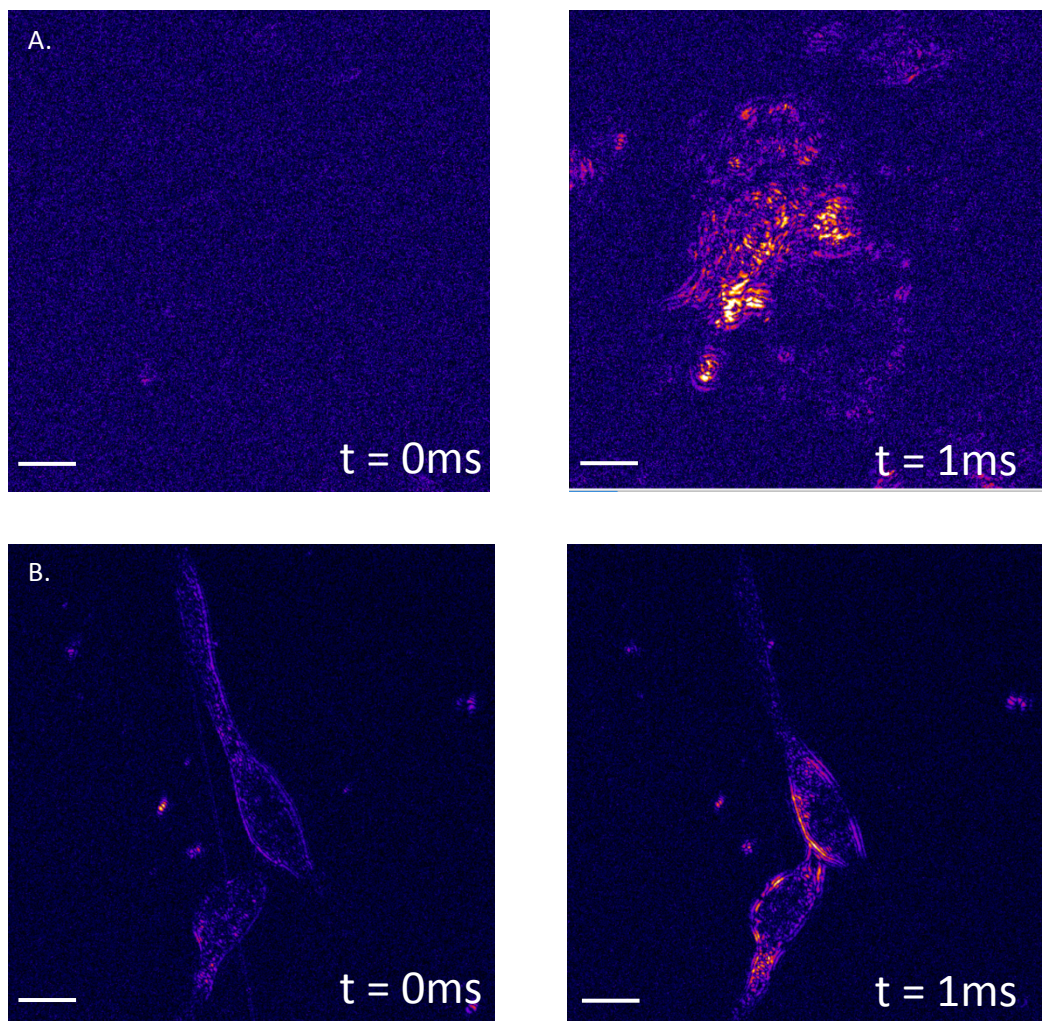


Figure 7.8, shows the contraction of hiPSC-cardiomyocytes (GE cytiva) seeded GelMA 5% constructs represented by motion maps obtained from image analysis of video data processed in Clyde Biosciences ImageJ plugin. The contour image (A) shows the no displacement of cell contractility at  $t = 0ms$  and the contraction of cardiomyocytes starting from bottom of the frame at  $t=10ms$  on a flat 2D well surface bottom coated with fibronectin, (B) shows the no displacement of cell contractility at  $t = 0ms$  and the contraction of hiPSc-cardiomyocytes at  $t=10ms$  in a 3D 5% GelMA hydrogel scaffold exposed to mechanical stimulations at 3.4MHz

on a periodic cycle. The single cell contraction was observed at  $\geq 40\times$  magnification (Scale bar:  $10\mu\text{m}$ )

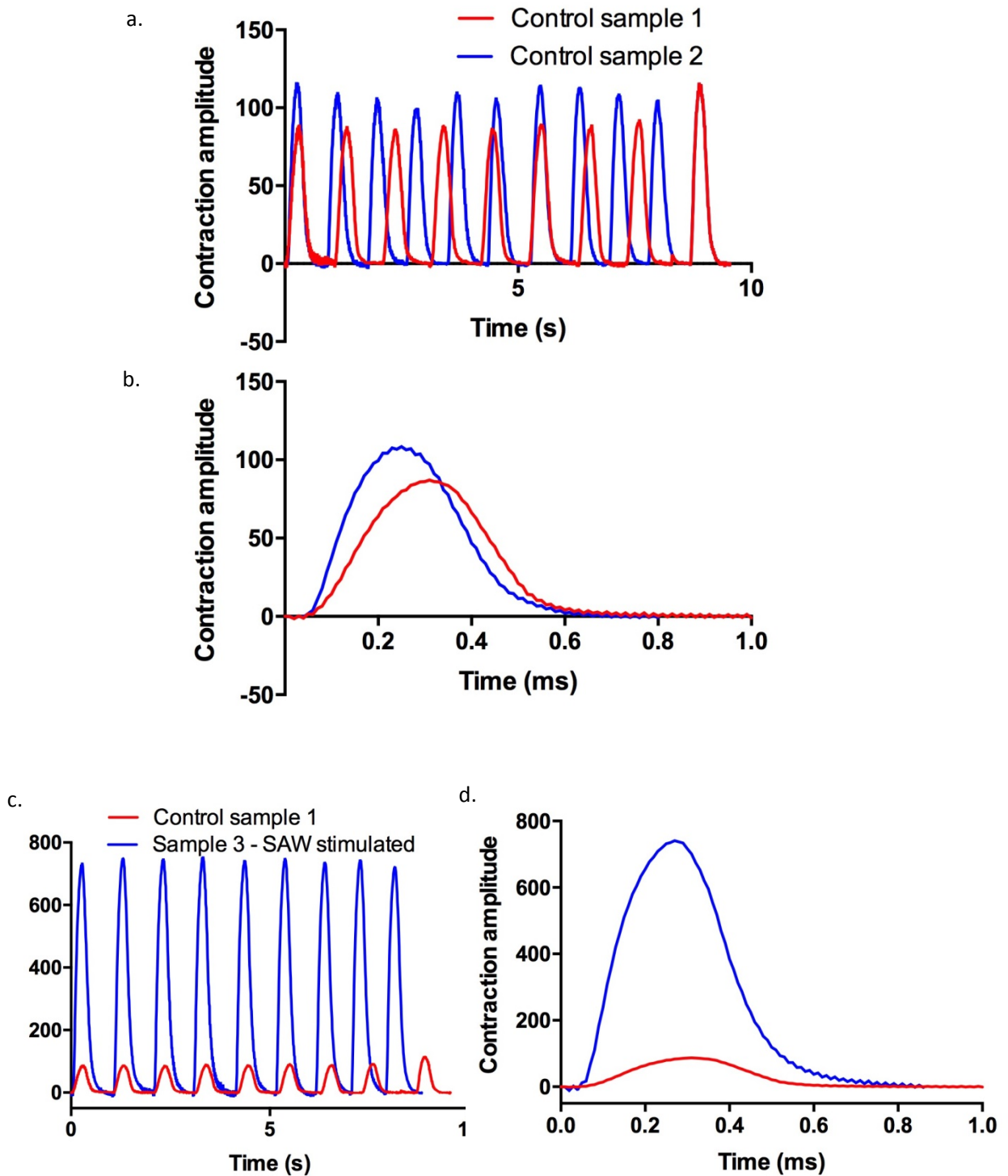


Figure 7.9, contraction rates of hiPSC-cardiomyocytes in three different samples. The video was visually observed and the data quantified using ImageJ plugin that was developed by

Clyde Biosciences. The plugin will record 100 frames of images taken in 10 secs and create a series of contour images as shown earlier. A video processing algorithm based on “block-matching” methodology was written in Matlab and linked into ImageJ. The different dark and bright spots are then quantified through the plugin automatically with respect to time, pixel density and cell displacement. Image a) shows control sample 1 consisting of cell seeded on a 2D surface of well-plate coated with fibronectin to allow cell adhesion has shown 1/5<sup>th</sup> of lower amplitude when compared to sample 2 consisting of cells seeded into 3D hydrogel scaffold for duration of 1msec, b) shows the contraction amplitude of both the control samples in 1ms, c) shows the contraction amplitude of cardiomyocytes 8-fold times higher than the control samples due to cell alignment and mechanical stimulation over 10sec, d) shows the higher amplitude of contraction of cells in 3D micro-patterned and mechanical stimulated sample in 1ms.

The primary cardiac muscle cells, cardiomyocytes, that were seeded on a traditional flat surface of a well-plate and encapsulated in the 3D matrix displayed contractions in each of the three samples as observed in Figure 7.9. The contractions of hiPSC-cardiomyocytes in the control sample 1 and 2 were 8-fold time weaker when compared to SAW stimulated GelMA hydrogel. This indicated that the traditional plastic substrates and random distribution of cells do not adequately mimic functionalized properties. Due to the alignment of cells, spindle shape, mechanical stimulation and elasticity of the GelMA biomaterial, the contractility of cardiomyocytes was enhanced and uniform during culture days. Figure 7.10, shows the quantified data of contraction amplitude of the three different samples with subsets of three individual experimental data. These in-vitro studies also suggest that the contractile behaviour of cardiomyocytes decreased as the culturing days increased for all the samples.

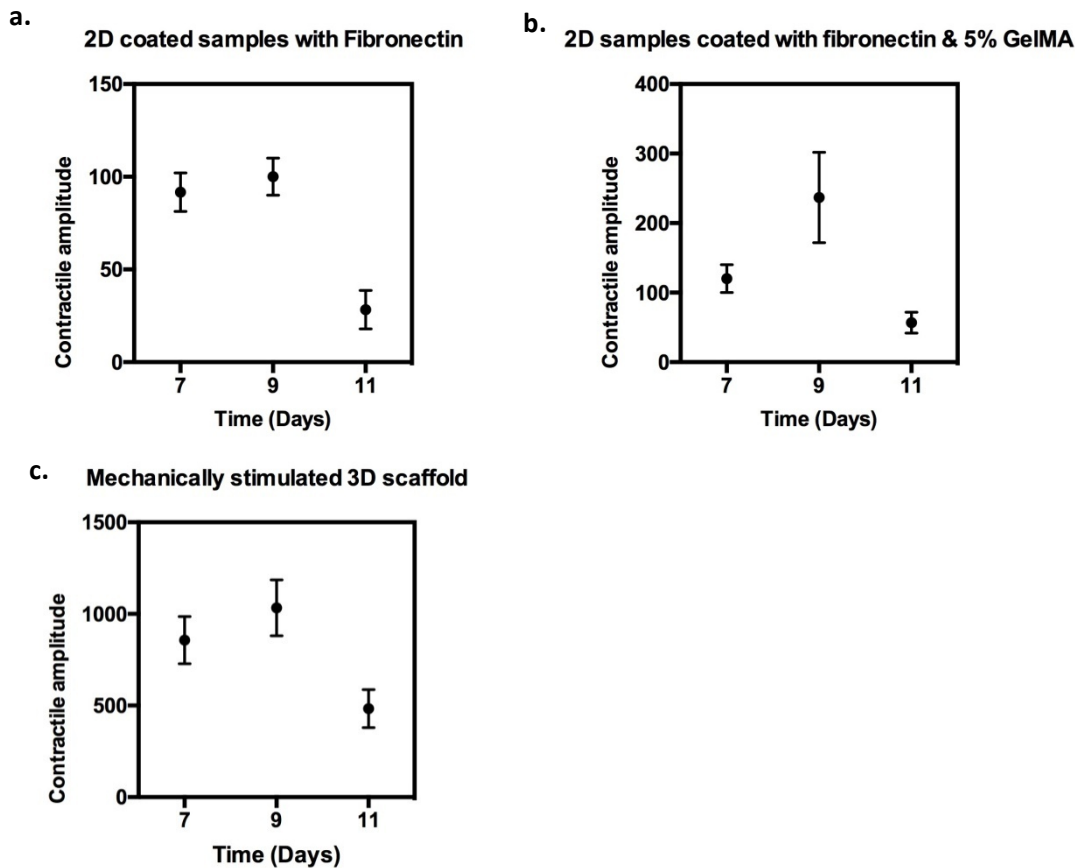


Figure 7.10, quantifying contraction of cardiomyocytes seeded in different mediums, a) the contraction amplitude on 2D coated cell culture well plate with fibronectin yielded the peak contraction on day of  $100 \pm 10$  contractions, but b) when cells were seeded with 5% GelMA hydrogel the contraction amplitude increased on the day of maturation (day9), c) and when the scaffolds were mechanical stimulated periodically during the in-vitro culture days the contractions were significantly higher on day 9 with peak reaching  $1000 \pm 100$  contractions. The experiments were repeated at least three times ( $n \geq 3$ ) compared to the three different samples.

Cardiomyocytes cultured on a flat 2D surface started contracting after 3 days and the ones cultured in 3D hydrogel scaffold started contraction after day 7, however the maturation day of cells was indicated as being day 9 according the GE Cytiva Plus hiPSC-cardiomyocytes guidelines. The beating of the cells could be clearly observed on single cells that were not in contact and also the cells that formed contact with neighbouring cells. It was observed that the aligned cells contracted parallel to the neighbouring aligned cells whereas the cells seeded randomly on 2D surface on fibronectin surface and hydrogel structure contracted without any preferred direction. The reason for sequential contraction of cells due to the alignment could be due to the aligned distribution of actin filaments and sarcomeric  $\alpha$ -actinin and essential

formation of gap junctions. The micro-arrangement of cytoskeleton provided an adhesion traction force between the cells and matrix.

The patterning gave the cells spatial distance and alignment that promoted better cell-cell contact to produce higher magnitude of contractions as opposed to cells that were randomly distributed in the 2D and 3D structures. This aggregation and elongated spindle shape of cardiomyocytes exposed to the SAW stimulated region enhanced the contraction forces and maintained their phenotype.

### **7.5 Effects of mechanical stimulation on action potentials and calcium transients**

To investigate the role of cardiac micro- and macrostructures in action potential generation and conduction in-vitro different samples were prepared using commercially available hiPSC-cardiomyocytes (GE Cytiva) in 5% GelMA scaffold and fibronectin coated wells. The advanced structural and functional maturation of engineered 3D cardiac tissues were compared with age-matched 2D monolayer samples coated in fibronectin. The action potentials, calcium transients and contraction amplitudes were optically mapped for 2D and 3D in different mediums to determine how the resulting changes affect the electrical and mechanical function of cardiomyocytes to engineer cardiac patches.

The hiPSC-cardiomyocytes exhibited spontaneous action potential synchronous to their contractions at the maturation day 9 (Figure 7.11). The formation of cell-cell connection allowed the spontaneous generation and travel of cardiac action potentials and contractions across the network.

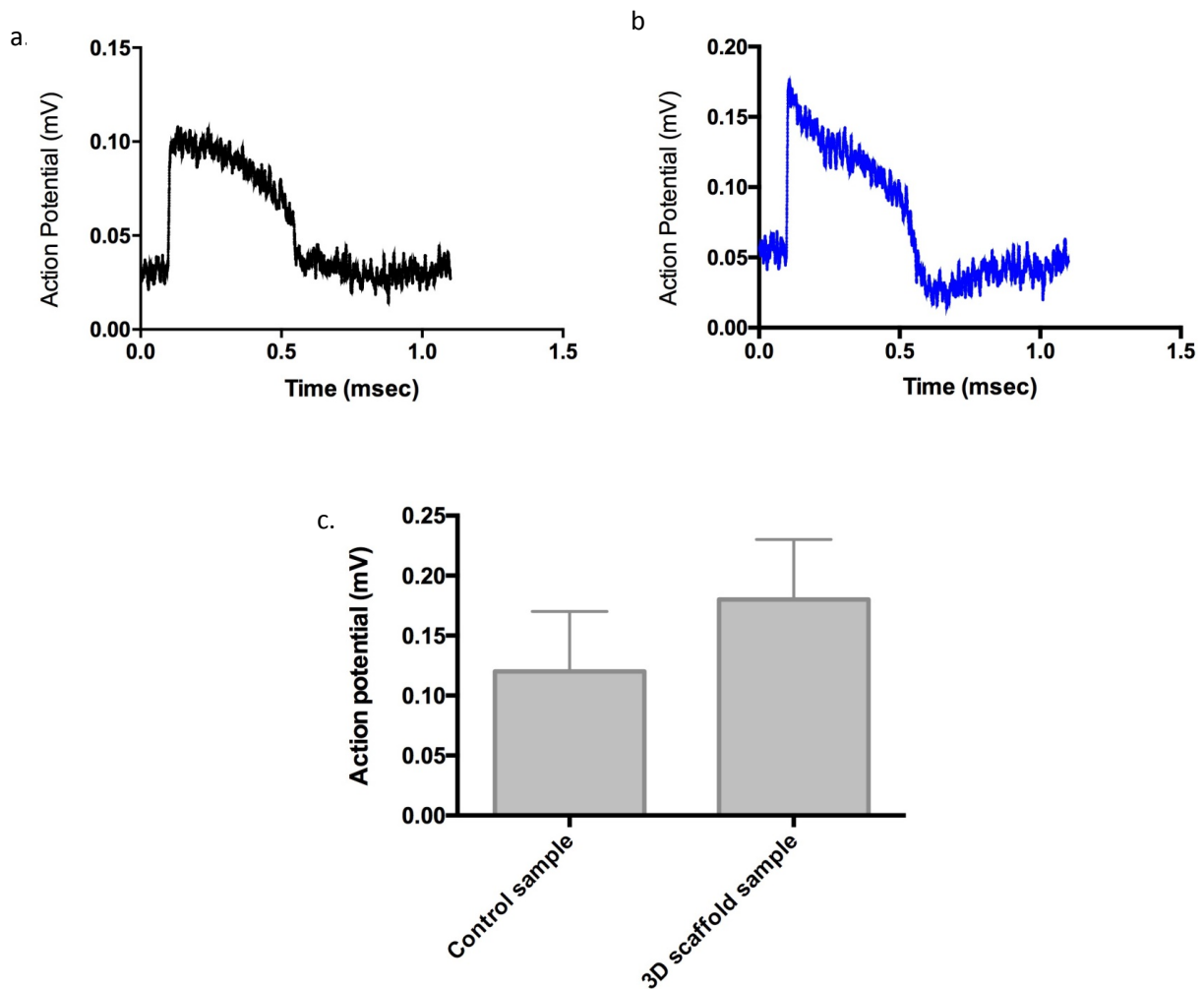


Figure 7.11, Spontaneous action potential and ion channel recording, a) the generated action potentials stained with voltage-sensitive dye di-4 ANEPPS in a control sample of 2D flat surface coated with fibronectin and, b) 3D scaffold 5% GelMA hydrogel sample which was stimulated periodically with SAWs at 3.4MHz, c) show an increase in magnitude of action potential when comparing both the samples for at least three samples ( $n \geq 3$ ).

The hiPSC-cardiomyocytes displayed spontaneous AP's synchronous to their contractions as shown in Figure (7.11). di-4-ANEPPS potentiometric dye has lower phototoxicity and are commonly used for optical mapping of whole heart [205]. The dye responded to increase in membrane potential (hyperpolarization) with decrease in fluorescence emission when excited at their optimal wavelengths. The amplitude (0.18mV) and duration (1ms) of the electrical activity were optically measured for cells in 3D constructs on day 9 of maturation. It was noted that the magnitude of the AP was higher for cardiomyocytes in encapsulated in 3D matrix and patterned and stimulated using SAWs. This propagation of excitation and

contraction meant the progressive formation of cell-cell contact therefore promoting gap junctions and propagating pacing signals.

Cardiac excitation-contraction coupling in cardiomyocytes is due to a vital process called calcium cycling [205]. The excitation-contraction of cardiomyocytes is crucial for native function of heart and calcium ( $\text{Ca}^{2+}$ ) is the central dogma to this coupling. Action potentials cause  $\text{Ca}^{2+}$  influx through L-type voltage gated  $\text{Ca}^{2+}$  channels that trigger the release of these ions from intracellular stores of the sarcoplasmic reticulum (SR) therefore activating contraction. During a heart failure, dysregulation of  $\text{Ca}^{2+}$  homeostasis may activate  $\text{Ca}^{2+}$  dependent currents that influence AP duration and trigger membrane depolarization [204]. Therefore to mimic native heart function it is important to study the intracellular  $\text{Ca}^{2+}$  processes in cardiomyocytes that contribute to contractile dysfunction and arrhythmogenesis in failing hearts. Simultaneous measurements of AP and  $\text{Ca}^{2+}$  wave propagation are important to understand and get an insight of acquired arrhythmias associated with heart failure.

The choice of calcium sensitive dyes is important for acquiring accurate measurements of amplitude and time course of  $[\text{Ca}^{2+}]_i$  transients. Dyes such as Fluo-4, Fluo-3 and Fura-2 have shown high affinity for  $\text{Ca}^{2+}$  that can artificially prolong the  $\text{Ca}^{2+}$  transients. This study utilizes Fura-2 (non acetoxymethyl ester (AM) form) dye that allows cell specific calcium mapping and chronic imaging over days. The hiPSC-cardiomyocytes were loaded with Fura-2 AM and the phasic  $\text{Ca}^{2+}$  signals were measured (Figure 7.12)

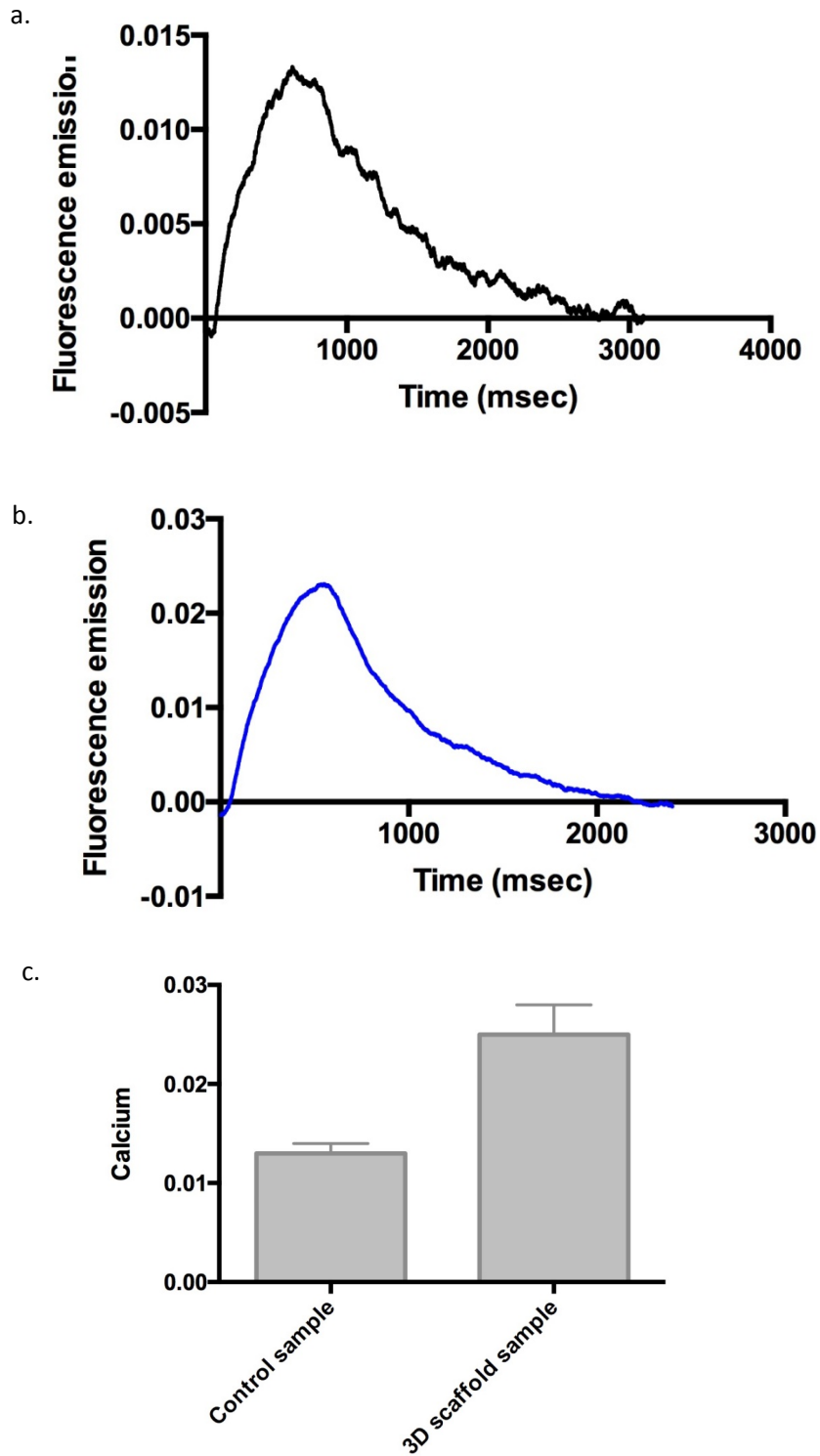


Figure 7.12, Recording of calcium transients were measured as peak fluorescence in Fura-2 AM (340/380nm) cultured a) on flat surface coated with fibronectin, b) cultured in a 3D scaffold of 5% GelMA and micropatterned, c) comparing magnitude of fluorescence intensity between the two different samples. At least three samples ( $n \geq 3$ ) were experimentally tested for measuring calcium transients.

The cells in both the samples were illuminated at 340nm and 380nm for fura-2 AM excitation and the excitation duration for each wavelength was 50ms with 1s delay between frame sets. To analyse the calcium transients each cell was traced and a region of interest was defined. During the experiments, cell data for fura-2 was normalized for each sample to the initial 340nm/380nm fluorescence ratio and recorded as a function of time. The measurements have shown an increase in peak response of cells in 3D hydrogel matrix as opposed to traditional method on flat surface.

The improved uniformity of cell alignment in the 3D hydrogel has shown an increase in action potential propagation as compared to cardiomyocytes being cultured on a 2D platform coated with fibronectin. Intracellular Calcium ( $\text{Ca}^{2+}$ ) concentration ( $[\text{Ca}^{2+}]_i$  transients) play an important role in many cellular processes. Cardiac excitation-contraction (EC)  $[\text{Ca}^{2+}]_i$  transients were measured optically by using fluorescent  $\text{Ca}^{2+}$  indicators (Fura-2) in cardiomyocytes. Fura-2 permeated through the cell membranes that made the application of this  $\text{Ca}^{2+}$  easier to measure. The  $[\text{Ca}^{2+}]_i$  transient was increased in the hydrogel concentration in a 3D matrix than on plane 2D substrate. The hydrogel scaffolds thus provided a better and natural cellular microenvironment for cells to proliferate and migrate in order to create engineered functional tissues and for disease modelling applications as well.

## 7.6 Conclusion

In summary, this Chapter has demonstrated the engineering of a novel platform for mechanically stimulating cardiac cells in 3D hydrogel matrix using surface acoustic waves and the influence of it on the electrophysiological properties in order to regenerate a myocardium.

The co-cultured scaffolds containing cardiac fibroblasts and cardiomyocytes from neonatal rats exhibited beating characteristics from day 6 onwards until 12 in 5% GelMA concentration hydrogel. At the maturation day (day 9) the beating observed was at maximum of 49 beats/min ( $\pm 10$  beats/.min) when the cells were matured. This resulted in a synchronous uniform beating of aligned cells due to the formation of networked gap junctions and cell-cell communication. The effect of periodically mechanically stimulating hiPSC-cardiomyocytes yielded that the cells when cyclically stimulated with surface acoustic waves at 3.4MHz formed an elongated spindle shape as opposed to cells in different control samples that has

spherical and triangular shapes. It was observed that the cells in scaffolds that were mechanically stimulated were growing in an elongated manner as opposed to natural growth observed in control growth. SAWs stimulations were cyclically applied during the culture days (3, 5, 7, 9) in order to allow cell adhesion and growth and avoid contamination of cells in the first three days of experiments. This effect of SAWs on cell shape and orientation at the aligned nodes affected the electrophysiological behaviour.

The generated micro-pattern of cells using acoustic waves in the 3D scaffold to produce engineered tissue constructs yielded better contractility amplitude as well. The amplitude of contraction was significantly higher in samples that were exposed to alignment and mechanical stimulations in the 3D hydrogel scaffold than the cells randomly distributed on a flat 2D surface coated with fibronectin. The quantitative measurements showed for each of the sample contractions were maximal on the day of cell maturation and gradually declined as the number of culturing days increased. Since hydrogels consist of a high percentage of water during remodeling the cells exert tractional forces on the matrix that makes the gel compact and releases water [68]. During this compaction process cells get closer and form functional connections with one another creating a tissue resembling native myocardium that conducts electric impulses and beat synchronously [73].

To further investigate the behavioural response of hiPSC-cardiomyocytes in GelMA, optical measurement techniques were employed to measure action potentials and calcium transients. Optical mapping techniques have evolved to an essential technology for studying cardiovascular function and disease. The magnitude and pattern of action potential and measurement of intracellular calcium transient were quantified by image analysis of video data to reveal the electrophysiological properties. As expected the cardiomyocytes in 3D hydrogel scaffold showed higher action potential amplitude and calcium transient against cardiomyocytes seeded on a 2D platform. The cardiomyocytes readily transformed the 3D micro-environment mimicking the native structure to produce spontaneous contractions and action potentials. These findings demonstrate that the engineered 3D scaffold of 5% GelMA hydrogel encapsulated with cardiac fibroblasts and cardiac myocytes have higher and better cell-cell communication to allows synchronous contraction of cells which can be useful for next generation cardiac tissue substitutes for regenerative medicine and disease modelling applications. This control and development of cell growth can be employed to create a heart tissue patch with improved functionality providing synchronous beating.

## Chapter 8

### Conclusion and Future Work

#### 8.1 Conclusion

There is growing interest in using tissue engineering for controlling and *a priori* programming of the 3D disposition of cells in hydrogels. This project explored and understood the concepts and challenges faced in the bottom-up approaches in cardiac tissue engineering. This project addressed the need for designing and constructing a microscale biotechnology system to sustain and control cell organization and produce a functionalized engineered tissue heart construct. The investigation in the design process reflected main factors to mimic the native environment for cardiac cell growth such as architecture, chemical and mechanical stimuli, gradients and cell-cell and cell-scaffold communications and formation of myofibers such as gap junctions.

The application of lab-on-a-chip techniques to produce stacks of 3D-cell sheets provided an opportunity to explore the use of surface acoustic waves. The techniques for designing photomasks of slanted-finger IDTs and microfabrication were developed during the project. The problem of poor adhesion of metal layers during the metal evaporation process are addressed. For example the use of 20nm of titanium layer improved the adhesion of gold layer presenting significant promise for future work. The patterned SFIDTs were characterized to determine the working ranges of input frequencies, aperture, temperature changes and reproducibility in different mediums.

The biomaterial that was synthesized in this project called gelatin methacrylate was shown to be a promising matrix to work with surface acoustic wave based devices due to low viscosity, gelation properties and control over mechanical properties. GelMA hydrogel was synthesized from a natural polymer gelatin. The introduction of photo-crosslinkable methacryloyl substitution groups allowed fast gelation upon exposure to UV light irradiation in presence of photo-initiator. Rheological parameters were measured which allowed tailoring the degree of methacrylation concentration, initiator concentration and UV exposure time to suit with the surface acoustic waves. Due to the presence of RGD motifs and MMP-degradable amino acid sequences, GelMA has shown excellent biocompatibility and bioactivity for promoting cell adhesion and proliferation.

The use of surface acoustic waves for cell manipulation and alignment proved successful. The design of SFIDTs and experimental procedures for confining a range of particles were developed and tested. This work was able to integrate the SSAWs effectively within the hydrogel not only in 1D but 2D. The manipulation experiments revealed cardiomyocytes and cardiac fibroblasts, the native constituents of heart muscle tissue, were aligned with high fidelity and cell viability when patterned at 3.4MHz and 6.4MHz SSAWs generated on LiNbO<sub>3</sub> substrate using SFIDTs in 5% GelMA (w/v). The choice of synthesizing 5% GelMA however allowed surface acoustic waves to manipulate adherent and non-adherent cells in the hydrogel medium with high accuracy, speed and scalability.

The patterned cell fidelity was maintained during the culturing days that promoted cell growth in 3D hydrogel scaffold in the design and tested PMMA chamber. The work faced the effects of fluid motion and streaming before creating standing waves. The problem of turbulence and streaming was addressed by tuning to lower input frequencies and power levels. The chamber and the setup were carefully designed by taking the following into consideration – allowing coupling of SAWs in the hydrogel to create cell alignments; no pre-treatment procedures; the need to create micro-patterning over macroscale array in the chamber to produce feasible tissue constructs to *in vivo* implantation; biocompatible; easy to handle; allow rapid processing times. Standing-surface acoustic waves have shown to manipulate cardiac fibroblasts and cardiomyocytes using sound waves produced gently on a piezoelectric lithium niobate substrate. The amplitude of z-direction displacement of waves generated by input RF was found in range of nm scale which indicate the radiation forces that act on the cells will not alter their characteristics.

A second technique, dielectrophoresis, was used to complement the SAW device. However, this approach has been shown to have a dependency on conductivity of medium. It also required close proximity of cell to the electrodes and direct contact of the scaffold with the parallel array of electrodes. These resulted in poor maintenance of scaffold due to the Joule heating effect of the electrodes causing the hydrogel scaffold to denature. These hurdles precluded the studies of dielectrophoresis on the platform built. In addition, COMSOL Multiphysics software was used to interpret theoretical model of experimental results using acoustic and electrostatics modules. The results simulated showed the close to precise simulation of real-time experiments in measuring cell velocity, alignment time and measuring acoustic and dielectrophoretic forces.

The aim of this work was to understand and address the challenges faced in bottom-up approach of tissue engineering to produce a viable methodology of creating patterned cells to produce stacks of cell sheets to form a larger module of tissue.

In order to investigate the cytoskeleton of the produced engineered 3D cardiac constructs co-cultured of cardiomyocytes (heart muscle cells) and cardiac fibroblasts were immunostained to study the expression of cardiac proteins. Enhanced cytoskeletal organization with specific cardiac protein expression and synchronous contraction of the cells were observed. Using immunohistochemistry techniques cells were labelled F-actin, DAPI, Sarcomeric alpha-actinin, connexin-43 and troponin I to investigate the cell proliferation and growth in the aligned nodes and hydrogel and investigated using fluorescent and confocal microscopes.

In addition to patterning and aligning cells using SAWs, SAWs were also used for mechanically stimulating cells encapsulated in the hydrogels. The experimental results were tested with control samples under traditional conditions such as flat 2D surface. The electrophysiological responses observed between the samples yielded significant differences in magnitude of contractility, action potential and calcium transients. Due to the mechanical stimulation, orthogonal to the created patterns, the cells formed into elongated spindle shape which affected the growth of cells at the alignments as opposed to random distributed cells. This cell morphology shown in elongated forms have known to influence the formation of sarcomeres at the pressure gradient points in the hydrogel scaffold for producing synchronous amplified contractions. In these systems, action potentials were compared to a traditional 2D sample suspended in cell culture media.

In summary, this work has shown a platform where pressure-gradient manipulation can be controlled by tuning multiple frequencies to move suspended cells in hydrogel thereby creating a contamination free, contactless and label free method for creating spatial cell manipulation. This allowed cells to maintain their native state without pre-treatments. This work has shown that SSAW based devices are not bulky and require no mechanical moving parts. It is a single and easily integratable device that allows rapid patterning of cells and produces multiple samples in a short duration with ease of use and versatility. 3D scaffolds cultured in-vitro on this platform were easy to be recovered as an intact cell sheet. These cardiac sheets could be easily transplanted in-vivo in the heart tissues of animal models due to the presences of cardiac fibroblasts and cardiomyocytes to enhance cells transplant efficiency and effective cardiac tissue regeneration.

## 8.2 Future Work Introduction

While the scale of cells micrometre range, subcellular structure and protein sizes are of the order of nanometres. There have been major challenges faced in developing functional substitutes to replace damaged heart tissues. In comparison to native heart tissue microenvironment, the macroporous scaffold does seem to have poor electrically conductive fibres and lack nanofibrous architectures at sub-micron level (10-100nm diameter) which potentially means they are mechanically weaker than native heart tissues. Recent advances in nanotechnology have led to design and development of devices and scaffolds with nanoscale features to investigate cellular processes for medical applications.

## 8.3 Nano-Patterning in Tissue Engineering

Hybrid materials consisting of nanofibers have shown improved cell adhesion, viability and the ability to direct cells to self-assemble in three dimensions [192]. Nanoscale fibres composed of biological with or without synthetic polymers can be patterned into various orientations to influence cell and tissue behaviour. These fibres are called nanofibers which can mimic structure, morphology and influence tissue growth. The most common methodology for fabricating nanofiber scaffolds is electrospinning (Figure 8.1) [191].

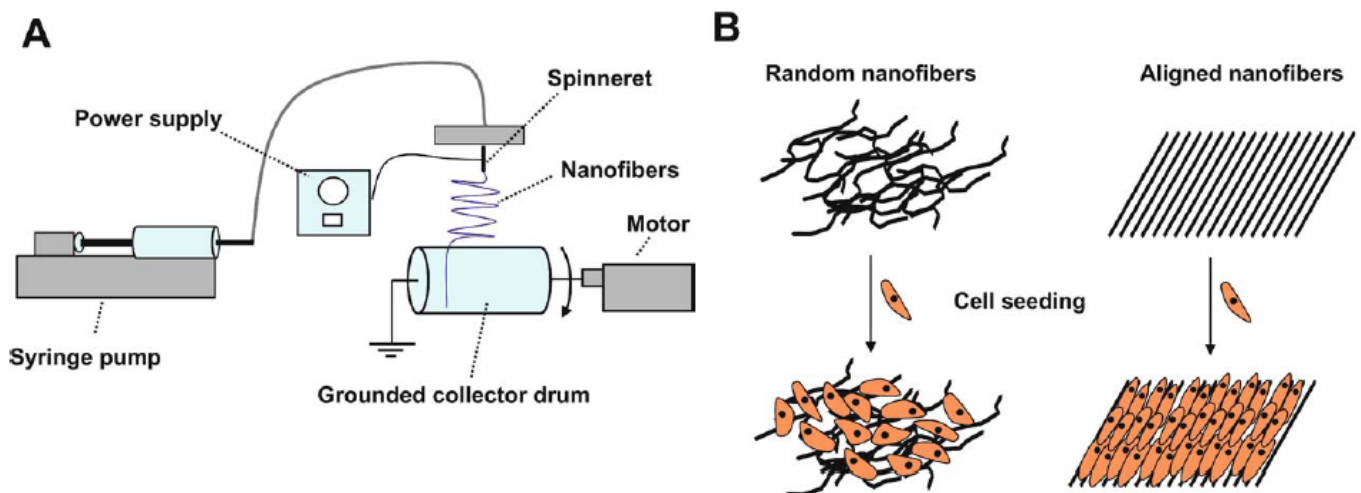


Figure 8.1, a) schematic representation of electrospinning nanofibers for tissue engineering, b) anisotropic nanofibers aligned to organize cells to enhance cell-cell interactions and create tissue-like structure [191]

Electrospinning can be employed for both biological and synthetic polymers that are biocompatible and biodegradable in nanoscale. The surface tension of the charged droplet is overcome by applying an electric field at the tip of the spinneret that causes a jet of polymer solution to travel from edge of droplet toward the collector substrate. The result is the deposition of thin polymer fibres on collector substrate. Figure 8.1b, shows parallel alignment of cells seeded on anisotropic nanofibers to allow influenced cell migration.

However, the use of this device is bulky and the width of the fibres produced may vary. Current assembly methods provide inadequate spatial control over the nanowires. Chen et al. [194] have shown alignment of nanowires using surface acoustic waves that provides high throughput from SAW based devices (Figure 8.2).

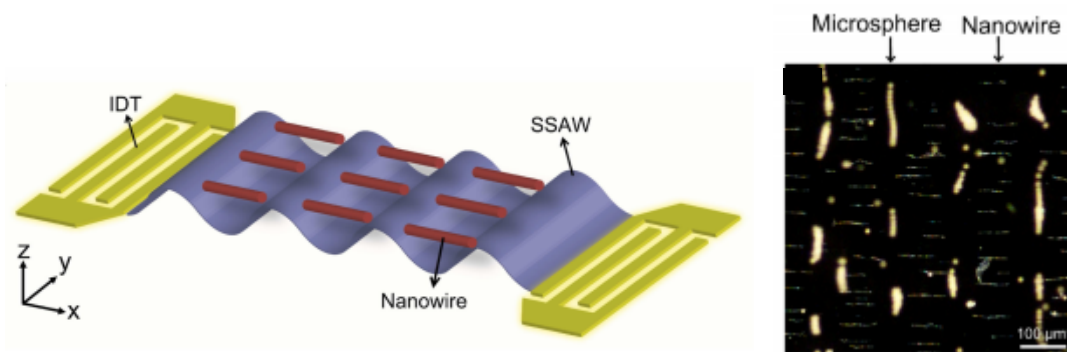


Figure 8.2, schematic representation of 1D nanowire patterning using SSAWs, b) shows patterning of Silver (Ag) nanowires and microspheres in 1D SSAW field showing their relative position with respect to alignment [194].

The authors have shown patterning of Ag nanowires and microspheres in a  $10 \times 10 \text{ mm}^2$  microchamber of height  $50 \mu\text{m}$  on  $\text{LiNbO}_3$  substrate which saw the beads travel towards the pressure nodes.

This ability to control the structure of nanotubes/nanowires means that SAW based devices could be a versatile tool for creating engineering tissue constructs with tuneable hydrogel mechanical properties. SR Shin et al. [192] have shown that addition of carbon nanotubes (CNTs) in GelMA has improved mechanical and electrophysiological properties of the hydrogel. CNTs bridged the pores in the GelMA by forming electrical conductive nanofibers which also strengthened the hydrogel. This has shown to promote cell adhesion, maturation and cell-cell electrical coupling to produce cardiac patches.

Thus by patterning both the cells and nanowires using a SSAW device would improve 3D scaffolds of therapeutic value of current cardiac patches by addressing improved viability, ultrastructural morphology, mechanical, adhesive and conducting properties and functionality and morphogenesis of engineered cardiac tissues. SSAW based method can therefore offer a new dimension of versatility and tunability to creating engineered tissue patches.

#### **8.4 Creating responsive hydrogels using SAWs**

There is a growing interest in developing intelligent (or smart) materials which have drug delivery, sensor and processors functions. Stimuli-responsive hydrogels respond to the change in their surroundings such as composition, temperature, pH and electric field [195]. SAWs can be employed to produce stimuli-responsive hydrogels as self-oscillating hydrogels for biomimetic applications. Stimuli-responsive hydrogels have three different functions – mechanical motion; mass transport and conversion and transmission of information. Electrically stimulated polyelectrolyte gels, organogels, gels with CNTs have been devised [196]. Magnetically field driven actuating system was designed using PVA gels containing magnetite ( $\text{Fe}_3\text{O}_4$ ) particles which provides dynamic motion in response to magnetic field [193]. SAW based devices can be implemented to develop drug delivery systems in order to improve drug pharmacokinetics and bio distribution in a pulsatile controlled rate. This system would only release the drug when it is needed and stops the release at a normal state under mechanical stimulation of acoustic waves in hydrogels.

Schroeder et al. [197] have used low frequency ultrasound for triggering liposomal drug release by physical means as a proof-of-concept pointing to controlled drug delivery using ultrasound. The repeated ultrasound-triggering on demand delivery system in the crosslinked hydrogel to maintain model drug containing liposomes in close proximity to gas filled microbubbles was used to enhance release on ultrasound application. The system developed could have different drug payloads and allow patterns of release depending on the liposomal drug loading, concentration, pulse time and pulse intensity (Figure 8.3). Despite having the addition of liposomes and microbubbles the viscoelasticity of the hydrogel remained intact.

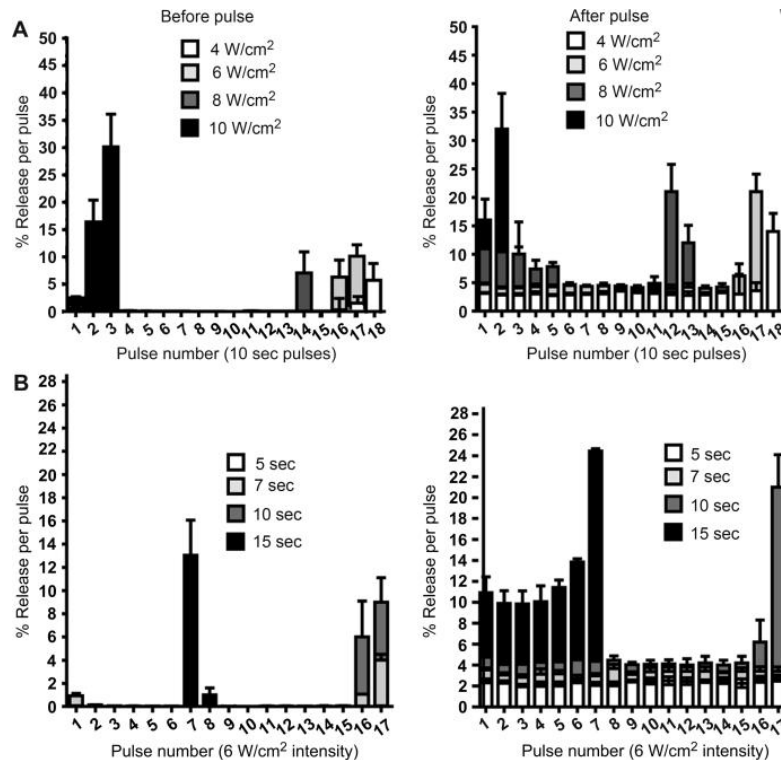


Figure 8.3, shows the effect of low frequency ultrasound pulse intensity (A) and duration (B) on release of trypan blue (dye) in hydrogel (dextran-CHO/CMC-ADH) at 37°C [198]

In addition Kelley et al [199] have shown the application of ultrasound on Type I collagen to control the microstructure during the hydrogel fabrication.

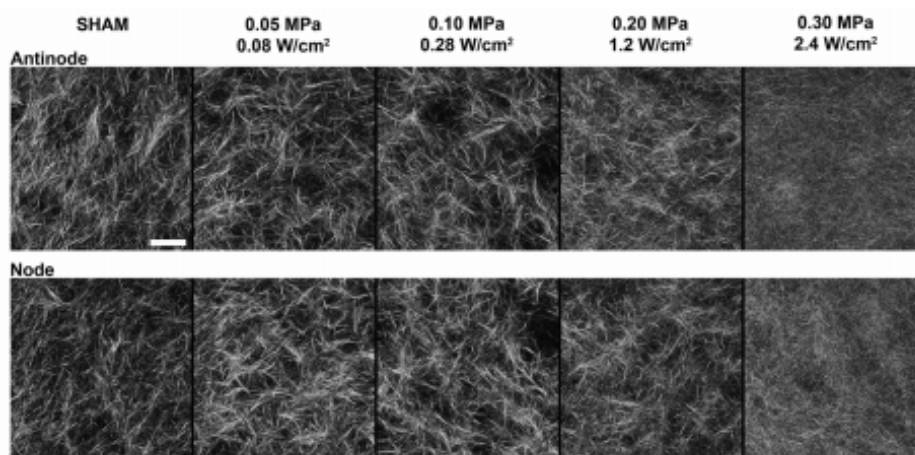


Figure 8.4, shows the ultrasound standing wave field exposure altering collagen fibre microstructure collected antinode(A) and node (B) using second harmonic generation microscopy (SHGM) [199]

SEM and SHGM images have shown that at higher frequency (8MHz) a large collagen sample produced denser network of short, thin fibrils at the centre of the sample and long and thicker fibrils outside the ultrasound beam region (Figure 8.4). The fibroblasts that were seeded in this gel migrated rapidly into small circular aggregates around the beam area and clustered fibroblasts remodelled the central dense sheets [199].

To date there has been no research published using surface acoustic waves to modify hydrogels and create a stimuli-responsive hydrogels for creating engineering tissue constructs and therapeutic applications. Numerous parameters can be controlled, without any chemical or physical treatment of cells, hydrogel, by changing the concentration of drug, modulating the acoustic waves, duration and intensity of the waves. The added advantage of non-invasiveness and site-specific control of the microstructure using acoustic devices have the potential to produce 3D scaffold with well-defined mechanical and biological properties with smart behaviours.

## **8.5 In Summary**

Recent advances have shown an increase in synthesizing advanced biomaterials using nanocomposites to produce stimuli-responsive scaffolds at nanoscale due to the signification mechanical, physical, chemical and electrical properties with the microenvironment. The type of nanofeatures should be non-toxic and not interfere with the cell behaviour when encapsulated in the biomaterial. This will however change the property of porous networks in the hydrogel, allow it to become more electrical conductive to generate higher magnitude action potentials and beating and be thermoresponsive. Surface acoustic wave based devices can be further investigated to study the behaviour of cell proliferation and differentiation in presence of such nanomaterials in the 3D architecture to draw a comparison with the work conducted here. Moreover, acoustic waves can also be employed to change the matrix network of the hydrogel structures by mechanical stimulating for applications such as drug delivery as a platform that offers minimal intervention and a standalone device at regulated pulse rates.

## References

1. Boccaccini, A. and Harding, S. (2011). Myocardial tissue engineering. Berlin: Springer.
2. Lanza, R., Langer, R. and Vacanti, J. (n.d.). Principles of tissue engineering, ISBN: 978-0-12-436630-5, First Edition
3. Obradović, B. (2012). Cell and tissue engineering. Berlin: Springer.
4. Palsson, B. and Bhatia, S. (2004). Tissue engineering. Upper Saddle River, N.J.: Pearson Prentice Hall.
5. Artmann, G. and Chien, S. (2008). Bioengineering in cell and tissue research. Berlin: Springer.
6. Fuchs JR, Nasser BA, Vacanti (2001) *Ann Thorac Surg* 72:577
7. Laurencin CT, Ambrosio AMA, Borden MD, Cooper JA (1999) *Annu Rev Biomed Eng* 1:9
8. Widmer MS, Mikos AG (1998) Fabrication of biodegradable polymer scaffolds for tissue engineering. In: Patrick CW, Mikos AG, McIntire LV (eds) *Frontiers in tissue engineering*. Pergamon, Oxford, p 107
9. Katti DS, Laurencin CT (2003) Synthetic biomedical polymers for tissue engineering and drug delivery. In: Shonaik
10. Udelson, J.E., Patten, R.D., Konstam, M.A.: New concepts in post-infarction ventricular remodeling. *Rev. Cardiovasc. Med.* 4(Suppl 3), S3–S12 (2003)
11. Anversa, P., Li, P., Zhang, X., Olivetti, G. and Capasso, J. (1993). Ischaemic myocardial injury and ventricular remodelling. *Cardiovascular Research*, 27(2), pp.145-157.
12. Zimmermann, W.H., Cesnjevar, R.: Cardiac tissue engineering: implications for pediatric heart surgery. *Pediatr. Cardiol.* 30(5), 716–723 (2009)
13. Akhyari, P., Kamiya, H., Haverich, A., et al.: Myocardial tissue engineering: the extracellular matrix. *Eur. J. Cardiothorac. Surg.* 34(2), 229–241 (2008)
14. Suuronen, E. and Ruel, M. (n.d.). Biomaterials for cardiac regeneration.

15. Li, R. and Weisel, R. (2014). Cardiac regeneration and repair. Cambridge: Woodhead Publishing.
16. Alenghat, F. and Ingber, D. (2002). Mechanotransduction: All Signals Point to Cytoskeleton, Matrix, and Integrins. *Science Signaling*, 2002(119), pp.pe6-pe6.
17. Curtis, A. and Riehle, M. (2001). Tissue engineering: the biophysical background. *Physics in Medicine and Biology*, 46(4), pp.R47-R65.
18. Katz BZ, Zamir E, Bershadsky A, Kam Z, Yamada KM, Geiger B (2000) *Mol Biol Cell* 11:1047
19. Discher, D. (2005). Tissue Cells Feel and Respond to the Stiffness of Their Substrate. *Science*, 310(5751), pp.1139-1143.
20. Davis, G., Bayless, K. and Mavila, A. (2002). Molecular basis of endothelial cell morphogenesis in three-dimensional extracellular matrices. *Anat. Rec.*, 268(3), pp.252-275.
21. Burridge, K., Fath, K., Kelly, T., Nuckolls, G. and Turner, C. (1988). Focal Adhesions: Transmembrane Junctions Between the Extracellular Matrix and the Cytoskeleton. *Annual Review of Cell Biology*, 4(1), pp.487-525.
22. Huang, S. and Ingber, D. (2000). Shape-Dependent Control of Cell Growth, Differentiation, and Apoptosis: Switching between Attractors in Cell Regulatory Networks. *Experimental Cell Research*, 261(1), pp.91-103.
23. Williams DF (1999) *The Williams dictionary of biomaterials*. Liverpool University Press, Liverpool
24. Barbucci R (ed) (2002) *Integrated biomaterial science*. Kluwer/Plenum, New York
25. Reis, R. and Weiner, S. (2004). Learning from nature how to design new implantable biomaterials. Dordrecht: Kluwer Academic Publishers.
26. Balguid, A., Mol, A., van Vlimmeren, M., Baaijens, F. and Bouten, C. (2008). Hypoxia Induces Near-Native Mechanical Properties in Engineered Heart Valve Tissue. *Circulation*, 119(2), pp.290-297.

27. Wiklund, M., Radel, S. and Hawkes, J. (2013). Acoustofluidics 21: ultrasound-enhanced immunoassays and particle sensors. *Lab Chip*, 13(1), pp.25-39.
28. Khademhosseini, A., Langer, R., Borenstein, J. and Vacanti, J. (2006). Microscale technologies for tissue engineering and biology. *Proceedings of the National Academy of Sciences*, 103(8), pp.2480-2487.
29. Braschler, T., Demierre, N., Nascimento, E., Silva, T., Oliva, A. and Renaud, P. (2008). Continuous separation of cells by balanced dielectrophoretic forces at multiple frequencies. *Lab Chip*, 8(2), pp.280-286.
30. Cui, H., Voldman, J., He, X. and Lim, K. (2009). Separation of particles by pulsed dielectrophoresis. *Lab on a Chip*, 9(16), p.2306.
31. Andres, J. (1953). Acoustic Streaming at Low Reynolds Numbers. *The Journal of the Acoustical Society of America*, 25(5), p.932.
32. Wixforth, A., Strobl, C., Gauer, C., Toegl, A., Scriba, J. and v. Guttenberg, Z. (2004). Acoustic manipulation of small droplets. *Anal Bioanal Chem*, 379(7-8), pp.982-991.
33. Guttenberg, Z., Rathgeber, A., Keller, S., Rädler, J., Wixforth, A., Kostur, M., Schindler, M. and Talkner, P. (2004). Flow profiling of a surface-acoustic-wave nanopump. *Physical Review E*, 70(5).
34. Li, H., Friend, J. and Yeo, L. (2007). Surface acoustic wave concentration of particle and bioparticle suspensions. *Biomedical Microdevices*, 9(5), pp.647-656.
35. Morita, T., Kurosawa, M. and Higuchi, T. (1999). Simulation of surface acoustic wave motor with spherical slider. *IEEE Transactions on Ultrasonics, Ferroelectrics and Frequency Control*, 46(4), pp.929-934.
36. Rocha-Gaso, M., March-Iborra, C., Montoya-Baides, Á. and Arnau-Vives, A. (2009). Surface Generated Acoustic Wave Biosensors for the Detection of Pathogens: A Review. *Sensors*, 9(7), pp.5740-5769.
37. Singh, R., Sankaranarayanan, S. and Bhethanabotla, V. (2010). Enhancement of acoustic streaming induced flow on a focused surface acoustic wave device: Implications for biosensing and microfluidics. *J. Appl. Phys.*, 107(2), p.024503.
38. Franke, T. and Wixforth, A. (2008). Microfluidics for Miniaturized Laboratories on a Chip. *ChemPhysChem*, 9(15), pp.2140-2156.

39. Yeo, L. and Friend, J. (2009). Ultrafast microfluidics using surface acoustic waves. *Biomicrofluidics*, 3(1), p.012002.
40. Qu, B., Wu, Z., Fang, F., Bai, Z., Yang, D. and Xu, S. (2008). A glass microfluidic chip for continuous blood cell sorting by a magnetic gradient without labeling. *Anal Bioanal Chem*, 392(7-8), pp.1317-1324.
41. Jellema, L.C. et al., 2009. Charge-based particle separation in microfluidic devices using combined hydrodynamic and electrokinetic effects. *Lab on a chip*, 9(13), pp.1914–25.
42. Baret, J.-C. et al., 2009. Fluorescence-activated droplet sorting (FADS): efficient microfluidic cell sorting based on enzymatic activity. *Lab on a chip*, 9(13), pp.1850–8.
43. Wang, Z. & Zhe, J., 2011. Recent advances in particle and droplet manipulation for lab-on-a-chip devices based on surface acoustic waves. *Lab on a chip*, 11(7), pp.1280–5.
44. Shung, K.K., 1985. Ultrasonic characterization of biological tissues. *Journal of biomechanical engineering*, 107(4), pp.309–14.
45. Hadjiargyrou, M. et al., 1998. Enhancement of fracture healing by low intensity ultrasound. *Clinical orthopaedics and related research*, (355 Suppl), pp.S216–29.
46. Wiklund, M., 2012. Acoustofluidics 12: Biocompatibility and cell viability in microfluidic acoustic resonators. *Lab on a chip*, 12(11), pp.2018–28.
47. Evander, M. & Nilsson, J., 2012. Acoustofluidics 20: applications in acoustic trapping. *Lab on a chip*, 12(22), pp.4667–76.
48. Spengler, J.F. et al., 2000. Observation of yeast cell movement and aggregation in a small-scale MHz-ultrasonic standing wave field. *Bioseparation*, 9(6), pp.329–41.
49. Bruus, H., 2012. Acoustofluidics 7: The acoustic radiation force on small particles. *Lab on a chip*, 12(6), pp.1014–21.
50. Ebisawa, K. et al., Ultrasound enhances transforming growth factor beta-mediated chondrocyte differentiation of human mesenchymal stem cells. *Tissue engineering*, 10(5-6), pp.921–9.
51. Lee, H.J. et al., 2006. Low-intensity ultrasound stimulation enhances chondrogenic differentiation in alginate culture of mesenchymal stem cells. *Artificial organs*, 30(9), pp.707–15.
52. Noriega, S. et al., 2007. Intermittent applications of continuous ultrasound on the viability, proliferation, morphology, and matrix production of chondrocytes in 3D matrices. *Tissue engineering*, 13(3), pp.611–8.

53. Fink, C. et al., 2000. Chronic stretch of engineered heart tissue induces hypertrophy and functional improvement. *FASEB journal : official publication of the Federation of American Societies for Experimental Biology*, 14(5), pp.669–79.
54. Hasanova, G.I. et al., 2011. The effect of ultrasound stimulation on the gene and protein expression of chondrocytes seeded in chitosan scaffolds. *Journal of Tissue Engineering and Regenerative Medicine*, 5(10), pp.815–822.
55. Coakley, W.T. et al., 2007. Cell manipulation in ultrasonic standing wave fields. *Journal of Chemical Technology & Biotechnology*, 44(1), pp.43–62
56. Hawkes, J.J., Barrow, D. & Coakley, W.T., 1998. Microparticle manipulation in millimetre scale ultrasonic standing wave chambers. *Ultrasonics*, 36(9), pp.925–931.
57. Berghard Palsson, Sangeeta N. Bhatia, *Tissue Engineering*, Pearson Education, 2004
58. Bojana Obradovic, *Cell and Tissue Engineering*, Springer Academic Mind, 2011
59. Radisic, M. et al., 2004. Medium perfusion enables engineering of compact and contractile cardiac tissue. *American journal of physiology. Heart and circulatory physiology*, 286(2), pp.H507–16.
60. Robert P. Lanza, Robert Langer, Joseph Vacanti, *Principles of Tissue Engineering*, 2 nd Edition, 2014, Academic Press
61. British heart foundation, <https://www.bhf.org.uk/#>
62. Donate life America statistics, [donatelife.net/statistics](http://donatelife.net/statistics)
63. US Department of health And Human Services, Donation and Transplantation, [organdonor.gov](http://organdonor.gov)
64. Khademhosseini, A. et al., 2006. Microscale technologies for tissue engineering and biology. *Proceedings of the National Academy of Sciences of the United States of America*, 103(8), pp.2480–7.
65. John P. Fisher, Antonios G. Mikos, Joseph D. Bronzino, Donald R. Peterson, *Tissue Engineering Principles and Practices*, CRC Press, 2013
66. *Molecular, Cellular, and Tissue Engineering*, Joseph D , Bronzino Donald R. Peterson (2015), CRC Press
67. John P. Fisher, Antonios G. Mikos, Joseph D. Bronzino, Donald R. Peterson, *Tissue Engineering, Principles and Practices*, CRC Press, 2013
68. Eschenhagen, T. et al., 2002. Cardiac tissue engineering. *Transplant Immunology*, 9(2), pp.315–321.

69. O'Brien, F.J., 2011. Biomaterials & scaffolds for tissue engineering. *Materials Today*, 14(3), pp.88–95.
70. Gaetani, R. et al., 2012. Cardiac tissue engineering using tissue printing technology and human cardiac progenitor cells. *Biomaterials*, 33(6), pp.1782–1790.
71. Venugopal, J.R. et al., 2012. Biomaterial strategies for alleviation of myocardial infarction. *Journal of the Royal Society, Interface / the Royal Society*, 9(66), pp.1–19.
72. Pahnke, A., Montgomery, M. & Radisic, M., 2015. Spatial and Electrical Factors Regulating Cardiac Regeneration and Assembly. In *Biomaterials for Cardiac Regeneration*. Cham: Springer International Publishing, pp. 71–92.
73. Huebsch, N. et al., 2010. Harnessing traction-mediated manipulation of the cell/matrix interface to control stem-cell fate. *Nature materials*, 9(6), pp.518–26.
74. Hoummady, M. et al., 1997. Acoustic wave sensors: design, sensing mechanisms and applications. *Smart Materials and Structures*, 6(6), pp.647–657.
75. Mould, R.F., 2007. Pierre curie, 1859-1906. *Current oncology (Toronto, Ont.)*, 14(2), pp.74–82.
76. Polh, A., 2000. A review of wireless SAW sensors. *IEEE transactions on ultrasonics, ferroelectrics, and frequency control*, 47(2), pp.317–32
77. Länge, K. et al., 2006. Integration of a surface acoustic wave biosensor in a microfluidic polymer chip. *Biosensors and Bioelectronics*, 22(2), pp.227–232.
78. Gronewold, T.M.A., 2007. Surface acoustic wave sensors in the bioanalytical field: Recent trends and challenges. *Analytica Chimica Acta*, 603(2), pp.119–128.
79. Renaudin, A. et al., 2010. Integrated active mixing and biosensing using surface acoustic waves (SAW) and surface plasmon resonance (SPR) on a common substrate. *Lab on a chip*, 10(1), pp.111–5.
80. Lee, J. et al., 2011. Sensitive and simultaneous detection of cardiac markers in human serum using surface acoustic wave immunosensor. *Analytical chemistry*, 83(22), pp.8629–35.
81. M. S. Vijaya, *Piezoelectric materials and devices: Applications in engineering and medical sciences*, CRC Press, 2013
82. Jr., D.S.B. & Wohltjen, H., 2008. *Surface acoustic wave devices for chemical analysis*.
83. Lenshof, A., Magnusson, C. & Laurell, T., 2012. Acoustofluidics 8: applications of acoustophoresis in continuous flow microsystems. *Lab on a chip*, 12(7), pp.1210–23.
84. Adkins, L.R. & Hughes, A.J., 1972. Investigations of Surface Acoustic Wave Directional Couplers. *IEEE Transactions on Sonics and Ultrasonics*, 19(1), pp.45–58.

85. Schmid, L. et al., 2012. Novel surface acoustic wave (SAW)-driven closed PDMS flow chamber. *Microfluidics and Nanofluidics*, 12(1-4), pp.229–235.
86. Ruppel, C.C.W., Reindl, L. & Weigel, R., 2002. SAW devices and their wireless communications applications. *IEEE Microwave Magazine*, 3(2), pp.65–71.
87. Miller, D.L. et al., 2012. Overview of therapeutic ultrasound applications and safety considerations. *Journal of ultrasound in medicine : official journal of the American Institute of Ultrasound in Medicine*, 31(4), pp.623–34.
88. Wiklund, M., 2012. Acoustofluidics 12: Biocompatibility and cell viability in microfluidic acoustic resonators. *Lab on a chip*, 12(11), pp.2018–28.
89. Ding, X. et al., 2012. On-chip manipulation of single microparticles, cells, and organisms using surface acoustic waves. *Proceedings of the National Academy of Sciences of the United States of America*, 109(28), pp.11105–9.
90. Li, H. et al., 2009. Effect of surface acoustic waves on the viability, proliferation and differentiation of primary osteoblast-like cells. *Biomicrofluidics*, 3(3), p.34102.
91. Friend, J. & Yeo, L.Y., 2011. Microscale acoustofluidics: Microfluidics driven via acoustics and ultrasonics. *Reviews of Modern Physics*, 83(2), pp.647–704.
92. Polh, A., 2000. A review of wireless SAW sensors. *IEEE transactions on ultrasonics, ferroelectrics, and frequency control*, 47(2), pp.317–32.
93. Gronewold, T.M.A., 2007. Surface acoustic wave sensors in the bioanalytical field: Recent trends and challenges. *Analytica Chimica Acta*, 603(2), pp.119–128.
94. Bruus, H. et al., 2011. Forthcoming Lab on a Chip tutorial series on acoustofluidics: acoustofluidics-exploiting ultrasonic standing wave forces and acoustic streaming in microfluidic systems for cell and particle manipulation. *Lab on a chip*, 11(21), pp.3579–80.
95. Shi, J. et al., 2009. Acoustic tweezers: patterning cells and microparticles using standing surface acoustic waves (SSAW). *Lab on a chip*, 9(20), pp.2890–5.
96. Wood, C.D. et al., 2008. Alignment of particles in microfluidic systems using standing surface acoustic waves. *Applied Physics Letters*, 92(4), p.044104.
97. Gedge, M. & Hill, M., 2012. Acoustofluidics 17: theory and applications of surface acoustic wave devices for particle manipulation. *Lab on a chip*, 12(17), pp.2998–3007.
98. Ding, X. et al., 2013. Surface acoustic wave microfluidics. *Lab on a Chip*, 13(18), p.3626.
99. Auld, B. *Acoustic Fields and Waves in Solids*. New York: Wiley Press; 1973.

100. Nama, N. et al., 2015. Numerical study of acoustophoretic motion of particles in a PDMS microchannel driven by surface acoustic waves. *Lab on a chip*, 15(12), pp.2700–9.
101. Li, S. et al., 2013. An on-chip, multichannel droplet sorter using standing surface acoustic waves. *Analytical chemistry*, 85(11), pp.5468–74.
102. Wiklund, M., Green, R. & Ohlin, M., 2012. Acoustofluidics 14: Applications of acoustic streaming in microfluidic devices. *Lab on a chip*, 12(14), pp.2438–51.
103. Wixforth, A. et al., 2004. Acoustic manipulation of small droplets. *Analytical and bioanalytical chemistry*, 379(7-8), pp.982–91
104. Ahmed, D. et al., 2015. Acousto-plasmodfluidics: Acoustic modulation of surface plasmon resonance in microfluidic systems. *AIP advances*, 5(9), p.097161.
105. Vanneste, J. & Bühler, O., 2011. Streaming by leaky surface acoustic waves. *Proc. R. Soc. A*, 467, pp.1779–1800.
106. Li, Y. et al., 2012. Integrated microfluidics system using surface acoustic wave and electrowetting on dielectrics technology. *Biomicrofluidics*, 6(1), pp.12812–128129.
107. Du, X.Y. et al., 2009. Microfluidic pumps employing surface acoustic waves generated in ZnO thin films. *Journal of Applied Physics*, 105(2), p.024508.
108. Guldiken, R. et al., 2012. Sheathless size-based acoustic particle separation. *Sensors (Basel, Switzerland)*, 12(1), pp.905–22.
109. Frommelt, T. et al., 2008. Flow patterns and transport in Rayleigh surface acoustic wave streaming: combined finite element method and raytracing numerics versus experiments. *IEEE transactions on ultrasonics, ferroelectrics, and frequency control*, 55(10), pp.2298–305.
110. Laurell, T., Petersson, F. & Nilsson, A., 2007. Chip integrated strategies for acoustic separation and manipulation of cells and particles. *Chemical Society reviews*, 36(3), pp.492–506.
111. Moreau, S., Bailliet, H. & Valière, J.-C., 2008. Measurements of inner and outer streaming vortices in a standing waveguide using laser doppler velocimetry. *The Journal of the Acoustical Society of America*, 123(2), p.640.
112. Shi, J. et al., 2007. Focusing microparticles in a microfluidic channel with standing surface acoustic waves (SSAW)
113. Shi, J. et al., 2009. Acoustic tweezers: patterning cells and microparticles using standing surface acoustic waves (SSAW). *Lab on a chip*, 9(20), pp.2890–5.
114. Girardo, S. et al., 2008. Polydimethylsiloxane–LiNbO<sub>3</sub> surface acoustic wave micropump devices for fluid control into microchannels. *Lab on a Chip*, 8(9), p.1557.

115. Lin, S.-C.S., Mao, X. & Huang, T.J., 2012. Surface acoustic wave (SAW) acoustophoresis: now and beyond. *Lab on a chip*, 12(16), pp.2766–70.
116. Rogers, P.R., Friend, J.R. & Yeo, L.Y., 2010. Exploitation of surface acoustic waves to drive size-dependent microparticle concentration within a droplet. *Lab on a chip*, 10(21), pp.2979–85.
117. Sadhal, S.S., 2012. Acoustofluidics 13: Analysis of acoustic streaming by perturbation methods. *Lab on a chip*, 12(13), pp.2292–300.
118. Beyssen, D. et al., 2006. Microfluidic device based on surface acoustic wave. *Sensors and Actuators B: Chemical*, 118(1), pp.380–385.
119. Girardo, S. et al., 2008. Polydimethylsiloxane–LiNbO<sub>3</sub> surface acoustic wave micropump devices for fluid control into microchannels. *Lab on a Chip*, 8(9), p.1557
120. Wiklund, M., Green, R. & Ohlin, M., Acoustofluidics 14: Applications of acoustic streaming in microfluidic devices, *Lab Chip*, (2012), 12, pp. 2438–2451
121. Frampton, K., 2001. The scaling of acoustic streaming for application in microfluidic devices. *The Journal of the Acoustical Society of America*, 109(5), pp.2348–2348.
122. Yuen, W.T. et al., 2014. Aerosol Science and Technology The Use of Nonlinear Acoustics as an Energy- Efficient Technique for Aerosol Removal The Use of Nonlinear Acoustics as an Energy-Efficient Technique for Aerosol Removal. *Aerosol Science and Technology*, 48(9), pp.907–915.
123. T., A. et al., 2010. Optoelectronic Tweezers for the Manipulation of Cells, Microparticles, and Nanoparticles. In *Recent Optical and Photonic Technologies*. InTech.
124. Nelson, W.C. & Kim, C.-J. “CJ,” 2012. Droplet Actuation by Electrowetting-on-Dielectric (EWOD): A Review. *Journal of Adhesion Science and Technology*.
125. Tan, M.K., Friend, J.R. & Yeo, L.Y., 2007. Microparticle collection and concentration via a miniature surface acoustic wave device. *Lab on a chip*, 7(5), pp.618–25.
126. Ding, X. et al., 2012. Tunable patterning of microparticles and cells using standing surface acoustic waves. *Lab on a chip*, 12(14), pp.2491–7.
127. Falkovich, G. et al., 2005. Surface tension: floater clustering in a standing wave. *Nature*, 435(7045), pp.1045–6.
128. Xu, F. et al., 2011. The assembly of cell-encapsulating microscale hydrogels using acoustic waves. *Biomaterials*, 32(31), pp.7847–55.
129. Yeo, L.Y. & Friend, J.R., 2009. Ultrafast microfluidics using surface acoustic waves. *Biomicrofluidics*, 3(1), p.12002.

130. Wohltjen, H. & Dessy, R., 2002. Surface acoustic wave probe for chemical analysis. I. Introduction and instrument description.
131. Shi, J. et al., 2009. Continuous particle separation in a microfluidic channel via standing surface acoustic waves (SSAW). *Lab on a chip*, 9(23), pp.3354–9.
132. Ding, X. et al., 2012. Tunable patterning of microparticles and cells using standing surface acoustic waves. *Lab on a Chip*, 12(14), p.2491.
133. Luong, T.-D. & Nguyen, N.-T., *Surface Acoustic Wave Driven Microfluidics*.
134. Sadhal, S.S., 2012. Acoustofluidics 13: Analysis of acoustic streaming by perturbation methods. *Lab on a chip*, 12(13), pp.2292–300
135. Tan, M.K., Friend, J.R. & Yeo, L.Y., 2007. Microparticle collection and concentration via a miniature surface acoustic wave device. *Lab on a chip*, 7(5), pp.618–25.
136. Shi, J. et al., 2009. Acoustic tweezers: patterning cells and microparticles using standing surface acoustic waves (SSAW). *Lab on a chip*, 9(20), pp.2890–5.
137. Ding, X. et al., 2012. On-chip manipulation of single microparticles, cells, and organisms using surface acoustic waves. *Proceedings of the National Academy of Sciences*, 109(28), pp.11105–11109.
138. Thévoz, P. et al., 2010. Acoustophoretic synchronization of mammalian cells in microchannels. *Analytical chemistry*, 82(7), pp.3094–8.
139. Pethig, R., 2010. Review article-dielectrophoresis: status of the theory, technology, and applications. *Biomicrofluidics*, 4(2).
140. Ronald Pethig, *Lab-on- Chip Technologies*, PGEE11042, Bioelectronics, University of Edinburgh, 2012.
141. Thomas B. Jones, *Electromechanics of Particles*, Cambridge University Press, 2005.
142. Satish K. Gupta, *Modern's abc of Physics*, vol. II, Modern Publishers, 2005.
143. Pohl, H.A., 1951. The Motion and Precipitation of Suspensoids in Divergent Electric Fields. *Journal of Applied Physics*, 22(7), p.869.
144. Huang, Y. & Pethig, R., 1991. Electrode design for negative dielectrophoresis. *Measurement Science and Technology*, 2(12), pp.1142–1146.
145. Chung, C. et al., 2011. Dielectrophoretic Characterisation of Mammalian Cells above 100 MHz. *Journal of Electrical Bioimpedance*, 2(1), pp.64–71.
146. Collins, D.J., Alan, T. & Neild, A., 2014. Particle separation using virtual deterministic lateral displacement (vDLD). *Lab on a chip*, 14(9), pp.1595–603.

147. Wiklund, M. et al., 2006. Ultrasonic standing wave manipulation technology integrated into a dielectrophoretic chip. *Lab on a chip*, 6(12), pp.1537–44.
148. Guo, J., Kang, Y. & Ai, Y., 2015. Radiation dominated acoustophoresis driven by surface acoustic waves. *Journal of Colloid and Interface Science*, 455, pp.203–211.
149. Chung, G.-S. & Phan, D.-T., 2010. Finite element modeling of surface acoustic waves in piezoelectric thin films. *Journal of the Korean Physical Society*, 57(3), pp.446–450.
150. Surface Acoustic Wave Gas Sensor, **Application ID: 2129, COMSOL Multiphysics**
151. Thomas, R.S. et al., 2009. Negative DEP traps for single cell immobilisation. *Lab on a Chip*, 9(11), p.1534.
152. Madou, M.J., 2002. *Fundamentals of microfabrication : the science of miniaturization*, CRC Press.
153. Adams, T.M. & Layton, R.A., 2010. Creating and transferring patterns—Photolithography. In *Introductory MEMS*. Boston, MA: Springer US, pp. 65–94.
154. Adams, T.M. & Layton, R.A., 2010. Piezoelectric transducers. In *Introductory MEMS*. Boston, MA: Springer US, pp. 255–282.
155. Adams, T.M. & Layton, R.A., 2010. MEMS transducers—An overview of how they work. In *Introductory MEMS*. Boston, MA: Springer US, pp. 167–210.
156. Tkaczyk, T.S. & Society of Photo-optical Instrumentation Engineers., 2010. *Field guide to microscopy*, SPIE.
157. Anon, *Education in Microscopy and Digital Imaging*. Carl Zeiss Microscopy Online Campus. Available at: <http://zeiss-campus.magnet.fsu.edu/>.
158. Truernit, E., 2014. Phloem imaging. *Journal of experimental botany*, 65(7), pp.1681–8.
159. Polytec, Basic Principles of Vibrometry. Available at: <http://www.polytec.com/us/solutions/vibration-measurement/basic-principles-of-vibrometry/>.
160. Ahmadi, S. et al., 2004. Characterization of multi- and single-layer structure SAW sensor. In *Proceedings of IEEE Sensors, 2004*. IEEE, pp. 1129–1132.
161. Campbell, C., (1998). *Surface Acoustic Wave Devices for Mobile and Wireless Communications*. San Diego: Academic Press.
162. Chaudhary, M and Whitesides, G. (1992). How to make water run uphill. *Science*, 256(5063), pp. 1539-1541

163. Glynne-Jones, P. and Hill, M. (2013). Acoustofluidics 23: acoustic manipulation combined with other force fields. *Lab on a Chip*, 13(6), p.1003.
164. Hornsteiner, J., Born, E., Fischerauer, G. and Riha, E. (1998) Surface acoustic wave sensors for high temperature applications, *IEEE International Frequency Control Symposium 1998*
165. Jiao, Z., Nguyen, N.T. and Huang, X.(2007). Thermocapillary actuation of liquid plugs using a heater array. *Sens. Actuators A: Physical*, 140(2), pp. 145-155.
166. Luong, T., Nguyen, N. (2010).Surface Acoustic Wave Driven Microfluidics – A Review. *Micro and Nanosystems*, 2(3), pp.217-225
167. Pollack, M., Fair, R. and Shenderov, A. (2000). Electrowetting-based actuation of liquid droplets for microfluidic applications. *Appl. Phys. Lett.*, 77(11), p.1725-1726
168. Shi, J., Ahmed, D., Mao, X., Lin, S., Lawit, A and Huang, T. (2009). Acoustid tweezers: patterning cells and microparticles using standing surface acoustic waves (SSAW). *Lab on a Chip*, 9(20), p.2890-2895.
169. Wohltjen, H. and Dessy, R. (1979). Surface acoustivc wave probe for chemical analysis. I. Introduction and instrument description. *Analytical Chemistry*, 51 (9), pp. 1458-1464.
170. Yariv, A. and Yeh, P. (1984). *Optical Waves In Crystals: Propagation and Control of Laser Radiation*. New York: John Wiley and Sons.
171. Du Plessis, H.G., Perold, W.J. & Perold, W., Simulation of ZnO Enhanced SAW Gas Sensor.
172. Djabourov, M. and Papon, P. (1983).Influence of thermal treatments on the structure and stability of gelatin gels. *Polymer*, 24(5), pp.537-538
173. Du, Y., Lo, E., Ali, S. and Khademhosseini, A. (2008). Directed assembly of cell-laden microgels for fabrication of 3D tissue constructs. *Proceedings of National Academy of Sciences*, 105(28), pp.9522-9527.
174. Edman, P., Ekman, B. and Sjöholm, I. (1980). Immobilization of proteins in microspheres of biodegradable polyacryldextran. *Journal of Pharmaceutical Sciences*, 69(7), pp.838-842.
175. Engler, J. et al., (2006). Matrix elasticity directs stem cell lineage specification. *Cell*, 126(4), pp.677–689.
176. Engler, J. et al., (2007). Extracellular matrix elasticity directs stem cell differentiation. *Journal of Musculoskelet & Neuronal Interactions*, 7(4), p.335.
177. Guenet, M. (1992). *Thermoreversible Gelation of Polymers and Biopoly-mers*. New York: Academic Press, Chapter 3.
178. Ross-Murphy, B. (1997)Structure and Rheology of Gelatin Gels. *The Imaging Science Journal*, 45, pp.205-209.

179. Nijenhuis, K. (1981). Investigation into the ageing process in gels of gelatin/water systems by the measurement of their dynamic moduli: Part I. *Colloid & Polymer Sci*, 259(5), pp.522-530.
180. Nijenhuis, K. (1997). Thermoreversible networks: viscoelastic properties and structure of gels. *Advances Polymer Science*, 130, p.160-194.
181. Veis, A. (1964). *The Macromolecular Chemistry of Gelatin*. Academic Press.
182. Ward, G. and Courts, A. (1977). *The Science and Technology of Gelatin*. New York: Academic Press.
183. Panduranga-Rao, K. (1996). Recent developments of collagen-based materials for medical applications and drug delivery systems. *Journal of Biomaterials Science, Polymer Edition*, 7(7), pp.623-645.
184. Peppas, N. et al., (2006). Hydrogels in Biology and Medicine: From Molecular Principles to Bionanotechnology. *Adv. Mater.*, 18(11), pp.1345–1360.
185. Ross-Murphy, B. (1992). Structure and rheology of gelatin gels: recent progress. *Polymer*, 33, pp. 2622-2627.
186. Scherzer, T. et al., (1997). Electron beam curing of methacrylated gelatin. I. Dependence of the degree of cross-linking on the irradiation dose. *Journal of Applied Polymer Science*, 63(10), pp.1303-1312.
187. Nichol, J. et al., (2010). Cell-laden microengineered gelatin methacrylate hydrogels. *Biomaterials*, 31(21), pp.5536–5544.
188. Normand, V. et al., (2000). Gelation kinetics of gelatin: a master curve and network modelling. *Macromolecules*, vol.33, pp.1063-1071.
189. Kolesky, D.B. et al., 2014. 3D bioprinting of vascularized, heterogeneous cell-laden tissue constructs. *Advanced materials (Deerfield Beach, Fla.)*, 26(19), pp.3124–30. Available at: <http://www.ncbi.nlm.nih.gov/pubmed/24550124> [Accessed July 1, 2016].
190. An I. Van Den Bulcke, † et al., 2000. Structural and Rheological Properties of Methacrylamide Modified Gelatin Hydrogels.
191. Dvir, T. et al., 2011. Nanowired three-dimensional cardiac patches. *Nature Nanotechnology*, 6(11), pp.720–725.
192. Shin, S.R. et al., 2013. Carbon-Nanotube-Embedded Hydrogel Sheets for Engineering Cardiac Constructs and Bioactuators. *ACS Nano*, 2013, 7 (3), pp 2369–2380
193. Ahn, Y. et al., 2014. Highly Conductive and Flexible Silver Nanowire-Based Microelectrodes on Biocompatible Hydrogel. *ACS Appl. Mater. Interfaces*, 2014, 6 (21), pp 18401–18407

194. Chen, Y. et al., 2013. Tunable Nanowire Patterning Using Standing Surface Acoustic Waves, *ACS Nano*, 2013, 7 (4), pp 3306–3314
195. Yoshida, R. & Okano, T., 2010. Stimuli-Responsive Hydrogels and Their Application to Functional Materials. In *Biomedical Applications of Hydrogels Handbook*. New York, NY: Springer New York, pp. 19–43.
196. Osada, Y., Okuzaki, H. & Hori, H., 1992. A polymer gel with electrically driven motility. *Nature*, 355(6357), pp.242–244.
197. Yoshida, R., 2010. Design of self-oscillating gels and application to biomimetic actuators. *Sensors (Basel, Switzerland)*, 10(3), pp.1810–22.
198. Epstein-Barash, H. et al., 2010. A microcomposite hydrogel for repeated on-demand ultrasound-triggered drug delivery. *Biomaterials*, 31(19), pp.5208–5217.
199. Garvin, K.A. et al., 2013. Controlling collagen fiber microstructure in three-dimensional hydrogels using ultrasound. *The Journal of the Acoustical Society of America*, 134(2), p.1491.
200. Kanda, Keiichi, Takehisa Matsuda, and Takahiro Oka. "Mechanical Stress Induced Cellular Orientation And Phenotypic Modulation Of 3-D Cultured Smooth Muscle Cells". *ASAIO Journal* 39.3 (1993): M686-M690. Web.
201. Chung, Cindy et al. "Hydrogel Crosslinking Density Regulates Temporal Contractility Of Human Embryonic Stem Cell-Derived Cardiomyocytes In 3D Cultures". *Soft Matter* 8.39 (2012): 10141. Web.
202. Wang, Peng-Yuan et al. "Modulation Of Alignment, Elongation And Contraction Of Cardiomyocytes Through A Combination Of Nanotopography And Rigidity Of Substrates". *Acta Biomaterialia* 7.9 (2011): 3285-3293. Web.
203. Simmons, Chelsey S., Bryan C. Petzold, and Beth L. Pruitt. "Microsystems For Biomimetic Stimulation Of Cardiac Cells". *Lab on a Chip* 12.18 (2012): 3235. Web.
204. Herron, T. J., P. Lee, and J. Jalife. "Optical Imaging Of Voltage And Calcium In Cardiac Cells & Tissues". *Circulation Research* 110.4 (2012): 609-623. Web.
205. Annabi, Nasim et al. "Highly Elastic Micropatterned Hydrogel For Engineering Functional Cardiac Tissue". *Adv. Funct. Mater.* 23.39 (2013): 4950-4959. Web.
206. "Http://Www.Jeol.Co.Jp/En/Applications/Pdf/Sm/Sem\_Atoz\_All.Pdf". *JEOL, Serving advanced technology*. N.p., 2016. Web. 31 July 2016.
207. Gree, Adam. "The History And Working Principle Of The Scanning Electron Microscope (SEM)". *AZoNano.com*. N.p., 2015. Web. 31 July 2016.

208. "Confocal Microscopy". *Nikon's MicroscopyU*. N.p., 2016. Web. 31 July 2016.
209. Wilhem, S, B Grobler, and H Heinz. "Confocal Laser Scanning Microscopy Principles". <http://zeiss-campus.magnet.fsu.edu/referencelibrary/pdfs/ZeissConfocalPrinciples.pdf>. Web. 31 July 2016.
210. Sambrook, J., and D. W. Russell. "Molecular cloning. 3rd." *Cold Spring Harbor Laboratory Press, New York* 2 (2001): 8-1.
211. Ruoslahti, Erkki. "RGD AND OTHER RECOGNITION SEQUENCES FOR INTEGRINS". *Annual Review of Cell and Developmental Biology* 12.1 (1996): 697-715.
212. Barczyk, Malgorzata, Sergio Carracedo, and Donald Gullberg. "Integrins". *Cell and Tissue Research* 339.1 (2009): 269-280.
213. "The Effect Of Pore Size On Cell Adhesion In Collagen-GAG Scaffolds". *Sciencedirect.com*. N.p., 2016.
214. Chen, Pu et al. "Biotunable Acoustic Node Assembly Of Organoids". *Advanced Healthcare Materials* 4.13 (2015): 1937-1943.
215. Albrecht, Dirk R et al. "Probing The Role Of Multicellular Organization In Three-Dimensional Microenvironments". *Nature Methods* 3.5 (2006): 369-375.
216. Xu, Feng et al. "The Assembly Of Cell-Encapsulating Microscale Hydrogels Using Acoustic Waves". *Biomaterials* 32.31 (2011): 7847-7855.
217. Gorkov, L.P. "On the Forces Acting on a Small Particles in an Acoustical Field in an Ideal Fluid", *Sov. Phys. Dokl.* 6, (1962) 773-775
218. Barnkob, R., Augustsson, P., Laurell, T. Bruus, H., "Measuring the local pressure amplitude in microchannel acoustophoresis", *Lab Chip* 10, (2010) 563-570